



The
University
Of
Sheffield.

Department
Of
Mechanical
Engineering

System Dynamic Modelling of Wind Turbine Gearbox Under Normal and Transient Operating Conditions

Author:

Haider Rahman Dawood Al-Hamadani

Registration No: 130138613

February 2018

Supervisor:

Dr. Hui Long

Thesis submitted to the Department of Mechanical Engineering, University of
Sheffield in partial fulfilment of the requirements for the degree of

Doctor of Philosophy (PhD)

Abstract

Wind turbine gearbox (WTG) undergoes various and extreme operational conditions during the designed operational life of 20~25 years. Reliability analysis data shows that the premature failures occurred in some critical mechanical components in the WTG, such as gears and bearings. In current research of multibody system modelling, WTG components are generally modelled as lumped masses and isolated from the rest of the wind turbine (WT) drivetrain components. This approach may not adequately represent loading conditions that gears and bearings being subjected to therefore leading to the underestimation of effect of critical loads on the premature failures.

This study applied two modelling approaches for modelling multibody systems of the WTG: the pure torsional multibody system modelling and the rigid and discrete flexible multibody system modelling. Both approaches were used to investigate the dynamic response of different WTG configurations under normal operation and shutdown operating conditions. Field measured rotor torque data under normal operation and shutdown conditions, obtained from an operating WT, were used directly as rotor torque inputs for the modelled WTGs. The comparison of the dynamic response of WTG components during these two loading conditions shows that the shutdown condition is one of the most critical loading conditions that the WTG components may experience therefore may contribute to their premature failures.

The pure torsional multibody dynamic modelling with three different configurations of WTG design were developed by using MATLAB/Simulink. The model of each configuration captured more details of drivetrain dynamic behaviour than that of the widely used two-mass or five-mass drivetrain models. The influence of the WTG design configuration on the eigenfrequencies of the system and how they affected the dominant frequencies and gear meshing forces during normal operation and shutdown conditions were investigated in detail. Parametric study of variations of key variables of the WTG components was performed to investigate their effect on the dynamic responses of the system.

The rigid and discrete flexible multibody system modelling of WTG was developed by using SIMPACK software to model the dynamic behaviour of the critical components within the WTG during different operational conditions. The cross-coupling and clearance effect were considered in modelling bearings. The 'Slicing' approach was used to investigate the effects of gear misalignment and tilting along the gear axes. The developed rigid and discrete flexible multibody model of WTG can predict the gear tilting and the loads on gears and bearings during normal operation and shutdown conditions. For both gears and bearings within the WTG, load distribution, maximum contact stress on surface, subsurface stress distribution, and fatigue damage were investigated under normal operation and shutdown conditions.

This study shows that during normal operation and shutdown, the contact stress of gears in high speed stage is higher than that on other gears within the WTG and it exceeds the allowable material contact stress thus may contribute to higher fatigue damage during the WTG operation. This study also found that the number of rollers in contact with raceways of bearings changes consistently during normal operation however changes dramatically during shutdown condition. This results in occurrence of overloading condition and subjects the bearings to maximum contact stress higher than the recommended value therefore may contribute to higher fatigue damage of some bearings within the WTG. The findings of this study provide valuable insights into the dynamic behaviour of the WTG under normal and transient operating conditions. The results obtained would support the future development of condition monitoring and preventive maintenance of the critical components of gears and bearings in the WTG.

Acknowledgements

Thanks to Allah to be always with me to give guidance and mercy along my life, for his help and blesses to give me strength and patience to complete the thesis. I would like to extend my sincerest appreciation and my deep gratitude to my supervisor Dr. Hui Long. She has been my supervisor for more than four years, and her support and guidance has remained resolute throughout. I dedicate this thesis to: the man who causes my progress and success, my father and my first teacher, Mr. Rahman Dawood Al-Hamadani; to the symbol of the affection and kindness, my mother; Mrs. Amal Hussein Al-Hamadani. Special and deep thanks to the special person that I respect and love her from deep of my heart, my lovely wife Zina. Her psychological support through this important phase of my life is highly valued. Massive thanks to my kids which stands always beside me and supports me psychologically during the harsh times, my lovely princess Farah Al-Hamadani and my prince Ahmed Al-Hamadani. Special thanks to my friends, Mohanad, Haval, Firas, Ziad which supported me by advice and litany. My colleagues and fellows at work, Jasim Al-Bedhany and Hamza Al-Tameemi, Sheng and Zhaohua, you have always kept the office lively and full of interesting discussions, both about work and life in general, and have helped in keeping the stress levels out of shoulders, so a big thank you goes out to them too, it is a pleasure working alongside them. Grateful feelings go to my beloved country Iraq. The author would like to thank an anonymous industrial partner for providing the field data used in this work. Finally, I would like to acknowledge my sponsor, the Iraqi Ministry of Higher Education and Scientific Research (MOHESR) in Baghdad, and its representatives the Iraqi Cultural Attaché in London, Al-Furat Al-Awsat Technical University in Najaf and the Technical College (TCM) in Al-Mussaib, without their help and support, I would not have had the opportunity to study at this prestigious university, University of Sheffield, and be where I am today.

List of publications from this work

➤ Publications

H. Al-Hamadani, H. Long, and M. Cartmell, "Effects of model complexity on torsional dynamic responses of NREL 750 kw wind turbine drivetrain," in *Power Transmissions: Proceedings of the International Conference on Power Transmissions 2016 (ICPT 2016), Chongqing, PR China, 27-30 October 2016*, 2016, p. 205.

H. Al-Hamadani, T. An, M. King, and H. Long, "System dynamic modelling of three different wind turbine gearbox designs under transient loading conditions," *International Journal of Precision Engineering and Manufacturing*, vol. 18, pp. 1659-1668, 2017.

➤ Posters

"Effects of Torque Reversal on Gear Surface Damage in Wind Turbine Gearbox" at *11th TriboUK Conference 2014*, Sheffield, 6-7 April 2014.

"Field Measurement Data Analysis and Modeling of Wind Turbine Gearbox by using MATLAB" at *EPSRC Supergen Wind Hub General Assembly 2015*, Loughborough, 14 April 2015.

"Wind Turbine Gearbox Transient Load Analysis and Modelling" at *University of Sheffield Engineering Symposium (USES)*, Sheffield, 24 June 2015

"Multibody Dynamic Modelling of Wind Turbine Gearbox to Investigate Bearing and Gear Loading Under Different Operational Conditions" at *Supergen Wind Hub General Assembly 2016*, Glasgow, 26 May 2016.

"Multibody Dynamic Modelling of Wind Turbine Gearbox to Investigate Bearing and Gear Loading Under Different Operational Conditions" at *the 6th European Conference on Structural Control (EACS) 2016*, Sheffield, 11-13 July 2016.

"Multibody Dynamic Modelling of Wind Turbine Gearbox to Investigate Bearing and Gear Loading Under Different Operational Conditions" at *Engineering Researcher Symposium 2017*, Sheffield, 30 June 2017.

List of Contents

| | |
|--|-----------|
| Abstract | i |
| Acknowledgements | iii |
| List of publications from this work | iv |
| List of Contents | v |
| List of Figures..... | ix |
| List of Tables..... | xvii |
| Nomenclature and Abbreviations | xviii |
| 1 INTRODUCTION | 1 |
| 1.1 Background | 2 |
| 1.2 Research Problem..... | 3 |
| 1.3 Aim and Objectives..... | 4 |
| 1.4 Research Novelty and New Contributions | 5 |
| 1.5 Thesis Layout and Structure..... | 5 |
| 2 LITERATURE REVIEW | 8 |
| 2.1 Configurations of Wind Turbine Gearbox..... | 9 |
| 2.2 Wind Turbine Gearbox Loading Conditions | 11 |
| 2.3 Gear Tooth Contact Modelling..... | 14 |
| 2.4 Dynamic System Modelling of the Wind Turbine Gearbox..... | 18 |
| 2.5 Common Failure Modes of Wind Turbine Gearboxes Components ... | 22 |
| 2.6 Summary | 26 |
| 3 DATA ANALYSIS OF FIELD MEASURED TORQUE SPECTRUMS.. | 28 |
| 3.1 Field Data for Different Operational Conditions of 2MW Wind Turbine | 29 |
| 3.2 Rainflow Counting Method..... | 30 |
| 3.3 Damage Equivalent Load Analysis Method | 34 |
| 3.4 Results and Discussion | 35 |
| 3.4.1 Comparison Between Shutdown and Other Operational Conditions | 36 |
| 3.4.2 Variations of Torque Ranges and Cycles for Different Operational Conditions | 44 |

| | | |
|-------|---|-----|
| 3.4.3 | Damage Equivalent Load for Each Operational Condition | 48 |
| 3.5 | Summary | 50 |
| 4 | PURE TORSIONAL MULTIBODY DYNAMIC MODELLING OF WIND TURBINE DRIVETRAIN | 51 |
| 4.1 | Determination of Masses and Inertias of Wind Turbine Drivetrain | 52 |
| 4.2 | Mathematical Modelling and Equations of Motion | 60 |
| 4.2.1 | Lumped Mass Models with Fixed and Variable Speed Generator.. | 60 |
| 4.2.2 | Eigenmode and Eigenfrequency Analysis | 65 |
| 4.3 | MATLAB/Simulink Dynamic Modelling of Wind Turbine Drivetrain | 65 |
| 4.3.1 | Key Components and Planetary /Parallel Gear Configurations | 66 |
| 4.3.2 | Gear Tooth Load Calculation..... | 69 |
| 4.3.3 | Generator Model | 69 |
| 4.3.4 | Eigenfrequencies Analysis Using Control Design Tools | 71 |
| 4.4 | Gear Mesh Dynamic Excitation and Campbell Analysis | 71 |
| 4.5 | Wind Turbine Drivetrain Input Torque Spectrums and Upscaling Factors..... | 74 |
| 4.6 | Summary | 76 |
| 5 | RIGID AND DISCRETE FLEXIBLE MULTIBODY DYNAMIC MODELLING OF WIND TURBINE DRIVETRAIN | 77 |
| 5.1 | Modelling the Key Components of Wind Turbine Drivetrain | 78 |
| 5.2 | Bearings | 86 |
| 5.2.1 | Diagonal Bearing Stiffness Matrix Approximation..... | 87 |
| 5.2.2 | Consideration of Nonlinear Bearing Stiffness Characteristics and Cross-Coupling..... | 88 |
| 5.2.3 | Clearance Consideration | 90 |
| 5.2.4 | Bearing Roller Model | 91 |
| 5.3 | Hertzian Contact Stress Consideration for Gears and Bearings..... | 94 |
| 5.4 | Fatigue Damage of Wind Turbine Gearbox Components | 98 |
| 5.5 | Consideration of Non-Torque and Gravity Loads | 101 |
| 5.6 | Summary | 102 |
| 6 | RESULTS AND DISCUSSION OF PURE TORSIONAL MULTIBODY DYNAMIC MODELLING OF WIND TURBINE DRIVETRAINS..... | 103 |
| 6.1 | NREL750 kW WT Drivetrain Model | 104 |
| 6.1.1 | Model Validation | 104 |

| | | |
|-------|---|-----|
| 6.1.2 | Mode Shapes of Lumped Mass Models During Free Vibration with Fixed and Variable Generator Models | 109 |
| 6.1.3 | Effect of Variable Gear Mesh Stiffness on Drivetrain Dynamic Response | 114 |
| 6.1.4 | Frequency Excitation During Normal Operation and Shutdown ... | 115 |
| 6.2 | Models of 2MW and 3MW WT Drivetrains with Three Different Gearbox Configurations | 118 |
| 6.2.1 | Wind Turbine Drivetrains Resonance Caused by Gear Mesh Excitation..... | 118 |
| 6.2.2 | Load Distribution on Key Components During Normal Operation and Shutdown | 124 |
| 6.2.3 | WT Drivetrains Dynamic Excitation During Normal Operation and Shutdown | 126 |
| 6.2.4 | Influence of HSS Stiffness on WT Drivetrain Natural Frequencies | 128 |
| 6.3 | Summary | 129 |
| 7 | RESULTS AND DISCUSSION OF RIGID AND DISCRETE FLEXIBLE MULTIBODY DYNAMIC MODELLING OF WIND TURBINE DRIVETRAINS | 131 |
| 7.1 | NREL750 kW WT Drivetrain Model | 132 |
| 7.1.1 | Model Validation | 132 |
| 7.1.2 | Cross-coupling Effect on Loads of Planetary Bearings Under Rated Torque and Normal Operation..... | 140 |
| 7.2 | 2MW WT Drivetrain Model..... | 144 |
| 7.2.1 | Load Distribution on Gears and Bearings During Normal Operation and Shutdown | 144 |
| 7.2.2 | Surface Contact Stress on Gears and Bearings During Normal Operation and Shutdown..... | 154 |
| 7.2.3 | Subsurface Contact Stresses of Gears and Bearings During Normal Operation and Shutdown..... | 162 |
| 7.2.4 | Gears and Bearings Fatigue Damage During Normal Operation and Shutdown | 165 |
| 7.3 | Summary | 170 |
| 8 | CONCLUSIONS AND FUTURE WORK | 171 |
| 8.1 | Conclusions | 171 |
| 8.1.1 | Conclusions from The Field Measured Data Analysis of 2MW Wind Turbine | 172 |

| | |
|---|-----|
| 8.1.2 Conclusions from Pure Torsional Multibody Dynamic Modelling of Different Wind Turbine Drivetrain Configurations | 173 |
| 8.1.3 Conclusions from Rigid and Discrete Flexible Multibody Dynamic Modelling of Wind Turbine Drivetrain | 174 |
| 8.1.4 Research Novelty and Contributions | 176 |
| 8.2 Suggestions for Future Work | 177 |
| REFERENCES..... | 179 |

List of Figures

| | |
|---|----|
| Figure 1.1: Total wind power wind power capacity for offshore wind turbines in EU, reproduced from [7]..... | 2 |
| Figure 2.1: Configuration of wind turbine drivetrain with gearbox [14] | 9 |
| Figure 2.2: Different configurations of wind turbine gearboxes..... | 10 |
| Figure 2.3: Measured wind turbine gearbox input torque during different operational conditions, adapted from [18] | 11 |
| Figure 2.4: Schematic of slicing approach of helical gears, adapted from [33] | 14 |
| Figure 2.5: Gear contact representation in pure torsional model..... | 15 |
| Figure 2.6: Comparison of two approaches using simulated results for gear contact load in different stages within the wind turbine gearbox [42] | 17 |
| Figure 2.7: Failure in wind turbine gearbox components (a) Bearing surface flaking [72] (b) High speed shaft gear surface damage[73]..... | 23 |
| Figure 3.1: Rainflow cycle counting method, adapted from [83]..... | 30 |
| Figure 3.2: Major steps of Rain-flow cycle counting method adapted from [85] | 31 |
| Figure 3.3: Rainflow counting method process (a) Original load history, (b-c) Rainflow cycle processing, (d) Rainflow matrix..... | 33 |
| Figure 3.4: Basic cyclic loading parameters [83] | 33 |
| Figure 3.5: Wöhler curve illustration with mean torque and damage cycles... | 34 |
| Figure 3.6: Comparison of the mean-range values of the HSS torque during different operational conditions..... | 37 |
| Figure 3.7: Comparison of the mean-range values of the LSS torque during different operational conditions..... | 39 |

Figure 3.8: Comparison of the mean-cycles values of the HSS torque during different operational conditions..... 41

Figure 3.9: Comparison of the mean-cycles values of the LSS torque during different operational conditions..... 43

Figure 3.10: Comparison of the range values of the HSS (top) and LSS (bottom) torque during different operational conditions 44

Figure 3.11: Comparison of the mean values of the HSS (top) and LSS (bottom) torque during different operational conditions 46

Figure 3.12: Comparison of cumulative torque cycles of HSS (top) and LSS (bottom) during four different operational conditions..... 47

Figure 3.13: Damage equivalent load for HSS (top) and LSS (bottom) per different operational conditions..... 49

Figure 4.1: CAD model for NREL multistage gearbox of 750kW WT (Drivetrain-D) consisting of a fixed ring planetary gear set with three planets and two parallel gear sets with two intermediate shafts and overall gearbox ratio of 1:81.49 55

Figure 4.2: Wind turbine drivetrains A, B and C and their gearboxes as CAD models, from the top to the bottom: Drivetrain-A (2 stage WTG, gearbox ratio of 1:34), Drivetrain-B (3 stage WTG, gearbox ratio of 1:115) and Drivetrain-C (3 stage WTG , gearbox ratio of 1:92) 56

Figure 4.3: Representation of NREL 750kW WT drivetrain with 11 DOF57

Figure 4.4: Five mass model representation of WT drivetrain. 61

Figure 4.5: Two mass model representation of WT drivetrain 62

Figure 4.6: MATLAB/Simulink model of a complete WT drivetrain during normal operation (top) and shutdown (bottom)..... 68

Figure 4.7:MATLAB/Simulink double feed induction generator model..... 70

| | |
|---|----|
| Figure 4.8: Eigenfrequency analysis by MTLAB/Simulink design tools for 2-mass model of WT drivetrain with variable generator model | 72 |
| Figure 4.9: Resonance analysis using Campbell diagram | 73 |
| Figure 4.10: Input torque time-history during normal operation (top) and shutdown (bottom) | 75 |
| Figure 4.11: MATLAB/Simulink model of the brake (top) and corresponding generator model (bottom) | 76 |
| Figure 5.1: Main components modelled in a wind turbine drivetrain | 78 |
| Figure 5.2: Multi body system modelling principal in SIMPACK. The letters BR refer to the 'Body Reference' of bodies A and B..... | 79 |
| Figure 5.3: Illustration of gear slicing model with five slices for parallel gear (right) and planetary gear (left) | 80 |
| Figure 5.4: Gear mesh stiffness estimation along the line of action, r_b , r_p , r_a and r_d are the base radius, the pitch radius, the addendum radius and the dedendum radius respectively..... | 81 |
| Figure 5.5: Contact mesh stiffness variation between the ring and planet gears for NREL 750kW WT during rated torque input..... | 82 |
| Figure 5.6: Flexible shaft representation of the main shaft within WT drivetrain | 83 |
| Figure 5.7: SIMPACK representation for sun, intermediate shaft and the spline with and without angular misalignment..... | 84 |
| Figure 5.8: SIMPACK kinematic tree diagrams for different gear stage | 85 |
| Figure 5.9: Commonly used roller bearings types in the wind turbine drivetrain | 86 |
| Figure 5.10: Roller bearings locations in the wind turbine drivetrain and nomenclature used..... | 87 |
| Figure 5.11: Diagonal bearing stiffness matrix..... | 88 |

| | |
|--|-----|
| Figure 5.12: Cross-coupling representation in bearing stiffness matrix | 89 |
| Figure 5.13: Axial and radial clearances in a roller bearing..... | 91 |
| Figure 5.14: Representation of roller lamina model within the roller bearing model | 93 |
| Figure 5.15: Hertzian line contact geometry of two cylinders..... | 94 |
| Figure 5.16: Normalised subsurface principal shear stress τ (left-half) and von Mises stress σ' (right-half) distribution for line contact of two cylinders. The points A and B indicate the value and location of maximum subsurface shear stress ($0.3P_{\max}$ at depth $0.78a$) and von Mises stress ($0.57P_{\max}$ at depth $0.7a$) respectively, a is half of the contact width and Z is the depth..... | 97 |
| Figure 5.17: Typical S-N curve..... | 98 |
| Figure 5.18: Consideration of pitching moment and gravity effects on wind turbine gearbox..... | 101 |
| Figure 6.1: Comparison of 750kW WT MATLAB/Simulink model results with GRC partners results [121], (a) Torque distribution (b) Ring-planet contact load (c) Sun-planet contact load..... | 105 |
| Figure 6.2: Results of MTLAB/Simulink 750kW WT multibody system model with 11-mass, LSS and HSS speed (top), power(bottom)..... | 108 |
| Figure 6.3: Mode shapes of 2 mass model for WT drivetrain with fixed (left) and variable (right) speed generator | 109 |
| Figure 6.4: Mode shapes of 5 mass model for WT drivetrain with fixed (left) and variable (right) speed generator | 110 |
| Figure 6.5: Mode shapes of 11 mass model for WT drivetrain with fixed (left) and variable (right) speed generator | 110 |
| Figure 6.6 : Mode shapes corresponding to the natural frequencies of 5-mass model of the 750kW WT with variable speed generator..... | 111 |

| | |
|--|-----|
| Figure 6.7: Frequency response function (FRF) for 2, 5 and 11 mass model of WT drivetrain with fixed speed generator. | 112 |
| Figure 6.8: Frequency response function (FRF) of WT drivetrain with fixed and variable speed generator, 2 mass model (top), 5 mass model (middle), 11 mass model (bottom)..... | 113 |
| Figure 6.9: FRF of the drivetrain using fixed speed generator model and fixed gear mesh stiffness values..... | 115 |
| Figure 6.10: HSS torque for 750kW WT during normal operation, time history (top) and FFT analysis (bottom)..... | 116 |
| Figure 6.11: HSS torque for 750kW WT during shutdown, time history (top) and FFT analysis (bottom)..... | 117 |
| Figure 6.12: Comparison of simulated and field measured HSS torque histories of Drivetrain-C during normal operation (top) and shutdown (bottom) conditions | 119 |
| Figure 6.13: Gearboxes natural frequency comparison (a) Drivetrain-A and B (b) Drivetrain-B and C..... | 120 |
| Figure 6.14: WT drivetrain Campbell diagram (a) Drivetrain-A (b) Drivetrain-B (c) Drivetrain-C..... | 122 |
| Figure 6.15: Meshing force of sun-planet over time of Drivetrain-C during normal operation (top) and shutdown (bottom)..... | 123 |
| Figure 6.16: Range-Mean of meshing forces of sun-planet of Drivetrain-C during normal operation and shutdown..... | 124 |
| Figure 6.17: Maximum shaft torque ratios of three drivetrains during normal operation (top) and shutdown (bottom)..... | 125 |
| Figure 6.18: Shaft torque range ratio of three drivetrains during normal operation and shutdown..... | 126 |

| | |
|---|-----|
| Figure 6.19: HSS torque in time and frequency domains during shutdown: (a, c and e) Torque spectrum of Drivetrain-A, B and C (b, d and f) Corresponding FFT analysis of Drivetrain -A, B and C..... | 127 |
| Figure 6.20: The influence of HSS stiffness on eigenfrequencies of Drivetrain-A | 128 |
| Figure 7.1 : Upwind bearing load of planet ‘A’ under rated input torque for 750 kW WTG during one planet carrier rotation. MBS model of this study (right) and LaCava [34] dynamometer test (in black) and their MBS models (left) .. | 133 |
| Figure 7.2: Downwind bearing load of planet ‘A’ under rated input torque for 750 kW WTG during one planet carrier rotation. MBS model of this study (right) and LaCava [34] dynamometer test (in black) with their MBS models (left)..... | 133 |
| Figure 7.3: The out of phase of upwind bearings load of planets A, B and C under rated input torque for 750 kW WTG during rotation of the planet carrier. | 134 |
| Figure 7.4: Comparison of contact stress distribution between the ring and planet gears along the face width under rated torque input. NREL ‘Round Robin’ project [121] (top) and this study (bottom) | 135 |
| Figure 7.5: Comparison of calculated tilt angle of planet B and its bearings force for UW and DW bearings during rated input torque. This study (bottom) and measurement [124] (top) | 136 |
| Figure 7.6: Load sharing factor of planet gears during normal operation of NREL 750kW WT. This study (right) and LaCava measurement [34] (left)..... | 137 |
| Figure 7.7: Planet B and C load sharing factor variation with planet tilt angle during normal operation of NREL 750kW WT. This study (top and middle) and test results ([34] (bottom) | 139 |
| Figure 7.8: Planet bearings radial loads during rated torque and normal operation..... | 141 |
| Figure 7.9: Upwind and downwind bearing load distribution within one carrier rotation during rated input torque (top) and normal operation (bottom).... | 142 |

| | |
|--|-----|
| Figure 7.10: FFT analysis of planet bearings loads for UW (top) and DW (bottom) bearings during normal operation | 143 |
| Figure 7.11: Variation of circumferential gear contact load and frequency histogram in different stages during normal operation..... | 145 |
| Figure 7.12: Variation of downwind bearing load and related frequency histogram during normal operation..... | 146 |
| Figure 7.13: Histograms of bearing load ranges of planet gear bearings during normal operation..... | 147 |
| Figure 7.14: Variation of circumferential gear contact loads and related frequency histograms in different stages during shutdown..... | 149 |
| Figure 7.15: Comparison of maximum gear contact loads during normal operation and shutdown..... | 150 |
| Figure 7.16: Variation of downwind bearing loads and related frequency histograms during shutdown | 151 |
| Figure 7.17: Comparison of load range histograms of UW and DW planet gear bearings during shutdown..... | 152 |
| Figure 7.18: Comparison of maximum bearing loads during normal operation and shutdown..... | 153 |
| Figure 7.19: Maximum gear contact stress distributions during normal operation..... | 154 |
| Figure 7.20: Maximum gear contact stress distributions during shutdown ... | 155 |
| Figure 7.21: Comparison of maximum gear contact stress during normal operation and shutdown..... | 156 |
| Figure 7.22: Maximum bearing contact stress distributions during normal operation..... | 157 |
| Figure 7.23: Maximum bearing contact stress distributions during shutdown operation..... | 158 |

| | |
|--|-----|
| Figure 7.24: Comparison of ratios of maximum bearing contact stress and the recommended allowable contact stress during normal operation and shutdown..... | 160 |
| Figure 7.25: Number of rollers in contact for UW bearing A during normal operation (top) and shutdown (bottom)..... | 161 |
| Figure 7.26: Maximum subsurface stresses and depths in gears during normal operation and shutdown, maximum shear stress (top) and maximum von Mises stress (bottom)..... | 162 |
| Figure 7.27: Maximum subsurface shear stress and depth in bearings during normal operation (top) and shutdown (bottom)..... | 163 |
| Figure 7.28: Maximum subsurface von Mises stress and depth in bearings during normal operation (top) and shutdown (bottom)..... | 164 |
| Figure 7.29: Operation hours for wind turbine corresponding to wind speed according to IEC 61400-4..... | 166 |
| Figure 7.30: Histogram of maximum contact stress of HSS stage gears (top) and comparisons with the allowable contact stress recommended by ISO 6336-5 (bottom) | 168 |
| Figure 7.31: Comparison of gear fatigue damage during normal operation and shutdown..... | 169 |
| Figure 7.32: Comparison of bearing fatigue damage during normal operation and shutdown..... | 170 |

List of Tables

| | |
|---|-----|
| Table 2.1: Classification of Gear modes of failure, adapted from [74] | 24 |
| Table 3.1: Wind Turbine Specifications | 30 |
| Table 4.1: Design parameters of three different WT drivetrains..... | 54 |
| Table 4.2: Parameters of mechanical components of 750kW WT drivetrain.. | 58 |
| Table 4.3: Mechanical components parameters of drivetrains A, B and C | 59 |
| Table 4.4: Equivalent Simulink blocks for the mechanical components..... | 67 |
| Table 4.5: Representations of epicyclic and parallel gear stage in MATLAB/Simulink..... | 68 |
| Table 4.6: Generator parameters of drivetrains A, B, C and D | 70 |
| Table 4.7: Number of teeth of three WT drivetrain gearboxes..... | 73 |
| Table 4.8: Gear mesh frequencies of WTGs of drivetrain A, B and C..... | 73 |
| Table 6.1: Comparison of frequency values of different lumped mass models of 750kW WT drivetrain (Hz) | 106 |
| Table 6.2: Frequency comparison for 2 and 5-mass models of wind turbine drivetrain..... | 107 |
| Table 6.3: Different mesh stiffness values used for planetary stage of 750kW WT gearbox | 114 |
| Table 6.4: Natural frequencies of three WT drivetrain configurations | 120 |
| Table 7.1: Hours of operation and time factor at different wind speeds | 167 |
| Table 7.2: Adjusted factor time scaling for different gears..... | 167 |

Nomenclature and Abbreviations

| | |
|--------------------|--|
| a | Half contact width |
| BS | British standard |
| β | Gear helix angle |
| CAD | Computer aided design |
| CRB | Cylindrical roller bearing |
| C_{shaft} | Torsional damping of shaft |
| C_{mesh} | Mesh damping coefficient |
| C_{LSS} | Low speed shaft damping coefficient |
| C_{IS} | Damping coefficient of the intermediate shaft |
| C_{HSS} | High speed shaft damping coefficient |
| C_{RP} | Planetary gear, Ring-Planet mesh damping coefficient |
| C_{SP} | Planetary gear, Sun-Planet mesh damping coefficient |
| C_{GP} | Gear-Pinion mesh damping coefficient |
| C | Damping coefficient matrix |
| C_{eff} | Effective damping coefficient |
| C_a | Bearing axial clearance |
| C_r | Bearing radial clearance |
| C_s | Bearing contact stiffness |
| DOF | Degree of freedom |
| DW | Down wind |
| DEL | Damage equivalent load |
| $D_{1,2}$ | Rotor diameter for wind turbine 1 and 2 |
| δ | Deflection |
| E | Modulus of elasticity |
| FE | Finite element |
| F_{max} | Maximum contact load |
| F_r | Bearing radial force |
| Φ | Eigenmodes |
| GRC | Gearbox reliability collaborative |
| G | Modulus of rigidity |
| HAWT | Horizontal axis wind turbine |
| HSS | High speed shaft |
| ISS | Intermediate speed shaft |
| ISO | International organization for standardization |
| J | Inertia matrix |
| J_b | Inertia of blades |
| J_h | Inertia of hub |
| J_{rotor} | Inertia of rotor |
| J_{PC} | Inertia of planetary carrier |
| J_P | Inertia of planet |
| J_S | Inertia of sun gear |
| J_G | Inertia of gear or pinion |

| | |
|---|---|
| J_{gen} | Inertia of the generator |
| K_{shaft} | Torsional stiffness of shaft |
| K_{LSS} | Low speed shaft stiffness |
| K_{IS} | Stiffness of the intermediate shaft |
| K_{HSS} | High speed shaft stiffness |
| K_{gen} | Electrical torsional stiffness |
| k_{mesh} | Gear mesh stiffness |
| k_{gear} | Gear stiffness |
| K_{RP} | Planetary gear, Ring-Planet mesh stiffness |
| K_{SP} | Planetary gear, Sun-Planet mesh stiffness |
| K_{GP} | Gear-Pinion mesh stiffness |
| K | Stiffness matrix |
| K_{eff} | Effective stiffness |
| k | Stiffness |
| LSS | Low speed shaft |
| L_b | Length of blade |
| MBS | Multi body system |
| M_b | Mass of rotor blades |
| m | Slop of S-N curve |
| NREL | National renewable energy laboratory |
| N | Number of cycles |
| $N_{1,2,3}$ | Gearbox stages ratios |
| P_{max} | Maximum contact pressure |
| PLC | Planet carrier |
| $P_{W,R}$ | Weibull or Rayleigh portability distribution |
| Q | Torque vector |
| RFC | Rainflow cycles counts |
| r_b | Gear base radius |
| SRB | Spherical rollers bearing |
| $\sigma_{xx}, \sigma_{yy}, \sigma_{zz}$ | Orthogonal normal stresses |
| $\sigma_1, \sigma_2, \sigma_3$ | Principal stresses |
| σ' | Von Mises stress |
| TRB | Tapered rollers bearings |
| T_{rot} | Rotor input torque |
| T_{gen} | Generator torque |
| T_i | Mean torque in bin 'i' |
| τ_{max} | Maximum unidirectional, subsurface shear stress |
| $\theta_{x,y,z}$ | Angular displacement |
| UW | Up wind |
| U_{hub} | Average wind speeds at the wind turbine hub |
| VAWT | Vertical axis wind turbine |
| WT | Wind turbine |
| WTG | Wind turbine gearbox |
| ω_n | Eigenfrequencies |

| | |
|---------|---------------------|
| X,Y,Z | Linear displacement |
| ζ | Damping ratio |
| Z | Subsurface depth |

1

INTRODUCTION

Wind turbine (WT) gearboxes are frequently replaced within a six to eight-year period, which is considerably shorter than the designed life of 20 years [1]. The premature failures of the gearbox key components, such as the bearings and the gears, are caused by the high loads and torques experienced by the drivetrain, especially because the size of modern WTs has been steadily increased during the last decades [2]. The wind turbine gearbox (WTG) can often account for up to 13% of the total cost of a WT, with further expenses are incurred due to the difficulty of replacing failed mechanical components, especially in offshore operation environment [3]. Reducing the component failures and downtime of the gearbox will make wind energy more economically viable in achieving sustainable generation of wind energy. However, the fact that the WT gearbox consists of large number of moving mechanical components which increases the likelihood of failure; this is a concern as the replacement of large components in offshore environments is expensive. Obtaining field measurement data for WTG, such as the torque of the low speed or high-speed shaft, during different operational conditions is normally costly. However, simulation data is cheaper as the simulation of dynamic loads can support the design of the WT drivetrain. This study focuses on investigating the dynamic response of different WT drivetrain with different WTG configurations under normal operation and unplanned shutdown conditions by using different MBS modelling approaches.

The developed models can capture more details of drivetrain dynamic behaviour than that of the widely used in literature. In this Chapter the research background, research problem, the aim and objectives of this study will be outlined. Finally, the thesis structure will be presented.

1.1 Background

Wind technology has been rapidly developing in recent years. The limited natural reserves of oil and gas provide a major incentive for using renewable energy sources, such as the wind, to generate electricity [4]. Generating electricity from renewable and clean energy sources has also been part of global efforts in recent decades to reduce harmful emissions and their impact on the environment. As a result, the wind energy industry has seen a rapid growth and development in the last decade, especially in Europe and the United State [5]. During 2016, around 82 GW of the total installed capability was just in the United States alone [5] while around 153 GW of the total installed capacity had been installed in Europe alone [5]. By the end of 2030, about 256-397 GW of wind power will be installed in Europe only [6] with 38 and 85 GW just in the UK and Germany [6]. Figure 1.1 illustrates the historical and predicted growth in EU capacity projection of the offshore WT since 2008. By 2020 the total capacity installation of the offshore WT capacity will be about 7 GW [7].

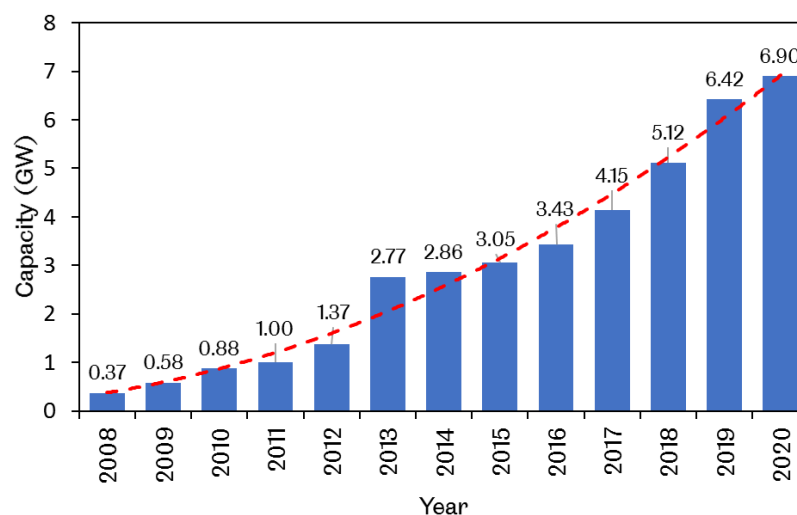


Figure 1.1: Total wind power capacity for offshore wind turbines in EU, reproduced from [7]

However, some mechanical components of the WT will need replacing during its technically designed life. The WT industry faces serious challenges of

reducing the cost of wind energy and tackling the premature failures of mechanical components, such as gears and bearings, before the end of the designed life [8]. The premature failure of these components affects the downtime of the WT and increases the cost of overall maintenance.

There are very limited information and failure data regarding the WTG and its components. WTG failure can be caused by many factors such as the overload of WTG bearings during the extreme loading conditions or excessive torque reversal under braking conditions. The trend of industry toward manufacturing turbines of ever larger size presents real challenge in the form of a significant increase in the rate of gearbox failure which is proportional directly with the size of turbine [9]. It has been observed that the overall downtime of WT per year is caused mainly by gearbox failure [10]. According to the long term statistics issued by “National Renewable Energy Laboratory” (NREL), during just one month around 37 WT failure cases were recorded, more than 20 of which were due to gears failure [11]. Gears and bearings failure in the WTG can be attributed to the excessive load conditions [12]. Gearbox failure contributes to significant level of gear replacement which eventually increase the cost of power generated by the wind [12]. Replacing a WTG requires the use of heavy duty equipment such as cranes to lift out the damaged gearbox. This is an expensive procedure, and almost impossible in adverse weather conditions experienced in offshore operation [13].

This highlights the importance of research in this sector of industry to provide more economic benefits for businesses and the end users alike. Increasing the reliability of wind turbines will decrease the WT downtime and increase the confidence in this technology and certify its status as a critical source of renewable electricity generation.

1.2 Research Problem

The limited understanding of the root causes behind the premature failures of WTGs imposes serious challenges on the WT makers. It has been observed that gearbox failure is responsible for most of the downtime of WT. Premature failure of the gearbox reduces the service life of the WT, causes unplanned shutdown, early components replacement, and increases the overall cost of wind power. The failures of gears and bearings under transient load are

considered as one of the most frequent observed types of failures that can contribute significantly to gearbox replacement. This study aims to investigate the dynamic behaviour and loading on the WTG key components, the gears and the bearings, under normal and transient conditions. A clear understanding of how these mechanical components dynamically behave within the WTG under the transient events would potentially lead to increased reliability and availability of WTs, which would eventually reduce the overall cost of wind power.

1.3 Aim and Objectives

This study aims to investigate and understand the dynamic response behaviour of the overall WT drivetrain with different gearbox configurations and different power rating under normal and transient operational conditions, to study how the key components of WTG, i.e. the gears and the bearings, behave under different extreme events such as the shutdown, to study the surface and subsurface stress level and the corresponding damage on gears and bearings under the condition of transient load, and to estimate the remaining service life of gears and bearings in operation. To achieve this, the following objectives are going to be reached:

1. To examine and analyse large set of field load measurement data obtained from an operating WT for four different operational conditions comprising, normal operation, shutdown (i.e. unplanned stop), normal stop (i.e. planned stop) and start-up. The analyses of torque spectrums of these operational conditions would be carried out by using the rainflow cycle counts (RFC) method recommended by the international standard IEC 61400-4 and the damage equivalent load (DEL) method.
2. To define which field measurement torque spectrum causes the highest and lowest damage than the other events to use them as a direct input to the multibody system (MBS) models that will be developed.
3. Develop a pure torsional MBS models of complete WT drivetrains with different WTG configurations and different levels of complexity. The dynamic response of WT drivetrains under free and forced vibration will be investigated.

4. Increase the complexity of the WTG models and improve modelling accuracy to capture more complex dynamic response behaviour by developing MBS dynamic model of the WTG with six degrees of freedom per component, allowing the loads and stresses on the corresponding gears and bearings to be investigated during different transient conditions.
5. To investigate the influence of transient load such as the shutdown on surface and subsurface contact stress on gears and bearing and associated damages and failures within the lifetime of these components.

1.4 Research Novelty and New Contributions

The key research novelty and contributions from this study are related to develop new MBS models can captures more details of WTG dynamic behaviour operating under transit loads. The pure torsional MBS models for WTG developed in this study consider the effect of torque reversal on the gear meshing contact forces within the WTG during unplanned shutdown. In MBS models for WTG with 6 DOF per component, the bearings model considered the cross-coupling effect between the rollers and the races. The contact between the roller and the races is represented by using a lamina model. This advance model for bearings within the WTG is important especially for the planet gear downwind bearings to capture more details of bearing loads operating under different operational conditions.

1.5 Thesis Layout and Structure

This thesis comprises eight chapters. A short description of each Chapter can be found as follows:

Chapter 2: Literature review. This Chapter includes a summary of the commonly used WTG configurations according to the international standard IEC 61400-4. It also introduces the loading conditions experienced by the key components of a gearbox, the bearing and the gears, and their common failure modes. The previous modelling approaches used for the WT drivetrain are then presented to clarify their advantages and disadvantages. A review of the methods for gear tooth contact and bearing contact modelling is presented.

Finally, at the end of the chapter, the conclusions drawn from the previous research are summarised to identify the research gaps and to define research objectives of this project.

Chapter 3: Data Analysis of Field Measured Torque Spectrums. This Chapter focuses on processing large sets of WT field measurement data for different operational conditions and conversion of time domain data of a complicated loading history into number of loading levels and cycles by using rainflow counting method. The damage caused by each operational condition is calculated by using the damage equivalent load method. The main purpose of this analysis is to show which operational condition could causes the most damage to WTG components and to use it later as a direct input to the WT drivetrain MBS developed in Chapters 4 and 5.

Chapter 4: Pure Torsional Multibody Dynamic Modelling of Wind Turbine Drivetrain. This Chapter presents the required parameters calculated by CAD models and simulation methodologies to develop a pure torsional model of the WT drivetrain with different levels of complexity using constant and variable generator models. The required models are developed analytically and by using MATLAB/Simulink software. The consideration of gear mesh stiffness, the gears and the shafts within the MATLAB/Simulink environment are also presented. Eigen frequency analysis is presented analytically and by using MATLAB/Simulink control tools. The calculations of gear mesh frequency and Campbell resonance analysis are also presented to study the probability of WT drivetrain resonance under different operational conditions.

Chapter 5: Rigid and Discrete Flexible Multibody Dynamic Modelling of Wind Turbine Drivetrain. This Chapter focuses on the development of advance MBS models for two different WT drivetrains operating under normal operation and shutdown by using SIMAPCK MBS software. The cross-coupling effect and the clearance are both considered in modelling bearings within the WTG. The contact between the roller and the raceway within the roller bearing model has been considered. The 'Slicing' approach has been used to investigate the effects of gear misalignment and tilting along the gear axes. The

surface and subsurface stresses and corresponding damage on bearings and gears have been investigated.

Chapter 6: Results and Discussion of Pure Torsional Multibody Dynamic Modelling of Wind Turbine Drivetrains. This Chapter reports the modelling results of the pure torsional model of WT drivetrain with single degree of freedom (DOF) per component during free and forced vibrations. The results of the models are compared and validated with those published in literature for the same WT drivetrain and with the results obtained from the same models developed analytically in Chapter 4. The effects of three different WTG configurations, recommended by the international standard IEC 61400-4 and operated WT with high and low gearbox speed ratio, on the dynamic response of the WT drivetrain and the probability of resonance within the operational speed range have been investigated. The dynamic responses of WT drivetrain during normal operation and unplanned shutdown have been analysed. The variations of gear contact loads during normal operation and shutdown have been compared.

Chapter 7: Results and Discussion of Rigid and Discrete Flexible Multibody Dynamic Modelling of Wind Turbine Drivetrains. This Chapter reports the results obtained from the rigid and discrete flexible MBS dynamic modelling of WTG of two WTs with similar gearbox configuration but different power rate these are, NREL 750kW WT and 2MW WT. The developed model of NREL 750kW is validated with measured data for the same WTG. The loads on gears and bearings within the 2MW WTG, the maximum contact stresses on surface, subsurface stress distribution, and fatigue damage during the WTG lifetime are investigated under normal operation and shutdown conditions.

Chapter 8: Conclusions and Future work. This Chapter summarises and highlights this study important findings and the suggestions for the possible future work.

2

LITERATURE REVIEW

The common types of gearboxes used in wind turbine (WT) drivetrains and then the loading conditions they experience during the wind turbine's lifetime are summarised in this chapter. The common multibody system dynamic modelling approaches for the wind turbine gearbox (WTG) components (i.e. gears and bearings) and their contact within the WTG are reviewed. The overall aim of this literature review is to gain better understanding of the transient loading conditions occurring during the operation of the WT and how they contribute in premature failure of the key components of the WTG, the gears and the bearings, earlier than the designed lifetime. Moreover, to identify potential areas of research through examination of similar work done within this area and analyse knowledge gaps revealed in the current dynamic system models for WTGs that demand further investigation. In addition, to gain better understanding of the damage mechanisms behind the excessive load to which the gears and bearings within the WTG are subjected and how these contribute to shortening their life.

2.1 Configurations of Wind Turbine Gearbox

The WTG is considered as the most important and expensive parts in WT construction which represents about 12% to 13% of the total value of a 5MW WT [3]. The gearbox connects the main components of the WT such as the main shaft, the generator, the nacelle, the blades control mechanism and the mechanical brake as shown in Figure 2.1 [14].

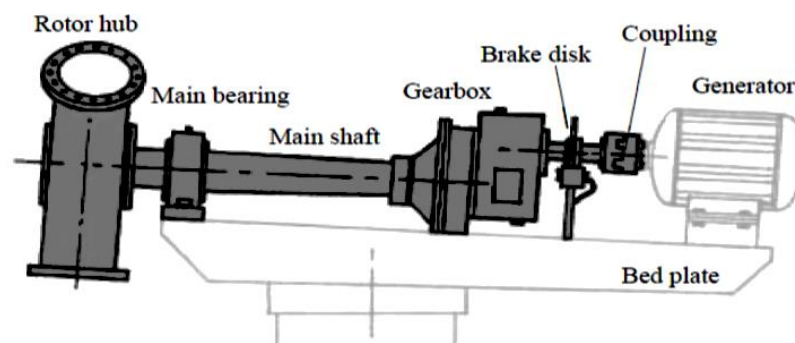


Figure 2.1: Configuration of wind turbine drivetrain with gearbox [14]

The main role of the wind turbine's gearbox is to increase the low rotational speed and high torque of the rotor shaft, the low speed shaft (LSS), in several gear stages, to higher speed and lower output torque on the high-speed shaft (HSS) needed to drive the generator. The variable of rotor torque serves as an input to the gearbox and subjects each component of the WTG to high transient loads, which are frequently absorbed by the gears and bearings. Depending on the required output speed to be fed into the generator, the common configurations used in WTG are shown in Figure 2.2. As shown in Figure 2.2(b), this type of WT gearbox designed with three stages comprise, epicyclic (i.e. planetary) gear stage with three planet gears or more followed by two parallel gear stages. The gears in planetary stage rotate with low speed rate because it is connected to the rotor shaft of the WT which has a speed depending on the wind speed. In another commonly used gearbox configuration design, shown in Figure 2.2(c), the parallel gear stages can be replaced by another planetary gear set [15]. Epicyclic gear (i.e. the planetary gear) stage comprises of an annulus gear (i.e. the ring), planet gears supported by a planet carrier and sun gear.

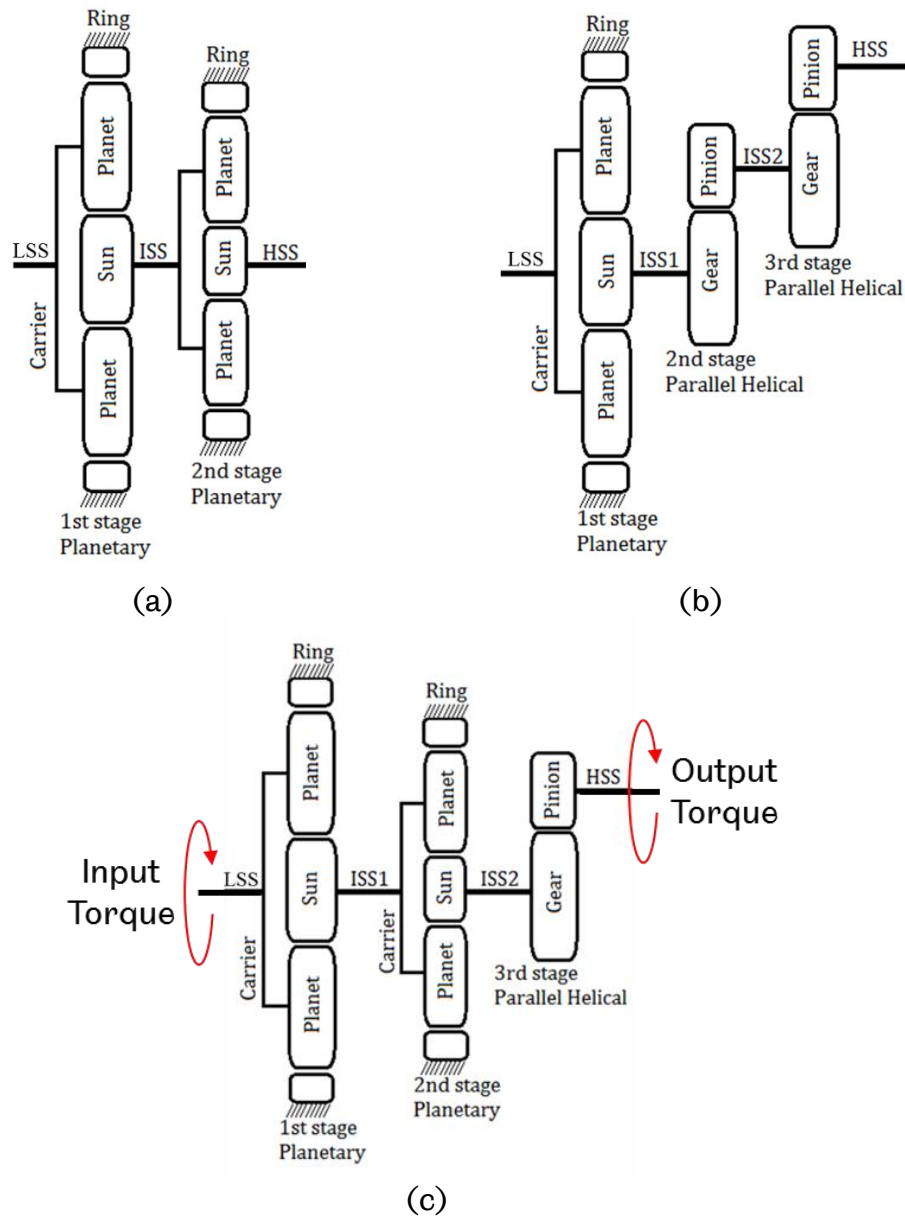


Figure 2.2: Different configurations of wind turbine gearboxes.

In all WTG configurations shown in Figure 2.2, the ring gear is normally unable to rotate and is fixed on gearbox case. The shaft that connects the low speed stage with the high-speed stage within the WTG is usually called the intermediate speed shaft (ISS). The effect of different WTG configurations on the dynamic response of the WT drivetrain under different operational conditions will be examined in this study.

2.2 Wind Turbine Gearbox Loading Conditions

The various loading conditions that are experienced periodically by the WTG, such as power production, system faultiness, start up, normal stop and emergency shutdown, can be summarised in terms of WT design requirement standards [16, 17]. The stochastic nature of wind variation places the WT components under unpredictable operational loading conditions. Several studies have been undertaken to estimate the considerable impact of variable loads on the gearbox's designed lifetime during operating conditions such as normal operation, low wind speed and shutdown. The torque reversal in short time period under the low wind speed exhibits harmful influence that leads to gearbox failure. The main problem of the reversal motion is the impact load caused by the backlash of gear meshing teeth and the clearances in the bearings.

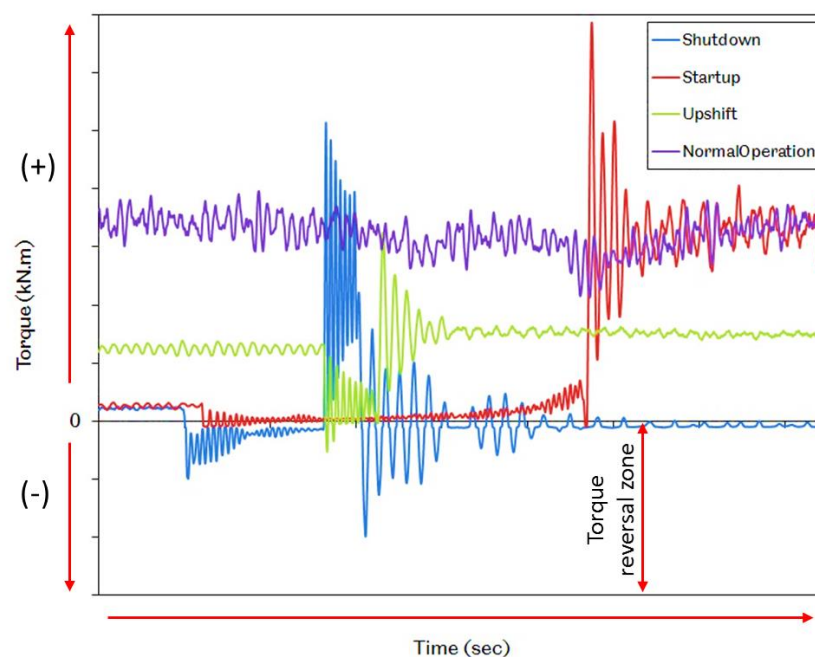


Figure 2.3: Measured wind turbine gearbox input torque during different operational conditions, adapted from [18]

The problem of torque reversal during low wind speed has been managed by using various speed generator controllers in specific types of wind turbines [19]. Sutherland et al. [20] concluded that the frequent impact forces on gears caused by torque reversal could lead to real fatigue damage in gear teeth before they complete their expected life.

As shown in Figure 2.3, excessive torque reversal mostly occurs during extreme operational conditions [18], such as shutdown, start-up, upshift, and at wind speeds above the cut-off speed or loss of grid connection [10]. Torque reversal occurs when the torque value changes sign from positive to negative as shown in Figure 2.3. Shutdown normally occurs when there is a fault in the WT system. Further studies have shown that after the brake engages with the high-speed shaft (HSS) disc, there is random oscillation with high amplitude of the torque between the positive and negative values in a very short period as shown in Figure 2.3. This phenomenon has severe influence on the life of WTG components [21, 22]. Another study focused on low speed shaft (LSS) torque variations during the emergency stop after occurrence of grid loss connection and brake engagement. The LSS torque fluctuation with high amplitude causes excessive torque reversal that remains in the WTG for a considerable period even after the brake has fully stopped the high speed shaft (HSS) [10]. Furthermore, this phenomenon has harmful influence on the planet gear stage bearings which results in high level of damage due to their subjection to high levels of load [8].

The data collection from the field under various operational conditions provides an invaluable source of information for real loading conditions of the WT drivetrain system because it gives useful indication about the real dynamic load variations in the time domain [23-25]. A technical report published by the National Renewable Energy Laboratory (NREL) presents WT torque measurement data recorded in field operation. Torque sensors were fixed on the HSS to measure the torque and bending moment in different operational events such as start-up and braking, to verify the influence of the braking system on torque levels for HSS and its behaviour during the braking events. Fourier Fast Transformation (FFT) was used to convert the torque from time domain to frequency domain to estimate the occurrence of the high amplitude of load frequency over the braking [26].

Although field load measurement is useful, it is a time consuming and expensive operation. To overcome these drawbacks, many modelling studies related to WT loading conditions in different operational conditions have used commercial simulation software. A simulation study done by the University of Strathclyde together with "Romax" Technology focused on using commercial

software to investigate the influence of the transient events on bearings load of the WTG during normal and emergency stop caused by grid loss [8]. Without the need for sensors, the LSS and HSS torque was simulated. The forces shared by all bearings in the WTG were used to calculate the damage on bearings according to ISO281 standard [8]. The results of this study were not validated with any measured data. The outcome of this study highlighted that the event of emergency stop is threefold more harmful than the controlled normal stop [8]. A similar conclusion has also been reached by a different study done by Romax Technology [27]. The life prediction of WTG bearings was investigated.

“Romax” software was used to model the complete drivetrain of NREL 750 kW WT with 6 degrees of freedom (DOF) per component. The main bearings misalignment for the 2 and 3-point suspensions of the drivetrain was analysed. The non-torsional load effects including rotor weight and rotor pitching moment, were considered. The outcome of this study shows that the non-torsional loads have harsh influence on main shaft bearings and downwind planet carrier bearing. The non-torsional loads increase the chance of bearings damage occurrence by more than threefold [27]. “Romax” software has been used in another study to simulate the dynamic response of a NREL 750kW WT subjected to transient dynamic event. The simulated LSS torque was used as an input for a purely torsional WT drivetrain model with lower degree of freedom [28]. All the shafts were modelled as Bernoulli beams. The transient load is represented in this study by electrical faults for 0.1 second. The stress distribution on gears and bearings over this transient load was estimated [28]. The input load variations for the WTG for three different concepts of rotor suspension during the emergency stop were also investigated by using commercial software. It was found that with the rotor hub suspended by two bearings, most axial loads are soaked up by the spherical roller bearings of the main shaft and have no effect on the WT gearbox loads [29]. This agrees with the finding of another two studies done by NREL [30] and Scott et al. [8].

Despite the simplicity of the models presented in previous simulation studies done by using commercial software, they can be used to simulate various loading conditions that are experienced frequently by the WT drivetrain system, particularly in the gearbox gears and bearings.

2.3 Gear Tooth Contact Modelling

Although the WTG components are enclosed in housing filled with lubricant, metal to metal contact may occur between the gear teeth over the abnormal and extreme loading conditions during braking, such as unplanned shutdown [31]. The simplest gear contact modelling method is to use a linear spring to connect two wheels under compression [32]. The model ignores the damping and assumes no contact loss. Other methods of modelling the gear contact have been developed by considering the majority part of the contact area between two gears during the meshing. 'Slicing' approach has been used to divide area under contact across the gear face width into multi 'slices' (i.e. segments) and the gear contact represented by groups of springs and dampers as shown in Figure 2.4 [33].

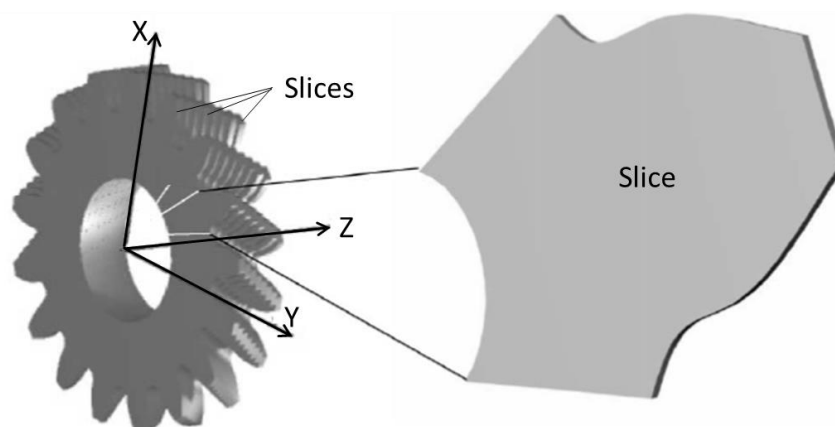


Figure 2.4: Schematic of slicing approach of helical gears, adapted from [33]

This 'Slicing' approach produce accurate analysis for the gears in contact within the contact area in case of helical gear, due to the forces in gear axial direction produced by gear meshing causing gears tilt about their radial axis. This leads to gear shaft displacement and induces the shaft misalignment [34]. In WT application the optimum number of slices per gear contact model is 35 [35]. The same approach was later developed to calculate the contact force during gear mesh in short contact periods [36]. Moreover, three different points of gear meshing were considered instead of studying the whole contact area. These points included: the mesh in point, the pitch point and the mesh out point [36]. This study concluded that the gear contact forces have negative values at low wind speed. This means that the contact of gear surfaces occurs on both sides of a gear tooth [19].

Peeters' work [32] concentrated on studying dynamic behaviour of the WT drivetrain system. The tooth contact forces were calculated in simple form by taking the tooth deflections captured by the gear's mesh stiffness spring into account and then multiplying these by the gear mesh stiffness, as illustrated in Figure 2.5.

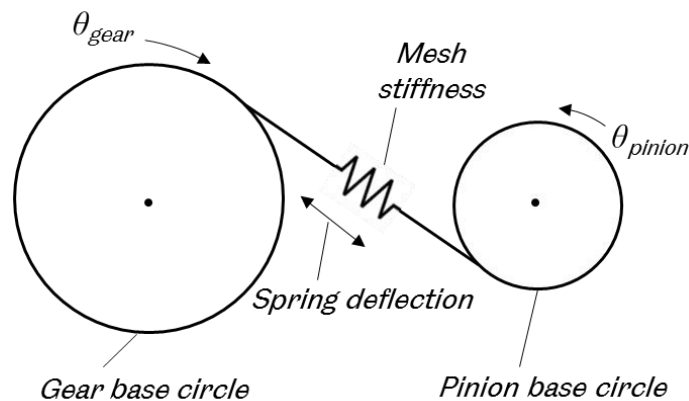


Figure 2.5: Gear contact representation in pure torsional model

The effect of damping, backlash in gear meshing force was ignored. The mesh stiffness values for all gears were taken as constant but individual values and modelled as a linear spring [32]. Another study considered factors that had been ignored in previous studies [37]. Dynamic behaviour and the gear contact force of the planetary gear system were investigated by using multibody system (MBS) dynamic modelling which considered factors including: gear tooth stiffness, damping, friction and the non-linearity in gear tooth backlash. A single value of tooth contact stiffness was used as a mean value in addition to the variation of stiffness with the time of meshing [37]. It was concluded that the transmission error has minor influence when taking the friction effect in the mesh area into account [38].

Heege [39] developed a numerical and experimental model of WT drivetrain to investigate and estimate the effect of backlash and the transient load on the WTG. The normal load on gears, the axial forces on planets gear and the gear displacement were estimated. The rotor and the generator torque were simulated during the normal operation, the generator engagement, the brake engagement and stopping. Any change in the direction of rotor torque would give an indication of gear backlash occurrence [39].

A study by the Sandia National Laboratories investigated fatigue load on WTG gears in two different types of wind turbine: horizontal axis WT (HAWT) and vertical axis WT (VAWT). The torque shared by each individual gear was estimated and then analysed by the rainflow counting method. The number of load cycles that contribute to stress variations on gear teeth was calculated. The high cycle fatigue due to bending of the gear teeth was estimated. The study shows that high sample rate is important in the case of measuring LSS torque because with low sample rate the highest value of load could be missed and the low frequency cycles could disappear [40].

The influence of the transient load during the shutdown and the start-up of NREL 750 kW WTG on WTG bearings load has been investigated [41]. 'SIMPACT' MBS software was used to model the WTG. The results illustrate that the flexibility of LSS has noticeable influence on the main shaft bearings load which is higher in shutdown case than that in start-up. The gears were modelled as rigid bodies with discrete flexibility by using the slicing method. The radial forces on planet bearings and the gear contact forces were measured experimentally during both events. The comparison between the experimental and simulation results for the bearing loads shows good agreement. It is obvious that the measured and simulated loads of the bearings during the shutdown event are higher than the loads in start-up [41]. Study has also been carried out of the long-term effect of gear transmission loads on the 5 MW offshore WT during various operational conditions [42]. The rotor torque was simulated and then used as an input for the WTG. The transmission load for each stage was estimated by using two approaches: multi body system (MBS) method and the simplified analytical method. In the latter case, the internal gear dynamic effect was ignored, and the damping parameters were assumed to be zero. The results obtained by using both approaches show adequate accuracy and good agreement as shown in Figure 2.6 [42]. A similar simplified approach was used to estimate the gear transmission load by the same authors in a different study [43].

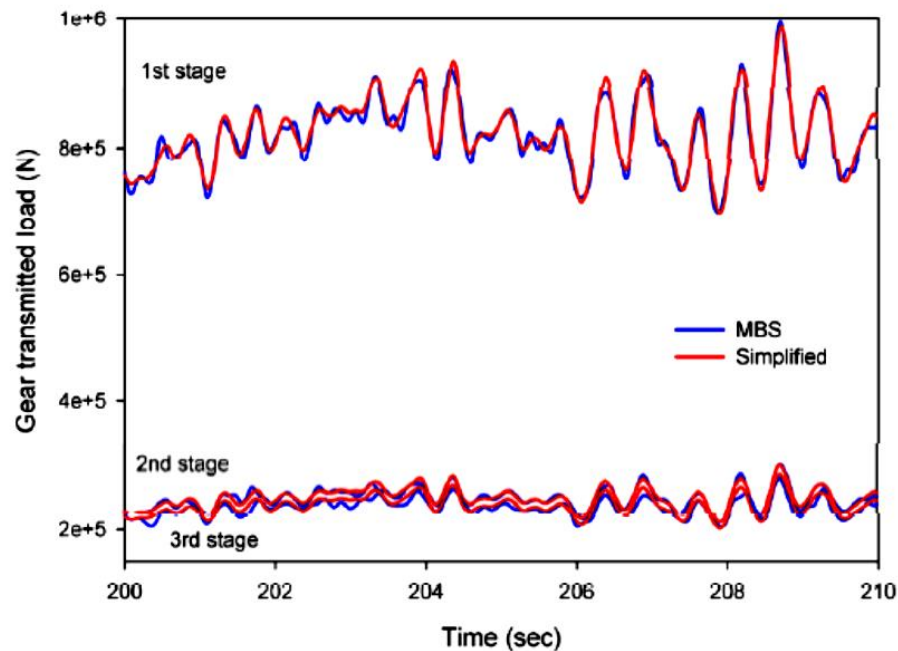


Figure 2.6: Comparison of two approaches using simulated results for gear contact load in different stages within the wind turbine gearbox [42]

Gear mesh stiffness and its influence on gear contact force have been investigated extensively by numerous published studies. Even if the driving gear is moving with constant speed, the driven gear will show a fluctuation because of 'transmission error' which causes excitation forces at the gear mesh. These forces can pass through the shaft and the bearings, causing the gearbox as a whole to vibrate [44]. The effect of mesh stiffness parameters on the dynamic behaviour of planetary gears has been investigated [45]. Fourier series has been used to formulate the mesh stiffness variation in planetary spur gear stages. The rectangular wave is often used to simulate the mesh stiffness between the spur gears [46]. For the planetary gear stage, there is a difference between the mesh phase of produced from the contact between the sun and the planet gears and the mesh phase produced by the contact between the ring and the planet gears. This has noticeable impact on the dynamic behaviour the planetary gear stage [47].

However, in WT applications the gear contact models ignored the effect of torque reversal occurrence on gear contact loads within the WTG during excessive transient loading conditions, such as the unplanned shutdown, and how this could affect the WTG bearings load and their lifetime.

2.4 Dynamic System Modelling of the Wind Turbine Gearbox

Several studies related to the multibody dynamic system (MBS) modelling of the WTG have been undertaken. These studies have focused on analysing and identifying the dynamic response behaviour of the WTG under different loading conditions. Torsional dynamic modelling of the WTG is used as a modelling approach because of its fast solution time and low computational cost. Shi et al. [48] developed a mathematical model for a complete WT drivetrain. A torsional multi body dynamic model was produced with single degree of freedom for each drivetrain component. The drivetrain shafts were modelled as torsional springs. The study assumed that all the gears in the WT gearbox were spur gears and considered a gearbox of three stages with configuration similar to that shown in Figure 2.1 (b). The equation of motion was extracted by using Lagrange equations. The gear mesh stiffness was modelled by linear spring varying with time using Fourier series. The gear contact forces in all gears within the WT drivetrain were investigated during normal operation [48]. The same model and parameters have been used in different research to investigate the influence of cracked gear teeth on the dynamic behaviour of the WT drivetrain [48]. The study concluded that the fault in gear teeth reduced the gear mesh stiffness and increased the noise [49].

Pure torsional models have been used successfully to produce approximations for torsional vibrations [50], angular velocities and accelerations [48], torques of low speed shaft (LSS) and high speed shaft (HSS) [51] and gear mesh forces [48]. If the bearing loads required to be modelled, the torsional model could be expanded to include the rotational and translational degrees of freedom [18]. In pure torsional models, the bearings are considered as linear springs [52]. Mandic et al. [50] proposed a damping control technique to monitor the input torques of LSS and used a controller to regulate the generator torque. The controller produced a resistive damping torque to reduce damping at natural frequencies of the system. This technique was shown to be able to reduce resonant oscillations, thus resulting in less damage to gearbox components. Similar modelling techniques were used by Girsang et al. [51] to represent the WT drivetrain using Simulink and loading conditions obtained by FAST software. By using a purely torsional model the drivetrain was simulated under

a variety of wind and grid loading conditions, allowing analysis of the dynamic interactions between components during transient loading conditions [50, 51].

Simulation tools could be used in the design development stage of WT gearbox configurations to reduce vibrations at resonant frequencies [51]. Torsional dynamic modelling of WT gearboxes is one of the commonly used modelling approaches because of its fast solution time and low computational costs. Meanwhile, the pure torsional model of WT drivetrain is computationally effective to capture the torsional loads, meshing forces of all gear stages and dynamic responses of key WT drivetrain components during free and forced vibrations.

Another approach that has been widely used recently for modelling the WTG is multibody system (MBS) modelling [53-57]. The main principle of this method is to consider the components as rigid or flexible bodies interconnected to each other by appropriate joints, using such as spring stiffness and damping elements. The dynamic behaviour of modelled elements and loads on internal components of the gearbox can be predicted under different operational conditions [9, 14, 58, 59]. Extensive work associated with WT drivetrain modelling has been done by Peeters [14]. The MBS dynamic models of the WTG with various levels of model complexity with their advantages and disadvantages were examined. His work examined three types of modelling approaches: first, the purely torsional multibody model where the gears are modelled as rigid bodies with single degree of freedom in torsional axis and connected to each other by linear springs. Such models are only able to calculate torsional loading effects. The second approach is the six DOF rigid multibody modelling with discrete flexibility; whilst this produces a more accurate model, the complexity of the gearbox modelling is increased. This model takes into account the influence of bearings stiffness in the WTG model. The bearings model is represented by a diagonal 6X6 stiffness matrix [34]. The component flexibility is represented by spring-damper systems. Such models facilitate a more detailed description of gear mesh and bearing stiffness. The third approach is fully flexible multibody modelling which increases the model's accuracy in terms of flexibility of gearbox components, compared to the second approach, through finite element (FE) modelling. This approach allows the visualisation of the influence of different subcomponent flexibilities;

however, it is computationally expensive. Similar approaches have been developed subsequently by Helsen [59]. The insight of the model's complexity and its influence on the dynamic behaviour of WTG was examined and validated experimentally. In addition, the level of gearbox model complexity was evaluated.

In the three previous studies, the influence of increasing the complexity of the model's WTG components on its dynamic behaviour under different loading conditions was examined. The torsional model is limited by the absence of load assessment on bearings as it concentrates only on torsional loads on gears. Although the 6 DOF rigid multibody models are more accurate, the approach is limited by its inability to evaluate the internal stresses and strains of gearbox components. To take the flexibility of the internal components of WTG into account, fully flexible multibody models have been developed. FE models have been used for flexible multibody modelling to estimate the stresses and deformation of the modelled components, but they incur high computational cost.

The flexible movement in WTG comes from flexible parts such as shafts, bearings and the gear meshing [34, 58, 60]. Increasing flexibility does not, however, always result in more accurate results. The addition of flexible components in the WTG model increases the model's complexity and slightly affects the eigen frequencies and affects the other modes much more [32]. LaCava et al. [34] observed theoretically and experimentally the influence on the bearings and gears loads of increasing the level of gearbox components' flexibility. Seven models were studied, with different levels of complexity. It was concluded that the flexibility of gearbox sub-components such as housing, carrier and the main shaft has noticeable influence on the loading of the planet bearings [34]. In different studies, it has been reported that using a flexible coupling with reasonable stiffness can reduce the torque amplitude of the high speed shaft [9, 32]. Increasing model complexity could have a small effect on accuracy at high computational cost [35].

Kahraman [61] developed a 10 DOF model for two parallel helical gears to study the influence of the helix angle on the dynamic response of the gear system. The study ignored the effect of the clearance in bearings, assuming that the mesh stiffness is constant and ignoring the effect of backlash. The mode

shapes for the gear system were investigated. The results indicate that the axial vibration of the gear system has low influence on the natural frequency value [61]. The results of this study are fairly accurate and have been validated by later gear modelling work that used a commercial software package called DADS [14]. The results of the Kahraman study are useful reference for validating the accuracy of modelling in the HSS stage [14]. However, investigating the different levels of modelling may help gearbox designers to improve the design and assess the dynamic behaviour of the chosen design under specific dynamic loads [14, 62]. In WT applications, flexible multi body simulation is required to: consider the number of degree of freedoms (DOFs), study the flexibility of gearbox individual components, and examine their deformation associated with their dynamic behaviour. FE methods have been used to model the HSS [32]. Different studies have reported that in comparison with rigid body system modelling, introducing component flexibility causes noticeable reduction in eigenvalues but has ignorable effect on frequencies [59, 63].

Modelling WTG components by using the FE approach takes considerable computational time. Other studies have shown that deformable body modelling using the FE approach is a conventional tool that can represent precisely the tooth geometry and modelling in the particular contact region between two gears in full mesh for assessing the gears deformation under variable loading conditions [64-67]. Recently, the MBS modelling approach has been widely used in combination with FE method to model the full WTG. As some gearbox subcomponents have small deformation, such as the planet carrier and the housing, FE simulation can be used to model these parts by using solid bodies to eliminate unnecessary degrees of freedom [59, 68]. Reducing the components' DOFs reduces the amount of computational time involved in FE. Moreover, FE analysis has been used to validate the results of dynamic behaviour obtained experimentally for gear housing and planetary gear systems with five planets. For different ranges of gear frequency, the accuracy of FE model outcome has been compared with the results of the experimental model. The outcome shows reasonable trend agreement and low error prediction percentage for natural frequency values [64].

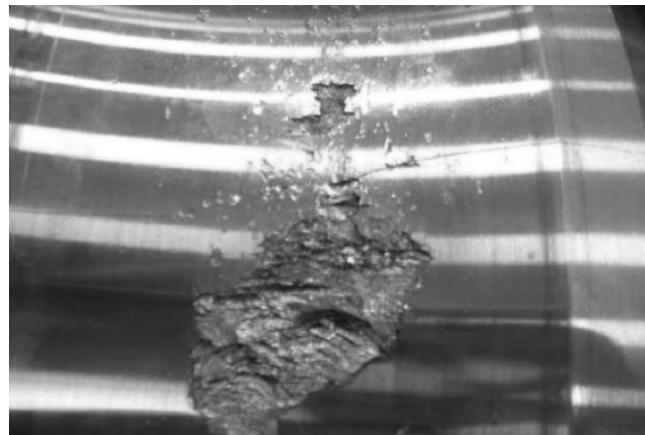
In a different study, carried out by NREL for a 750 kW WT, FE approach was used together with the 'SIMPACT' MBS modelling to model WTG subcomponents including: planet carrier rim, the planet carrier pins and planet

bearings. The outcome of this study shows that considering the planet carrier pins as rigid bodies instead of frictional contact pins slightly increases the frequencies amplitude for the whole planet carrier. However, considering the planet carrier pins as flexible bodies instead of rigid bodies reduces the frequencies amplitude of the planet carrier as well [69]. Increasing the WTG components flexibility does not, however, always produce accurate outcome. The flexible modelling of components does not have a huge impact on the gearbox components that are not in direct connection [60]. Considering the bearings as flexible instead of stiff bodies increases the number of degrees of freedom and this contributes to increasing the number of natural frequencies, especially in the normal direction of tooth contact [70].

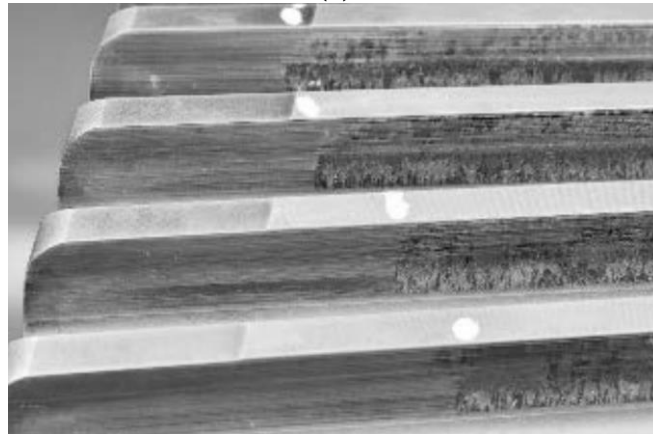
However, the existing pure torsional models for WTG assumed that the contact between the gears resented by linear spring working always under pressure and cannot capture the effect of torque reversal occurrence on the gear contact force. The bearing model within the MBS models with 6 DOF per components published in literature is repressed by diagonal stiffness matrix and do not consider the interaction between the rollers and the races

2.5 Common Failure Modes of Wind Turbine Gearboxes Components

Inadequate gearbox reliability has been a chronic issue in the wind power industry, accounting for the majority of profit warnings and downtime for turbines. The failures are largely due to the operating conditions encountered in wind applications which are not fully understood. Manufacturers have learned from past failures and have set and adhered to new design standards, yet gearbox lifetimes still fall short of the desired twenty years. For turbines in the field, necessary retrofits and replacements are time consuming, costly, and all too frequent. Due to the mechanically stressful nature of WT applications and the numerous moving parts and subsystems of a gearbox, maintenance is often necessary multiple times per year. A replacement or overhaul can cost as much as \$300,000 and accounts for the single largest amount of downtime in power production [71]. This cost presents a significant drawback for companies and entrepreneurs investing in wind power. Gearboxes installed in wind turbines are subject to unique torque and non-torque loads from the weight, motion, and wind loading of the rotor and blades.



(a)



(b)

Figure 2.7: Failure in wind turbine gearbox components (a) Bearing surface flaking [72] (b) High speed shaft gear surface damage[73]

Gears and bearings failure modes (see Figure 2.7) within the WTG are caused by many factors: inappropriate gear or bearing materials, faulty lubrication, faulty surface treatment, friction caused by sliding or rolling, unexpected velocities, stresses, excessive loads [72, 74, 75]. Table 2.1 illustrates the common failure modes of gears as reported in international standards ISO-10825 and BS-7848 [74]. The common modes of failure for gears within the WTG are: moderate and excessive wear, abrasion, tip root interference, surface fatigue, Hertzian fatigue (i.e. micropitting, macropitting and spalling), crushing, plastic flow, scuffing and fracture [10]. There are many recognised types of gear tooth surface damage. Although various surface treatment methods have been used to stiffen the surface under contact of the flank of gear tooth, such as carburising and nitriding, surface failure is a common occurrence in WTG gears.

Table 2.1: Classification of Gear modes of failure, adapted from [74]

| | | |
|--|---|---|
| 1. Indications of surface disturbances | 1.1 Sliding wear | 1.1.1 Normal wear (Running in wear) |
| | | 1.1.1.1 Moderate wear |
| | | 1.1.1.2 Polishing |
| | | 1.1.2 Abrasive wear |
| | | 1.1.3 Excessive wear |
| | | 1.1.4 Moderate scratching (Scoring) |
| | 1.2 Corrosion | 1.1.5 Severe scratching |
| | | 1.1.6 Interference wear |
| | | 1.2.1 Chemical corrosion |
| | 1.3 Overheating | 1.2.2 Fretting corrosion |
| | | 1.2.3 Scaling |
| | 1.4 Erosion | 1.4.1 Cavitation erosion |
| | | 1.4.2 Hydraulic erosion |
| | 1.5 Electric erosion | |
| | 2. Scuffing | |
| 3. Permanent deformations | 3.1 Indentation | |
| | 3.2 Plastic deformation | 3.2.1 Plastic deformation by rolling |
| | | 3.2.2 Plastic deformation by tooth hammer |
| | 3.3 Rippling | |
| | 3.4 Ridging | |
| | 3.5 Burrs | |
| 4. Surface fatigue | 4.1 Pitting | 4.1.1 Initial pitting |
| | | 4.1.2 Progressive pitting |
| | | 4.1.3 Micro pitting |
| | 4.2 Flake pitting | |
| | 4.3 Spalling | |
| | 4.4 Case crushing | |
| 5. Fissures and cracks | 5.1 Hardening cracks (Quench cracks) | |
| | 5.2 Grinding cracks | |
| | 5.3 Fatigue cracks | |
| 6. Tooth breakage | 6.1 Overload breakage | 6.1.1 Brittle fracture |
| | | 6.1.2 Ductile fracture |
| | | 6.1.3 Semi-brittle fracture |
| | 6.2 Tooth shear | |
| | 6.3 Breakage after plastic deformation (Smeared fracture) | |
| | 6.4 Fatigue breakage | 6.4.1 Bending fatigue |
| | | 6.4.2 Tooth breakage |

In WT application, gearbox eventual failure occurs through two main modes of gear failure: tooth breakage and surface failure [9, 12, 76, 77]. Tooth breakage starts with a root crack on the meshing side; followed by crack growth leading to complete fracture in one or more than one tooth. Surface failure starts with micro pits that then grow into bigger pits due to the combined effects of rolling and sliding loading on gear teeth [12] [74]. The formation of micro pits is a function of stress distribution below the contact surface and occurs due to the heavy rolling loading in frequent extreme loading events [12] [74]. Metal removed from the gear tooth contact surface forms spall debris suspended in oil film that comes between the tooth surfaces in contact and works as stress concentration points during gear rotation [12]. This phenomenon later causes abrasion [12]. The spall can be removed by using a sufficient filtering system [12]. In WT applications, the other failure modes are not thought to be as critical as the two listed previously. However, they could be important as they could cause damage which may initiate or accelerate failure caused by one of the above modes, so should not be ignored. Dong et al. [36] estimated the gear service life of the sun gear of the NREL 750 kW WTG. Only gear surface pitting was considered during the normal operation of WT and all other failure modes of surface and other operational conditions were ignored. In terms of pitting, the sun gear exhibited more influence than the planet gears because of the high ratio of contact pressure distribution [36]. The technical report produced by NREL [11] summarised that more than one mode of failure can be recognised in failed gears in different stages of the WTG. The same conclusion was reached by another NREL report [78].

The common failure mode of roller bearings were listed in the international standard [79]. Gearbox failure typically originates in the bearings. It has been found that 67% of WTG failures originated in the bearings with 47% represents the failure rate in high speed shaft (HSS) bearings [8]. The cylindrical roller bearings installed within the WTG in planetary stage are not designed for high and excessive radial loads which is exceeded the recommended levels during normal operation and emergency stop [75, 80]. The WT bearings failure will be much more likely under transient operating conditions [72]. With better understanding of the operating conditions gearboxes encounter in the field, more informed design decisions can be made, ultimately resulting in a more reliable and economical gearbox.

2.6 Summary

This section will summarise key findings from the literature and introduce approaches that will be investigated in this study. The literature review highlights the limitation of the available published work that deals with transient events and the corresponding torque reversal within the WTG, how it affects the gear and bearing contact load, gear and bearings dynamic behaviour, gears and bearing contact stress and consequently their lifetime within the WTG. Few papers have presented work examining loads during transient events such as WT unplanned shutdown, braking, overloading and its potential to cause WTG components' premature failure. WT shutdown induces high loads on gearbox bearings and magnifies the gear contact pressure that in turn causes them to fail prematurely. Although many studies have used commercial software to achieve accurate simulation for WTG dynamic behaviour, further effort should be made to assess possible failure modes of gearbox components, particularly the gears and bearings. This would help in estimating gearbox components' remaining service life when operating under extreme load events, considering the existence of torque reversal, and in proposing possible design improvement solutions.

1. Previous studies used simulated low speed shaft torque as a direct input to the developed models. In this study, field measured torque data (see Chapter 3) will be used as direct input to the WTG models developed and the experimental data will be used to validate the results of developed models (see Chapter 6 and 7).
2. The research in gear contact modelling was reviewed. It has been found that the simplified method calculated the transmission contact force with adequate accuracy when compared with the MBS modelling approach. The simplified method basically is a quasi-static form of the internal gear dynamic force and could be tested later in dynamic modelling work planned in this study. In this study pure torsional MBS model for WTG has been developed by using MATLAB/Simulink. The developed model is considered the gear contact under the effect of torque reversal as will explained in Chapter 4.
3. Dynamic system modelling was then reviewed. It must be noted that while increasing the model's flexibility could complicate the model, it does not however always result in more accurate results and has

sometimes ignorable influence on gearbox dynamic behaviour. Three gearbox model types were then discussed, and this highlighted the importance of the degree of freedom of gearbox components. It was found that using model with discrete flexibility with 6 DOF per component improves the accuracy of the model and contributes to sufficient modelling of gears and bearings. Extensive studies have highlighted that the FE approach is a conventional tool to represent deformations of the gear tooth geometry and for modelling the contact region between two gears in mesh and assessing the gears deformation under nonlinear loading conditions. However, although fully flexible multibody models for the WTG expand the insights on the influence of drivetrain subcomponent flexibilities, they are computationally expensive. In this study MBS modelling by using SIMPACK is used to develop WTG model with advance bearing model consider the off-diagonal terms in stiffness matrix and consider the interaction between the rollers and the races as will explained in Chapter 5.

4. In relation to gear failure modes, in the WTG, two key modes were highlighted as critical modes of gear failure, namely, tooth bending under high cyclic loads and surface contact fatigue. The previous research on gears has ignored two important factors: the variety of loading conditions on WTG, such as shutdown, and its effect on gear contacts which eventually contributes to gear tooth surface failure. The other failure modes, such as sliding wear, are not thought to be so critical. However, they could be important as they could cause damage which may initiate or accelerate failure caused by one of the above modes, so should not be ignored. Focusing on the effect shutdown as transient events, and which of these causes the most damaging loading on gear and bearing contact, will be the focus of this study as explained in Chapters 5 and 7.

3

DATA ANALYSIS OF FIELD MEASURED TORQUE SPECTRUMS

This Chapter discusses the processing of large sets of 2MW wind turbine field measurement data using the rainflow counting method and Damage Equivalent Load (DEL) analysis. It then examines each individual operating case separately and compares it with the shutdown event. The load measurement data of an operating wind turbine has been analysed in depth. Loading variations occurring during four operating conditions have been analysed and compared in detail. Rainflow counting method has been used to convert the time domain data of complicated loading history into number of loading levels and cycles. It was found that the correlations between the input shaft (i.e. the low speed shaft (LSS)) and the output shaft (i.e. the high speed shaft (HSS)), indicated that both shafts had similar variation trend of shaft torques but higher variation amplitude occurred for HSS. Moreover, the torque cycles distribution analysis for LSS and HSS during each individual operating condition highlighted the importance of focusing on the extreme events that the wind turbine experienced.

3.1 Field Data for Different Operational Conditions of 2MW Wind Turbine

The data recorded under four different operating conditions have been examined, comprising: start-up, normal operation, normal stop, and shutdown. During start-up, operation of the wind turbine started from the rest. The machine accelerated from rest till it reached rotor rated speed without grid connection, at which point the generator was switched online. During normal operation this involved: non-stop operation of the wind turbine at rated power and rated rotor speed. During the normal stop, the wind turbine was under continuous operation and then the rotor was gradually stopped after the aerodynamic braking by blades was initiated and the generator was disconnected, then the mechanical brake was engaged to force the wind turbine drivetrain to a completed halt gradually in a controlled way. During shutdown, the rotor operated normally and then the stop button was pressed, which led to initiation of aerodynamic braking by fast blade pitching, the mechanical brake was then engaged, followed by generator disengagement, which dragged the rotor abruptly to halt in fastest possible manner.

Based on the measured data, it was obvious that the wind turbine gearbox components experienced loads of variable amplitudes in random sequence, depending on the wind variations and operational controls of the wind turbine. The recorded data were large in size. For each set of data, the mean value, range value, maximum peak value, minimum valley value and reversal value have been calculated. It has been concluded that analysing all available data is highly useful as it gives possible explanations on how wind turbine drive train components behaves when exposed to certain events.

To ensure accuracy, the recordings of the torque spectrum were taken using high sample rate of 250 kHz. Because of the large volume of data only one operational case was processed, the shutdown, which is analysed and discussed in detail in this chapter. The results of shutdown case have been compared with the other operational conditions. However, no rotational speed records are available for LSS and HSS. The wind turbine specifications are listed in Table 3.1.

Table 3.1: Wind Turbine Specifications

| | |
|-------------------------|----------|
| Rated power | 2 MW |
| Rotor diameter | 80 m |
| Nominal rotor speed | 18.1 rpm |
| Nominal generator speed | 1680 rpm |
| Gear ratio | 1:92 |

3.2 Rainflow Counting Method

The rainflow counting method is the process of extracting and counting the number of load levels and corresponding load cycles in a complex load history where each cycle is linked with different load amplitudes. The rainflow cycle counting method was initially proposed by Matsuishi and Endo in 1968 [81] and then developed by Downing and Socie [82]. The usefulness of this method in handling any loading history is the fact that some understanding of fatigue load may be obtained using rainflow counting method without statistical extrapolation of stress ranges. The counting of peaks makes it possible to formalise a new diagram in form of histogram with the peaks attributed to a random load, history which can then be transformed into a load spectrum. In analysis of loading history, the rainflow histogram is often used because it provides a data presentation more easily to visualize the relationship between a specific loading level and the number of occurrences at the load level than by using typical time history plots [83]. Figure 3.1 shows an illustration of the rainflow counting method.

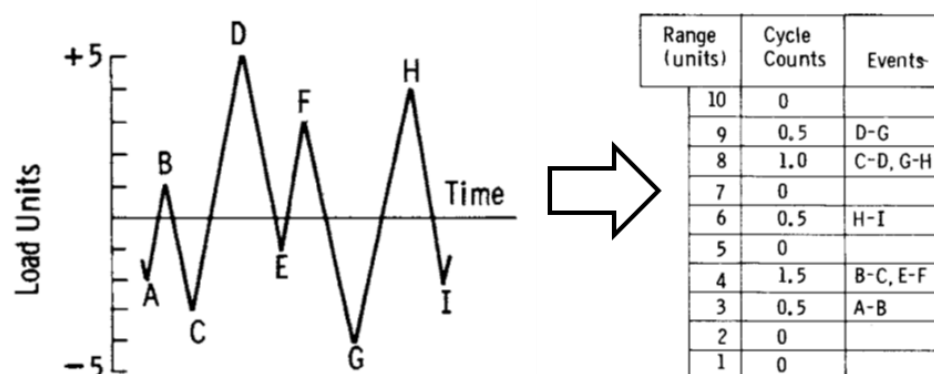


Figure 3.1: Rainflow cycle counting method, adapted from [83]

For fatigue failure analysis, the rainflow histogram of the load is very important since fatigue damage is determined using the load levels and their corresponding cycle counts. The international standard BS EN61400-1 recommends rainflow counting as a commonly accepted algorithm and very helpful tool in WT applications to accurately calculate the fatigue of the key components of the WTG [84].

The rainflow cycle counting technique, in its simple form, starts with using the load history as an input. Then the data are scanned to identify the available load peaks and valleys in the load time history provided, and finally rearranges to provide a new set of data. The new set of data starts with the maximum load peak or minimum load valley, whosoever is higher in absolute value, and then load amplitudes values and the number of levels are counted. In this Chapter the load cycles have been extracted by using an algorithm based on ASTM standard recommendations [83]. The following MATLAB code steps shown in Figure 3.2 summarises the major steps used in rainflow method.

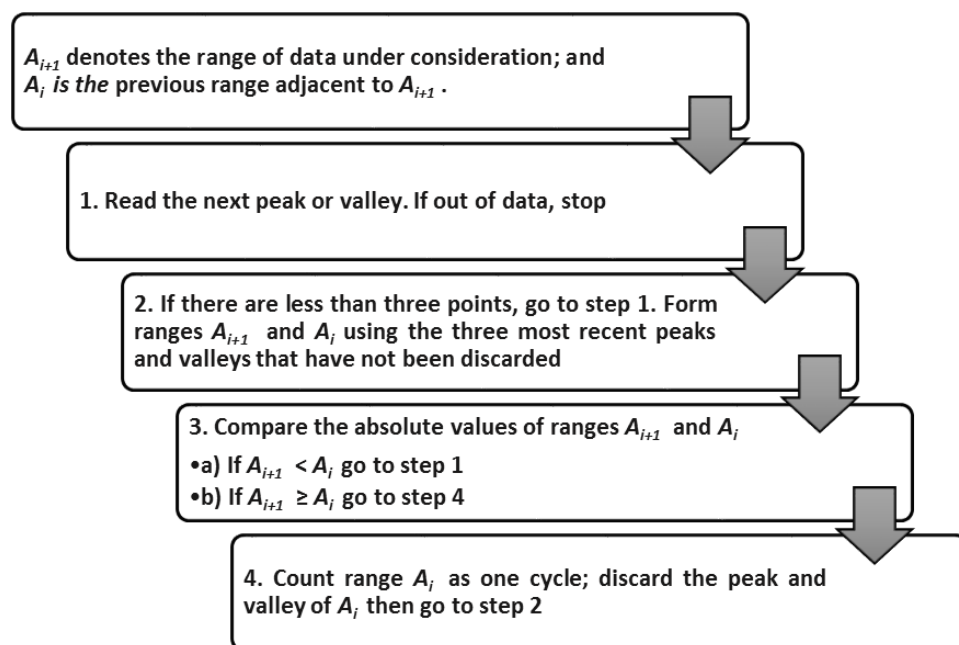


Figure 3.2: Major steps of Rain-flow cycle counting method adapted from [85]

The rainflow cycles counting approach has been used in MATLAB code to change the load history given in Figure 3.3(a) with seven points labelled by P1, P2, P3, P4, P5, P6 and P7, from time domain to cycles and ranges by the following steps:

1. Check the ranges A_i and A_{i+1} , where $A_i = |P1-P2|$ and $A_{i+1} = |P2-P3|$. If $A_{i+1} < A_i$ then take another ranges in point P4.
2. Check the new ranges A_i and A_{i+1} , where this time $A_i = |P2-P3|$ and $A_{i+1} = |P3-P4|$. If $A_{i+1} \geq A_i$ then $|P2-P3|$ is considered as one cycle, and the two points P2 and P3 should be neglected. As a result, the main load history of Figure 3.3(a) should be reduced to new one as shown in Figure 3.3(b).
3. Check the ranges $A_i = |P1-P4|$ and $A_{i+1} = |P4-P5|$. If $A_{i+1} < A_i$ then take another ranges in point P6.
4. Check the ranges $A_i = |P4-P5|$ and $A_{i+1} = |P5-P6|$. If $A_{i+1} \geq A_i$ then $|P4-P5|$ is considered as another one cycle. The two points P4 and P5 should be neglected. As a result, the adapted load history of shown in Figure 3.3(b) should be reduced to new one as shown in Figure 3.3(c).
5. Check the ranges $A_i = |P1-P6|$ and $A_{i+1} = |P6-P7|$. If $A_{i+1} \geq A_i$ then $|P1-P6|$ is considered as another new cycle. The two points P1 and P6 should be neglected. Checking the rest points of the load history shows that there are less than three points, thus the cycles count completed, and all the cells of the rainflow matrix (range, mean, cycles) are filled in as shown in Figure 3.3(d).

The full load range, ΔP , and the mean load, P_{mean} , can be calculated by using the following equations [83]:

$$P_{mean} = (P_{max} + P_{min}) / 2 \quad 3.1$$

$$\Delta P = P_{max} - P_{min} \quad 3.2$$

To define and analyse all the load data sets provided, ASTM standard [83] definitions for mean value, range value, spectrum, peak, valley and reversal have been used in this Chapter as given in Figure 3.4. However, the rainflow counting method has a weakness and limitation in term of the uncertainty of the rainflow output to identify which cycles follow the maximum loading case and which ones come before it. The rainflow method ignores the sequence of the cycle occurrence in specific range within the time domain.

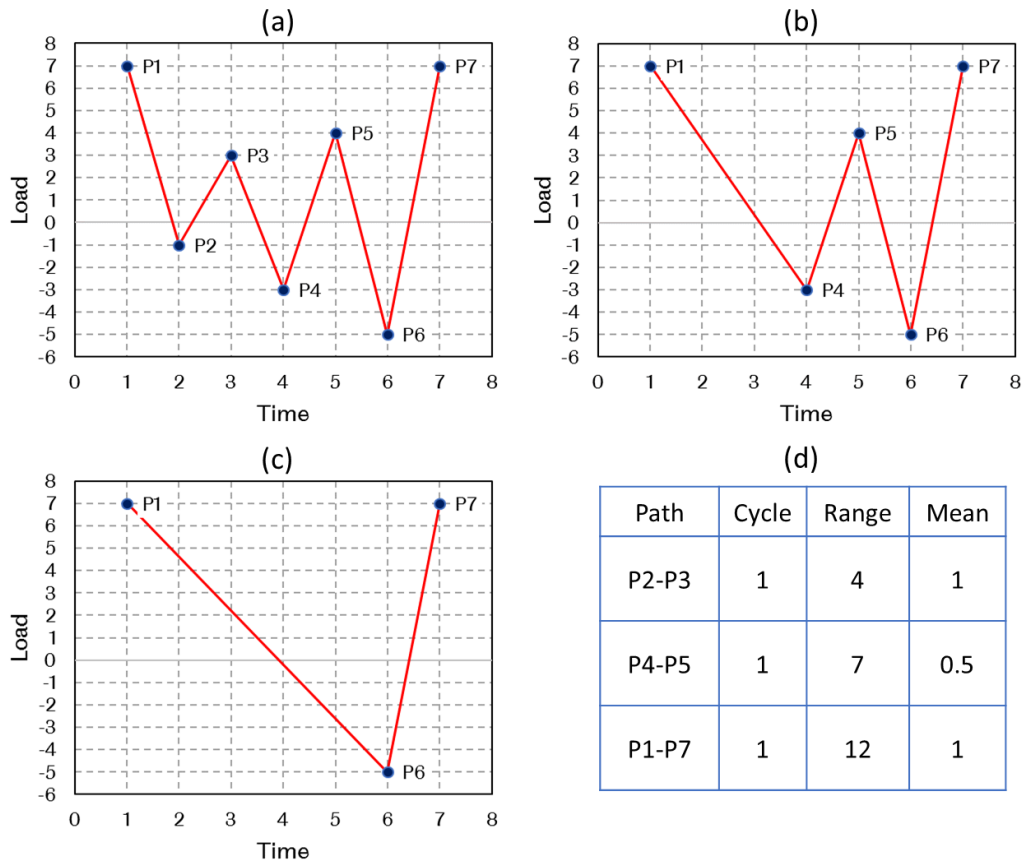


Figure 3.3: Rainflow counting method process (a) Original load history, (b-c) Rainflow cycle processing, (d) Rainflow matrix

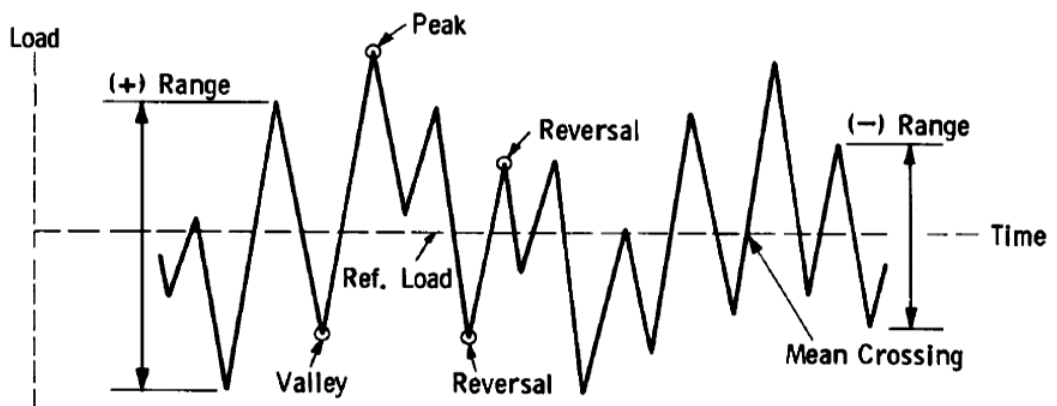


Figure 3.4: Basic cyclic loading parameters [83]

3.3 Damage Equivalent Load Analysis Method

The main purpose of this analysis is to show in which wind turbine operational condition most of the damage happens. The Damage Equivalent Load (DEL) can be calculated according to the international standard ISO/IEC 81400-4 [86]. Each torque spectrum and the rainflow cycle count the actual load time series. Then a simple Wöhler curve (i.e. T-N curve) formulation is used to calculate what constant range of 1 Hz waveform would give the same damage:

$$N = CT^{-p} \quad 3.3$$

Where N is the number of torque cycles, C is constant, T is the applied torque; p is the slope of Wöhler line as shown in Figure 3.5 .

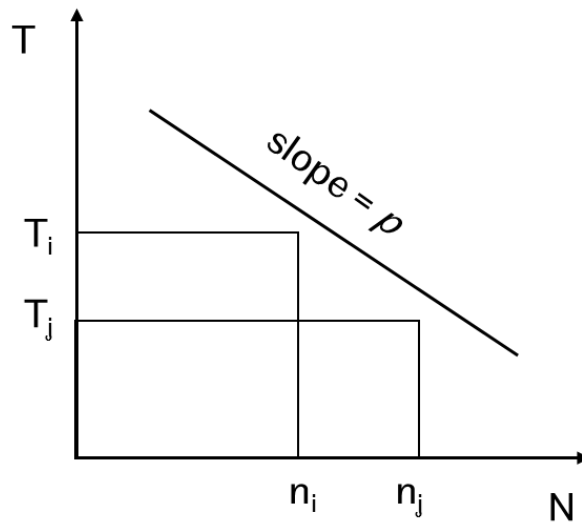


Figure 3.5: Wöhler curve illustration with mean torque and damage cycles

As explained before, the rainflow counting method transforms the torque spectrum from time domain to a set of means (i.e. T_i, T_j, \dots) and corresponding cycles (n_i, n_j, \dots). The damages caused by the mean torque in the bins 'i' and 'j' assumed to be equal and below the Wöhler line as illustrated in Figure 3.5 as the following:

$$T_i^p n_i = T_j^p n_j \quad 3.4$$

When n_i is the number of torque cycle corresponding to T_i which is higher than T_{i+1} , the equivalent number of cycles corresponding to it, n_{ia} , can be calculated as the following:

$$n_{ia} = n_i \left(\frac{T_i}{T_{i+1}} \right)^p \quad 3.5$$

Finally, the damage equivalent load (DEL) for a time period of torque spectrum can be calculated as the following:

$$DEL = \left(\frac{n_1 T_1^p + n_2 T_2^p + \dots + n_i T_i^p}{n_1 + n_2 + \dots + n_i} \right)^{1/p} \quad 3.6$$

Where $n_1 + n_2 + \dots + n_i$ is equal to the time period of torque spectrum in seconds, there are total time 1Hz cycles as the hertz is equivalent to the number of cycles per second, T_i and n_i represents the means and the corresponding cycles presented in the original time series. Using 1Hz DEL for loads testing is a generally well accepted practice. It is possible to use the simple T-N curve formulation to calculate the damage equivalent load for various time periods, such as 20 seconds of torque data. Any variable amplitude time series can be changed into any constant amplitude time series with any frequency and duration is required to cause the same amount of damage. By applying a T-N curve and then calculating some “proxy” damage and then take that damage and calculate what simple time series would generate the equivalent damage. The slope of Wöhler curve ‘ p ’ for steel is typically 3, 6 or 9 [86]. It is worth to mention that for most uses the DEL is nothing more than a metric to compare different time series of load in terms of which one causes higher damage than the other events.

3.4 Results and Discussion

The shutdown is a highly transient event that occurs in a very short time and which leads to high torque values. This unique loading condition might cause the most damaging condition for WTG components. This section analyses and discusses in depth the full set of data obtained from the measurement of a

shutdown event. Furthermore, the data of other three different operating conditions will be analysed and compared with the shutdown data. The HSS and LSS torque history in time domain for these four different operational conditions have been processed by using the rainflow counting cycle method.

3.4.1 Comparison Between Shutdown and Other Operational Conditions

Figure 3.6 illustrates the comparison of the Mean-Range distribution (without the load cycles) of the HSS torque during shutdown and normal operation, shutdown and normal stop, and shutdown and start-up respectively. Comparing the magnitude of the mean and range of HSS torque reveals noticeable differences under different operating conditions. When the shutdown event occurs, the mean value of HSS torque varies greatly than that under the other three operational conditions. The normal operation condition shows the narrowest mean torque values, distributed normally and symmetrically around the rated torque, with the maximum range value is approximately 3,800 Nm. The highest range for the HSS torque occurs during shutdown and exceeds 19,000 Nm, which is 5 times the HSS torque range value of the normal operation. During normal operation, all the mean values are positive, and no torque reversal occurrence are observed. Conversely, the torque reversal occurrence is obvious in other three operational conditions, where the highest mean value exceeding 4,000 Nm (in negative mean value) and taking place in shutdown. During the shutdown condition the pitching of the WT rotor blades is faster than normal operation in order to provide the required aerodynamic braking to stop the rotor by applying the brake on the disk while the rotor rotation contributes to torque reversal occurrence of higher amplitude than that occurring under other operational conditions.

It is obvious that during shutdown, the HSS torque displays the highest range and mean values above the rated torque compared to those occurring in normal operation, normal stop and start-up respectively as shown in Figure 3.6. This would have harmful consequences on gearbox components such as gears and bearings and could contribute to more overloading of the gearbox bearings and gears in the high-speed stage, greater than that in the low and intermediate stages within the WTG. Moreover, it is clear that the highest HSS torque range value occurs over the braking periods in very few cycles.

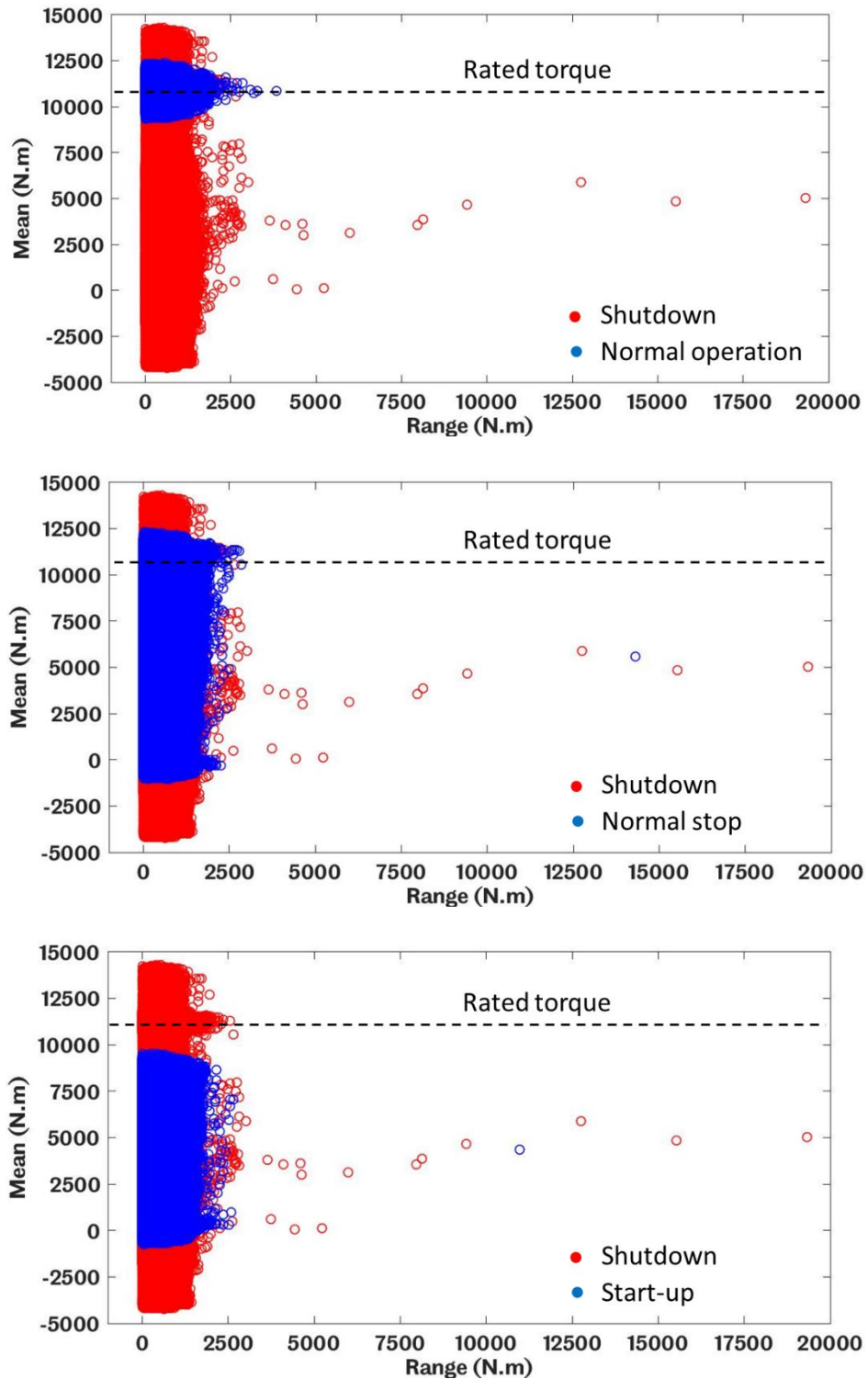


Figure 3.6: Comparison of the mean-range values of the HSS torque during different operational conditions

Figure 3.7 shows the Mean-Range distribution (without the load cycles) for LSS torque during shutdown versus other three different operational conditions (i.e. normal operation, normal stop, and start-up). The LSS torque shows similar Mean-Range variation as that of the HSS but higher values which are proportional to the wind turbine gearbox ratio. The normal operation shows the narrowest mean values distributed normally and symmetrically around the rated torque with maximum LSS torque range around 250,000 Nm. The highest range for the LSS torque occurs during shutdown and exceeds 2,000,000 Nm, which is 8 times that occurring in normal operation. The correlation between the LSS and HSS torque shows that both HSS and LSS shafts have the same variation pattern during various operational conditions but a higher-level load for the LSS.

For both HSS and LSS, the maximum value for torque reversal occurred when the braking action was trying to bring the rotor to the rest. Moreover, it may be possible to predict the behaviour of the HSS torque variation from the LSS torque and vice versa. The occurrence of torque reversals and negative mean values can be observed in the three operational conditions of start-up, shutdown and normal stop but not for normal operation.

Analysing the time history of the HSS and LSS torque by using the rainflow counting cycle method is highly important because the LSS torque data is the input load of WTG and eventually the HSS torque works as a direct input load to drive the generator. Obtaining greater understanding of the effects of torque variations on WTG for different operating conditions may contribute to finding solutions for eliminating premature failures of gearbox components.

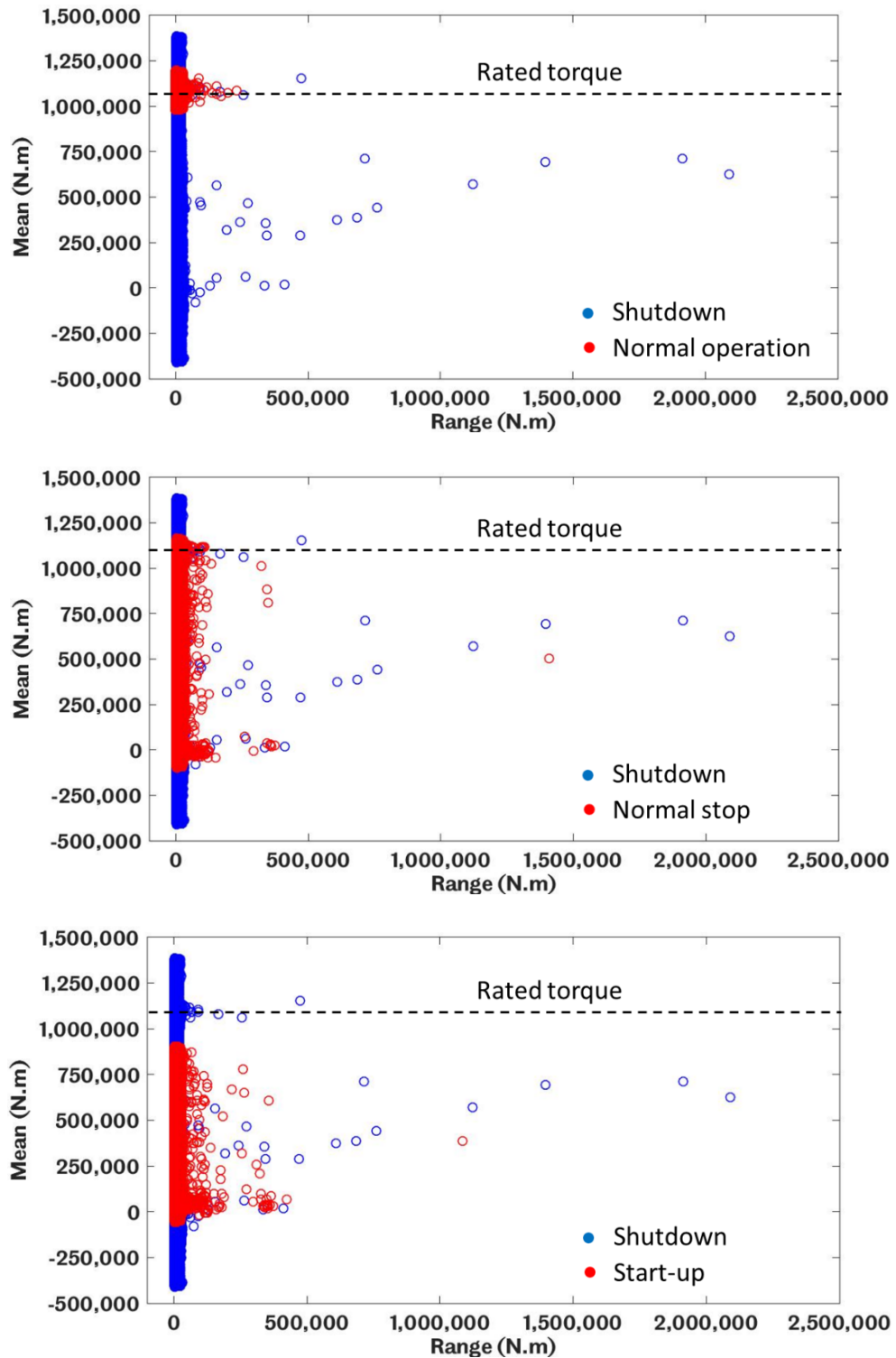


Figure 3.7: Comparison of the mean-range values of the LSS torque during different operational conditions

Figure 3.8 shows the Mean-Cycles distribution (without the load range) of the HSS torque during different operational conditions. Comparison of the mean values and cycles extracted from the HSS torque time history by using the rainflow counting method during different operational conditions produces important information. The highest number of cycles is around 280,000 cycles, occurring during the normal stop of the WT and corresponding with zero of HSS mean torque. The reason is that during the normal stop the WT is brought steadily down to the lowest speed (taking around 32 seconds), and then to a halt (taking around 48 seconds), with the braking torque occurring steadily and completely reversing during normal stop. During shutdown it takes shorter time, with harsher braking torque. In normal operation the torque cycle variation shows normal distribution around the rated torque of HSS torque of 11,000 Nm with narrow HSS mean torque range variation. The torque cycle distribution is non-uniform for shutdown, normal stop and start-up.

During the shutdown, normal stop and start-up, the highest number of HSS torque cycles corresponds with the zero-mean value. But for the start-up, the WT needs around 70 seconds of steady and completely reverse torque, to accelerate and overcome the huge inertia of the WT rotor and WTG components. After that the WT rotor starts to operate under the cut-in speed trying to reach the rated speed. During start-up, the field measurement data for the HSS torque stopped before the WT reached the rated HSS torque required for generator engagement.

The above explains why the highest mean value of the HSS torque during start-up condition is below 10,000 Nm as shown in Figure 3.8. However, the most effective cycles are those corresponding with the highest mean value, exceeds 145,000 Nm, and occurs when the brake is applied on the HSS side during shutdown condition, trying to bring the WT drivetrain to a halt and dragging the rotor abruptly to rest in the quickest way possible.

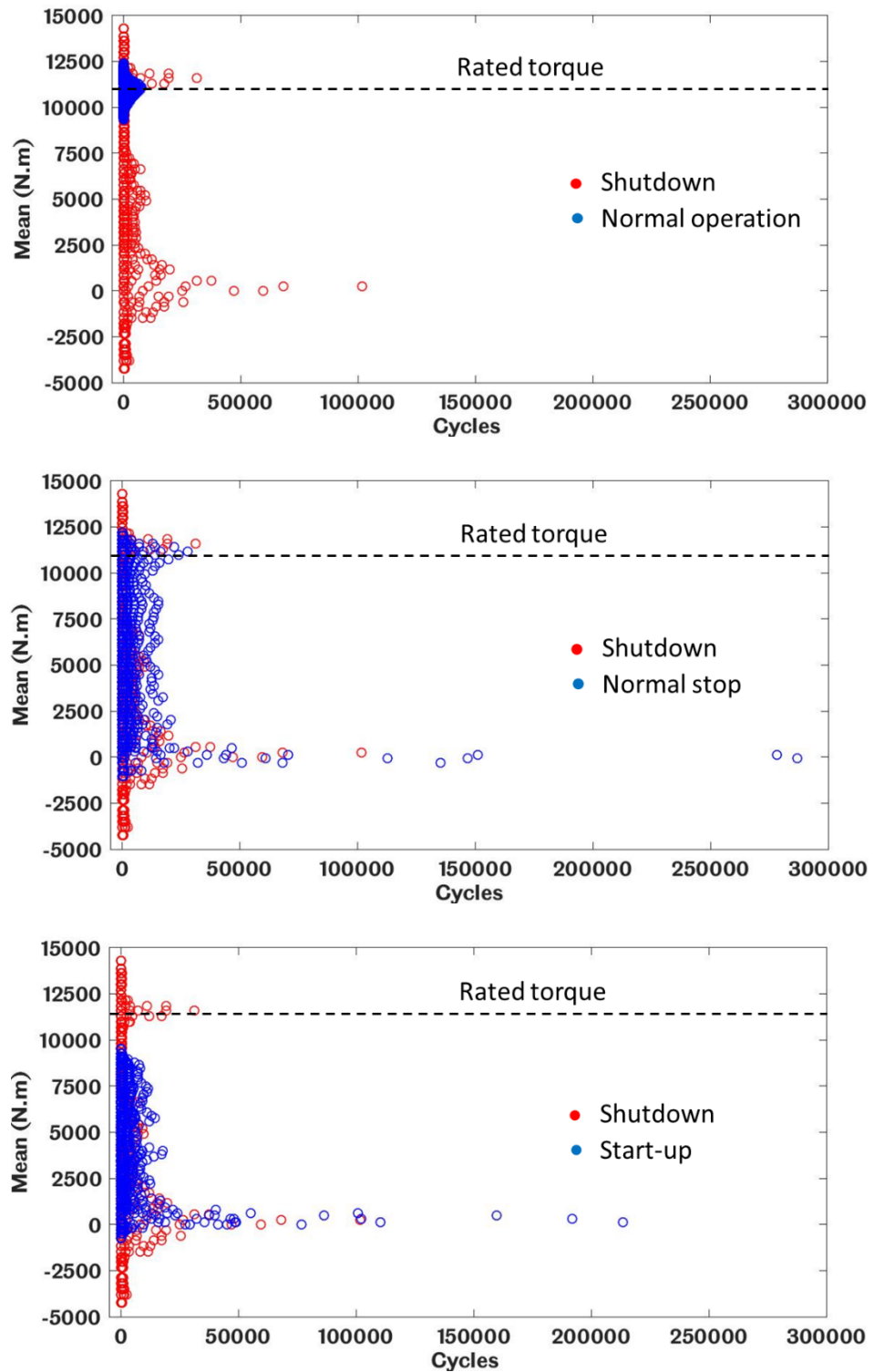


Figure 3.8: Comparison of the mean-cycles values of the HSS torque during different operational conditions

Figure 3.9 shows the comparison of Mean-Cycles distribution for the LSS torque during shutdown and the other operational conditions. The LSS torque shows similar Mean-Cycles variation of the HSS but with higher mean values in LSS than in HSS for all operational conditions. Moreover, again it is because the huge inertia of the rotor connected directly to the LSS being greater than that of the HSS, the high rotational speed for the HSS being higher than that of the LSS and the gear ratio (i.e. 1:92) of WTG being fairly high. Generally, the comparison between the LSS and HSS torque Mean-Cycles distribution shows a similar pattern during the four different operational conditions, with normal torque cycles distribution around the rated torque and narrow mean range during normal operation.

The analysis of the field load measurement data by using the rainflow counting cycle method shows no occurrence of torque reversals (no negative mean value) during the normal operation. However, torque reversal was observed in both LSS and HSS, but with different sequences and in dissimilar manner, in three different events, namely: start-up, normal stop and shutdown. Torque reversal occurs when the mean torque value sign changes from positive to negative. Consequently, high vibration loads produced by the rotor are absorbed by the gearbox which is loaded in an extreme manner and its components, gears and bearings, are therefore put under overload condition.

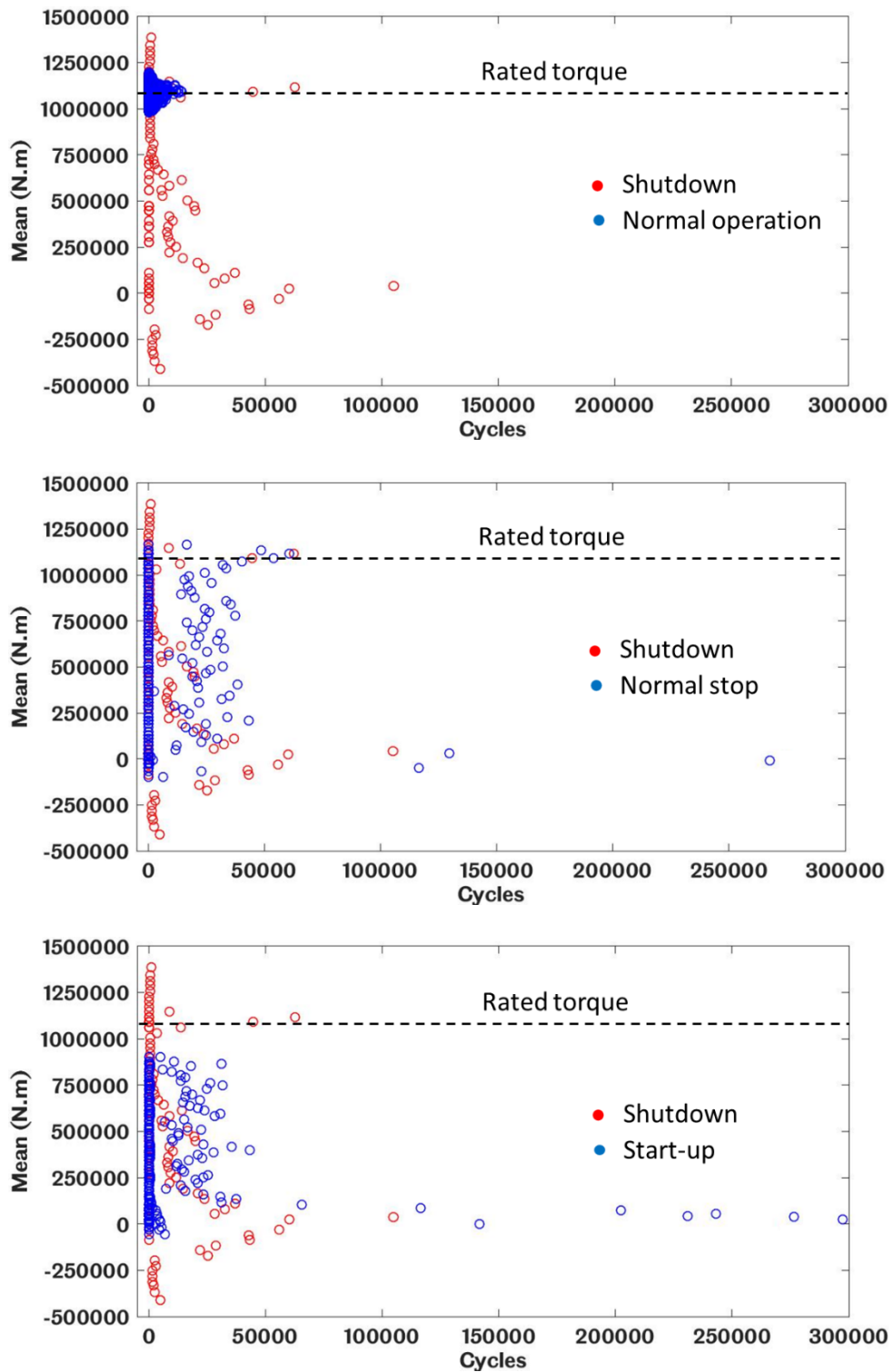


Figure 3.9: Comparison of the mean-cycles values of the LSS torque during different operational conditions

3.4.2 Variations of Torque Ranges and Cycles for Different Operational Conditions

Figure 3.10 shows the torque range distribution of the HSS (top) and LSS (bottom) (without the cycles and mean) during the four different operation conditions, shutdown, normal operation, normal stop and start-up. The highest range variation of torque for both LSS and HSS occurs during shutdown event, while the lowest one occurs in both shafts during normal operation. Again, the LSS torque shows similar range variation of the HSS but higher range values proportional with the WT gearbox ratio.

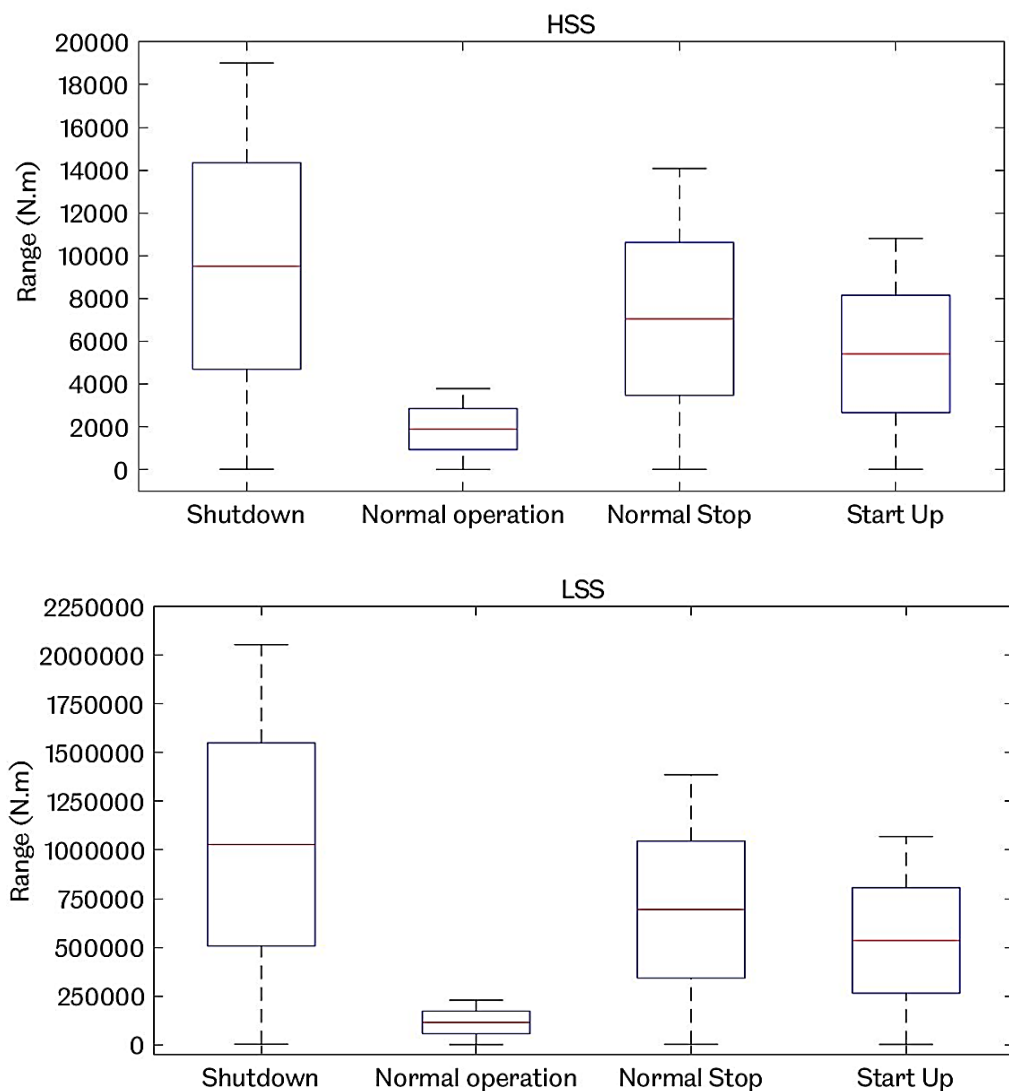


Figure 3.10: Comparison of the range values of the HSS (top) and LSS (bottom) torque during different operational conditions

As illustrated in Figure 3.10, during shutdown it is very clear that the torque ranges for both HSS and LSS spread out from the median (the middle line in box plot), splitting the distribution of the torque range into two equal groups (i.e. the lower extreme, the lower quartile, the upper quartile and the maximum extreme). This is not the case during the normal operation as the HSS and LSS torque range data are stacked and exhibit the lowest median. For the HSS the range median (the middle line in box plot) during shutdown is 5 times higher than that of normal operation, 1.3 times higher than that of normal stop and 1.76 times higher than that of start-up respectively. For the LSS the range median during shutdown is 8.9 times higher than that of normal operation, 1.5 times higher than that of normal stop and 1.92 times higher than that of start-up.

Figure 3.11 shows the mean distribution for the HSS and LSS torque (without the range and the cycles) during the four different operation conditions. Again, the LSS torque shows similar mean variation as that of the HSS but higher mean values for the LSS. The highest mean torque variation for both LSS and HSS occurs, as explained before, in shutdown while the lowest one occurs during normal operation.

The torque reversal occurrence, the negative mean value in Figure 3.11, is obvious in shutdown, normal stop and start-up, with the highest mean value recorded during shutdown. Normal operation appears to have higher median mean value (i.e. the middle line in box plot which is equal to the rated torque for both LSS and HSS). The mean value in normal operation does not vary as much as in the other operational condition. The greater the distance between the points in the boxplot, the more spread out the mean torque value. The latter case is obvious in shutdown.

For the HSS the median of the mean torque value during normal operation is 2 times higher than that of shutdown, 1.92 times higher than that of normal stop and 2.47 times higher than that of start-up. For the LSS the median of the mean value during normal operation is 2.2 times higher than that of shutdown, 2.1 times higher than that of normal stop and 2.6 times higher than that of start-up.

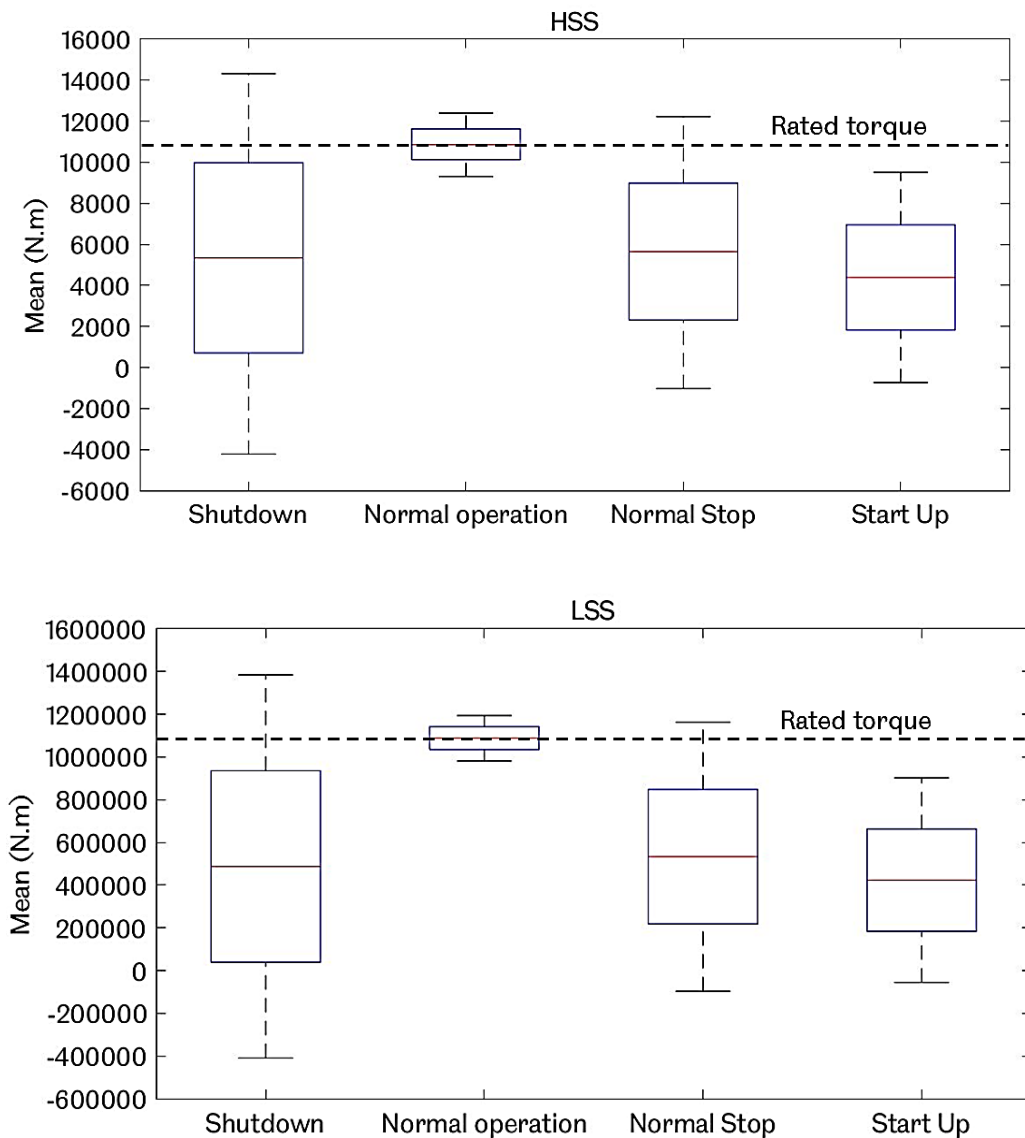


Figure 3.11: Comparison of the mean values of the HSS (top) and LSS (bottom) torque during different operational conditions

As shown in Figure 3.11, the maximum rate of torque reversal occurrence, the negative mean torque value, during the shutdown for both HSS and LSS is 4 times and 5.8 higher than that during the normal stop and start-up respectively. This is again, because during shutdown condition the WT starts braking by pitching the blades faster than usual to provide aerodynamic braking and then stopping the rotor by applying the brake on disk while the rotor running contribute on torque reversal occurrence with higher amplitude.

Figure 3.12 shows the histogram of torque range versus cumulative cycles for all operational conditions. It is clear that the highest torque ranges for both LSS and HSS occurs during shutdown condition and correspond with only fewer cycles. As expected the lowest torque range for both LSS and HSS occurs during normal operation. During the four operation conditions, for both LSS and HSS shafts, the highest number of cumulative cycles always correspond to the lowest torque range value. The effect of these load cycles on the lifetime of gears and bearings within the WTG will be investigated in Chapter 7.

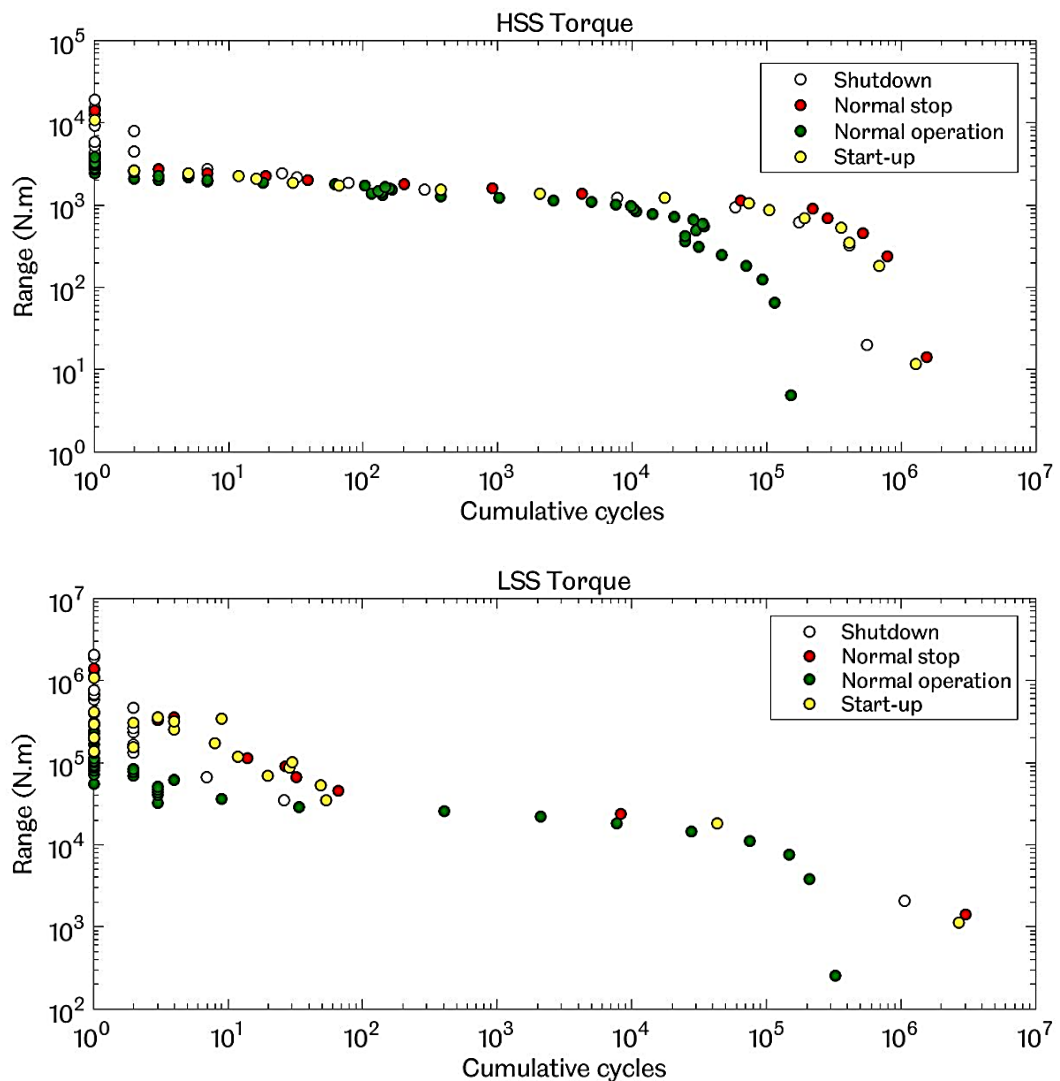


Figure 3.12: Comparison of cumulative torque cycles of HSS (top) and LSS (bottom) during four different operational conditions

The cumulative torque cycle histogram for HSS and LSS indicate that the shutdown event has harmful consequences on wind turbine gearbox components because the occurrence of some high torque amplitude values for both shafts, which exceed the rated torque and occurs with low number of torque cycle.

3.4.3 Damage Equivalent Load for Each Operational Condition

Figure 3.13 illustrates the DEL derived from both HSS and LSS torque values during normal operation, shutdown, normal stop and start-up. The mean values of HSS and LSS torque, are calculated by using the rainflow counting cycle method, is shown along the horizontal axis. The DEL, calculated according to the procedure explained before in section 3.3.3, is shown along the vertical axis. The slope of T-N curve of 6 for steel was used in DEL analysis. The main purpose of this analysis is to show which operational condition causes most of the damage. The damage corresponding with the transient events such as shutdown is 3.65 higher than that occurring in normal operation, 1.43 higher than start-up and 1.1 higher than normal stop in both HSS and LSS. This draws the attention to study the damage of the critical WTG components, the gears and bearings, caused by the transient events. As shown in Figure 3.6 and Figure 3.7, the mean torque during braking for HSS and LSS occurs in a high range and this contributed to much higher damage as illustrated in Figure 3.13.

The comparison of total damage occurred during various operational conditions shows that damage to the HSS and LSS was the highest during shutdown condition and occurred within torque ranges lower than the rated torque. As illustrated in Figure 3.13, the damage to both shafts, the HSS and the LSS, was of higher magnitude during brake engagement on the HSS side in combination with the highest torque range and low number of cycles. Conversely, lowest torque range magnitude combined with the highest torque cycles caused the lowest damage. For the HSS, the most damage occurred within the mean range of 5-7.5 kN.m and for the LSS occurs within the mean range 100 times that of the HSS, which is very close to the WTG ratio of 1:92.

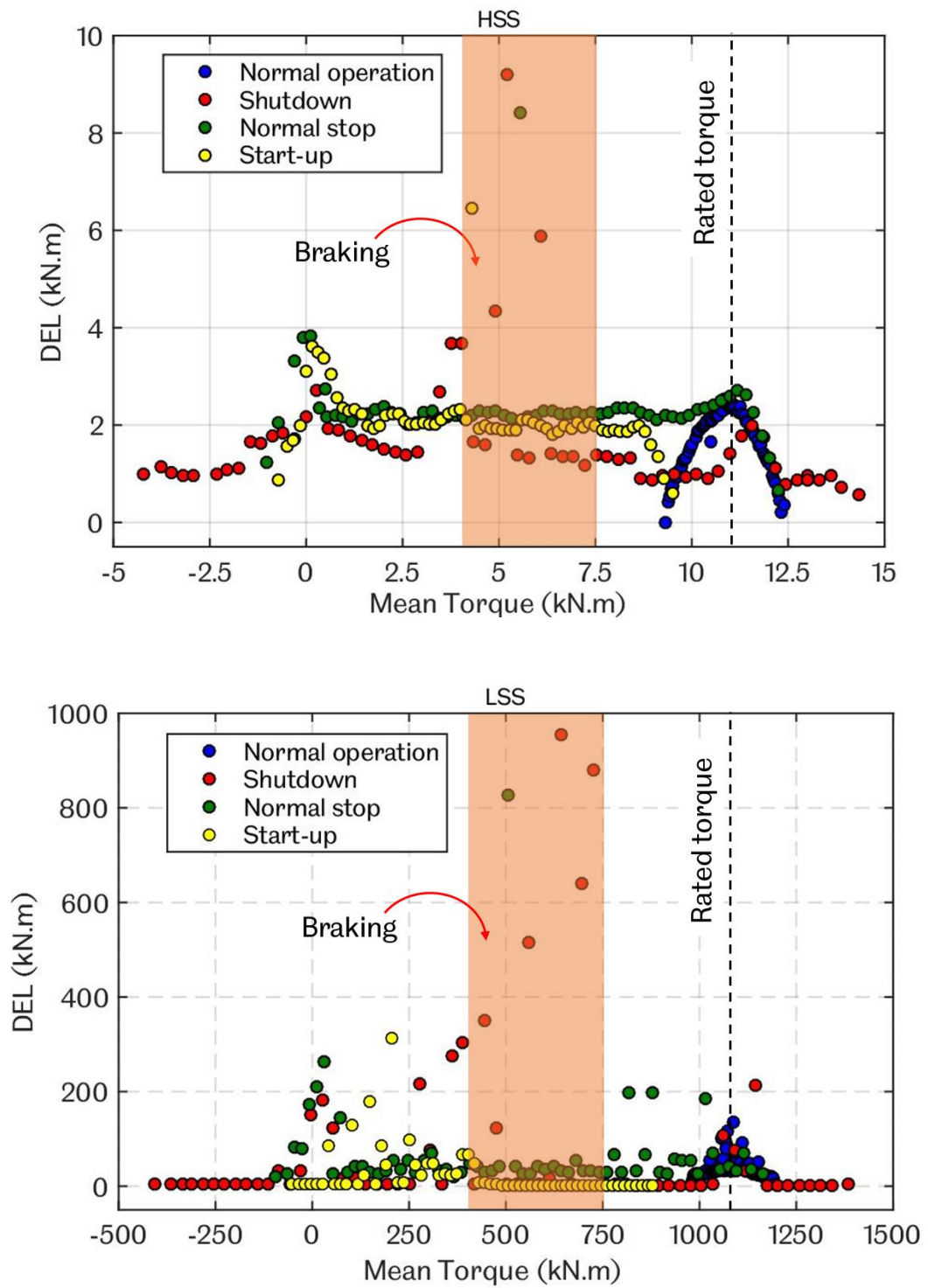


Figure 3.13: Damage equivalent load for HSS (top) and LSS (bottom) per different operational conditions

3.5 Summary

This Chapter has shown that the rainflow counting method, together with DEL, is an appropriate technique to analyse load history in time domain to derive the load cycles with corresponding ranges and damages under various load levels. The fact is that no overloading occurrence was observed during the normal operation condition highlights the importance of focusing on the extreme events that the WT may experience such as shutdown. During braking in shutdown and normal stop, the loading of the gearbox shafts is much higher than that in normal operation condition. Moreover, during shutdown, for both HSS and LSS, low number of torque cumulative cycles combined with high torque range occurs above the rated design torque. Conversely, high number of cumulative cycles with various torque amplitudes occur below the value of rated torque. The correlation between the LSS and HSS torque shows that both shafts have the same variation pattern during various operational conditions but with a higher-level load for LSS. For both HSS and LSS, the torque cycles occur during braking within the transient events, shutdown, normal stop and start-up, with high torque range, and produce a higher damage than that during the normal operation.

In the WT drivetrain, it is obvious that the torque reversal occurs during braking events only. This phenomenon could have considerable impact on the WTG critical components, the gears and bearings. The influence of torque reversal on gears and bearings contact forces and how it affects gears and bearings surface stress will be investigated in Chapters 5 and 7. During braking in shutdown, the gearbox shafts loading is much higher than normal operation condition. The effect of high range load cycles during transient load conditions on the fatigue lifetime of gears and bearings within the WTG will be investigated in Chapter 7.

4

PURE TORSIONAL MULTIBODY DYNAMIC MODELLING OF WIND TURBINE DRIVETRAIN

The torsional dynamic model for wind turbine gearboxes (WTGs) is one of the common used modelling approaches because of its fast solution time with low computational costs. The purely torsional multibody system (MBS) dynamic models developed in this Chapter are computationally effective comparison with MBS models developed in Chapter 5 and can capture the torsional loads and dynamic responses of key wind turbine (WT) drivetrain components during free and forced vibrations. The MBS models developed in this Chapter are considered the effect of torque reversal on gear meshing contact forces within the WTG during unplanned shutdown. The development of WT drivetrain dynamic models can be beneficial in understanding the loading behaviour and predicating the response of WT drivetrain components under transient loading conditions. The required parameters for the pure torsional WT drivetrain models have been calculated by using CAD models for the four different WTs, these are: 3MW with 2 stages gearbox (Drivetrain-A), 3MW with 3 stages gearbox (Drivetrain-B), 2MW with 3 stages gearbox (Drivetrain-C) and NREL 750kW (Drivetrain-D) with 3 stages gearbox.

The WTGs models developed in this study are the commonly used WTG configurations in the field according to the international standard IEC 61400-4. Full descriptions for each WT drivetrain and corresponding gearbox developed in this Chapter are shown in the following sections.

4.1 Determination of Masses and Inertias of Wind Turbine Drivetrain

Purely torsional dynamic models with lumped masses, using 2, 5 and 11 DOFs respectively, are developed to represent this drivetrain with a fixed or variable speed generator model. The gearbox components, including planet carrier, gears and shafts as well as the generator and the rotor are modelled, using one torsional DOF for each component in the rotational direction. The rotor assembly includes three blades and the rotor hub, which is connected to the gearbox through the LSS. The mass and inertia of the blades (M_b , J_b) can be calculated by the following formulas [87]:

$$M_b = 2.95 L_b^{2.13} \quad 4.1$$

$$J_b = 0.212 M_b L_b^2 n \quad 4.2$$

where, L_b is the length of the blade and n is the total number of blades. The total amount of polar moment of inertia of the rotor assembly as one lumped mass (J_{rotor}) can be calculated from the summation of the blades inertia and the inertia of the hub (J_h) [10]:

$$J_{rotor} = J_b + J_h \quad 4.3$$

The rotational stiffness is used to model the flexibility associated with each component in the torsional model, such as the shafts and gear mesh stiffness. In some studies, all the shafts of the WT drivetrain were considered to have constant cross section areas, therefore, the variable cross section area of each shaft was simplified as a solid cylinder or tube [48, 88]. In this study, the actual geometry of each drivetrain shaft has been modelled and the values of polar moment of inertia of the main shaft and shafts of the entire gearbox are

calculated from the CAD models. Through knowing the length of shaft L , the shaft modulus of rigidity G and shaft polar moment of inertia J , the torsional stiffness k_{shaft} and torsional damping C_{shaft} of each shaft can be calculated by:

$$k_{shaft} = \frac{J \cdot G}{L} \quad 4.4$$

$$C_{shaft} = 2\zeta_{shaft} \sqrt{J \cdot k_{shaft}} \quad 4.5$$

The shaft damping ratio ζ_{shaft} for steel can be taken as 0.005-0.007 [89] [90]. An average value of shaft damping ratio of 0.006 is used in this study. The generator resistance torque, which acts as a reactive loading to the drivetrain at the generator side, affects the WT drivetrain system when the generator engages or disengages with the electrical grid. In this study, the generator's electrical resistance torque is represented by a torsional spring. For NREL 750kW WT (Drivetrain-D), the value of the electrical torsional spring stiffness between the generator armature winding and magnetic field of the generator is $K_{gen} = 28,100$ N.m/rad. This value is taken from Mandic et al. [50], which has been calculated and validated experimentally for different operation conditions by the authors. The electrical torsional spring stiffness for Drivetrain-A, B and C is not available in the literature. For the purely torsional model, the gear mesh stiffness is modelled as a linear spring [32]. The gear mesh stiffness is a parameter that accounts for the meshing interaction between gear teeth. Gear meshing presents a complex dynamic relationship depending on several gear parameters such as gear material, helix angle, face width, base radius, mesh alignment, normal load, and number of teeth and can be calculated according to the international standard BS ISO6336-1 [91]. The gear mesh stiffness k_{mesh} can be determined as follows [32]:

$$k_{mesh} = k_{gear} (r_{b1} \cos \beta)^2 \quad 4.6$$

The mesh damping coefficient C_{mesh} can be determined as follows [92]:

$$C_{mesh} = 2\zeta_{mesh} \sqrt{\frac{k_{mesh} r_{b1}^2 r_{b2}^2 J_{b1} J_{b2}}{r_{b1}^2 J_{b1} + r_{b2}^2 J_{b2}}} \quad 4.7$$

Where r_{b1} , r_{b2} , J_{b1} and J_{b2} are the base radii and the inertias of the driving and driven gears, β is the helix angle of the gear. The gear mesh damping ratio ζ_{mesh} can be taken as 0.03-0.17 [92] [90]. An average value of gear mesh damping ratio of 0.1 is used. A CAD model for the NREL 750kW (Drivetrain-D), Drivetrain-A, B and C gearboxes has been created as shown in Figure 4.1 and Figure 4.2. The calculated parameters have been validated with data available in published literature [10, 50, 51].

Figure 4.3 shows the complete 750kW WT drivetrain (Drivetrain-D) representation of eleven lumped masses of 11 DOFs with consideration of gear mesh stiffness and gear mesh damping coefficient within the WTG.

For NREL 750kW WT drivetrain (Drivetrain-D), the shafts stiffness, the electrical stiffness value, the mass and polar moment inertia for all gearbox components, the gear ratios for each stage of the WT gearbox and the gear mesh stiffness used to develop the pure torsional multibody system for the WT drivetrain model are shown in Table 4.1 and Table 4.2. The required parameters for Drivetrain-A, B and C gearbox components are shown in Table 4.1 and Table 4.3.

Table 4.1: Design parameters of three different WT drivetrains

| Parameters | Drivetrain | | | |
|-------------------------|------------|-----------|-----------|-----------|
| | A | B | C | D |
| Rated power | 3 (MW) | 3 (MW) | 2 (MW) | 750 (kW) |
| Gearbox ratio | 1:34 | 1:115 | 1:92 | 1:81.49 |
| Gearbox stages | 2 | 3 | 3 | 3 |
| Gearbox | stage1 | Planetary | Planetary | Planetary |
| | stage2 | Planetary | Planetary | Parallel |
| | stage3 | - | Parallel | Parallel |
| Min. rotor speed (rpm) | 8.6 | 8.6 | 10.8 | 14.8 |
| Rated rotor speed (rpm) | 14.8 | 16.1 | 16 | 18.6 |
| Max. rotor speed (rpm) | 18.4 | 18.4 | 19.1 | 22.1 |

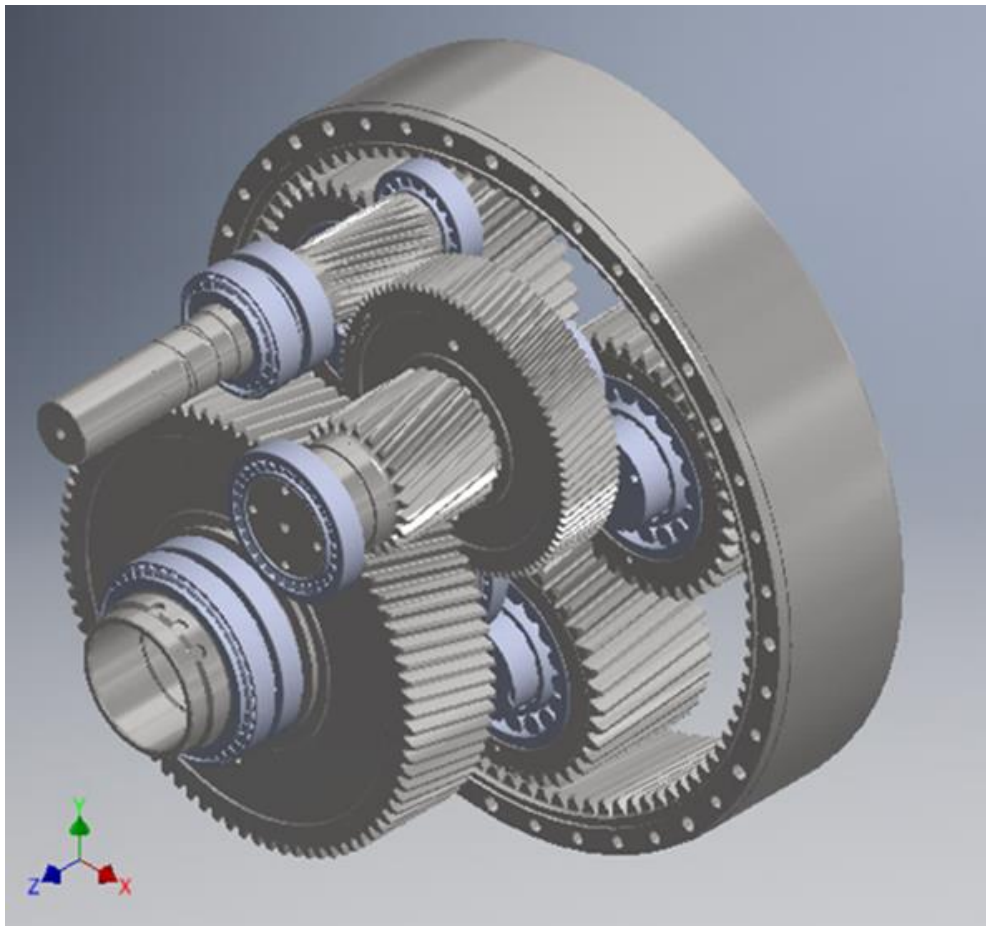


Figure 4.1: CAD model for NREL multistage gearbox of 750kW WT (Drivetrain-D) consisting of a fixed ring planetary gear set with three planets and two parallel gear sets with two intermediate shafts and overall gearbox ratio of 1:81.49

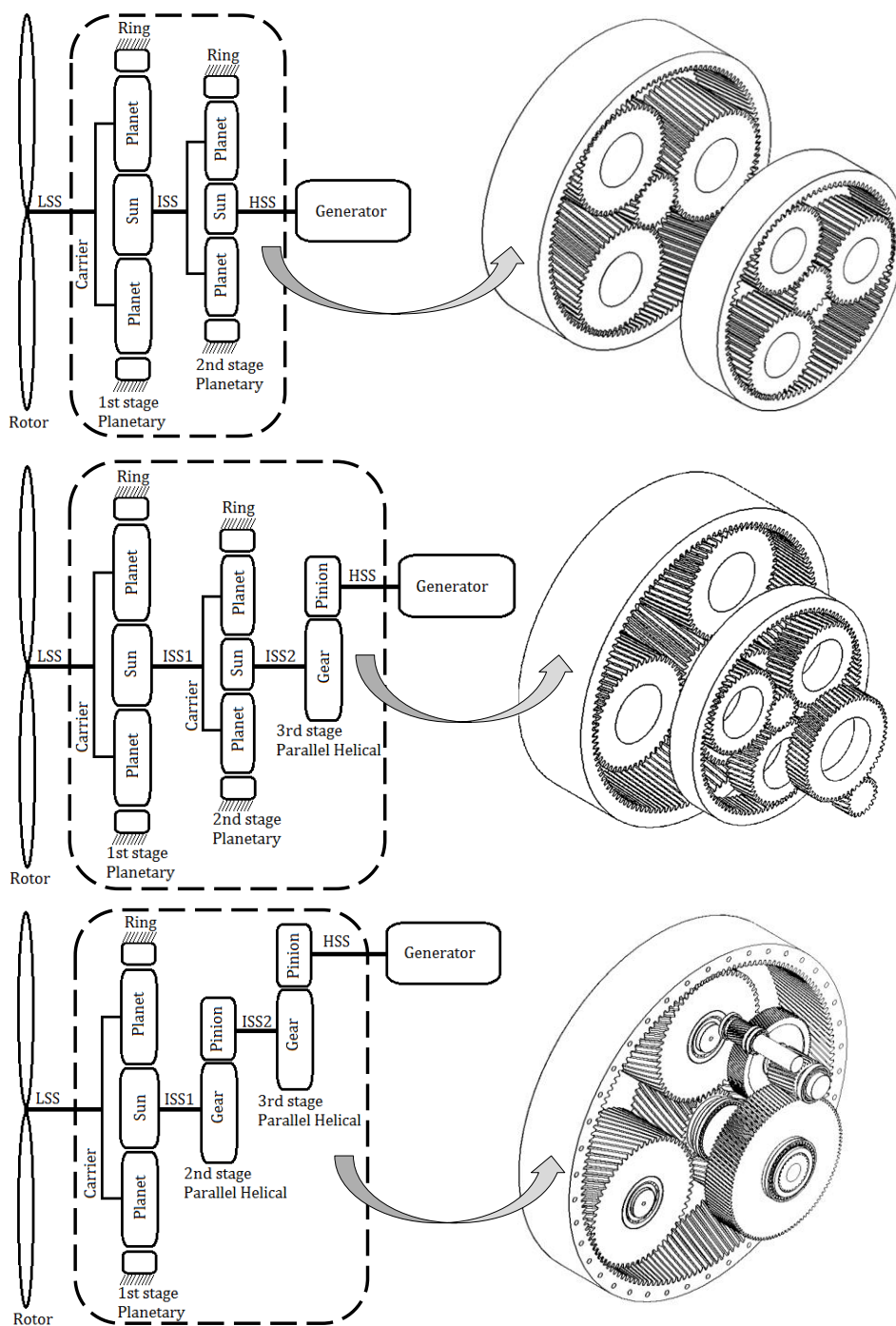
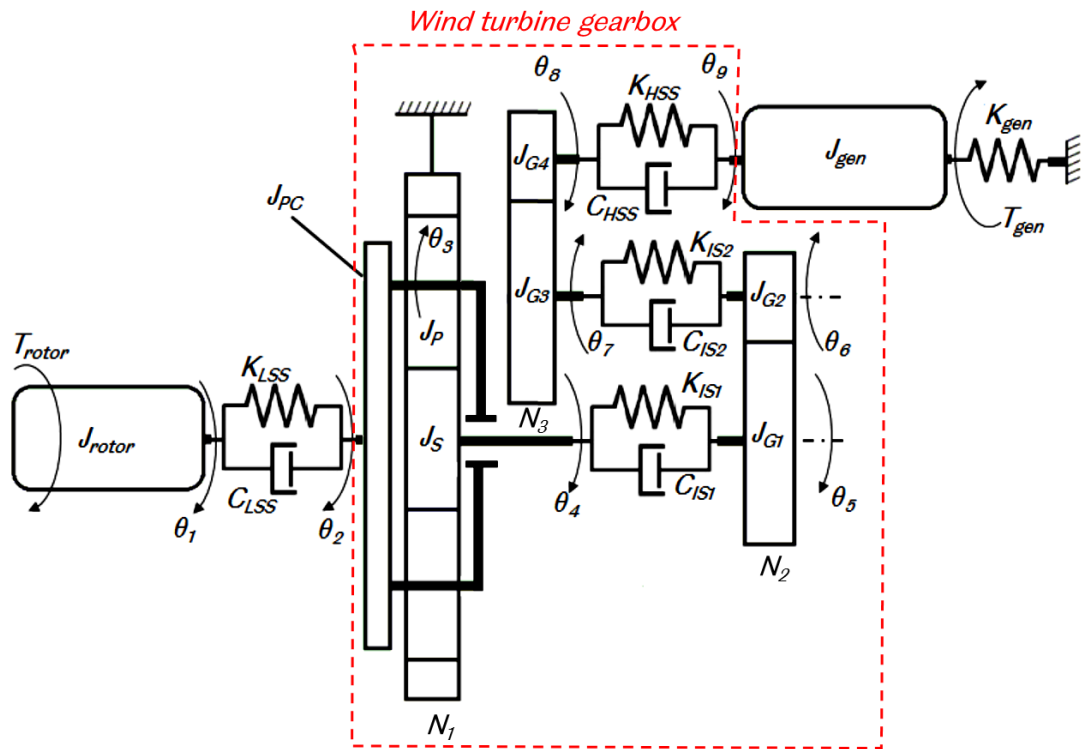
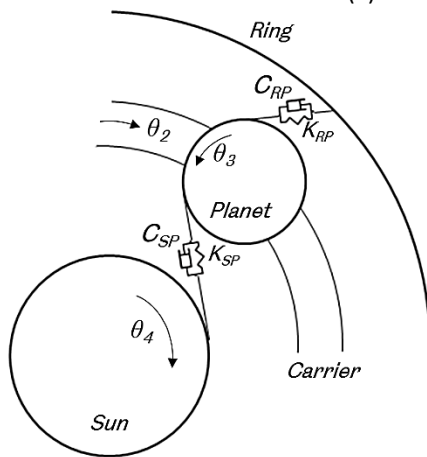


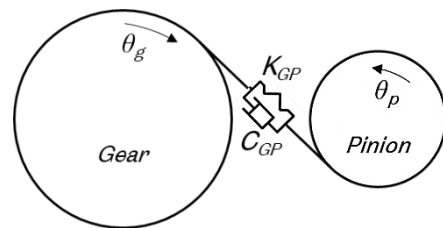
Figure 4.2: Wind turbine drivetrains A, B and C and their gearboxes as CAD models, from the top to the bottom: Drivetrain-A (2 stage WTG, gearbox ratio of 1:34), Drivetrain-B (3 stage WTG, gearbox ratio of 1:115) and Drivetrain-C (3 stage WTG, gearbox ratio of 1:92)



(a) Complete drivetrain



(b) Planetary stage representation



(c) Parallel stage representation

Figure 4.3: Representation of NREL 750kW WT drivetrain with 11 DOF

Table 4.2: Parameters of mechanical components of 750kW WT drivetrain

| Torsional stiffness of shafts and generator (N.m/rad) | | |
|---|--|----------|
| K_{LSS} | Low speed shaft stiffness | 3.69e+07 |
| K_{IS1} | Stiffness of the shaft connecting the sun gear to the 1 st parallel gear stage | 2.45e+07 |
| K_{IS2} | Stiffness of the shaft connecting the 1 st parallel gear stage to 2 nd parallel gear | 2.70e+08 |
| K_{HSS} | High speed shaft stiffness | 2.08e+06 |
| K_{gen} | Electrical torsional stiffness | 2.81e+04 |
| Torsional damping coefficient of shafts (N.m.s/rad) | | |
| C_{LSS} | Low speed shaft damping coefficient | 2.396 |
| C_{IS1} | Damping coefficient of the shaft connecting the sun gear to the 1 st parallel gear stage | 0.476 |
| C_{IS2} | Damping coefficient of the shaft connecting the 1 st parallel gear stage to 2 nd parallel gear | 5.561 |
| C_{HSS} | High speed shaft damping coefficient | 5.753 |
| Inertia of lumped masses (kg.m ²) | | |
| J_{rotor} | Inertia of the rotor | 998,138 |
| J_{PC} | Inertia of planetary carrier | 65.2 |
| J_P | Inertia of planet | 3.2 |
| J_S | Inertia of sun gear | 1.02 |
| J_{G1} | Inertia of gear in 1 st parallel stage | 31.72 |
| J_{G2} | Inertia of pinion in 1 st parallel stage | 0.4 |
| J_{G3} | Inertia of gear in 2 nd parallel stage | 3.42 |
| J_{G4} | Inertia of pinion in 2 nd parallel stage | 0.08 |
| J_{gen} | Inertia of the generator | 24 |
| Wind turbine gearbox ratios | | |
| N_1 | Gear ratio for planetary stage | 5.714 |
| N_2 | Gear ratio for 1 st parallel stage | 3.565 |
| N_3 | Gear ratio for 2 nd parallel stage | 4.00 |
| Gear mesh stiffness (N.m/rad) | | |
| K_{RP} | Planetary gear, Ring-Planet mesh stiffness | 5.86e+07 |
| K_{SP} | Planetary gear, Sun-Planet mesh stiffness | 5.86e+07 |
| K_{GP1} | 1 st parallel gear, Gear-Pinion mesh stiffness | 5.23e+07 |
| K_{GP2} | 2 nd parallel gear, Gear-Pinion mesh stiffness | 1.72e+07 |
| Gear mesh damping coefficient (N.m.s/rad) | | |
| C_{RP} | Planetary gear, Ring-Planet mesh damping coefficient | 3.13e+03 |
| C_{SP} | Planetary gear, Sun-Planet mesh damping coefficient | 0.812e+3 |
| C_{GP1} | 1 st parallel gear, Gear-Pinion mesh damping coefficient | 3.974e+3 |
| C_{GP2} | 2 nd parallel gear, Gear-Pinion mesh damping coefficient | 0.354e+3 |

Table 4.3: Mechanical components parameters of drivetrains A, B and C

| Parameters | Drivetrain | | |
|---|----------------------|----------------------|---------------------|
| | A | B | C |
| Rotor inertia (kg.m ²) | 2.67e+6 | 2.67e+6 | 6.03e+6 |
| Generator inertia (kg.m ²) | 680 | 680 | 60 |
| Stage 1 (2) Planet carrier inertia (kg.m ²) | 2.32e+3 (871.4) | 2.32e+3 (871.4) | 173.86 |
| Stage 1 (2) Ring gear inertia (kg.m ²) | 832.78 (233.79) | 2314 (226.1) | - |
| Stage 1 (2) Planet gear inertia (kg.m ²) | 37.119 (7.115) | 87.9 (9.0) | 356 |
| Stage 1 (2) Sun gear inertia (kg.m ²) | 2.187 (0.887) | 7.9 (0.4) | 29 |
| Stage 1 (2) Planet gear number | 3 (3) | 3 (3) | 3 |
| Stage 2 (3) Gear inertia (kg.m ²) | - | (17.7) | 270 (270) |
| Stage 2 (3) Pinion inertia (kgm ²) | - | (0.3) | 1.5 (2) |
| Stage 1 (2) Ring-Planet mesh stiffnesses (Nm/rad) | 1.54e+9 (1.62e+8) | 7.09e+8 (1.43e+8) | 1.22e+9 |
| Stage 1 (2) Sun-Planet mesh stiffnesses (Nm/rad) | 1.54e+9 (1.62e+8) | 7.09e+8 (1.43e+8) | 1.22e+9 |
| Stage 2 (3) Gear-Pinion mesh stiffnesses (Nm/rad) | - | (5.88e+8) | 1.63e+9 (5.7e+8) |
| LSS stiffness (Nm/rad) | 9.30e+9 | 9.30e+9 | 1.6e+8 |
| Stage 1,2 connecting shaft stiffness (Nm/rad) | 1.06e+8 | 1.06e+8 | 3.42e+8 |
| Stage 2,3 connecting shaft stiffness (Nm/rad) | - | 1.40e+7 | 1.85e+9 |
| HSS stiffness (Nm/rad) | 1.40e+7 | 1.95e+6 | 3.1e+8 |

4.2 Mathematical Modelling and Equations of Motion

4.2.1 Lumped Mass Models with Fixed and Variable Speed Generator

The 5-mass model with 5 DOF for WT drivetrain is shown in Figure 4.4. Each gearbox stage is combined as one effective mass. The gear mesh stiffness was ignored and the five effective inertias, with respect to the LSS side of the WT multistage gearbox, were calculated as follows:

$$J_1 = J_{rotor} \quad 4.8$$

$$J_2 = J_{pc} + N_1^2 J_s \quad 4.9$$

$$J_3 = N_1^2 J_{G1} + (N_1 N_2)^2 J_{G2} \quad 4.10$$

$$J_4 = (N_1 N_2)^2 J_{G3} + (N_1 N_2 N_3)^2 J_{G4} \quad 4.11$$

$$J_5 = (N_1 N_2 N_3)^2 J_{gen} \quad 4.12$$

The stiffnesses of the LSS, all gearbox shafts and the generator resistance torque for fixed speed generator are calculated as follows:

$$K_1 = K_{LSS} \quad 4.13$$

$$K_2 = N_1^2 K_{IS1} \quad 4.14$$

$$K_3 = (N_1 N_2)^2 K_{IS2} \quad 4.15$$

$$K_4 = (N_1 N_2 N_3)^2 K_{HSS} \quad 4.16$$

$$K_5 = (N_1 N_2 N_3)^2 K_{gen} \quad 4.17$$

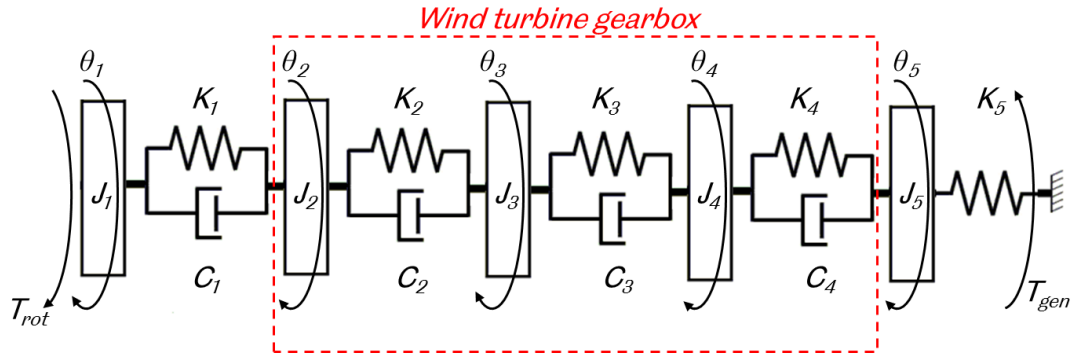


Figure 4.4: Five mass model representation of WT drivetrain.

The damping coefficients of the LSS, all gearbox shafts and the generator resistance torque for fixed speed generator are calculated as follows:

$$C_1 = C_{LSS} \quad 4.18$$

$$C_2 = N_1^2 C_{IS1} \quad 4.19$$

$$C_3 = (N_1 N_2)^2 C_{IS2} \quad 4.20$$

$$C_4 = (N_1 N_2 N_3)^2 C_{HSS} \quad 4.21$$

Lagrange's equation is used to find the equations of motion. For forced torsional vibration, the equations of motion of the torsional model of five mass drivetrain can be shown in matrix form as follows:

$$[J]\{\ddot{\theta}\} + [C]\{\dot{\theta}\} + [K]\{\theta\} = [Q] \quad 4.22$$

$$\theta = [\theta_1 \quad \theta_2 \quad \theta_3 \quad \theta_4 \quad \theta_5]^T \quad 4.23$$

$$J = \begin{pmatrix} J_1 & 0 & 0 & 0 & 0 \\ 0 & J_2 & 0 & 0 & 0 \\ 0 & 0 & J_3 & 0 & 0 \\ 0 & 0 & 0 & J_4 & 0 \\ 0 & 0 & 0 & 0 & J_5 \end{pmatrix} \quad 4.24$$

$$= \begin{bmatrix} C_1 & -C_1 & 0 & 0 & 0 \\ -C_1 & C_1 + C_2 & -C_2 & 0 & 0 \\ 0 & -C_2 & C_2 + C_3 & -C_3 & 0 \\ 0 & 0 & -C_3 & C_3 + C_4 & -C_4 \\ 0 & 0 & 0 & -C_4 & C_4 \end{bmatrix} \quad 4.25$$

$$K = \begin{bmatrix} K_1 & -K_1 & 0 & 0 & 0 \\ -K_1 & K_1 + K_2 & -K_2 & 0 & 0 \\ 0 & -K_2 & K_2 + K_3 & -K_3 & 0 \\ 0 & 0 & -K_3 & K_3 + K_4 & -K_4 \\ 0 & 0 & 0 & -K_4 & K_4 + K_5 \end{bmatrix} \quad 4.26$$

$$Q = [T_{rot} \quad 0 \quad 0 \quad 0 \quad -T_{gen}]^T \quad 4.27$$

Where J , K , C , Q and θ are the inertia matrix, the stiffness matrix, the damping coefficient matrix, the torque vector and the rotational displacement vector respectively. θ_1 , θ_2 , θ_3 , θ_4 and θ_5 are the torsional displacement of the rotor, input shaft of three stage of the gearbox and the generator.

The 2-mass model with 2 DOF for WT drivetrain is shown in Figure 4.5. The 2-mass model for WT drivetrain is widely used in aerodynamic codes such as FAST [93] and GH bladed [94]. The gearbox and the generator are combined as one effective mass while the other mass is the rotor (blades + hub).

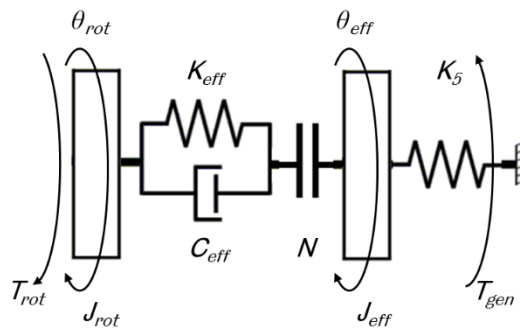


Figure 4.5: Two mass model representation of WT drivetrain

The equations of motion for the 2-mass drivetrain model can be derived from the 5-mass model that has been discussed early. The two effective inertias, with respect to the LSS and the multistage of the gearbox, can be calculated as follows:

$$J_{eff} = J_2 + J_3 + J_4 + J_5 \quad 4.28$$

$$\frac{1}{K_{eff}} = \frac{1}{K_1} + \frac{1}{K_2} + \frac{1}{K_3} + \frac{1}{K_4} \quad 4.29$$

$$\frac{1}{C_{eff}} = \frac{1}{C_1} + \frac{1}{C_2} + \frac{1}{C_3} + \frac{1}{C_4} \quad 4.30$$

For forced torsional vibration, the equations of motion of the torsional model of the two-mass drivetrain can be shown in matrix form as follows:

$$\theta = [\theta_{rot} \quad \theta_{eff}]^T \quad 4.31$$

$$Q = [T_{rot} \quad -T_{gen}]^T \quad 4.32$$

$$J = \begin{bmatrix} J_{rot} & 0 \\ 0 & J_{eff} \end{bmatrix} \quad 4.33$$

$$K = \begin{bmatrix} K_{eff} & -K_{eff} \\ -K_{eff} & K_5 + K_{eff} \end{bmatrix} \quad 4.34$$

$$C = \begin{bmatrix} C_{eff} & -C_{eff} \\ -C_{eff} & C_5 + C_{eff} \end{bmatrix} \quad 4.35$$

The equations of motion for the 11-mass drivetrain model shown in Figure 4.3 are listed below for a complete WT drivetrain which has 11 lumped masses of 11 DOFs and with consideration of gear mesh stiffness and gear mesh damping coefficient:

$$\begin{cases}
 J_1 \ddot{\theta}_1 + C_1 (\dot{\theta}_1 - \dot{\theta}_2) + K_1 (\theta_1 - \theta_2) = T_{rot} \\
 J_2 \ddot{\theta}_2 + C_1 (\dot{\theta}_1 - \dot{\theta}_2) + K_1 (\theta_1 - \theta_2) = \sum_{i=1}^3 F_{spi} r_2 + \sum_{i=1}^3 F_{rpi} r_2 \\
 J_3 \ddot{\theta}_3 = -F_{spi} r_3 + F_{rpi} r_3 \\
 J_4 \ddot{\theta}_4 + C_2 (\dot{\theta}_4 - \dot{\theta}_5) + K_2 (\theta_4 - \theta_5) = \sum_{i=1}^3 F_{spi} r_4 \\
 J_5 \ddot{\theta}_5 + C_2 (\dot{\theta}_4 - \dot{\theta}_5) + K_2 (\theta_4 - \theta_5) = -F_{5d} r_5 \\
 J_6 \ddot{\theta}_6 + C_3 (\dot{\theta}_6 - \dot{\theta}_7) + K_3 (\theta_6 - \theta_7) = F_{5d} r_6 \\
 J_7 \ddot{\theta}_7 + C_3 (\dot{\theta}_6 - \dot{\theta}_7) + K_3 (\theta_6 - \theta_7) = -F_{7d} r_7 \\
 J_8 \ddot{\theta}_8 + C_4 (\dot{\theta}_8 - \dot{\theta}_9) + K_4 (\theta_8 - \theta_9) = F_{7d} r_8 \\
 J_9 \ddot{\theta}_9 + C_4 (\dot{\theta}_8 - \dot{\theta}_9) + K_4 (\theta_8 - \theta_9) = -T_{gen}
 \end{cases} \quad 4.36$$

where,

$$\begin{cases}
 F_{spi} = K_{spi} (r_3 \theta_3 - r_4 \theta_4 + r_2 \cos(\alpha_{sp}) \theta_2) + C_{spi} (r_3 \dot{\theta}_3 - r_4 \dot{\theta}_4 + r_2 \cos(\alpha_{sp}) \dot{\theta}_2) \\
 F_{rpi} = K_{rpi} (r_2 \cos(\alpha_{rp}) \theta_2 - r_3 \theta_3) + C_{rpi} (r_2 \cos(\alpha_{rp}) \dot{\theta}_2 - r_3 \dot{\theta}_3) \\
 F_{5d} = K_{5d} (r_5 \theta_5 - r_6 \theta_6) + C_{5d} (r_5 \dot{\theta}_5 - r_6 \dot{\theta}_6) \\
 F_{7d} = K_{7d} (r_7 \theta_7 - r_8 \theta_8) + C_{7d} (r_7 \dot{\theta}_7 - r_8 \dot{\theta}_8)
 \end{cases} \quad 4.37$$

4.2.2 Eigenmode and Eigenfrequency Analysis

For the 2-mass, 5-mass and 11-mass models, when a variable generator speed model is considered, the K_{gen} is equal to zero thus it should be eliminated from the stiffness matrix which leads to free-free system normal modes. When a fixed generator speed model is considered, the K_{gen} is not equal to zero which leads to free-fixed system normal modes. For free force vibration considering both the fixed and variable speed generator models but ignoring the effect of damping coefficient, the eigenmodes and eigenfrequencies of the WT drivetrain system can be calculated using the following equation:

$$\begin{aligned}(K - \omega^2 J)\Phi &= 0, \\ \Phi_n^T J \Phi_n &= I_{nn}, \\ \Phi_n^T K \Phi_n &= \text{diag}(\omega_n^2)\end{aligned}\tag{4.38}$$

Where K , J is the stiffness and the inertia matrixes and Φ is the eigenmodes corresponding to the eigenfrequencies ω_n .

4.3 MATLAB/Simulink Dynamic Modelling of Wind Turbine Drivetrain

MATLAB is chosen as the modelling software because it is a readily available software package that is commonly used in industry. It has the advantage that the software is a 'white box' - the coding behind the software is known. This allows for more parameters to be inputted into the model increasing the level of complexity that can be achieved. The integrated Simulink environment within MATLAB enables this study to create dynamic models of complex WT drivetrain systems. The multibody dynamic system of WT drivetrain can then be excited by different input signals and simulated to obtain approximations for the dynamic response of the system. These results can then be exported into the MATLAB workspace for further analysis. The complexity of the dynamic model for the drivetrain is dependent on the main function of the developed model.

As one of the aim of this thesis is to understand the dynamic responses of the three different configurations of WT gearboxes under transient load conditions, modelling the drivetrain as a pure torsional model in MATLAB/Simulink is appropriate at this stage. In MATLAB/Simulink the Simscape library enables this study to model the individual mechanical components and the associated differential equations as blocks within Simulink. The related blocks are coupled by connecting them together and the software forms the supplementary equations that describe the motion of the whole system. It is efficient to create the models in Simulink/Simscape environment and to run simulations in order to obtain approximations of the dynamic responses [95].

4.3.1 Key Components and Planetary /Parallel Gear Configurations

The drivetrain is divided into groups of masses attached to each other by springs and dampers model. By using the Simulink library, the rotor, the generator and the gears masses can be represented by using the inertias blocks. The shafts within the WT drivetrain can be represented by using torsional springs available within the Simulink library environment. The key mechanical blocks used to model the drivetrain in Simulink for each component are displayed in Table 4.4. The inertia block, No.1 in Table 4.4, was sufficient for use to model all the rigid bodies within the WT drivetrain, such as the rotor, planetary carrier, gears and generator rotor. All the required parameters, such as the mass and inertia of the WT drivetrain dynamic models have been calculated by using CAD models that were explained before in section 4.1. The rotational stiffness and damping, No.2 and 3 in Table 4.4, are used to model the flexibility associated with the components in the torsional model, such as the shafts and gear contact. The 'Sun-Planet', the 'Ring-Planet' and the 'Simple Gear' blocks provided in the Simulink/Simscape environment, No.4, 5 and 6 in Table 4.4, apply the ratio that corresponds to the gear ratio in each gearbox stage, i.e. the planetary, intermediate and high-speed stage within the WT gearbox. Table 4.5 shows the representations of the dynamic model for the WT drivetrains shafts, planetary gear and parallel gear stage respectively, where each component and gear mesh stiffness and gear mesh damping are included.

The Simulink models for a complete WT drivetrain during normal operation and shutdown are shown in Figure 4.6. The required parameters for Simulink models of WT drivetrain with different gearbox configurations for all gearbox components have been explained before in section 4.1 and shown in Table 4.2 and Table 4.3.

Table 4.4: Equivalent Simulink blocks for the mechanical components




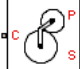

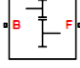
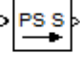
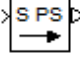


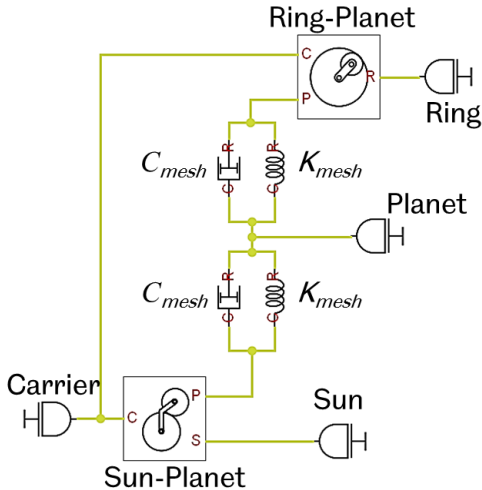


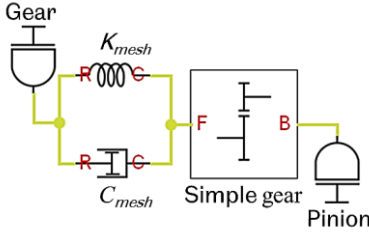
| No. | Simulink Block | Physical Equivalent |
|-----|--|---|
| 1 |  Inertia | Rotor Inertia Generator Inertia Planet, Ring, Sun, Gear, Pinion Inertia |
| 2 |  Rotational Stiffness | Shaft Stiffness Gear Mesh Stiffness |
| 3 |  Rotational Damping | Shaft Damping Gear Mesh Damping |
| 4 |  Sun - Planet | Sun-Planet Gear Ratio |
| 5 |  Ring - Planet | Ring-Planet Gear Ratio |
| 6 |  Simple Gear | Gear-Pinion Gear Ratio |
| 7 |  PS-Simulink Converter | It converts a Simscape physical input signal (PS) into a Simulink output signal (S) |
| 8 |  Simulink-PS Converter | It converts a Simulink input signal (S) into a Simscape physical signal (PS) |

Table 4.5: Representations of epicyclic and parallel gear stage in MATLAB/Simulink

| | Representation | | |
|-----------------|---|---|--|
| | CAD | Schematic | Simulink |
| Planetary Stage |  |  |  |
| Parallel Stage |  |  |  |

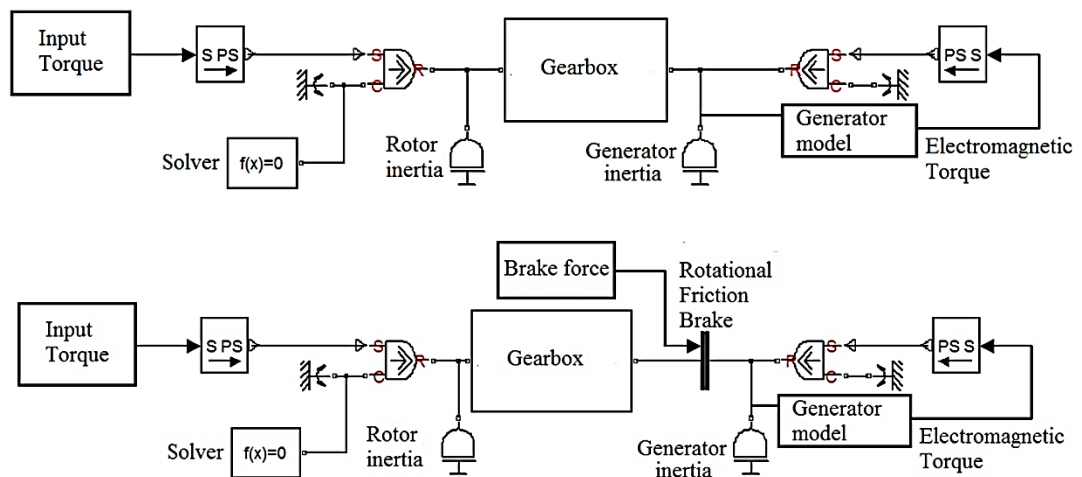


Figure 4.6: MATLAB/Simulink model of a complete WT drivetrain during normal operation (top) and shutdown (bottom)

4.3.2 Gear Tooth Load Calculation

The LSS torque is transfer to the WT gearbox through the planetary carrier, then to the WT gearbox shafts and bearings through the tooth contact of gears. For helical gears, the gear contact force has three components, tangential, radial and axial. The gear contact force F_{bt} along the line of contact tangent to the gear base circle can be calculated as follows:

$$F_{bt} = (r_{b1}\theta_1 - r_{b2}\theta_2)K_{mesh} + (r_{b1}\dot{\theta}_1 - r_{b2}\dot{\theta}_2)C_{mesh} \quad 4.39$$

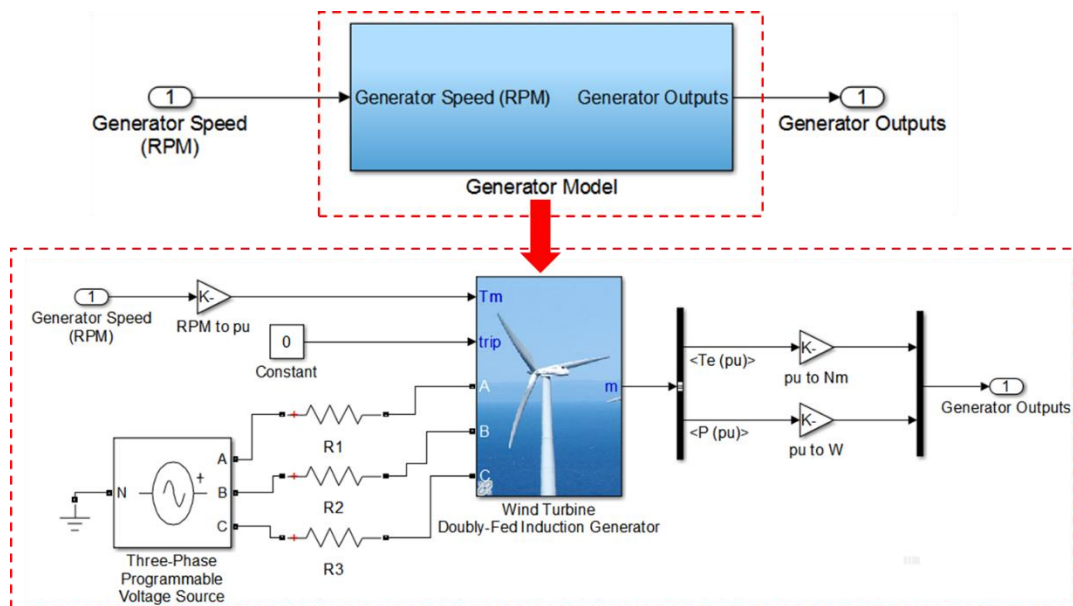
where r_{b1} , r_{b2} , θ_1 , θ_2 , $\dot{\theta}_1$ and $\dot{\theta}_2$ are the base radius, the angular displacement and the angular velocity of the pinion and the wheel, respectively; K_{mesh} and C_{mesh} are the gear mesh stiffness and the gear mesh damping coefficient which can be calculated by using the equations 4.6 and 4.7, respectively. The angular displacement and angular velocity for gears in contact can be measured in the MATLAB/Simulink environment by using the motion sensor block which will be explained later as shown in Figure 4.8.

4.3.3 Generator Model

In order to accurately model the drivetrain, a generator model in Simulink must be incorporated into the system model of the drivetrain to simulate the resistance torque supplied by the generator. This is important to ensure that the HSS speed is limited to the speed at which the generator can produce electricity. The generator resistance torque acts as a reactive loading to the drivetrain at the generator side and affects the WT drivetrain system when the generator engages (i.e. connected) with or disengages (i.e. disconnected) from the electrical grid. The gearbox ratio is 1:34 for Drivetrain-A, corresponding to a mid-speed generator thus a Permanent Magnet Generator (PMG) model is used in the modelling. For Drivetrain-B and Drivetrain-C, a Double-Fed Induction Generator (DFIG) model is used for both drivetrains because their generators operate in a higher speed range as shown in Figure 4.7. The generator models can provide generator resistance torque and controls the rotor speed for two different operational conditions: normal operation and shutdown. The generators parameters used in this study are shown in Table 4.6.

Table 4.6: Generator parameters of drivetrains A, B, C and D

| Parameters | Drivetrain | | | |
|-------------------------------|------------|------|------|-------|
| | A | B | C | D |
| Rated speed (RPM) | 515 | 1836 | 1680 | 1809 |
| Generator type | PMG | DFIG | DFIG | DFIG |
| Number of poles | 10 | 4 | 4 | 4 |
| Gird voltage (Volt) | 690 | 690 | 690 | 690 |
| Frequency (Hz) | 60 | 60 | 60 | 60 |
| Mutual inductance (Lm) | 0.32 | 3.0 | 3.0 | 2.56 |
| Stator leakage reactance (Ls) | 0.64 | 0.1 | 0.1 | 0.016 |
| Line inductance | 0.09 | 0.09 | 0.1 | 0.06 |

**Figure 4.7: MATLAB/Simulink double feed induction generator model**

4.3.4 Eigenfrequencies Analysis Using Control Design Tools

The natural frequency of the WT drivetrain with different gearbox configuration and different levels of model complexity of 2-mass, 5-mass and 11-mass can be calculated by using the facilities of the control system toolbox available within the MATLAB/Simulink environment. Eigenfrequency analysis of the WT drivetrain is performed by using the LSS torque as the input and the corresponding angular velocity of the generator as the output. The resulting eigenfrequencies are compared with that determined from the mathematical model analysis that was explained in section 4.2.2. The eigenfrequency analysis for the 2-mass model with variable generator speed model, i.e. the K_{gen} is equal to zero, is represented in Figure 4.8. Firstly, the WT drivetrain model should be provided with two inputs, the LSS torque and the generator torque, then the input and output points, i.e. the input torque and the output speed, should be set-up within the drivetrain model, as shown in Figure 4.8.

Finally, by running the linear analysis through the control design analysis tools available in the Simulink environment, the Bode diagram for the WT drivetrain can be drawn and the values of eigenfrequencies can be calculated.

4.4 Gear Mesh Dynamic Excitation and Campbell Analysis

The numbers of gear teeth of each WT gearbox gear for drivetrain-A, B and C are shown in Table 4.7. Through knowing the number of teeth on each gear and the speed ratio of each gear stage within the WT gearbox, the gear mesh frequency (GMF) can be calculated [96]. The GMF calculations of each stage within the gearbox of Drivetrains-A, B and C are shown in Table 4.8. The GMF results will be used later for evaluating the Campbell diagrams and resonance analysis. As illustrated in Figure 4.9, a potential resonance of the WT drivetrain occurs when the GMF (the diagonal lines) of each stage within the gearbox crosses the gearbox natural frequencies (the horizontal lines) within the zone of rotor operational speed (the red vertical lines).

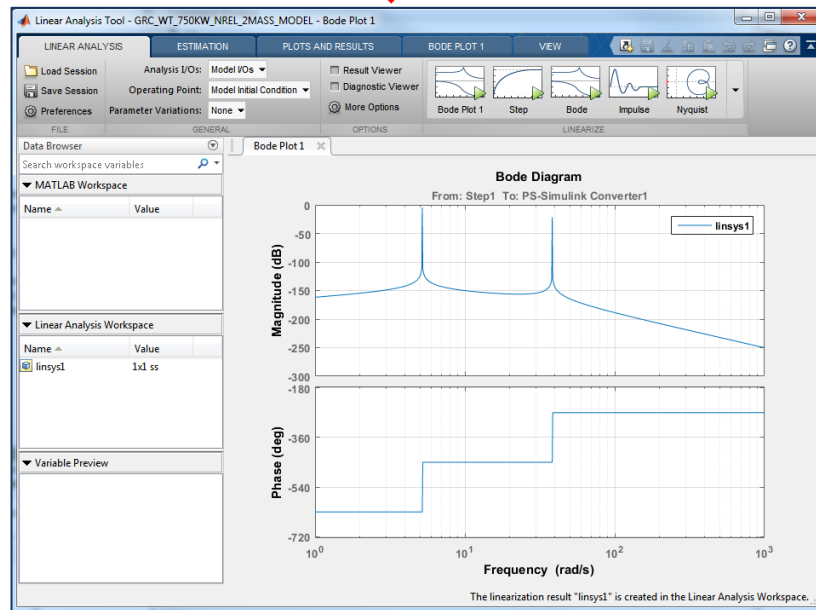
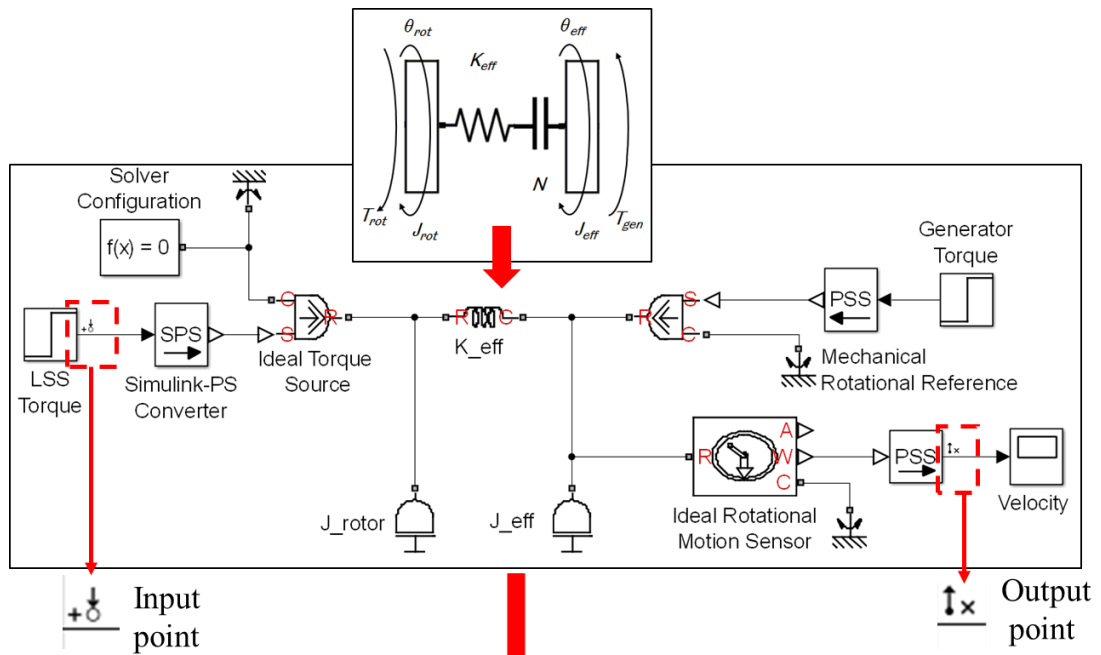


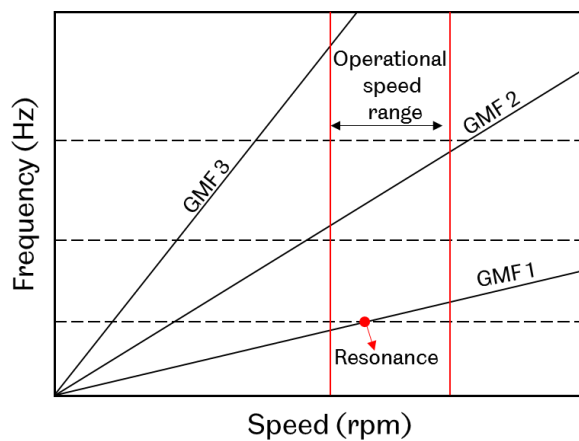
Figure 4.8: Eigenfrequency analysis by MTLAB/Simulink design tools for 2-mass model of WT drivetrain with variable generator model

Table 4.7: Number of teeth of three WT drivetrain gearboxes

| Gearbox stage | Number of teeth | | |
|--------------------|-----------------|--------|------------|
| | Ring gear/Gear | Planet | Sun/Pinion |
| Drivetrain-A | | | |
| Planetary stage I | 122 | 49 | 24 |
| Planetary stage II | 99 | 39 | 21 |
| Drivetrain-B | | | |
| Planetary stage I | 127 | 50 | 27 |
| Planetary stage II | 105 | 43 | 19 |
| Parallel stage III | 65 | - | 21 |
| Drivetrain-C | | | |
| Planetary stage I | 145 | 58 | 29 |
| Parallel stage II | 108 | - | 27 |
| Parallel stage III | 111 | - | 29 |

Table 4.8: Gear mesh frequencies of WTGs of drivetrain A, B and C

| GMF of gearbox | Drivetrain Orders | | |
|----------------|-------------------|-----------|-------|
| | A | B | C |
| stage I | 146x | 154x | 174x |
| stage II | 730x | 707.259x | 648x |
| stage III | - | 2419.575x | 2664x |

**Figure 4.9: Resonance analysis using Campbell diagram**

4.5 Wind Turbine Drivetrain Input Torque Spectrums and Upscaling Factors

Field measured rotor torque data under normal operation and shutdown conditions were obtained from a 2MW wind turbine in operation, as shown in Figure 4.10. These torque time-history are used directly as rotor torque inputs for the Drivetrain-C model. For Drivetrains A and B, the field measurements of torque spectrums under different operational conditions are not available. For each of these two drivetrains, the rotor torque input data is determined by applying a scaling factor to the field measured torque data of the 2MW WT, based on scaling relations given in [97-99]. It is assumed that the tip speed ratio of 3MW WTs is the same as that of the 2MW WT [99]. The scaling factor can be calculated using [99]:

$$\frac{T_1}{T_2} = \left(\frac{D_1}{D_2} \right)^3 \quad 4.40$$

where, T is the torque, D is the rotor diameter, 1 and 2 denote the original and scaled WTs respectively. The rotor torque spectrum measured for normal operation corresponds to the operational condition when the WT operates around the rotor rated speed, shown in Figure 4.10 (top). The shutdown condition shows that the WT firstly operates under normal operation and then the shutdown begins with the aerodynamic brake being applied on the rotor. The generator subsequently is switched off, and then the mechanical brake is applied, until the system comes to a complete stop, as shown in Figure 4.10 (bottom). It should be noted that the torque time-histories shown in Figure 4.10 is normalized with the rated input torque for confidential purpose.

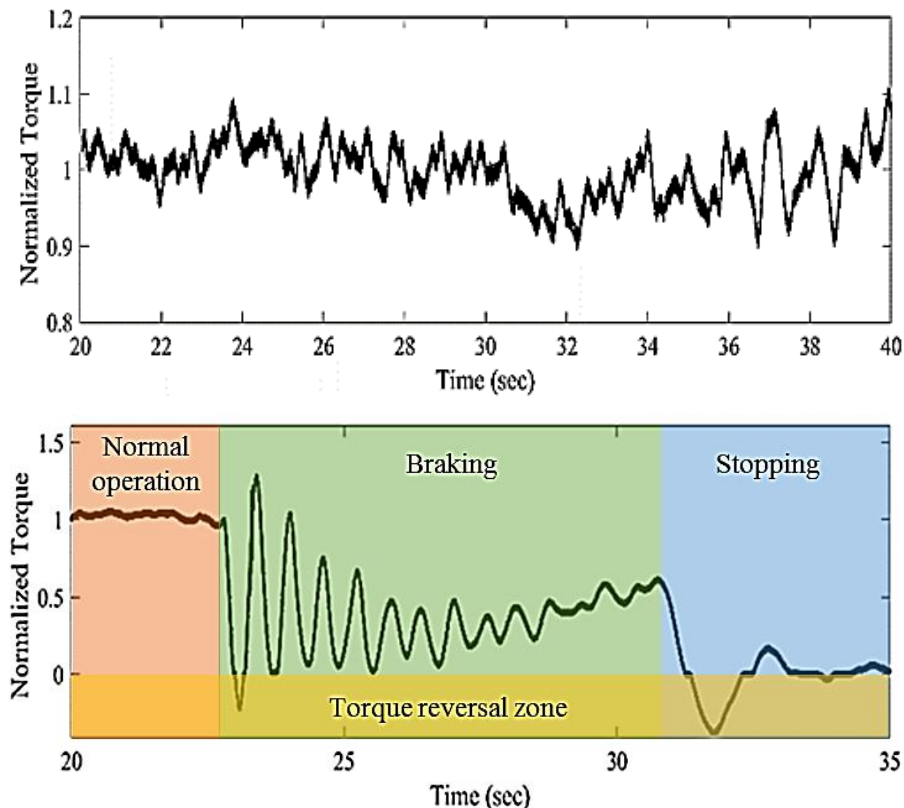


Figure 4.10: Input torque time-history during normal operation (top) and shutdown (bottom)

When simulating the drivetrain under shutdown condition by using MATLAB/Simulink, the rotor torque and generator resistance torque are not the only inputs required. Additional inputs are added to the Simulink model to create the braking torques, so that they can be synchronised with the rotor input torque modelled. During shutdown condition the generator is switched off when the aerodynamic brake is activated, therefore the generator model must be designed to respond to the event. The corresponding generator and brake models in MATLAB/Simulink are shown in Figure 4.11. A switch has been added to the generator model to ensure that when the aerodynamic brake is engaged the generator will be turned off, to reduce the torque to zero. Both aerodynamic and mechanical brakes produce resistance torques on the drivetrain; both brakes are simulated by using the friction brake function available in the MATLAB/Simulink library. No information about the braking system is available for the drivetrain system modelled thus a trial and error [75, 100] method is used to adjust the braking forces required by the two brakes.

Each brake has a zero force until the brake initiates; after which a constant resistive force is applied via the brake while the rotor slows down gradually.

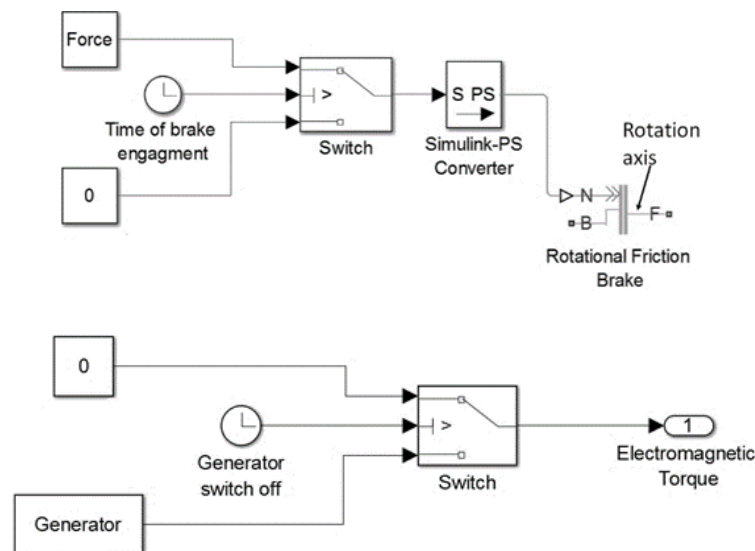


Figure 4.11: MATLAB/Simulink model of the brake (top) and corresponding generator model (bottom)

4.6 Summary

The pure torsional MBS dynamic models developed in this Chapter used single DOF for each key component within the WT drivetrain. These models considered the effect of torque reversal on gear meshing contact forces within the WTG during unplanned shutdown and can model the effect of generator engagement or diamagnet on the dynamic response of WT drivetrain. However, these models do not include the bearings. These models can be expanded to include the rotational and translational degrees of freedoms to model bearings thus providing further insights into the dynamic responses of the WT drivetrain. The gear mesh stiffness is modelled as a linear spring which reacts similarly when the meshing gears are under normal contact and reversed contact. The results obtained from the models developed in this Chapter will be presented in Chapter 6. A more realistic model may be developed to simulate more complex gear meshing behaviour caused by gear tooth interactions and to consider how the mesh stiffness would change during transient operational conditions when torque reversals occur. The development of advance rigid and discrete flexible MBS dynamic modelling methods will be presented in Chapter 5.

5

RIGID AND DISCRETE FLEXIBLE MULTIBODY DYNAMIC MODELLING OF WIND TURBINE DRIVETRAIN

The torsional multibody system model (MBS) model for the WT drivetrains and WTG presented in Chapter 4 were simple, with a single DOF per component and ignored the existence of bearings. In this chapter, the MBS modelling methods are developed for the key components of the WT drivetrain by rigid and flexible bodies with 6 DOFs per component by using SIMPACK MBS software. The advantages of combining the rigid and flexible bodies in contact for modelling the WTG under different operational conditions are also presented. The cross-coupling effect, i.e. the off-diagonal terms in stiffness matrix, and the radial and axial clearance, the contact between the roller and the raceway within the roller bearing model have been considered in bearing model within the WTG. The developed model can predict the out of phase loads of planet gear bearings and planet gears. The results are then used to determine the maximum surface contact and subsurface stresses on gears and bearings within the WTG. The bearing roller load, roller deflection, the contact stress between the roller and the raceway and how many rollers are in contact during different operational conditions are also obtained. Fatigue damage of the key components for a WTG, the gear and bearings, is then estimated.

5.1 Modelling the Key Components of Wind Turbine Drivetrain

Figure 5.1 shows the system layout for a WT drivetrain with the coordinate system and displacement directions indicated by X , Y , Z , θ_x , θ_y and θ_z respectively, which will be referred to throughout this chapter. All components are shown in Figure 5.1, the main shaft, main bearings, and the gearbox components are modelled in this Chapter by using SIMPACK multibody system (MBS) dynamic software with three rotational DOFs and three translational DOFs per component, except for the bedplate and the gearbox housing, which are assumed to be rigid. The ring gear of the WTG also serves as part of the gearbox housing. The gearbox parts are modelled with 6-DOF in total per component, while the rotor (i.e. the hub and the blades) and the generator rotor are modelled as mass with only one DOF in the θ_z direction. The methods for modelling the WT drivetrain components are described in this section.

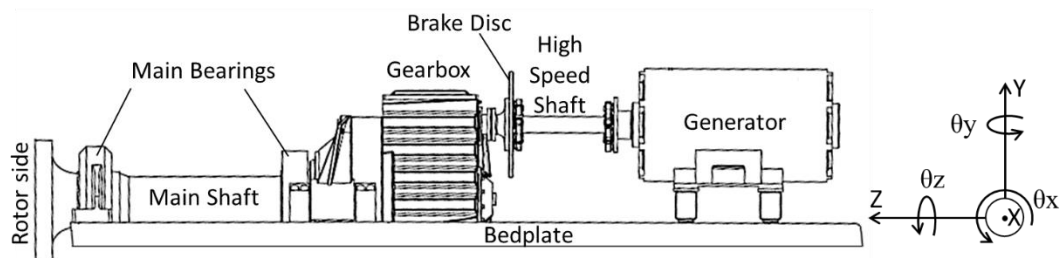


Figure 5.1: Main components modelled in a wind turbine drivetrain

The mass and inertia of each gearbox component must be input into a SIMPACK body element. In SIMPACK modelling of the key components of WTG can be represented by bodies connected to each other by joints that defining the type of motion between them and the number of the DOFs. The interaction between these bodies can be represented by the force element in the forms of springs and dampers as shown in Figure 5.2. The equation of motion between two rigid bodies with consideration of the translation and rotational movements can be written as follows:

$$\begin{pmatrix} F \\ T \end{pmatrix} = \begin{pmatrix} m & 0 \\ 0 & I \end{pmatrix} \begin{pmatrix} a \\ \alpha \end{pmatrix} + \begin{pmatrix} \omega \times m \cdot v \\ \omega \times I \cdot v \end{pmatrix} \quad 5.1$$

Where m and I are the mass and the inertia of the body, F and T are the force and the torque acting on the body, a and α are the linear and angular acceleration, v and ω are the linear and angular velocity respectively. The body element models the mass and inertia of a system component in all 6 DOFs, representing a component's mass matrix. Component masses have already been determined by using CAD models as discussed in Chapter 3.

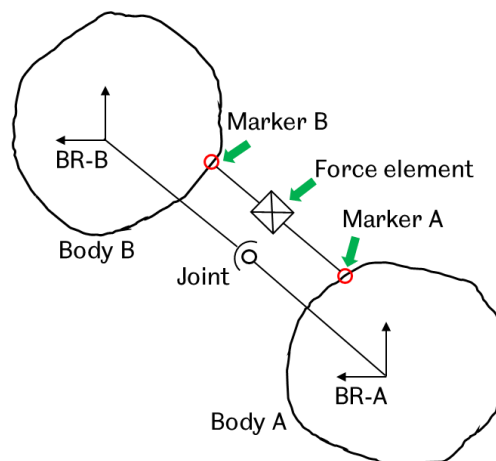


Figure 5.2: Multi body system modelling principle in SIMPACK. The letters BR refer to the 'Body Reference' of bodies A and B

The inertia of complicated shaped components can be found by using the CAD models discussed in Chapter 3. It is assumed that the masses and inertias of the bearings are negligible when calculating the dynamics of the entire gearbox. The inertia of the WT rotor, the hub and the blades can be calculated as discussed in Chapter 3.

As this study is mainly concerned with the loading conditions of the WTG gears and bearings during normal operation and shutdown condition. Effects of the rotor movement in axial direction on the loading of gears and bearings are ignored in this study.

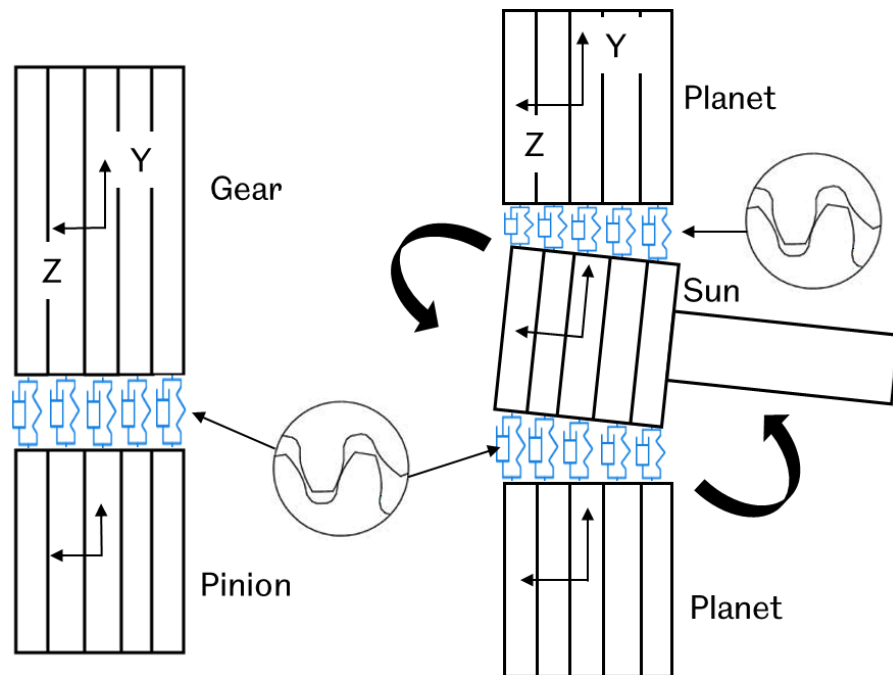


Figure 5.3: Illustration of gear slicing model with five slices for parallel gear (right) and planetary gear (left)

The WTG gears are modelled as rigid bodies of 6 DOFs with consideration of aspects of tooth microgeometry such as the tooth lead, tooth tip and tooth crown. Gear contact is flexible and represented by multi-sets of springs and dampers and modelled in SIMPACK MBS software by using the “slices” model. The “slice” model for gear contact, using a 35 slices along the tooth face width, was selected [34], and was found to be accurate. The chosen number of slices along the tooth face width influenced the accuracy of the results. It has been found that the number of slices producing accurate results at a high computational cost [34]. A 35 slices model has been found to be the best compromise between computational cost and accuracy [34]. A SIMPACK MBS model representation of the gear meshing between the sun gear and the three planetary gears in the low speed stage of the gearbox is shown in Figure 5.3. The SIMPACK force element (FE) 225 represents the mesh between two gear elements [101] and takes into account many parameters such as, involute teeth profile, the helix angle for helical gears, gear initial rotation angle, backlash, tooth modification and shape factor, variation of gear axes, gear movement and gear material. When using FE-225, the contact mesh stiffness between two gears is a variable and it can be calculated by using the following:

$$k_{mesh}(\varphi) = k_{max} \left(\left(1 - \left(1 - \frac{k_{min}}{k_{max}} \right) \cdot \left(\frac{s(\varphi)}{\max(s_1, s_2)} \right)^2 \right) \right) \quad 5.2$$

$$\begin{aligned} s(\varphi) &= r_b \varphi, \\ s_1 &\leq s(\varphi) \leq s_2 \end{aligned} \quad 5.3$$

where, s_1 and s_2 are the lengths of the contact path segment, φ is the pressure angle, as shown in Figure 5.4. The maximum and minimum gear contact mesh stiffness, k_{max} and k_{min} , can be calculated according to DIN3990 as follows [102, 103]:

$$\begin{aligned} k_{max} &= 14 \times 10^9 \times \frac{E}{2.1 \times 10^{11}} \times b \times Y, \\ k_{min} &= SR \times k_{max} \end{aligned} \quad 5.4$$

where E is the modulus of elasticity of gear material, b and Y are the gear face width and the gear shape factor and SR is the stiffness ratio.

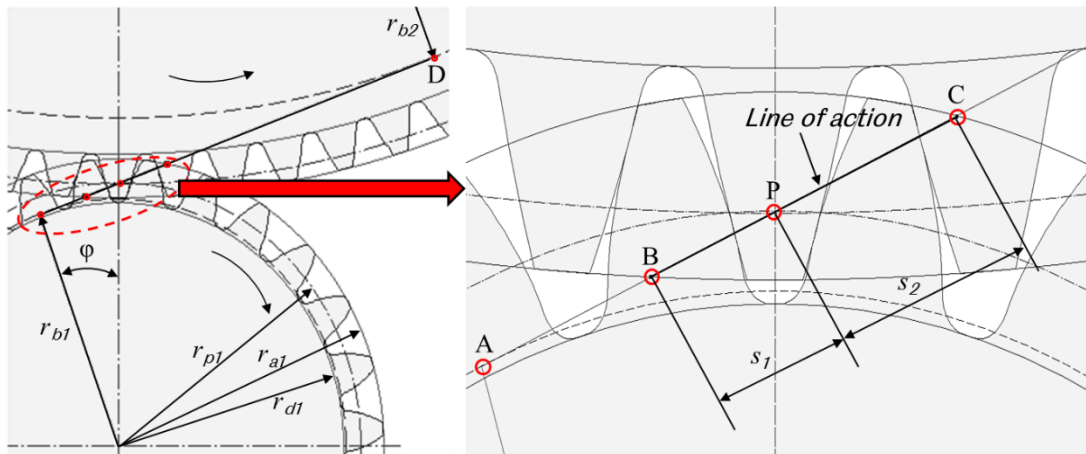


Figure 5.4: Gear mesh stiffness estimation along the line of action, r_b , r_p , r_a and r_d are the base radius, the pitch radius, the addendum radius and the dedendum radius respectively

The conventional gear contact mesh stiffness variation, $k_{mesh}(\varphi)$, of helical gear for single and double tooth contact between the ring and the planet gears during a constant torque input is calculated by SIMPACK, as shown in Figure 5.5.

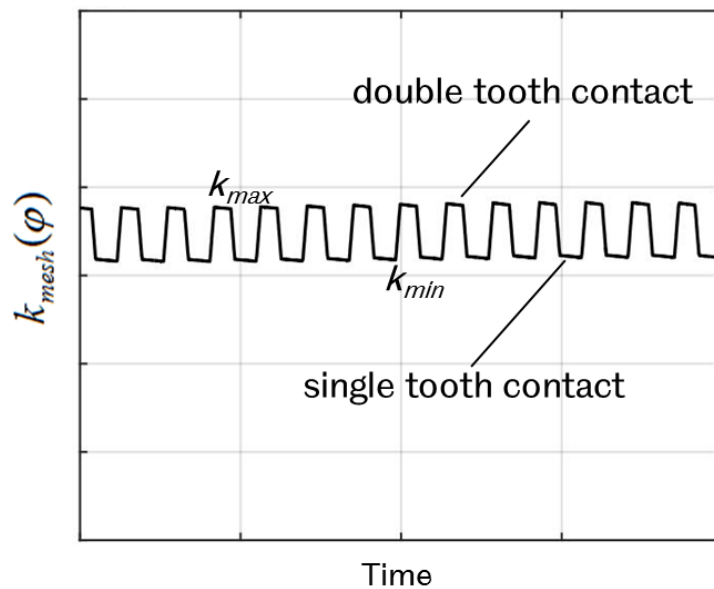


Figure 5.5: Contact mesh stiffness variation between the ring and planet gears for NREL 750kW WT during rated torque input

The flexible shafts within the WTG are the most important components for improving the WTG modelling because they influence the bearings and gears loads [34]. In SIMPACK MBS, to model the flexible shafts there are two approaches that can be used: Euler-Bernoulli beam and Timoshenko beam methods. The advantages and disadvantages of both approaches along with their limitations in terms of results accuracy can be tested. One of the limitations of Euler-Bernoulli for shaft model is the ignorance of the shearing effects in shafts. Therefore, it is recommended for long, thin shafts. As all the WTG shafts within the WTG are thick and short and the effect of shearing within the shafts needs to be considered. Therefore, the shafts of WTG were modelled in SIMPACK using SIMBEAM based on Timoshenko finite element beam elements [104]. As shown in Figure 5.6, the WT main shaft is represented by a group of nodes with 6 DOFs per node. In each segment within a shaft, the cross-section area is represented by two nodes to model the three-dimensional motion of the rotating shaft. The load and flexion at each node are determined from the bending, twist and axial deflections.

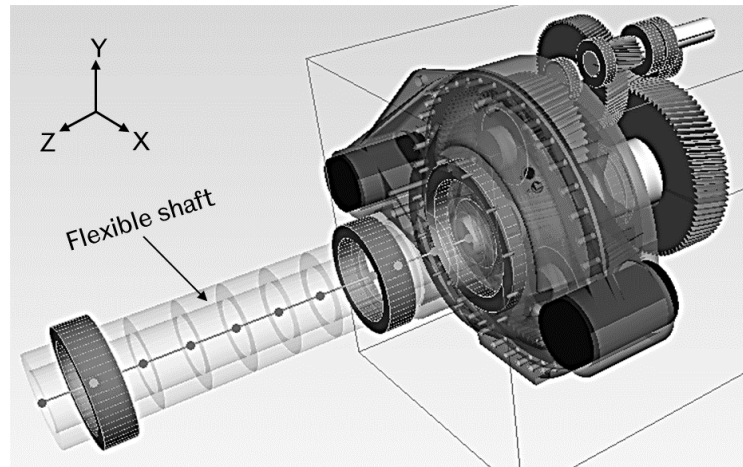


Figure 5.6: Flexible shaft representation of the main shaft within WT drivetrain

Investigation of unbalanced load sharing between planet gears and planet bearings was required in this study. Hence, the planet carrier was modelled by using SIMPACK MBS as a flexible body to provide unbalanced radial force sharing between planet gear bearings pair, the UW and the DW. The flexible planet carrier model is coupled with the main shaft model with a shrink disk upwind of the gearbox. The results of the difference between the planet gear bearings pair, the upwind and downwind, radial load for each planet gear within the planetary gear stage will be presented and investigated in Chapter 7. The connection between the carrier pins and the planet carrier is assumed to be flexible and accomplished by using the bushing force element, FE-43 with 6 DOFs represented by stiffness matrix as follows [34]:

$$K = \text{dia} \begin{vmatrix} k_{XX} & & & & & \\ & k_{YY} & & & & \\ & & k_{ZZ} & & & \\ & & & k_{\theta X} & & \\ & & & & k_{\theta Y} & \\ & & & & & k_{\theta Z} \end{vmatrix} \quad 5.5$$

The conventional WTGs uses the spline coupling to connect the sun gear shaft with the intermediate stage hollow shaft via spline sleeve to allow the sun gear to move freely in vertical (i.e. Y) and horizontal (i.e. X) directions. The spline sleeve then transfers the rotational motion from the first intermediate shaft (i.e. ISS1) to the second intermediate stage shaft (i.e. ISS2) via parallel gear stage (see Figure 5.10). The sun gear moves with partially bounded DOF can centralise within the planet gears, promoting sun-planet gear contact load sharing. In this study, the coupling between the shafts, the sun gear spline shaft and the intermediate shaft sleeve, is modelled in SIMPACK by using the Spline

Coupling FE-242. The geometry of the spline and the sleeve are considered, and both are modelled as rigid bodies having flexible contact by using the FE-242 with 35 slices along the face width. The connection between the sun gear and its shaft with the intermediate speed shaft (IMS), is modelled as a spherical joint which has a rigid connection in 4-DOF these are: the horizontal (i.e. X), vertical (i.e. Y), axial (i.e. Z) and rotational in Z (i.e. θ_z) direction. However, it has an unbound connection in 2-DOF these are: the rotational in X (i.e. θ_x) and the rotational in Y (i.e. θ_y). These free unrestrained DOF (i.e. θ_x and θ_y) are important for modelling the pitch and yaw movements for sun gear within the planetary gear stage [34]. The three planet gears sun gear are partially restricted the movements of the sun gear in the θ_x and θ_y direction, which makes the maximum displacements in these directions to be generally small, around 0.1 mm for NREL 750kW WT during normal operation [105].

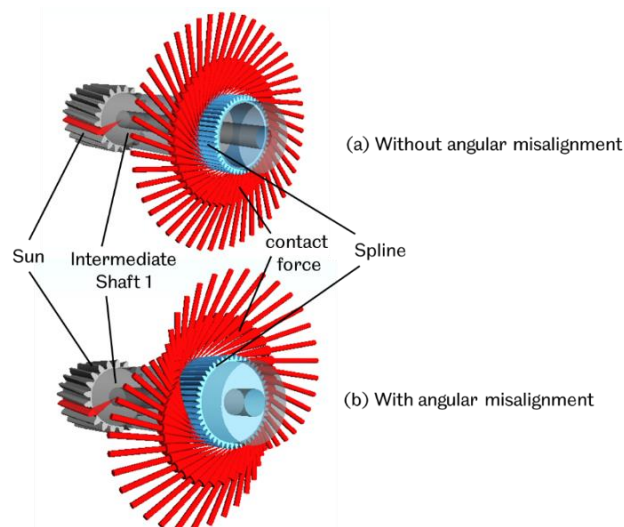


Figure 5.7: SIMPACK representation for sun, intermediate shaft and the spline with and without angular misalignment

Figure 5.7 shows the SIMPACK MBS model of the sun gear, sun shaft and spline connection as explained above, with and without angular misalignment. The red arrows represent the contact forces between the spline and the sleeve which act on the tooth face width and have normal distribution if the angular misalignment is absent however, it is not the normally distributed when the angular misalignment is present. The connections between the WTG's key components with relative DOFs for the parallel gear and planetary gear stage are summarised in the kinematic tree diagrams shown in Figure 5.8.

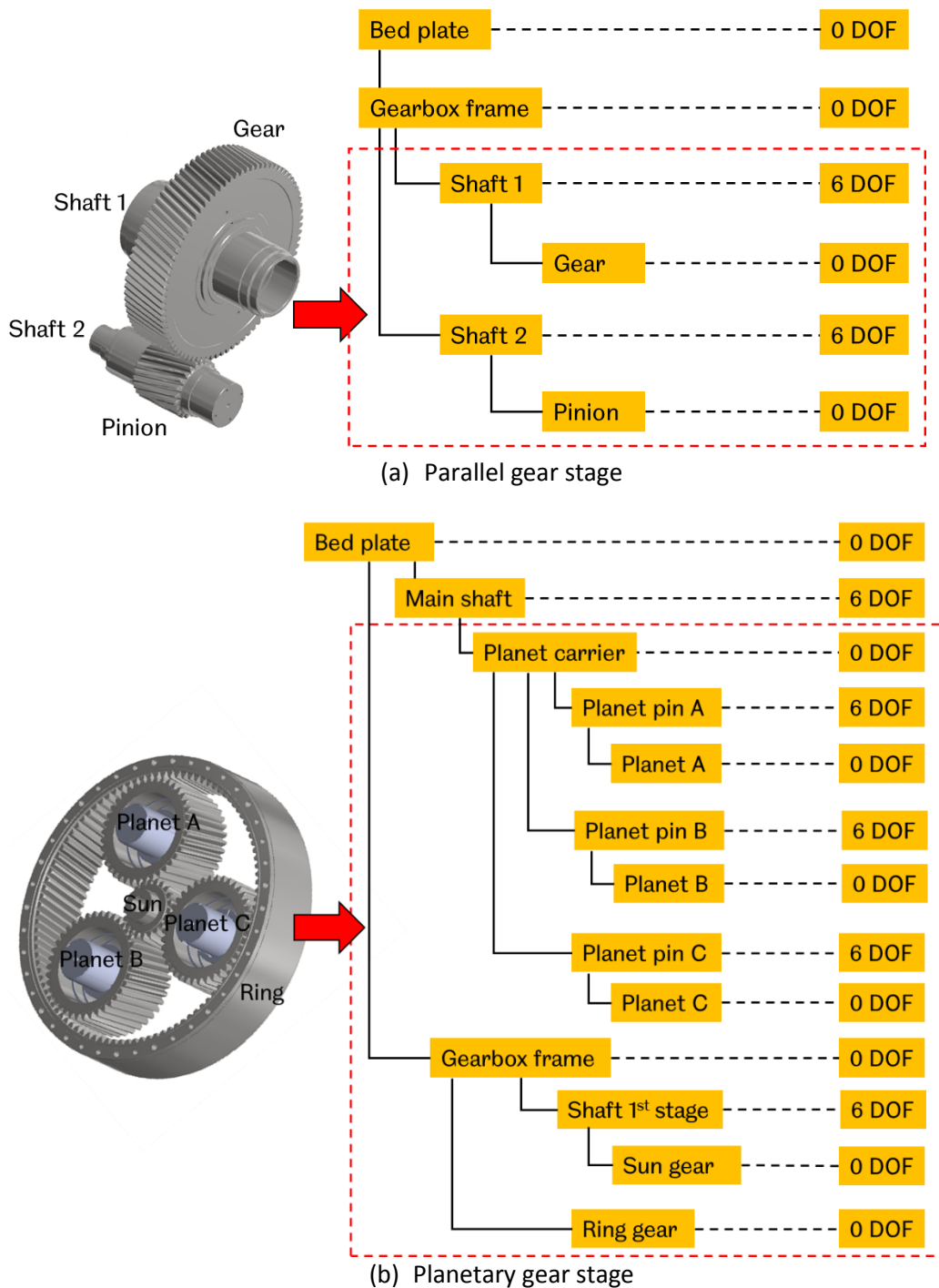


Figure 5.8: SIMPACK kinematic tree diagrams for different gear stage

5.2 Bearings

The WT drivetrain uses roller bearings to meet the WTG loading conditions and design life requirements. Several roller bearings types are employed in the WT drivetrain such as cylindrical, taper and spherical roller bearings. The roller bearing has a set of rollers that rotating between the inner and the outer ring as shown in Figure 5.9.

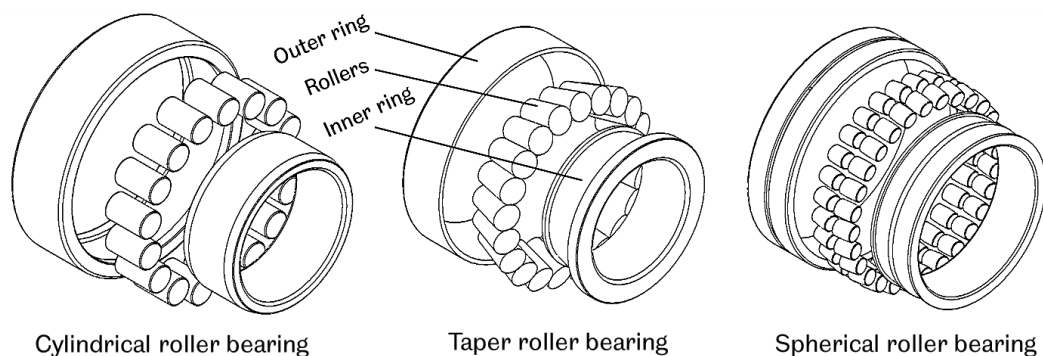


Figure 5.9: Commonly used roller bearings types in the wind turbine drivetrain

As illustrated in Figure 5.10, in the WT drivetrain the main shaft is supported by two spherical roller bearings (SRB), labelled as IN-A and IN-B. For the 1st gear stage of the WTG, the planet carrier is supported by two cylindrical roller bearings (CRB), labelled as PLC-A and PLC-B. Each planet gear is supported by two identical CRBs, labelled as UW (Up Wind) and DW (Down Wind). For the intermediate gear stage 1 and 2, ISS1 and ISS2 and the high-speed stage, HSS, each parallel shaft is supported by a CRB on the upwind side of the assembly, labelled as ISS1-A, ISS2-A, HSS-A, and by two back-to-back mounted, duplex tapered roller bearings (TRB) on the downwind side, labelled as ISS1-B, C, ISS2-B, C and HSS-B and C.

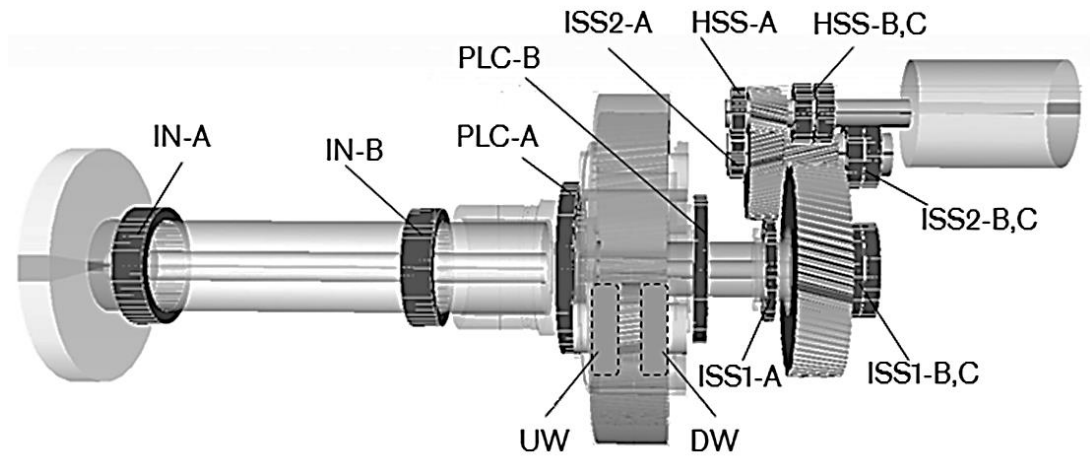


Figure 5.10: Roller bearings locations in the wind turbine drivetrain and nomenclature used

5.2.1 Diagonal Bearing Stiffness Matrix Approximation

The WT main shaft bearings and the gearbox bearings can be modelled as rigid bodies with 6 DOFs for each bearing. Bearing stiffness in radial, rotational and tilt directions can be described using a typical diagonal stiffness matrix [34]. The bearing stiffness can be calculated by dividing the loads by the corresponding displacements to determine the main diagonal elements of the stiffness matrix. The damping matrix component could be very similar to the stiffness matrix form [75]. Generally, the radial and axial displacement for all bearings within the WTG are relatively small and this can be used to estimate the bearings stiffness and damping coefficients. The effects of the off-diagonal stiffness elements are usually neglected by only considering the diagonal stiffness matrix for modelling bearings. If the main goal for WT drivetrain MBS model is to achieve good fidelity then the effect of the off-diagonal stiffness terms should be included since they can be responsible for additional harmonics in dynamic system [106]. In a bearing model using a diagonal stiffness matrix method, the zero values of the off-diagonal terms assume that the bearing strain caused by perpendicular forces and moments is small enough to be considered negligible. Therefore, the bearing model can be simplified. Bearing stiffness can be described using a stiffness matrix as shown in Figure 5.11. When the value for torsional stiffness in axial direction (i.e. $k_{\theta_z \theta_z}$)

is equal to zero, it means that the bearing raceway is fixed in XY plane, (i.e. the inner ring for planet gear bearings and the outer ring for bearings at the other WTG stages) , and this the DOF represents the rotation along the planet pin or shaft axis for the free of rotation raceways.

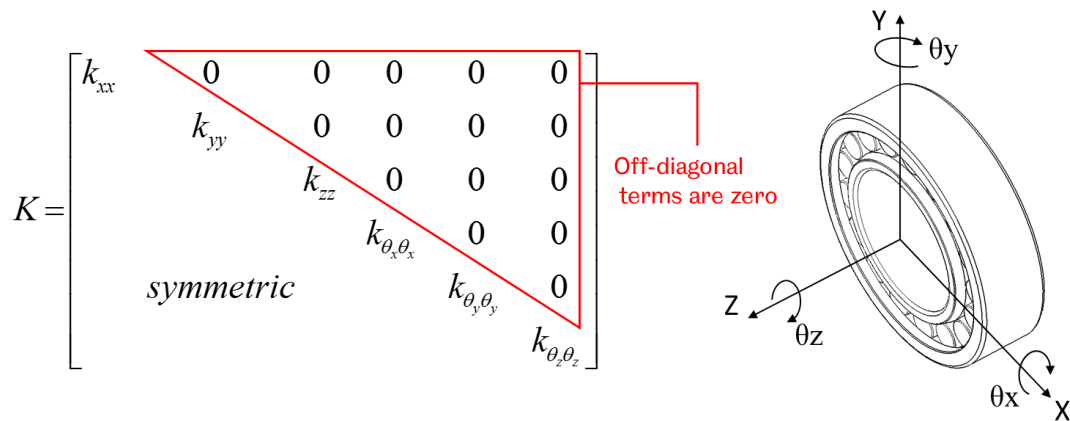


Figure 5.11: Diagonal bearing stiffness matrix

5.2.2 Consideration of Nonlinear Bearing Stiffness Characteristics and Cross-Coupling

In this study, the effect of the off-diagonal stiffness in bearing modelling is considered and the modelling method is described in this section. In the traditional diagonal matrix method that used extensively to represent the dynamic behaviour of bearings in MBS with 6 DOFs, the stiffness matrix elements for each bearing, including bearing stiffnesses in radial, rotational and tilt directions, are assumed to be constant and the model ignores the contact between the bearing components, the rollers and the races, and how many rollers are in contact under the loading conditions.

Constant values for the diagonal terms in the bearing stiffness matrix assume linear stiffness variation associated with bearing deflection. This could be considered as a fair claim in case of small shaft displacements for all bearings shafts within the WTG [107].

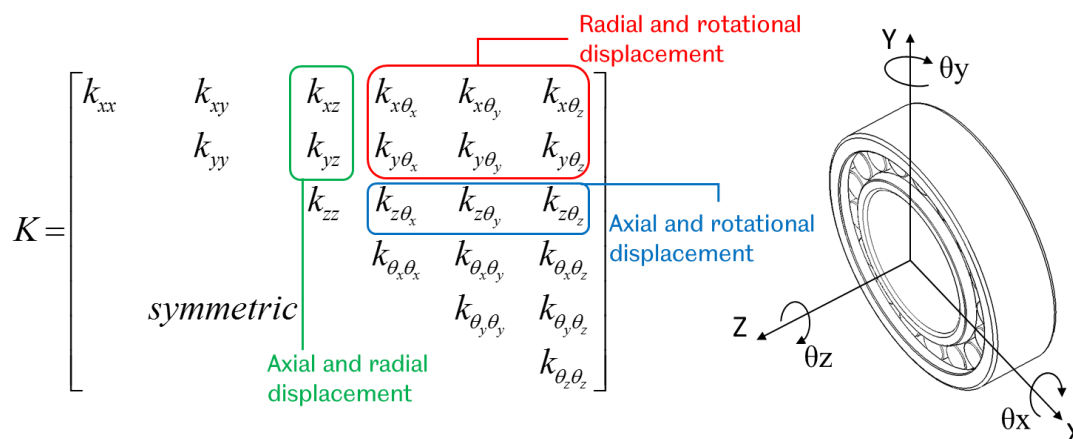


Figure 5.12: Cross-coupling representation in bearing stiffness matrix

To consider the interaction between the rollers and the races within the bearing model, the cross-coupling effect represented by the off-diagonal elements in the bearing stiffness matrix should be considered as shown in Figure 5.12. SIMAPCK MBS software provides the option of choosing many different roller bearings models by using the force element FE-88 which has the function to model different roller bearings types such as CRB, TRB and SRB, depending on the bearing real geometry which must be compatible with ISO 16281 [108]. The bearing geometry inputs required, include; number of rolling elements, rolling element diameter, radial clearance, axial clearance, the effective diameters of the bearing (bore diameter, pitch diameter, outer and inner diameter), effective contact length and diameter of bearing rollers, axial support direction of bearing (positive or negative), cage rotation, bearing friction, roller crown radius for SRB, angle of contact which is zero for CRB and non-zero for TRB and SRB. To calculate bearing stiffness matrix 'K' with consideration of the bearing geometry, nonlinear contact between the races and the rollers, bearing deflection \bar{Q} and the applied moments and forces on bearing \bar{F} in the bearing model are determined by the SIMPACK MBS software by using the analytical formulae described as follows:

$$Q = \{X, Y, Z, \theta_x, \theta_y, \theta_z\} \quad 5.6$$

$$F = \{F_x, F_y, F_z, M_{\theta_x}, M_{\theta_y}, M_{\theta_z}\} \quad 5.7$$

$$K = \begin{bmatrix} \frac{\partial F_x}{\partial X} & \frac{\partial F_x}{\partial Y} & \frac{\partial F_x}{\partial Z} & \frac{\partial F_x}{\partial \theta_x} & \frac{\partial F_x}{\partial \theta_y} & \frac{\partial F_x}{\partial \theta_z} \\ & \frac{\partial F_y}{\partial Y} & \frac{\partial F_y}{\partial Z} & \frac{\partial F_y}{\partial \theta_x} & \frac{\partial F_y}{\partial \theta_y} & \frac{\partial F_y}{\partial \theta_z} \\ & & \frac{\partial F_z}{\partial Z} & \frac{\partial F_z}{\partial \theta_x} & \frac{\partial F_z}{\partial \theta_y} & \frac{\partial F_z}{\partial \theta_z} \\ & & & \frac{\partial M_{\theta_x}}{\partial \theta_x} & \frac{\partial M_{\theta_x}}{\partial \theta_y} & \frac{\partial M_{\theta_x}}{\partial \theta_z} \\ & & & & \frac{\partial M_{\theta_y}}{\partial \theta_y} & \frac{\partial M_{\theta_y}}{\partial \theta_z} \\ & & & & & \frac{\partial M_{\theta_z}}{\partial \theta_z} \end{bmatrix} \quad 5.8$$

symmetric

5.2.3 Clearance Consideration

Bearing radial and axial clearances influence the rotation between the rollers and the raceways. In the case of fixed outer raceway, such as the main shaft, intermediate and high-speed bearings within the WT drivetrain, the radial and axial clearances in bearing can be defined as the highest displacement of the inner race in radial and axial direction respectively. This is not the case in planet gear bearings as the inner race is fixed on the planet carrier and the outer race rotation corresponds to planet gear motion. In SIMPACK MBS, the force element FE-88 is used to model the bearings of the main shaft and the WTG. The bearing radial and axial clearances for all bearing models within the WT drivetrain are considered. The representation of axial and radial clearances in the SIMPACK roller bearing model is illustrated in Figure 5.13.

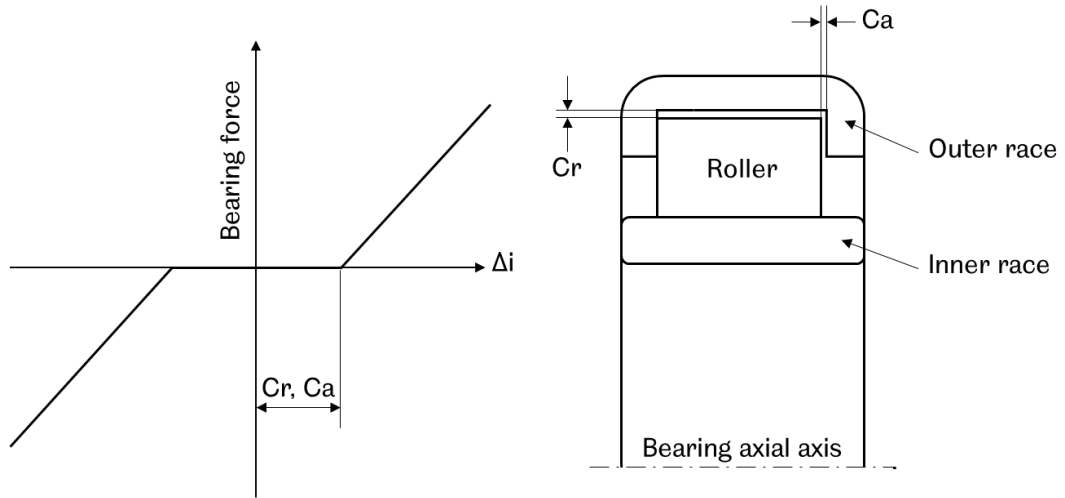


Figure 5.13: Axial and radial clearances in a roller bearing

The single roller (see Figure 5.14) deflection Δi within the roller bearing with radial and axial clearances is calculated by using the following formula [109]:

$$\Delta i = (\delta_{ri} - Cr) \cdot \cos(\psi_i) + (\delta_{ai} - Ca) \cdot \sin(\psi_i) \quad 5.9$$

Where ψ_i is the nominal contact angle between the roller and the race, δ_{ri} and δ_{ai} are the radial and axial deflection of the roller, Cr and Ca are the radial and axial bearing clearances.

5.2.4 Bearing Roller Model

The contact between the roller and the race is represented using the laminae roller model [110] by dividing the roller in contact with the raceway into series of thin slices parallel to the bearing radial plane, as shown in Figure 5.14. The contact load between of roller j per laminae k and the race for CRB, TRB can be calculated as follows [111]:

$$F_{j,k} = C_s \cdot \delta_{j,k}^{1.11} \quad 5.10$$

For SRB, the contact load between roller j per laminae k and the race can be calculated as follows [111]:

$$F_{j,k} = C_s \cdot \delta_{j,k}^{1.5} \quad 5.11$$

Where $F_{j,k}$ is the contact load between roller and the race, C_s is the contact stiffness and $\delta_{j,k}$ is the slice deflection within the lamina model for roller. In this study, the contact between the bearing rollers and the raceways is assumed to be line contact. For this contact consideration, the stiffness of contact for each slice per line of contact, C_s , of width w can be calculated as follows:

$$C_s = \frac{0.7117 \times w^{0.889}}{\left(\frac{1-\nu_1^2}{E_1} + \frac{1-\nu_2^2}{E_2} \right)} \quad 5.12$$

Where ν_1, ν_2 and E_1, E_2 are the Poisson's ratio and modulus of elasticity of roller and raceway materials.

The bearing model created within the SIMPACK MBS environment is accomplished by using the force element FE-88 and has the capability to calculate:

- The radial and axial bearing force,
- The tilting and axial bearing torque,
- The axial and radial roller displacement,
- The tilting angle of roller,
- The number of loaded rollers,
- The maximum roller load and maximum roller deflection,
- The maximum Hertzian contact pressure between the bearing rollers and the raceway.

The method of calculating the maximum Hertzian contact pressure between the roller elements and the bearing outer or inner raceways is described in the following section.

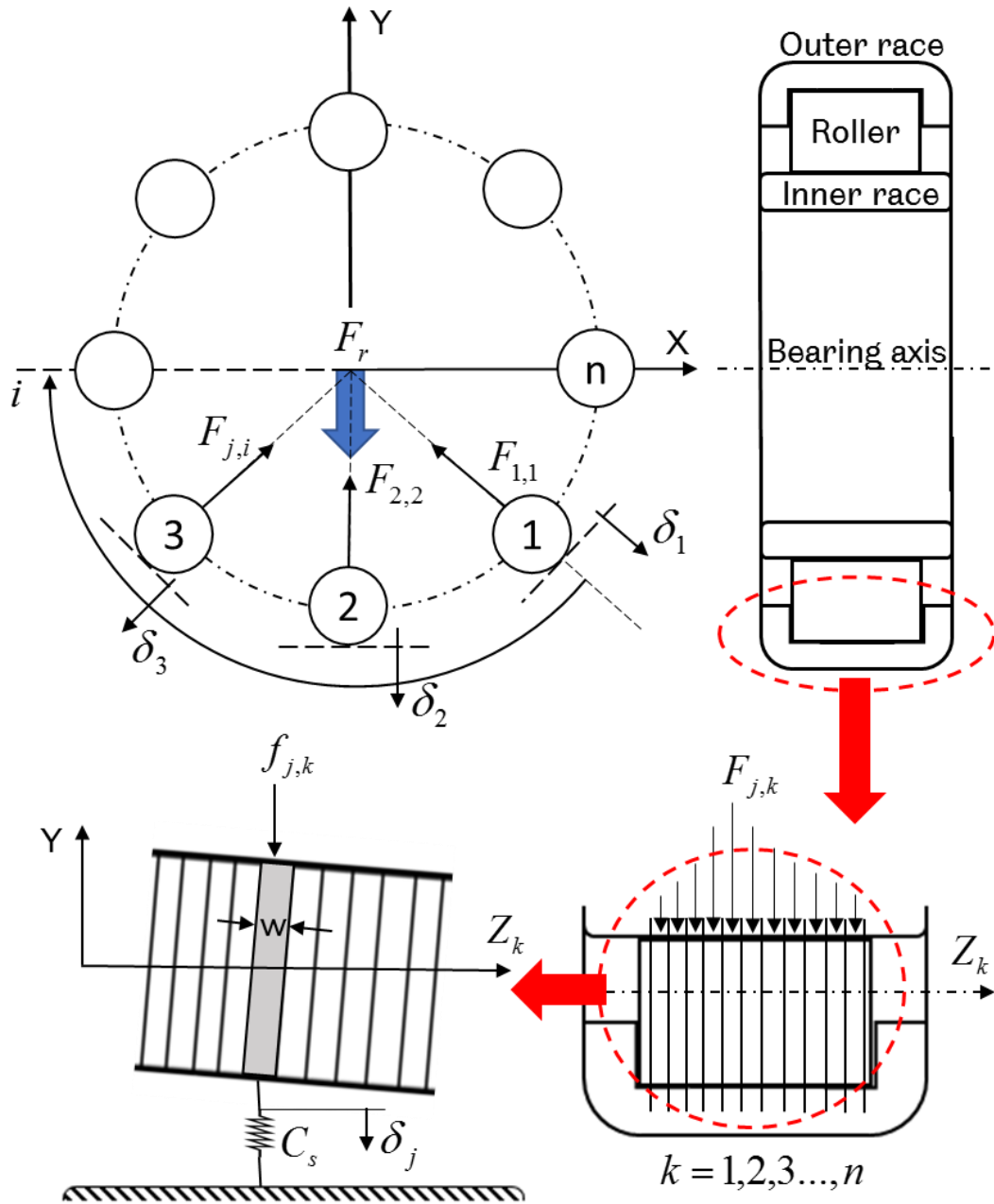


Figure 5.14: Representation of roller lamina model within the roller bearing model

5.3 Hertzian Contact Stress Consideration for Gears and Bearings

The surface contact stress, subsurface shear stress and von Mises stress distributions for all gears and roller bearings within the WTG are investigated in this study by using Hertzian theory [112]. In the SIMPACK MBS, the contact between the gear teeth is represented by two cylinders in contact, with radius function of gear base radius and contact pressure angel. The contact between the roller and the inner or outer raceway is represented by two cylinders in contact, with radius equal to roller radius and the roller bearing race radius. The contact patch between the two cylinders is in the shape of a rectangle with length L equals to the gear face width or bearing roller length with contact width equals to $2a$, as shown in Figure 5.15. In SIMPACK MBS, the contact between the two cylinders for both gears and roller bearings are considered as line contact.

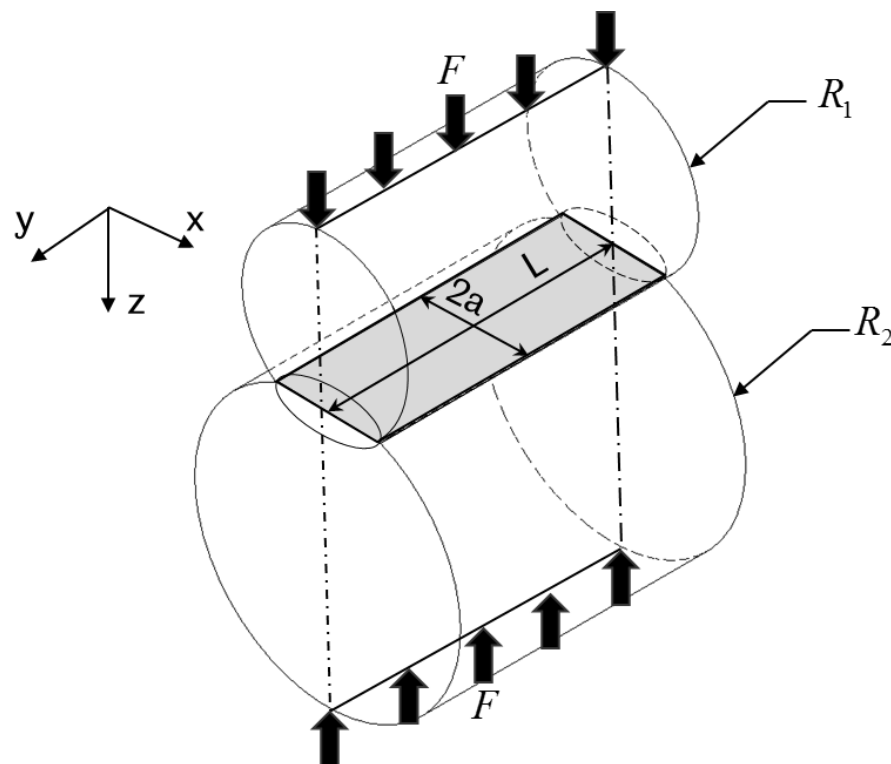


Figure 5.15: Hertzian line contact geometry of two cylinders

The geometry constant of two cylinders in contact is normally a function of the cylinders radii R_1 and R_2 as follows:

$$R = \frac{1}{2} \left(\frac{1}{R_1} + \frac{1}{R_2} \right) \quad 5.13$$

The half contact width of the rectangle shown in Figure 5.15 can be calculated as follows:

$$a = \sqrt{\frac{4 \times F \times R}{\pi \times L \times E_R}} \quad 5.14$$

$$\frac{1}{E_R} = \frac{1 - \nu_1^2}{E_1} + \frac{1 - \nu_2^2}{E_2} \quad 5.15$$

Where F is normal contact force between the two objects in contact, ν_1 and ν_2 are the two objects in contact Poisson's ratio and E_1 and E_2 represent the modules of elasticity of cylinder 1 and 2 respectively. For line contact between the two cylinders, the maximum Hertzian contact pressure is calculated in SIMPACK MBS software by using:

$$P_{\max} = \frac{2 \times F_{\max}}{\pi \times L \times a} \quad 5.16$$

The Hertzian contact pressure distribution is calculated by using:

$$P = P_{\max} \sqrt{1 - \frac{x^2}{a^2}} \quad 5.17$$

The subsurface stresses distribution along Z axis can be calculated by using the following equations [113]:

$$\sigma_{yy} = -2\nu P_{\max} \left(\sqrt{1 + \frac{z^2}{a^2}} - \left| \frac{z}{a} \right| \right) \quad 5.18$$

$$\sigma_{xx} = -P_{\max} \left(\frac{1 + 2\frac{z^2}{a^2}}{\sqrt{1 + \frac{z^2}{a^2}}} - 2\left| \frac{z}{a} \right| \right) \quad 5.19$$

$$\sigma_{zz} = \frac{-P_{\max}}{\sqrt{1 + \frac{z^2}{a^2}}} \quad 5.20$$

The maximum, unidirectional, subsurface shear stress and von Mises stress distribution is shown in Figure 5.16 and can be calculated by using the following:

$$\tau_{\max} = \frac{\sigma_{xx} - \sigma_{zz}}{2} \quad 5.21$$

$$\sigma' = \sqrt{\frac{1}{2} \left[(\sigma_{xx} - \sigma_{zz})^2 + (\sigma_{zz} - \sigma_{yy})^2 + (\sigma_{yy} - \sigma_{xx})^2 + 6(\tau_{xy}^2 + \tau_{yz}^2 + \tau_{zx}^2) \right]} \quad 5.22$$

For pure rolling, the maximum subsurface shear stress τ_{\max} , point A in Figure 5.16, is 0.3 of the maximum contact pressure P_{\max} and located at depth of $0.78a$ [113, 114]. The maximum von Mises stress σ'_{\max} , point B in Figure 5.16, is 0.57 of the maximum contact pressure P_{\max} and located at depth of $0.7a$ [114, 115].

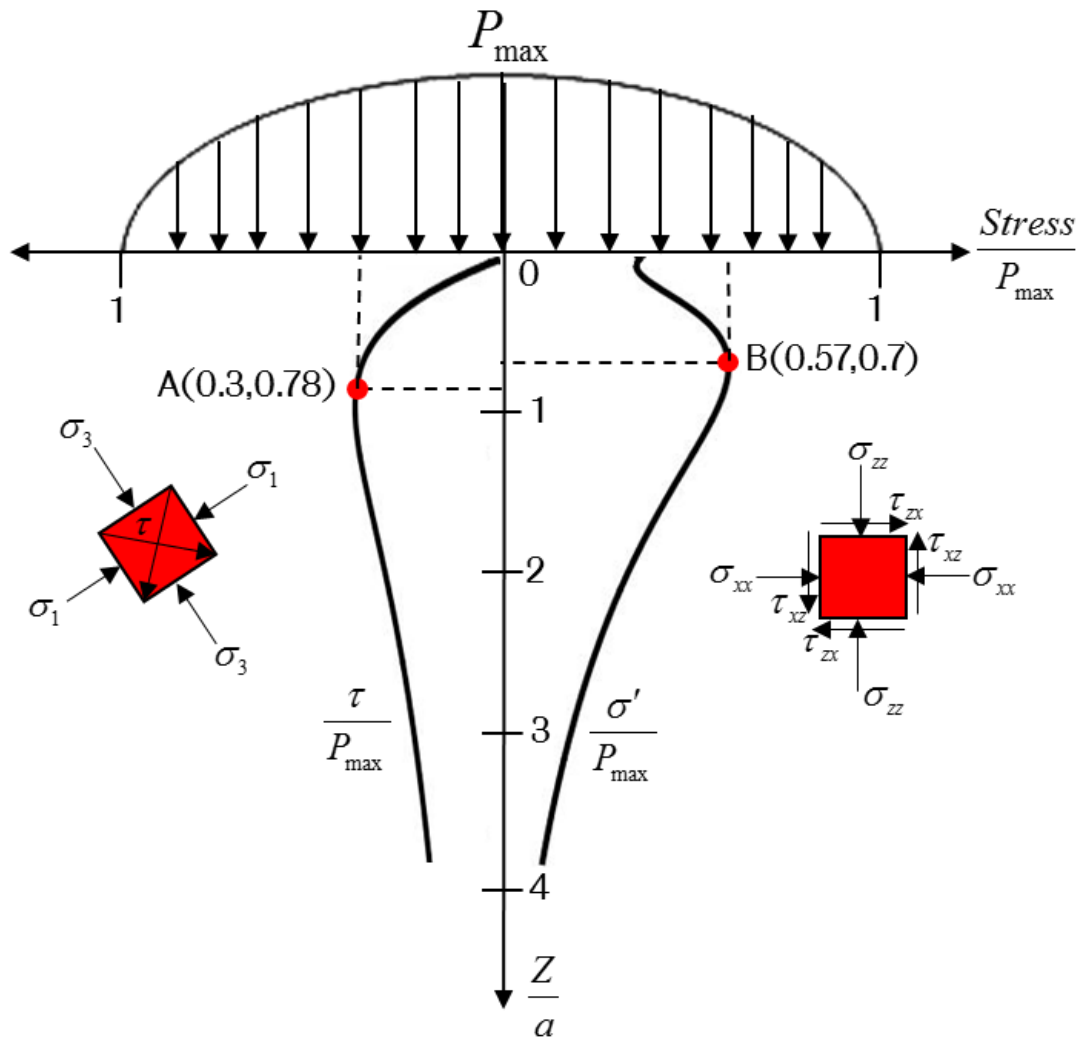


Figure 5.16: Normalised subsurface principal shear stress τ (left-half) and von Mises stress σ' (right-half) distribution for line contact of two cylinders. The points A and B indicate the value and location of maximum subsurface shear stress ($0.3P_{\max}$ at depth $0.78a$) and von Mises stress ($0.57P_{\max}$ at depth $0.7a$) respectively, a is half of the contact width and Z is the depth

5.4 Fatigue Damage of Wind Turbine Gearbox Components

During the simulation using the SIMPACK MBS software, the WTG model subjected to different operational conditions. The time series of maximum Hertzian surface contact stress on gears and bearings within the WTG are calculated. The rainflow counting method discussed in Chapter 3 is used to analyse the stress data by converting the time domain results of a complicated stress history into number of stress ranges $\sigma_{1,2,\dots,i}$ and stress cycles $n_{1,2,\dots,i}$.

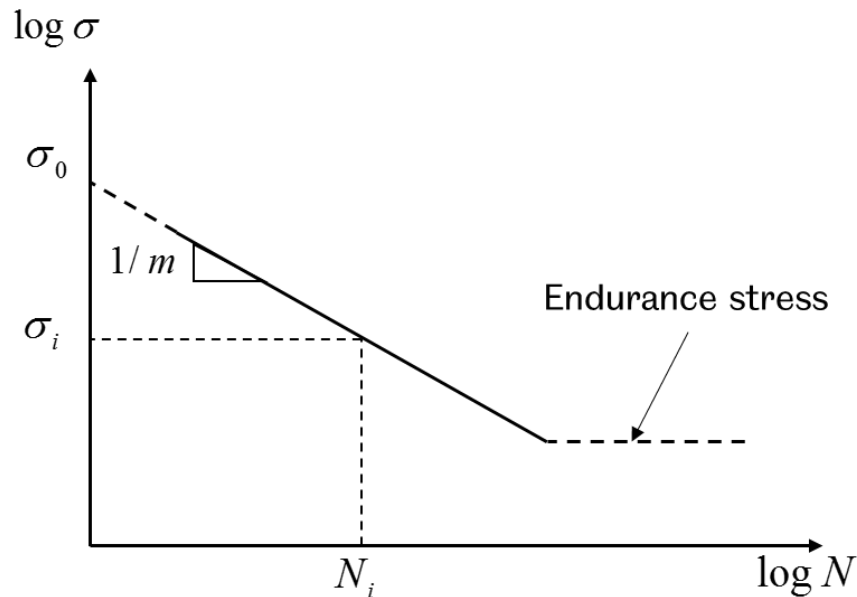


Figure 5.17: Typical S-N curve

The Palmgren-Miner rule [116, 117] is utilised to calculate the accumulated gear fatigue damage D_{gear} within the WTG caused by each applied stress cycle as follows:

$$D_{gear} = \sum \frac{n_{1,2,\dots,i}}{N_{1,2,\dots,i}} = \sum n_{1,2,\dots,i} \frac{\sigma_{1,2,\dots,i}^m}{\sigma_0^m} \quad 5.23$$

$$\sigma_{1,2,\dots,i} = \frac{\sigma_0}{N_{1,2,\dots,i}^{1/m}} \quad 5.24$$

Where m is the slope of S-N curve, σ_0 is the maximum stress amplitude within the S-N (Wöhler) curve, the intersection between the S-N curve and the vertical axis, and N_i is the number of cycles to failure as illustrated in Figure 5.17. The Lundberg-Palmgren rule [118] is utilised to calculate the bearings service life within the WTG operating under the applied surface stress cycles during different operational conditions as follows:

$$P_r \times L^{1/b} = Const. \quad 5.25$$

where P_r and L are the radial load on bearing and bearing life respectively, b is equal to 10/3 because in this study all the bearings within the WTG are roller bearings. In the case of ball bearings, b is equal to 3. According to the Palmgren-Miner rule [116, 117], the accumulated bearing fatigue damage caused by each applied stress cycles can be calculated as follows:

$$D_{bearing} = \sum_{i=1}^j \frac{l_i}{L_i} \quad 5.26$$

$$L_i = \frac{L_{10} \times C_r^b}{P_i^b} \quad 5.27$$

where L_i is the bearing load cycles to failure corresponding with range of load P_i ; C_r is the bearing's basic rated load. The accumulative fatigue damage for the WTG components, the gears and bearings, within WT drivetrain is calculated for a short-term simulation period of the WT drivetrain at rated wind speed. In fact, it does not represent the whole design life for WTG key components. The damage of gears and bearings within the WTG is calculated

for the short term. However, D_{gear} and $D_{bearing}$ can be used to calculate the long term damage of these mechanical parts [43, 119] corresponding to WT design life of 20 years and operating under design load condition (DLC) as the following:

$$D_{LG}^{DLC} = 20_{years} \times D_{gear} \times P_{W,R} \quad 5.28$$

$$D_{LB}^{DLC} = 20_{years} \times D_{bearing} \times P_{W,R} \quad 5.29$$

Where D_{LG}^{DLC} and D_{LB}^{DLC} are the damage of gears and bearings operating under DLC while $P_{W,R}$ is the Weibull or Rayleigh portability cumulative distribution function, which may be represented by [17, 84]:

$$P_W(U_{hub}) = 1 - \exp \left[- \left(\frac{U_{hub}}{C} \right)^k \right] \quad 5.30$$

$$P_R(U_{hub}) = 1 - \exp \left[- \pi \left(\frac{U_{hub}}{2U_{ave}} \right)^2 \right] \quad 5.31$$

$$U_{ave} = \begin{cases} C \frac{\sqrt{\pi}}{2}, k = 2 \\ C \Gamma \left(1 + \frac{1}{k} \right), k \neq 2 \end{cases} \quad 5.32$$

Where U_{hub} and U_{ave} are the respective average wind speeds at the WT hub for a short period, i.e.10 minutes, and a long period, i.e. annually; while C , k and Γ are scale, shape parameters and gamma function respectively. In this study the shape factor k is equal to 2 which is the case when Weibull portability cumulative distribution is identical to Rayleigh distribution. Moreover, the damages of gears and bearings within the WTG are investigated under two DLCs these are normal operation and shutdown conditions.

5.5 Consideration of Non-Torque and Gravity Loads

Gearboxes installed in wind turbines are subject to unique operating conditions, namely the non-torque loading imposed on the main shaft. Non-torque loading occurs when the weight, motion, and wind pressure of the rotor and blades transmit forces other than torque to the main shaft; instead of just torsional rotation, these drivetrains encounter Non-torque loading. The non-torque loads such as the WTG pitching moments are caused by the WT's rotor due to their heavy weight and the gravity influence which affect the planet gear contact load of the planetary stage, the planet gear bearings load and the out of phase loads within the WTG [120]. Therefore, they both should be considered in the WT drivetrain MBS model. In the WT drivetrain model using the SIMPACK MBS software the input torque and the generator resistance torque are not the only inputs to the MBS model. The field measurement moment data and the gravity are also inputted to the model as illustrated in Figure 5.18. The Co-Simulation function [109] available in the SIMAPCK MBS software is used to read the field measurement moment time history from MATLAB worksheet then use it as an input in the location indicated in Figure 5.18 (i.e. the pitch moment) by using the Force/Torque force element type 93 (i.e. FE-93). The gravity is specified in direction indicated in Figure 5.18 (i.e. gravity vector) in Y direction by using SIMPACK gravity element.

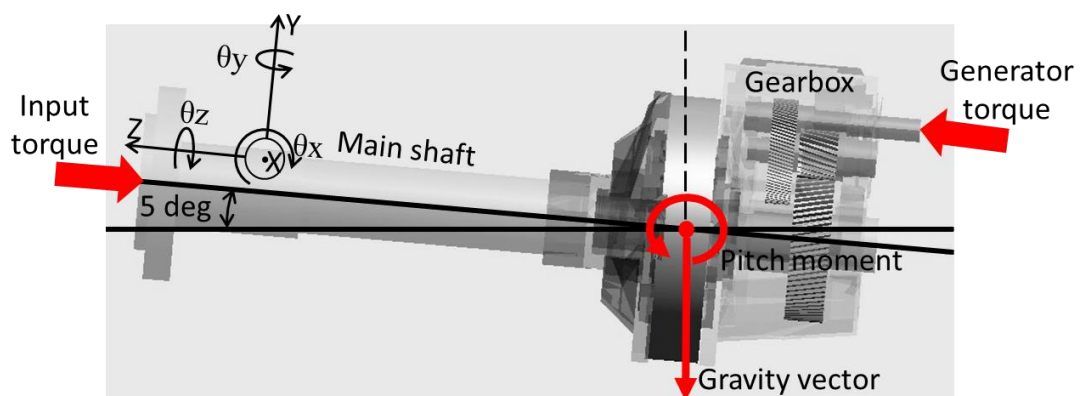


Figure 5.18: Consideration of pitching moment and gravity effects on wind turbine gearbox

It is worth to mention that the generator models that were modelled by MATLAB/Simulink for use in Chapter 4 are used in this Chapter to produce the required generator resistance torque and connected with SIMAPCK MBS WTG models by using Co-Simulation function [109] available in the SIMAPCK MBS software.

5.6 Summary

The methodologies used to model the key components of the WT drivetrain with 6 DOFs per components, including the shafts, planet carrier, carrier pins, gears and the bearings were summarised in this Chapter. By developing more advance MBS model, the bearing clearance, bearing roller contact with bearing raceway, gear contact and gear tilt within the WTG were investigated during two different DLCs, normal operation and shutdown. The existing MBS models used extensively the diagonal stiffness matrix to model the bearings within the WTG. These models have clear limitations when compare it with the experimental tests. Advance model for bearing contact, rollers and raceways contact within the WTG is important in MBS model especially for the planet gear downwind bearings to capture more details of bearing loads operating under transient operational conditions such the unplanned shutdown. The methods for determining short term and long term cumulative fatigue damage for gears and bearings within the WTG during the normal operation and shutdown were presented. The results obtained by the modelling methods presented in this Chapter will be discussed in Chapter 7.

6

RESULTS AND DISCUSSION OF PURE TORSIONAL MULTIBODY DYNAMIC MODELLING OF WIND TURBINE DRIVETRAINS

The wind turbine (WT) drivetrain undergoes various operational conditions and its design configuration affects how the gearbox components react to transient loading conditions. This Chapter investigates the system dynamic response of three different WT drivetrain configurations under normal and shutdown operations. As presented in Chapter 4, the pure torsional multibody dynamic models are developed by using MATLAB/Simulink, including the turbine rotor, the gearbox components and the generator. The model of each configuration captures more details of drivetrain dynamic behaviour, such as the torsional deformation and dynamic responses of key mechanical components of the WT drivetrain, than that captured by widely used two-mass or five-mass drivetrain models.

As described in Chapter 4, the required parameters for building multistage gearbox dynamic models are obtained by developing CAD models. In this Chapter, eigenfrequency analysis of the WT drivetrains is performed by using MATLAB/Simulink control design tools. The influence of the WT drivetrain

design configuration on the eigenfrequencies of the system and how they affect the dominant frequencies and the meshing forces of gears of the gearbox during normal operation and shutdown are discussed in detail. Parametric study of key variables of the drivetrain components is performed and how these affect the dynamic responses of the system is investigated.

6.1 NREL750 kW WT Drivetrain Model

6.1.1 Model Validation

Phase one of the 'Round-Robin' validation process [121] involved comparing the following NREL 750 kW gearbox modelling results with "gearbox reliability collaborative" (GRC) partners anonymously who were only identifiable the letters A-F where each member used independent modelling software to model the 750 kW WTG (see Chapter 4 Figures 4.1 and 4.3), to validate the models' accuracy, which includes comparing torque distribution in gearbox shafts and the contact load components on sun-planet gear and ring-planet gear. These results will be used to validate the gearbox model developed by using MATLAB/Simulink described in Chapter 4 (see Figure 4.6) of this thesis.

The first validation stage of the model developed in this study is to compare torque and gear load distributions throughout the NREL 750kW gearbox with that obtained by all GRC partners. The MATLAB/Simulink model representing the NREL 750 kW drivetrain is loaded at rated torque and is operated under steady state condition, torque distributions through the gearbox and the gear contact load of ring-planet gear and sun-planet gear are obtained. The result comparisons with the GRC partners are shown in Figure 6.1.

The results of the developed model of WTG agreed with those of GRC round-robin, with torque levels and gear contact load level that were close to those of GRC partners. No results were available for HSS torque comparison. All percentage differences are within acceptable levels. The small levels of error are likely to be due to the inaccuracy of the assumptions made in Chapter 4 when developing the gearbox model.

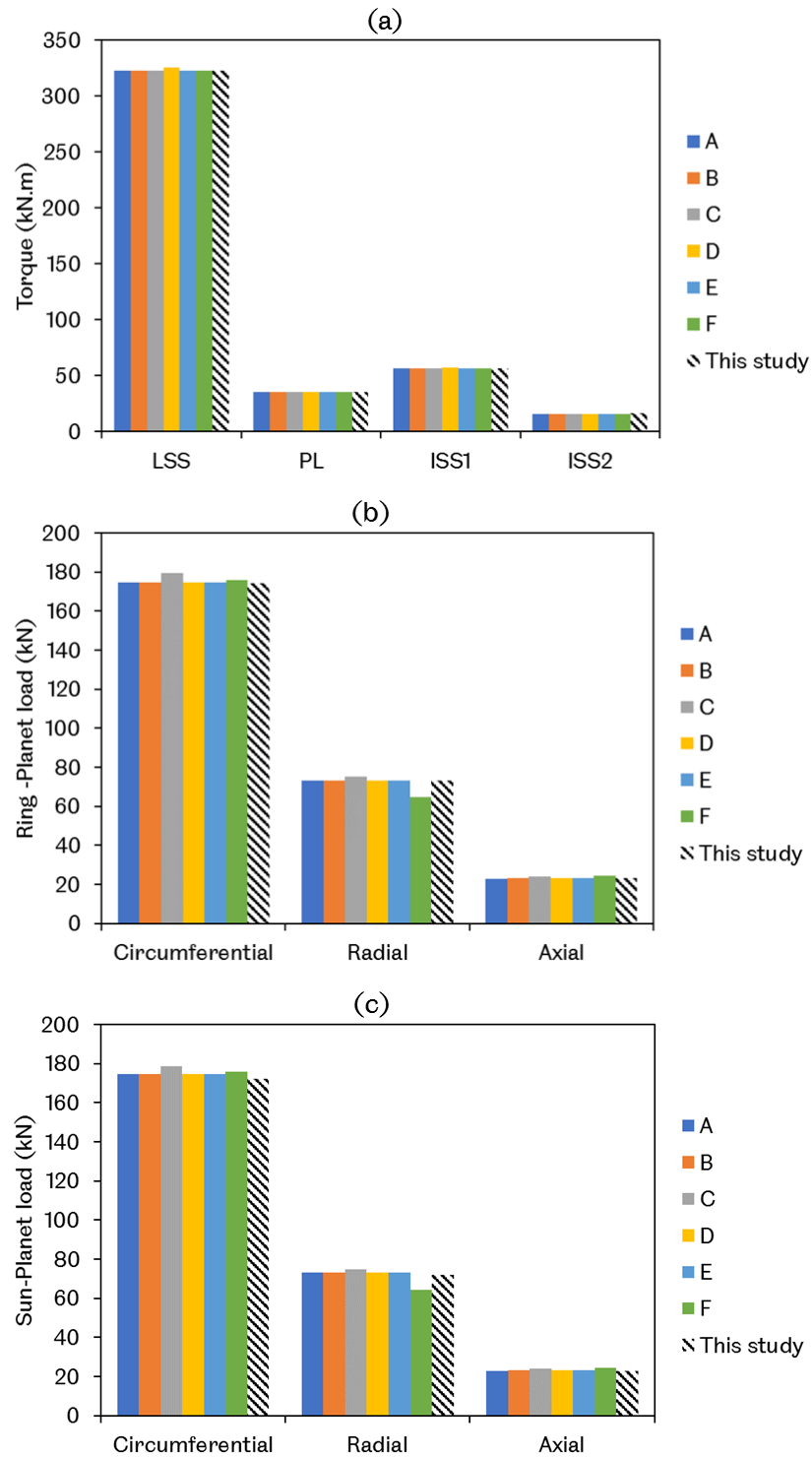


Figure 6.1: Comparison of 750kW WT MATLAB/Simulink model results with GRC partners results [121], (a) Torque distribution (b) Ring-planet contact load (c) Sun-planet contact load

The second stage of the model validation was to calculate the 750kW WT drivetrain natural frequency of the developed MATLAB/Simulink models with different levels of complexity by using MATLAB/Simulink control design tools and to compare these with the experimental [50, 51] and analytical [50, 51] results obtained by previous studies. The comparison analysis of the calculated eigenfrequencies for different drivetrain models, using both fixed and variable generator speed models, is summarised in Table 6.1 and Table 6.2. The results of the natural eigenfrequencies are compared with those available in published literature [50, 51] and show good agreement.

Exciting the drivetrain system at any of these eigenfrequencies will lead to amplified loads in the WT drivetrain. The experimental and analytical values of the 1st and 2nd natural frequencies of two mass model of the 750kW WT drivetrain are listed in Table 6.1 [50, 51]. These two frequency readings are very close to the one calculated from the MATLAB/Simulink model developed in this study and show better agreement than the models developed by [50, 51].

Table 6.1: Comparison of frequency values of different lumped mass models of 750kW WT drivetrain (Hz)

| Mode | Experimental and analytical | | 2-Mass Model | | 5-Mass Model | | 11-Mass Model | |
|------|-----------------------------|------------------|----------------|----------------|----------------|----------------|----------------|----------------|
| | Constant speed* | Variable speed** | Constant speed | Variable speed | Constant speed | Variable speed | Constant speed | Variable speed |
| 1 | 0.806 | 0 | 0.864 | 0 | 0.864 | 0 | 0.841 | 0 |
| 2 | / | 2.32 | 5.888 | 2.524 | 5.889 | 2.524 | 5.859 | 2.44 |
| 3 | / | / | / | / | 312 | 312 | 154 | 154 |
| 4 | / | / | / | / | 402 | 402 | 307 | 307 |
| 5 | / | / | / | / | 1974 | 1974 | 353 | 353 |
| 6 | / | / | / | / | / | / | 748 | 748 |
| 7 | / | / | / | / | / | / | 1020 | 1020 |
| 8 | / | / | / | / | / | / | 1530 | 1530 |
| 9 | / | / | / | / | / | / | 4398 | 4397 |

* (Mandic et al., 2012)

** (Girsang et al., 2014)

Table 6.2: Frequency comparison for 2 and 5-mass models of wind turbine drivetrain

| 2-Mass model | | |
|---------------|-------------------|---------------------|
| Mode | This study | Mandic et al., 2012 |
| 1 | 5.1951 (rad/sec) | 5.1972 (rad/sec) |
| 2 | 38.2748 (rad/sec) | 38.2818 (rad/sec) |
| 5- Mass model | | |
| 1 | 0.826 (Hz) | 0.83 (Hz) |
| 2 | 6.092 (Hz) | 6.09 (Hz) |
| 3 | 291.987 (Hz) | 291.8 (Hz) |
| 4 | 371.528 (Hz) | 371.3 (Hz) |
| 5 | 1974.245 (Hz) | 1974 (Hz) |

The final stage of the model validation is to operate the NREL 750kW WT MATLAB/Simulink model under normal operation. The MBS model developed by MATLAB/Simulink is injected by two inputs, the field measured LSS torque on the rotor side and generator resistance torque produced by the generator model on the HSS side. The generator speed sensor measures the input speed to the generator received from the HSS to ensure that the generator speed always within the synchronise speed level. Figure 6.2 (top) shows the LSS and the HSS speed during 90 seconds of normal operation. The LSS velocity levels out at rated speed of 22.4 RPM. Comparing the LSS signal calculated by the developed MATLAB/Simulink models to the NREL measured speed signal [18], the behaviour of the system dynamics is well replicated, with similar oscillation magnitudes of 0.8 RPM and an average velocity of 22.44 RPM compared to 22.4 RPM with an error of 0.18%. As shown in Figure 6.2 (top), the velocity of the HSS oscillates up and down by 5 RPM around the 1809 RPM close to the rated speed of the generator. This oscillation magnitude seems reasonable, so it can therefore be assumed that the simulation is accurate. Figure 6.2 (bottom) shows the generated power during 90 second of normal operation. The power levels out at rated power of 750kW which gives another indication that the system dynamic behaviour is well replicated.

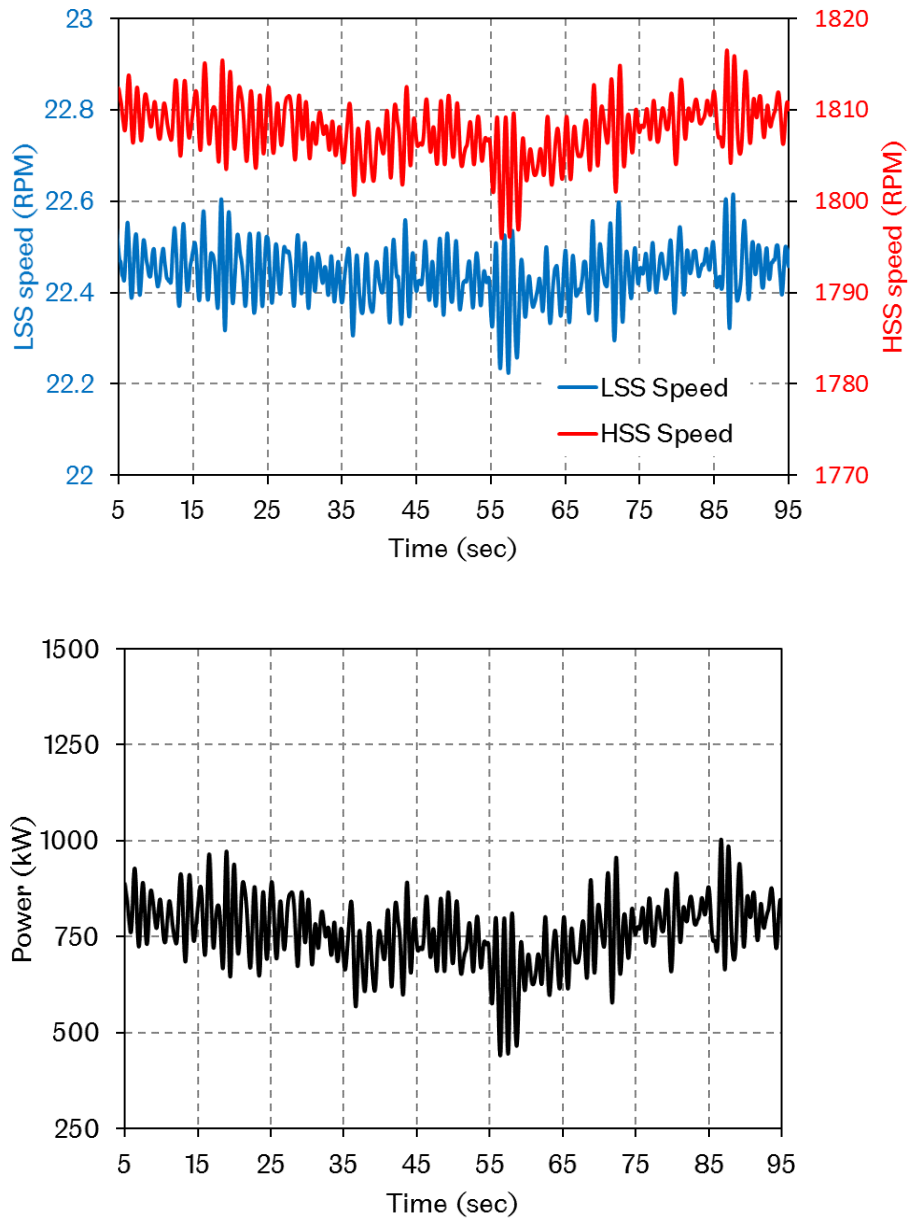


Figure 6.2: Results of MATLAB/Simulink 750kW WT multibody system model with 11-mass, LSS and HSS speed (top), power(bottom)

6.1.2 Mode Shapes of Lumped Mass Models During Free Vibration with Fixed and Variable Generator Models

The eigenvectors analysis of WT drivetrain for 2, 5 and 11-mass models with fixed and variable speed generator are illustrated in Figure 6.3, Figure 6.4 and Figure 6.5 respectively. The mode shape is a specific pattern of vibration executed by the WT drivetrain system at specific frequency. The vertical axis in these figures represents the mode shape displacement value which is relative, and the maximum value is taken as one. The DOF axis in these figures represents the effective masses within the WT drivetrain model while the horizontal axis represents the frequency order with values shown in Table 6.1. The variable generator model (i.e. generator disconnected) represented by eliminating the electrical torsional stiffness, has significant influence on the mode shape of the drivetrain components. Increasing the DOF of the model produces more complex mode shapes and enables more accurate description of the torsional vibration of the WT drivetrain. It is impossible to predict the frequency and the related mode shapes for the WT gearbox by using a simple DOF model such as the 2-mass model. The absence of the torsional electrical spring in the variable generator model has a clear effect on the mode shape of the 2- mass model at frequency of 0 HZ, and all the WT drivetrain masses vibrate in alignment on the same axis. Similarly, the absence of the torsional electrical spring in the variable generator has the same influence on the mode shapes of 0 Hz for the WT drivetrain for the 5 and 11 -mass models. The mode shape relating to 0 Hz frequency is called the generator mode.

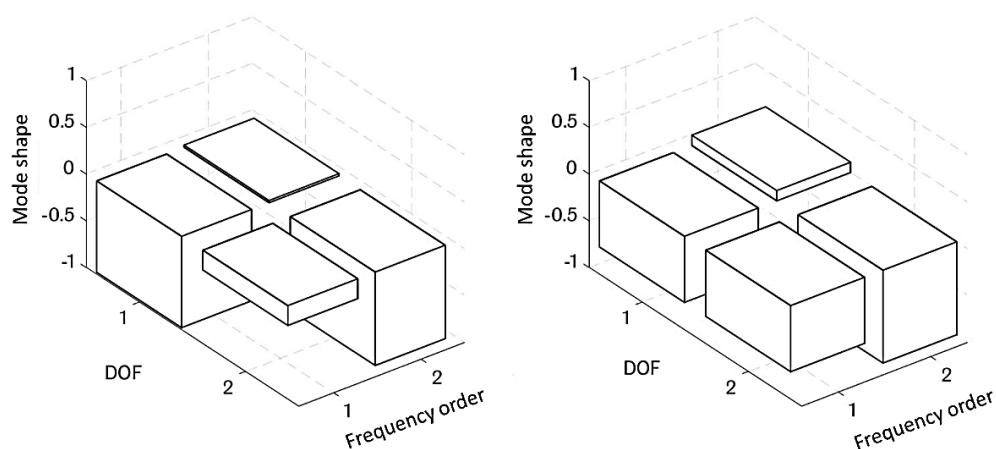


Figure 6.3: Mode shapes of 2 mass model for WT drivetrain with fixed (left) and variable (right) speed generator

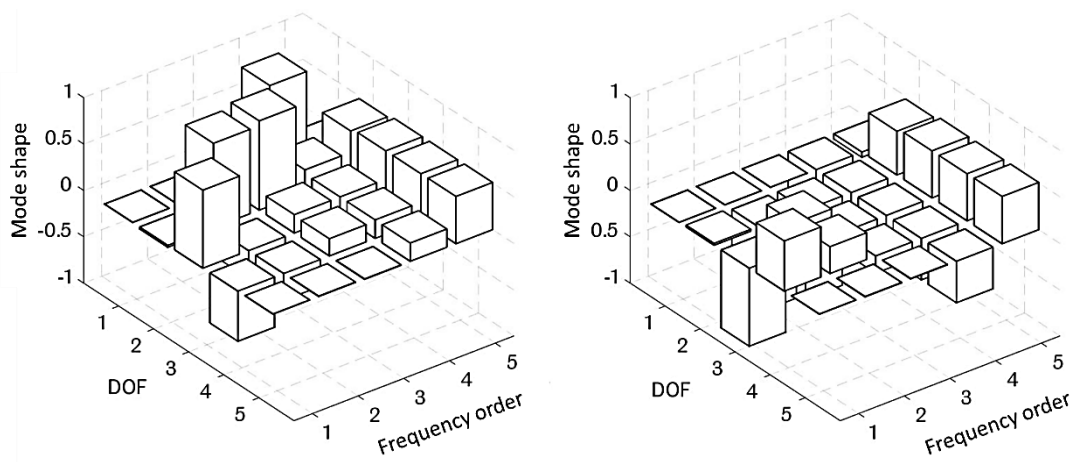


Figure 6.4: Mode shapes of 5 mass model for WT drivetrain with fixed (left) and variable (right) speed generator

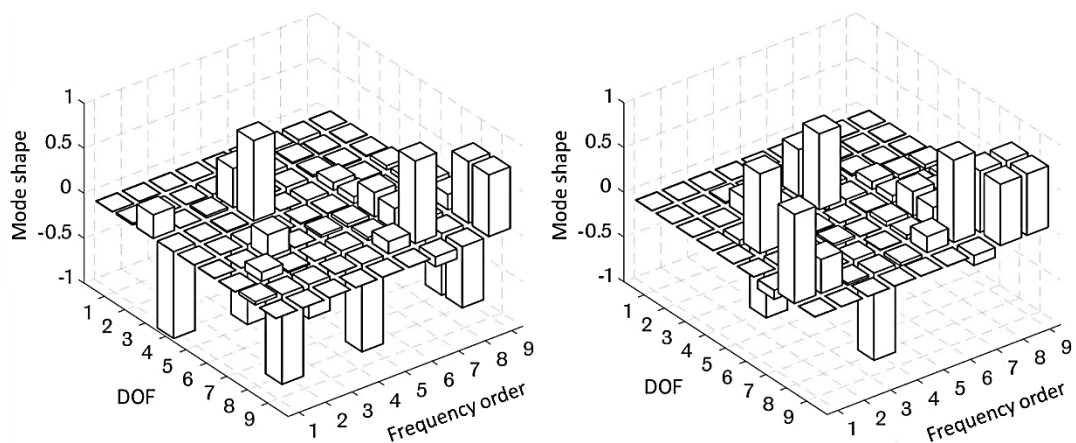


Figure 6.5: Mode shapes of 11 mass model for WT drivetrain with fixed (left) and variable (right) speed generator

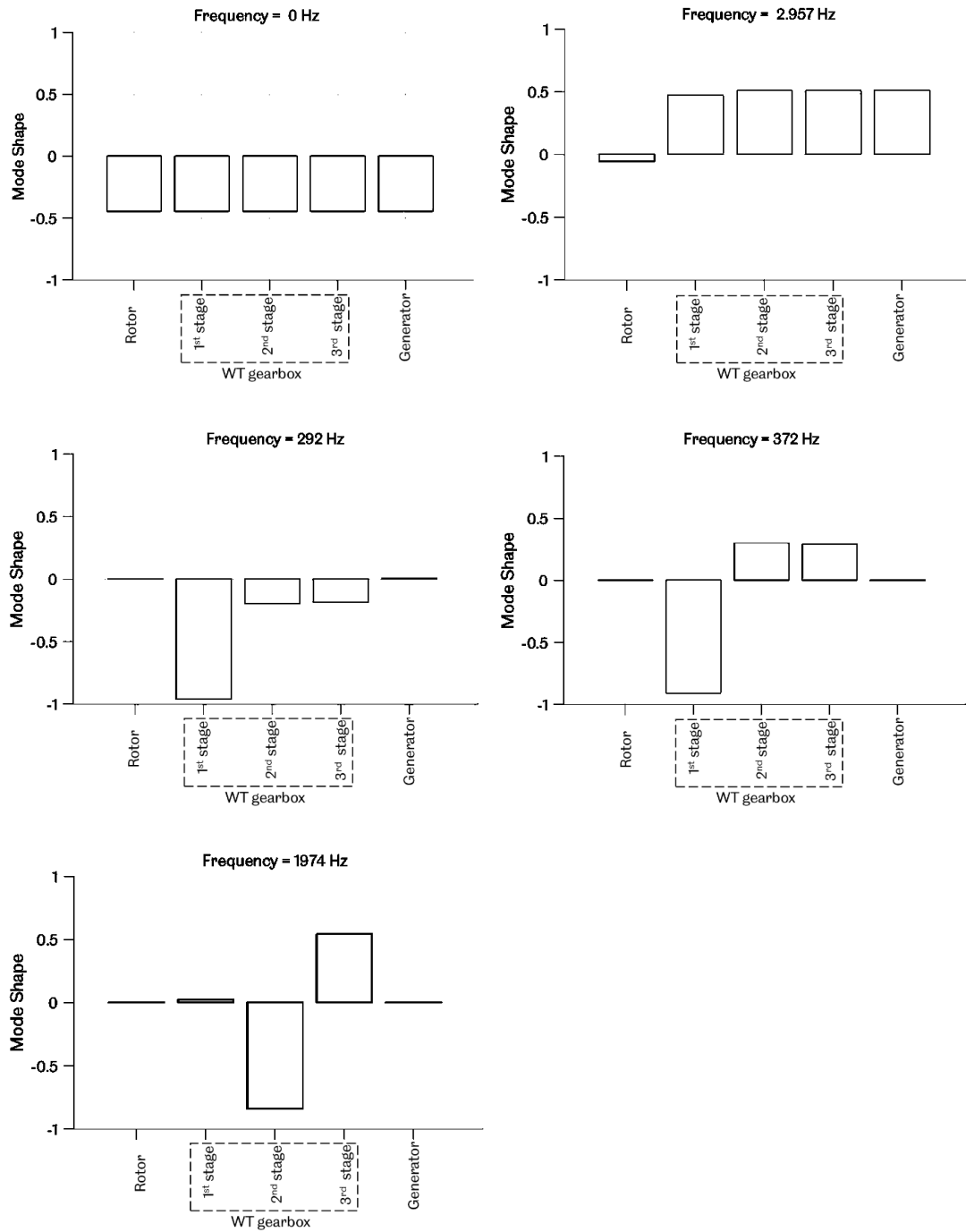


Figure 6.6 : Mode shapes corresponding to the natural frequencies of 5-mass model of the 750kW WT with variable speed generator

The Bode diagrams for the WT drivetrain shown in Figure 6.6, Figure 6.7 and Figure 6.8 can be drawn and the values of eigenfrequencies can be calculated by following the procedure explained before in section 4.3.4. Figure 6.6 illustrates the mode shapes of the NREL 750kW WT with the variable speed generator. At the frequency 2.957 Hz (i.e. the 1st natural frequency), all the drivetrain effective masses vibrate around the heaviest mass (i.e. the rotor mass). The mode shape relating to 1st frequency is called the LSS mode. At the frequency 292 Hz (i.e. the 2nd natural frequency) the WT gearbox effective masses vibrate around the HSS stage effective mass. The mode shape relating to 2nd frequency is called the HSS mode. All other mode shapes at the frequencies of 372 Hz and 1974 Hz relate to the WT gearbox. However, when the fixed speed generator model is used, the order of the LSS and generator frequencies is changed, thus the three lowest frequencies represent the responses of the LSS, generator and the HSS respectively.

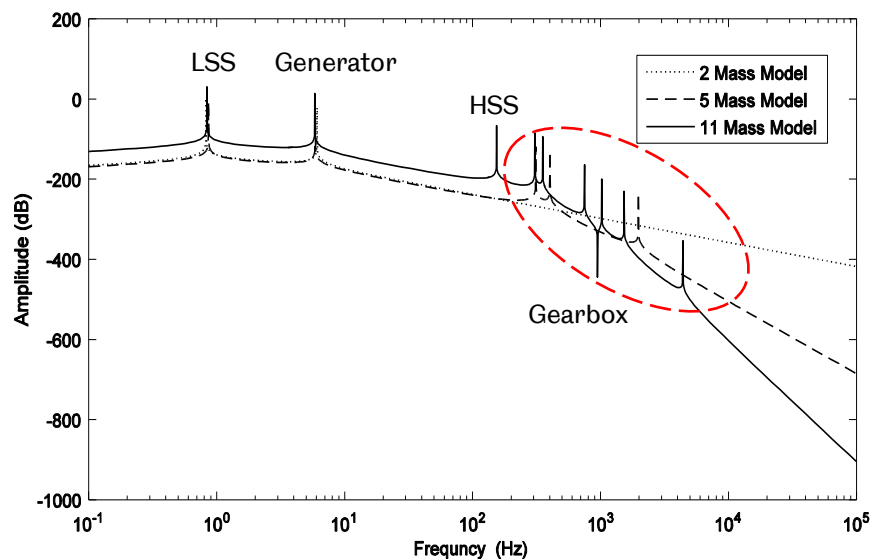


Figure 6.7: Frequency response function (FRF) for 2, 5 and 11 mass model of WT drivetrain with fixed speed generator.

Figure 6.7 summarises the frequency response function (FRF) calculations for the WT drivetrain with fixed speed generator for three different models with different levels of degree of freedom. Comparing three different models with different levels of DOF gives important indications about the dynamic behaviour that the wind turbine gearbox components, such as shafts and gears, may experience.

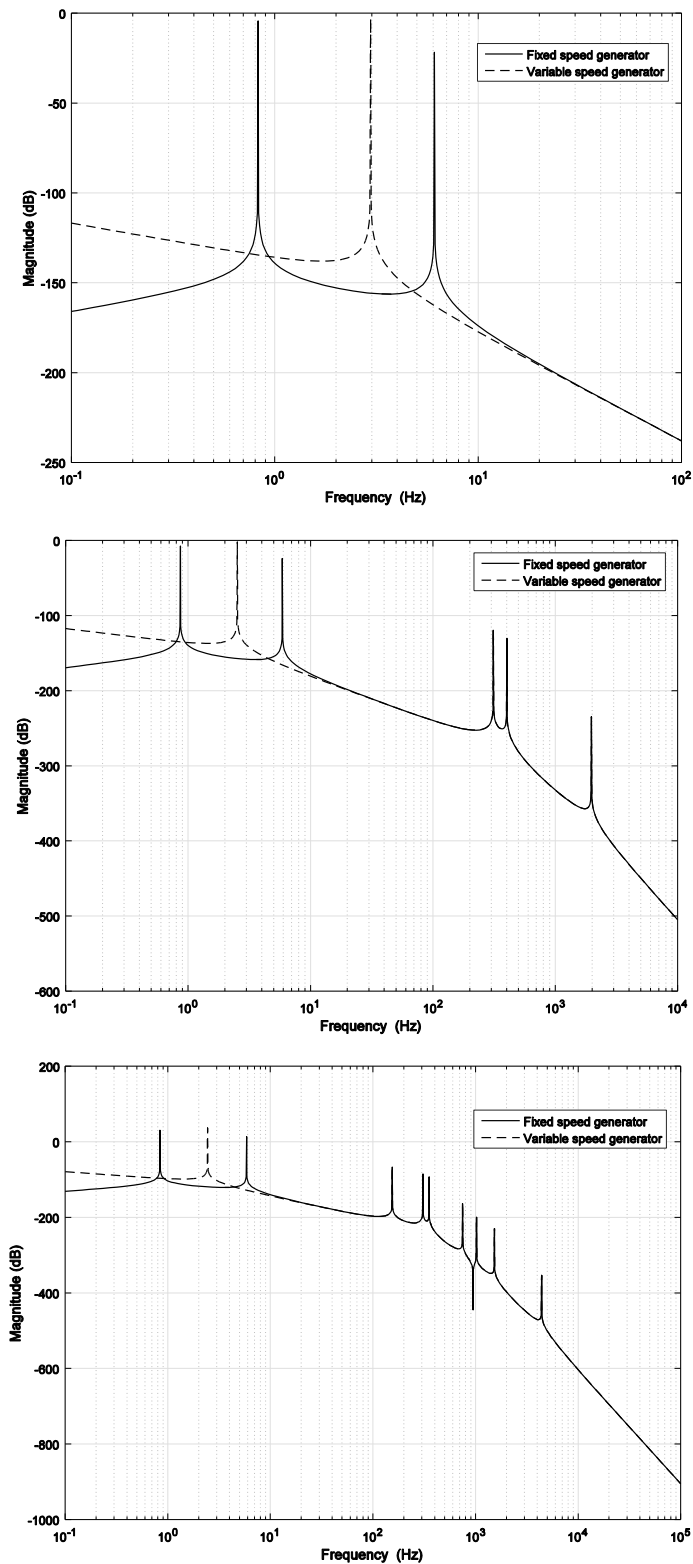


Figure 6.8: Frequency response function (FRF) of WT drivetrain with fixed and variable speed generator, 2 mass model (top), 5 mass model (middle), 11 mass model (bottom).

Figure 6.8 shows the Bode diagram for each of the three drivetrain models with fixed and variable speed generator, namely, 2-mass model, 5-mass model and 11-mass model. The latter model considers a higher DOFs and takes the gear mesh stiffness into account. This contributes across a wider frequency region and influences higher frequency amplitude characteristics. The fixed speed generator (i.e. generator connected), which is modelled here with a torsional electrical spring, influences the low order natural frequencies, the 1st and 2nd frequency, and reduces their values from 0.864, 5.888 Hz to 0, 2.524 Hz respectively. It has been concluded that the variable speed generator model (i.e. generator disconnected) has no effect on the highest order frequencies. For the fixed speed generator model, the first three modes for all models with various DOFs represent the frequencies of the LSS, generator and the HSS respectively, while the remaining modes represent the gearbox frequencies.

6.1.3 Effect of Variable Gear Mesh Stiffness on Drivetrain Dynamic Response

Based on data available in published literature, four different values which have been used for gear mesh stiffness of the planetary gear stage of the 750kW WT gearbox. These values are summarised in Table 6.3. The effects of different gear mesh stiffness values on the dynamic responses of the WT drivetrain are compared.

Table 6.3: Different mesh stiffness values used for planetary stage of 750kW WT gearbox

| Source | Mesh stiffness value | | Units |
|--------------------|----------------------|-----------------------|--------------------|
| | Planet-Sun | Planet- Ring | |
| Guo et al., 2012 | 16.9×10^9 | 19.2×10^9 | N/m |
| Link et al., 2013 | - | 4.35×10^{12} | Nm/rad |
| Hong et al., 2014 | 5×10^8 | - | N/m |
| Bruce et al., 2015 | 13.1×10^9 | 13.1×10^9 | N/m ² * |

*per unit face width

Figure 6.9 shows the influence of different gear mesh stiffness values (given in Table 6.3) on eigenfrequencies, using the 11-mass MATLAB/Simulink model with the fixed speed generator. Increasing the gear mesh stiffness value results in a wider frequency range and increases the frequencies of the gearbox components but has no impact on the lowest natural frequencies of the

drivetrain components, i.e. the LSS, the generator and the HSS. A higher gear mesh stiffness appears to transmit more severe loads to the WTG. This phenomenon is a result of shift-up in the WTG eigenfrequency due to the higher gear mesh stiffness and vice versa.

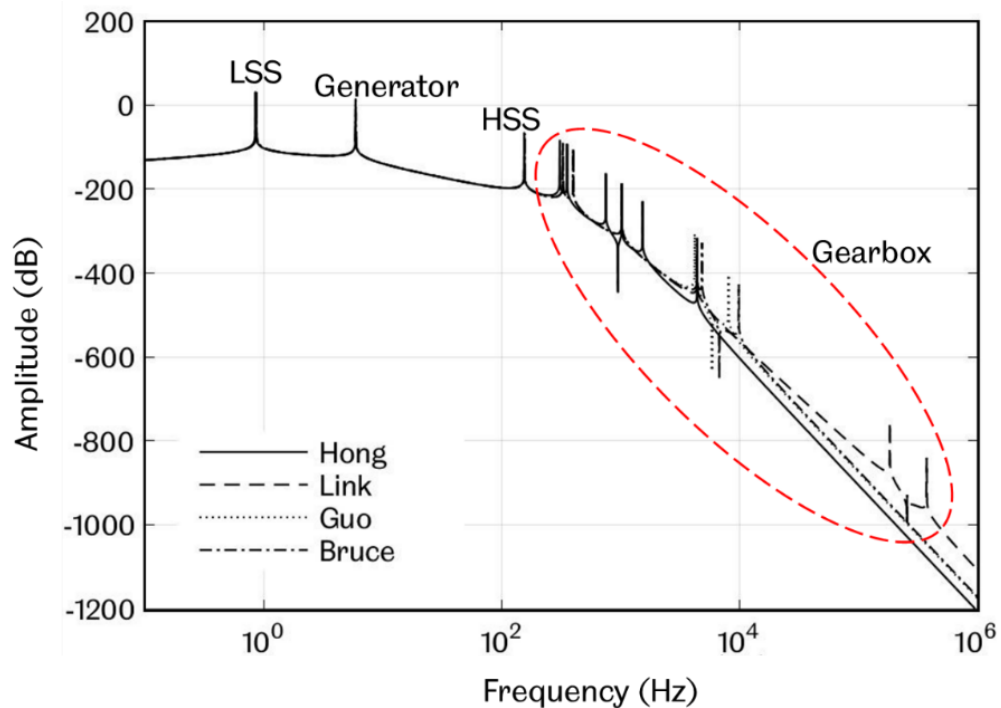


Figure 6.9: FRF of the drivetrain using fixed speed generator model and fixed gear mesh stiffness values

6.1.4 Frequency Excitation During Normal Operation and Shutdown

Numerical analysis of the torque load calculated from the MATLAB/Simulink models of the drivetrain is performed by using Fast Fourier Transform (FFT). Figure 6.10 and Figure 6.11 illustrated the simulation results in time domain and the FFT analysis in frequency domain of the HSS torque during normal operation and shutdown, respectively. In normal operation, the frequency spectrum shows the dominant frequency is 0.84 Hz which is close to the estimated natural frequency of the LSS and thus may cause system resonance and load amplification. During shutdown the most dominant frequency is 2.61 Hz, which is very close to the estimated natural frequency of the generator (i.e. 2.44 Hz) and may also contribute to resonance of the drivetrain system. The

results give the FRF calculations for the WT drivetrain with fixed and variable speed generator for 2, 5 and 11 mass models with the corresponding mode shapes. The results also show the influence of variable gear mesh stiffness on eigenfrequencies. Therefore, these results can show how the WT drivetrain behaves dynamically with different level of complexity and how that could influence the eigenfrequencies of the WT gearbox. The different levels of modelling can help gearbox designers to improve the design and assess the dynamic behaviour of a chosen design under specific dynamic loads.

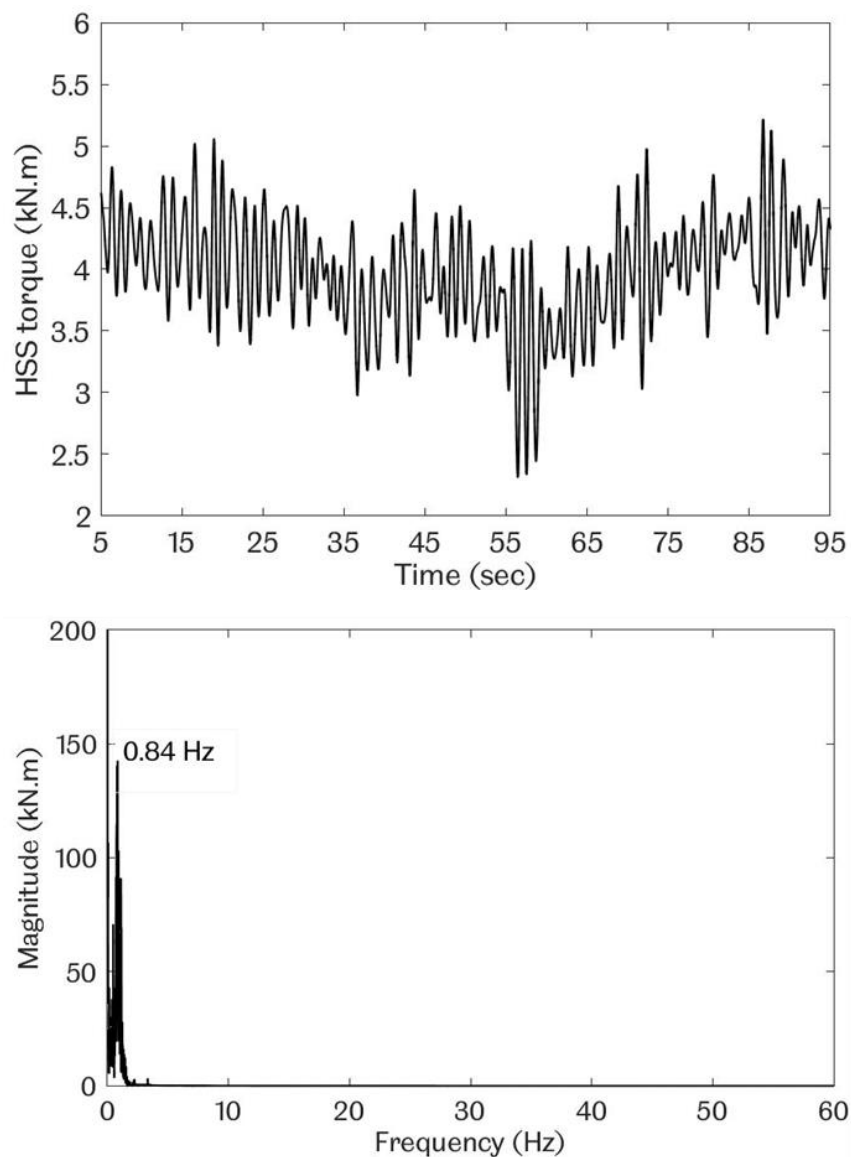


Figure 6.10: HSS torque for 750kW WT during normal operation, time history (top) and FFT analysis (bottom)

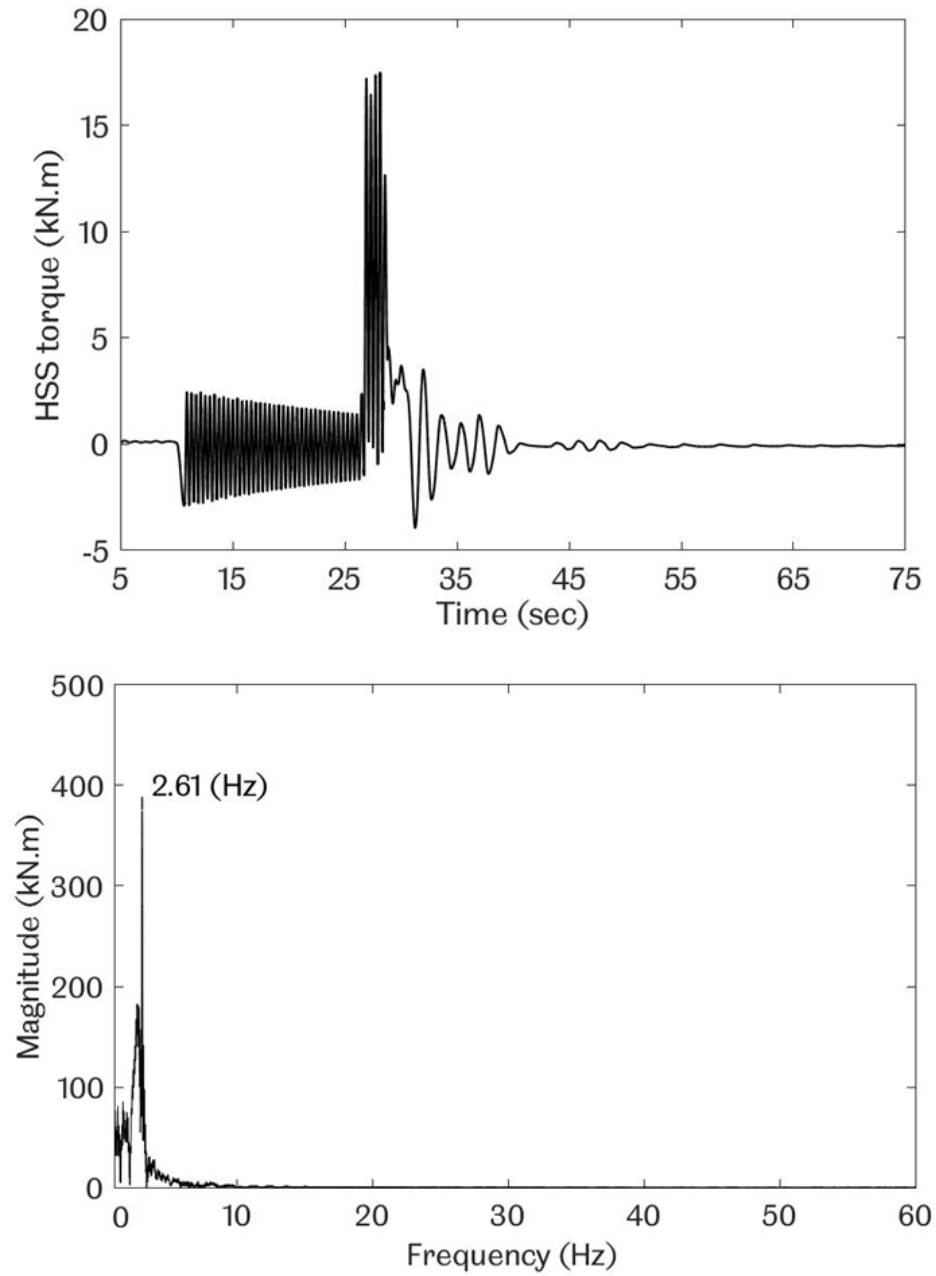


Figure 6.11: HSS torque for 750kW WT during shutdown, time history (top) and FFT analysis (bottom)

6.2 Models of 2MW and 3MW WT Drivetrains with Three Different Gearbox Configurations

The development of WT drivetrain dynamic models can be beneficial in understanding the loading behaviour and predicating the response of WT drivetrain components under transient loading conditions. This section investigates the dynamic response of three different gearbox configurations of the WT drivetrain, Drivetrains A, B and C, which are designed by using CAD software as discussed in Chapter 4 (see Figure 4.2). The gearbox design parameters are presented in Chapter 4 (see Table 4.3). The complete drivetrains are modelled by MATLAB/Simulink. The WT drivetrains with the three different gearbox configurations are simulated under normal operation and shutdown respectively to evaluate the dynamic response of the system under transient events. A comparison of system dynamic behaviour is made for different gearbox configurations to understand their potential for load reduction on key components of WT gearbox. The MATLAB/Simulink model is used for simulating Drivetrain-C during normal operation and shutdown conditions, using the field measured torque spectrums from a 2MW WT which has the same drivetrain and gearbox configuration as that of Drivetrain-C. The comparison between simulated and field measured HSS torque histories during normal operation and shutdown conditions for Drivetrain-C shown in Figure 6.12, validating the MATLAB/Simulink system dynamic model developed.

6.2.1 Wind Turbine Drivetrains Resonance Caused by Gear Mesh Excitation

This section presents the results of the responses of three different WT drivetrain configurations under free vibration, normal operation and shutdown conditions. The natural frequencies and the vibration modes of gearboxes of Drivetrains-A, B and C are presented in Table 6.4. Figure 6.13 illustrates the tendency of the gearbox natural frequency with the gearbox mode for Drivetrains-A and B and Drivetrains-B and C respectively. The results show that either increasing the number of gearbox stage or the drivetrain rated power results in reduction of the natural frequencies.

Avoiding resonance is a key part of WT drivetrain design due to the severe consequences it could bring to the drivetrain system. When the WT drivetrain

is excited under the transient conditions it is important to establish whether the system is vibrating close to the natural frequencies. Resonance phenomena can occur when the exciting frequency of the system corresponds to the natural frequencies. This can have a significant impact on the WT drivetrain, causing premature failure of some components and is therefore an important consideration in system dynamic studies.

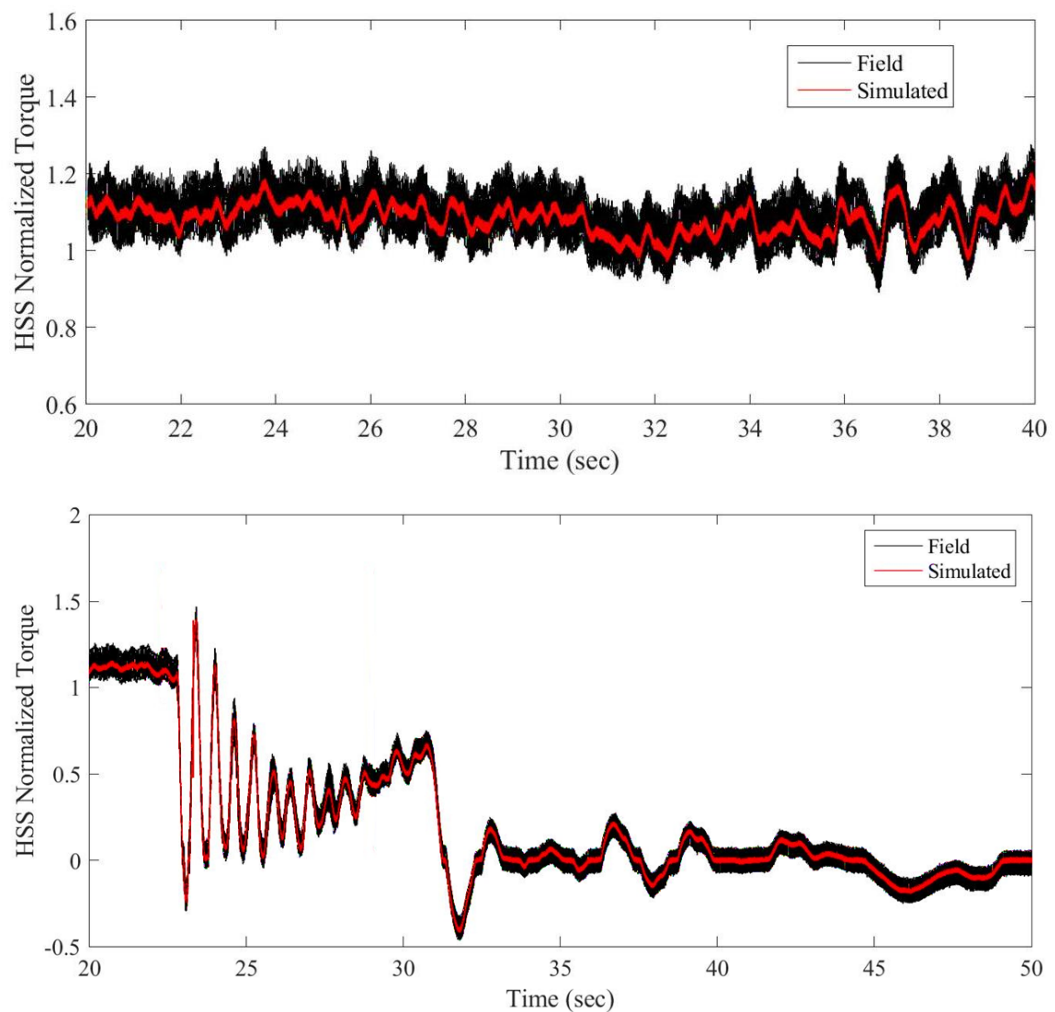


Figure 6.12: Comparison of simulated and field measured HSS torque histories of Drivetrain-C during normal operation (top) and shutdown (bottom) conditions

Table 6.4: Natural frequencies of three WT drivetrain configurations

| Mode | Drivetrain frequency (Hz) | | | Description | |
|------|---------------------------|---------|------|-----------------------|--------------|
| | A | B | C | | |
| 1 | 0 | 0 | 0 | Generator static mode | |
| 2 | 9.049 | 4.54 | 2.37 | LSS mode | |
| 3 | 111.9 | 58.21 | 213 | HSS mode | |
| 4 | 352.8 | 190.74 | 257 | 1 st | Gearbox mode |
| 5 | 766.2 | 308.70 | 431 | 2 nd | |
| 6 | 1086 | 538.61 | 834 | 3 rd | |
| 7 | 2246 | 666.46 | 1720 | 4 th | |
| 8 | 3902 | 1597.35 | 2110 | 5 th | |
| 9 | - | 2552.25 | 3750 | 6 th | |
| 10 | - | 2733.50 | - | 7 th | |

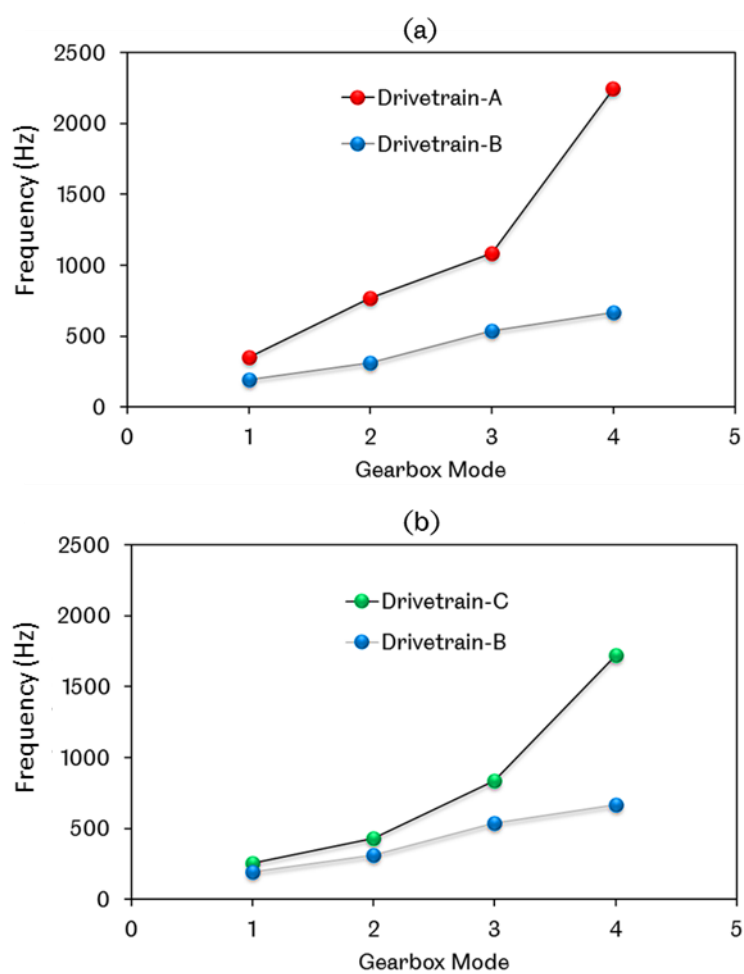
**Figure 6.13: Gearboxes natural frequency comparison (a) Drivetrain-A and B (b) Drivetrain-B and C**

Figure 6.14 shows the Campbell diagrams for the gearboxes of Drivetrain-A, B and C respectively. Drivetrain resonance may occur when the diagonal lines, the GMF of each stage, cross the horizontal lines, representing the gearbox natural frequencies within the zone of rotor operational speed. For the lowest gearbox ratio, Drivetrain-A with gearbox of two stage, the 1st and 2nd GMF of the 2nd stage cross the lines of the 1st and 2nd gearbox vibration mode during the low and high-speed conditions, which should be avoided. Increasing the number of gearbox stage from two to three without changing the WT rated power and, then comparing Drivetrains-A and B shows that the drivetrain system dynamic behaviour is not changed by moving away from the resonance occurrence, in contrast, making it more likely to happen. One of the options to minimise the resonance is to up-shift the range of operational speed or to down-shift the WT power from 3MW to 2MW by reducing the number of teeth of gears using Drivetrain-C, as shown in Figure 6.14(c).

Simulations of the three drivetrains under normal operation and shutdown conditions are conducted using the field measurement of torque spectrums discussed in Chapter 4 (see Figure 4.10). Figure 6.15 shows the meshing force between the sun and the planet gears in the planetary stage of WT gearbox in Drivetrain-C during normal operation and shutdown. In shutdown, the maximum meshing forces between the sun and planet gears show considerable variations than during normal operation, as shown in Figure 6.15. The meshing forces in time domain for both events have been processed by using the rainflow counting method discussed in Chapter 3 [82]. The meshing forces processed by rainflow counting method are presented in Figure 6.16. It shows the Range-Mean distribution of meshing forces between the sun and planet gears during shutdown and normal operation. When the shutdown event occurs, the mean value of the meshing force varies in a much wider band region than that observed during normal operation. The normal operation shows a narrow distribution of mean value of meshing force with a range around 88 kN while it exceeds 440 kN during shutdown. During normal operation, there is no occurrence of gear meshing force reversals. This is not the case in shutdown, with gear meshing force mean value of around 100 kN (negative), as shown in Figure 6.16.

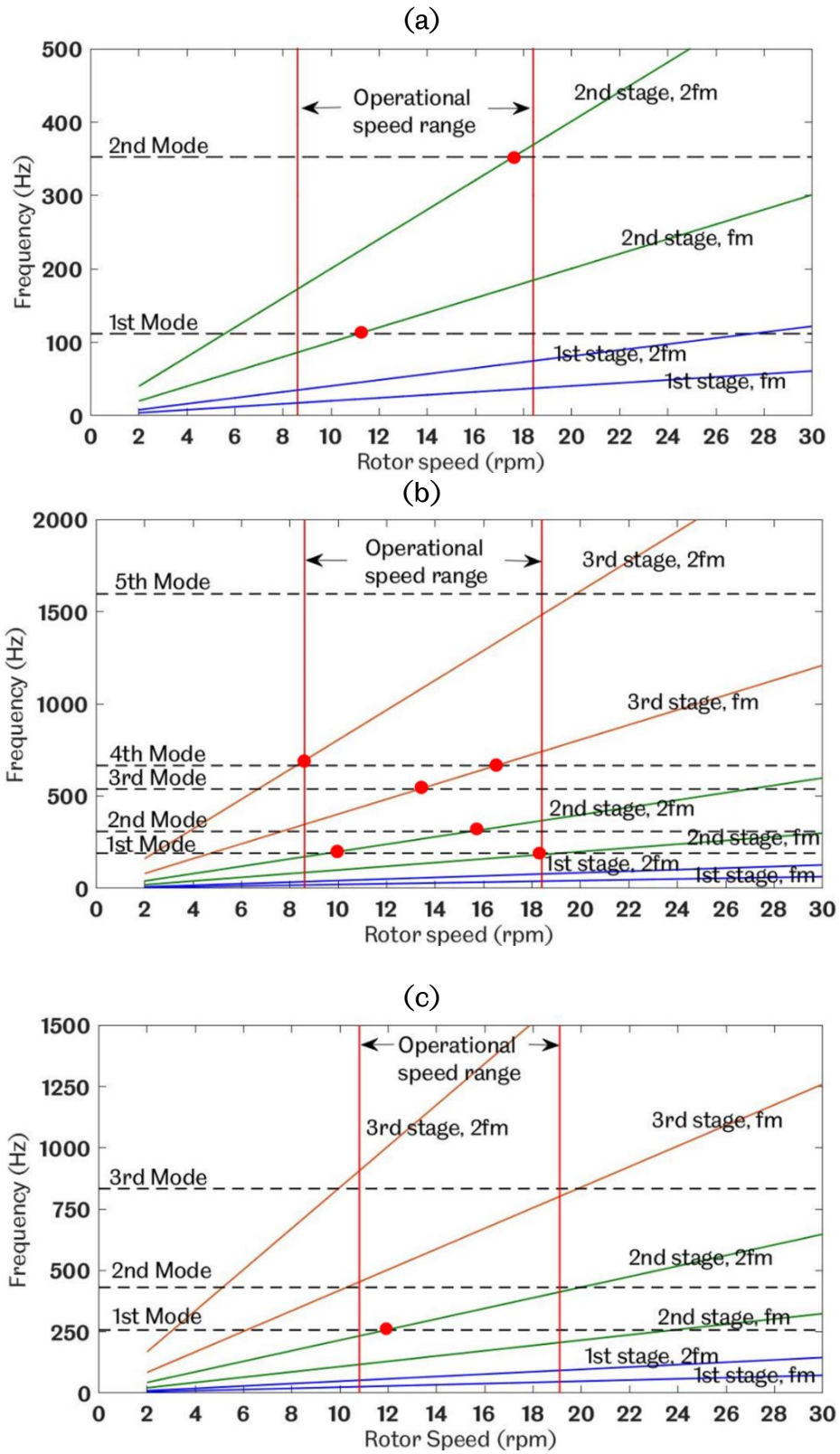


Figure 6.14: WT drivetrain Campbell diagram (a) Drivetrain-A (b) Drivetrain-B (c) Drivetrain-C

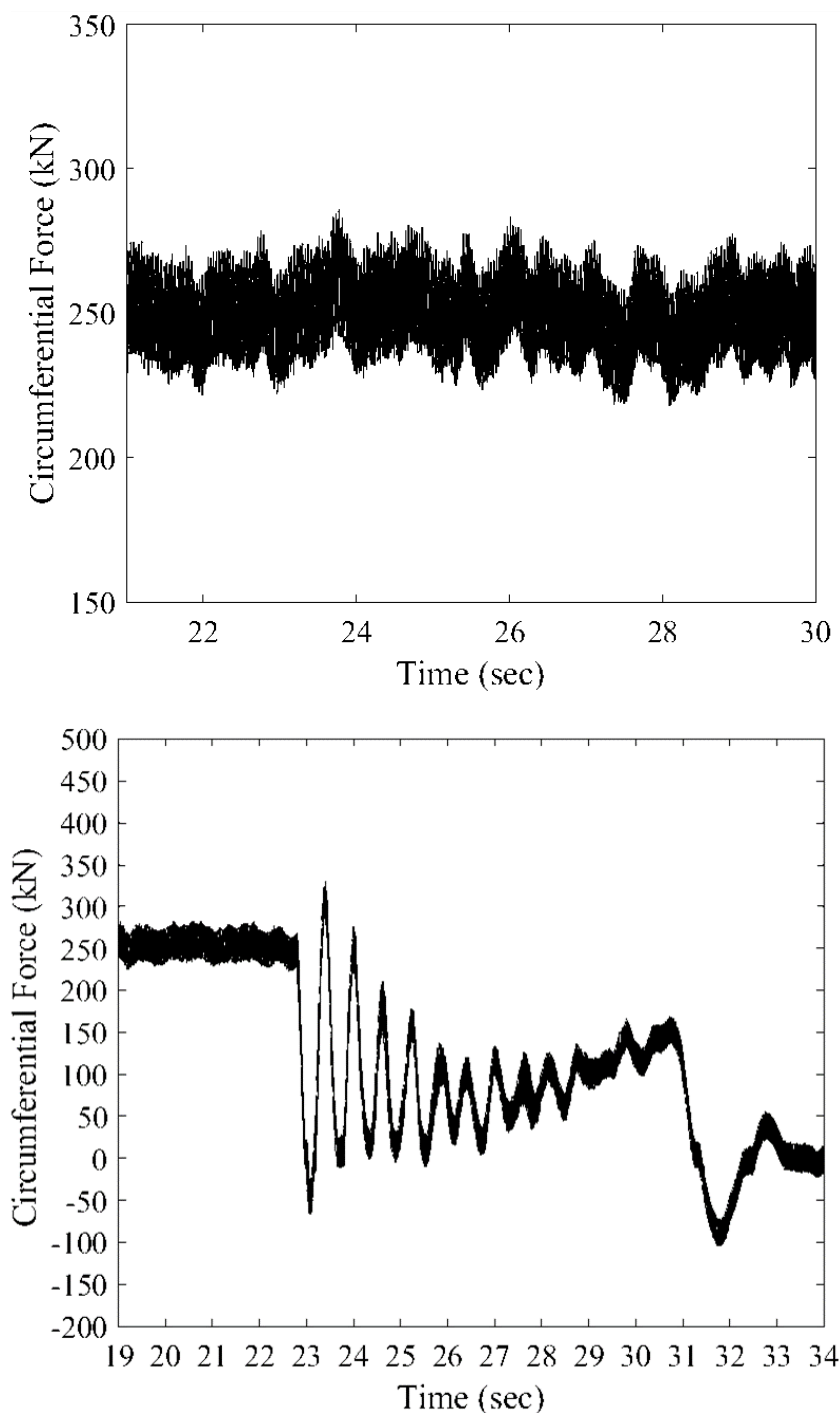


Figure 6.15: Meshing force of sun-planet over time of Drivetrain-C during normal operation (top) and shutdown (bottom)

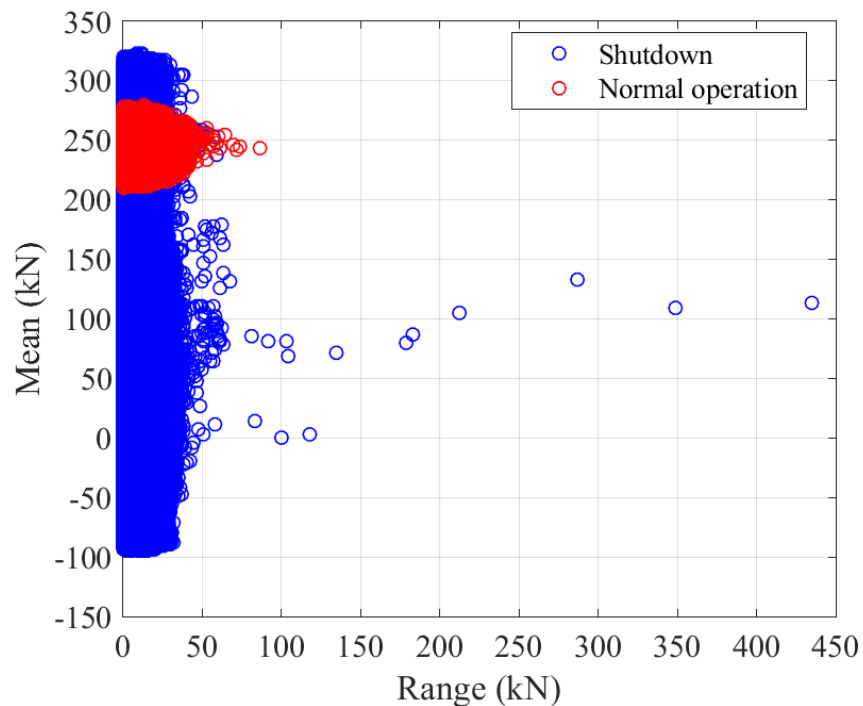


Figure 6.16: Range-Mean of meshing forces of sun-planet of Drivetrain-C during normal operation and shutdown

6.2.2 Load Distribution on Key Components During Normal Operation and Shutdown

The torque ratio, defined as the ratio of a transient torque value over the rated torque of the shaft, is used to evaluate the dynamic loading of the drivetrain. The maximum torque ratios during normal operation and shutdown for the LSS, intermediate shafts 1 and 2 (ISS1 and ISS2) and HSS are shown in Figure 6.17. For Drivetrain-B, the maximum values of shaft torque in normal operation correspond to 1.26 times the rated torque, for the LSS, ISS1 and HSS respectively as shown in Figure 6.17 (top). These values are below 1.35, the factor of safety for design loads as recommended in the WT design requirement standards [122]. These levels of torsional loads are not likely to contribute to premature failure problem, as excessive loading is not observed for the three drivetrains modelled during normal operation. During the shutdown, however, the torsional loads are at a maximum for all the shafts when the mechanical brake is being applied. This is an indication of a higher level of torsional vibrations within the system as shown in Figure 6.17 (bottom).

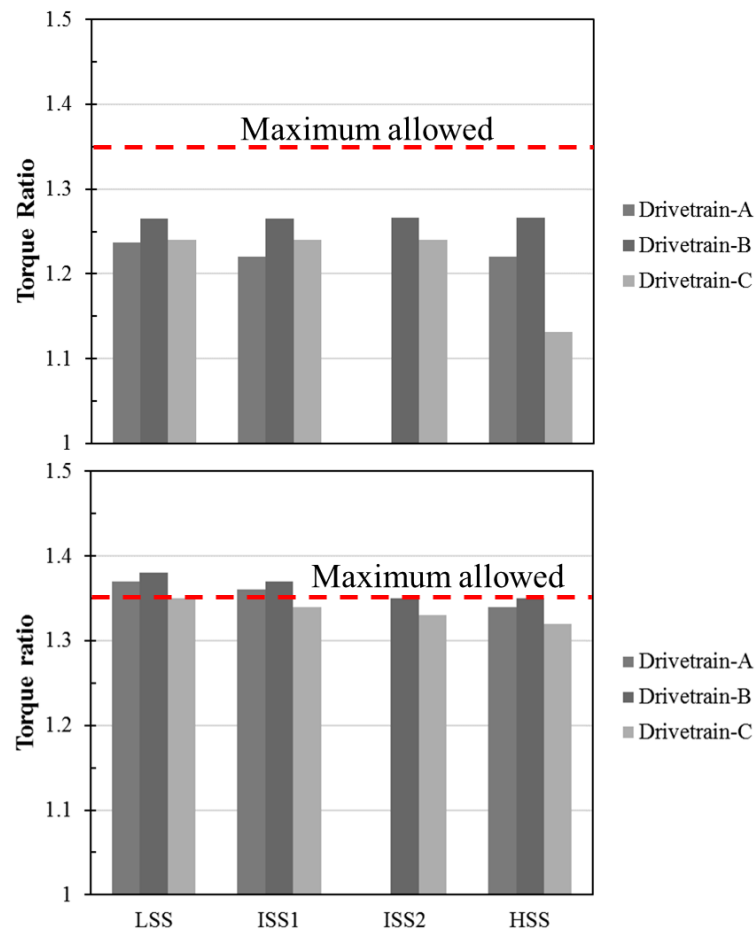


Figure 6.17: Maximum shaft torque ratios of three drivetrains during normal operation (top) and shutdown (bottom)

During shutdown, it has been found that the lowest torque ratio is 1.32 (HSS in Drivetrain-C) and the highest torque ratio is 1.38 (LSS in Drivetrain-B). For Drivetrains A and B, the torque ratios for LSS and ISS1 exceed the recommended value of 1.35 [122]. Furthermore, Figure 6.18 shows that the range of torsional loads of the gearbox shafts for the three configurations is considerably higher during shutdown; the ratio of maximum torque range for all shafts of Drivetrains A, B and C is 5 to 6.5 times higher than during normal operation. It is stated that at least 1000 shutdown procedures may occur on a WT per year [123], hence, if the ranges of torsional loads during these transient conditions are considerably higher than during normal operation, these high load conditions could cause damage to some key mechanical components. Due to the occurrence of resonance and high torsional loads during shutdown condition, this could contribute to premature failure problems in WT gearbox components.

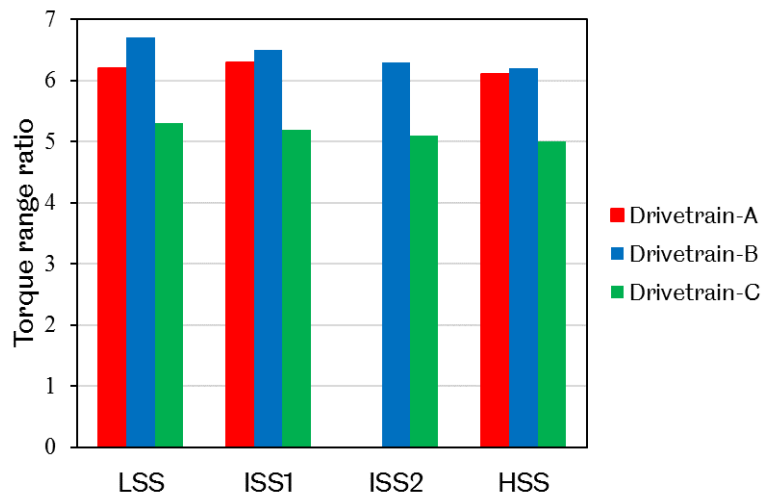


Figure 6.18: Shaft torque range ratio of three drivetrains during normal operation and shutdown

6.2.3 WT Drivetrains Dynamic Excitation During Normal Operation and Shutdown

Figure 6.19(a) shows the HSS torque transmitted in time domain for Drivetrain-A during shutdown. The Fast Fourier Transform (FFT) is computed for the torque time histories during normal operation and shutdown, for the HSS of Drivetrains-A, B and C. During normal operation, the system is not excited at high amplitudes or near its natural frequencies as there are no peak values observed. In these conditions, there is a relatively low risk of resonance occurring. Figure 6.19(b), (c) and (d) show that when the mechanical brake is engaged during shutdown, the most dominant frequencies are 9.1 Hz, 4.664 Hz and 2.503 Hz for Drivetrains-A, B and C respectively. These frequency values are very close to the calculated natural frequencies of the LSS shown in Table 6.1 (i.e. 9.049 Hz, 4.54 Hz, 2.37 Hz). They are close enough to suggest that there is high possibility for the system to be excited at its natural frequencies, possibly causing damage to key components. This may also result in resonance of the drivetrain system and loads amplification. This highlights the importance of developing dynamic models of drivetrain systems and simulating them under transient loading conditions, as the high torsional loads would not be apparent if the dynamic response were obtained exclusively under normal operation. This shows how important system dynamic modelling is as a tool in the design process, as the gearbox parameters can be modified to achieve a desirable dynamic response under transient conditions.

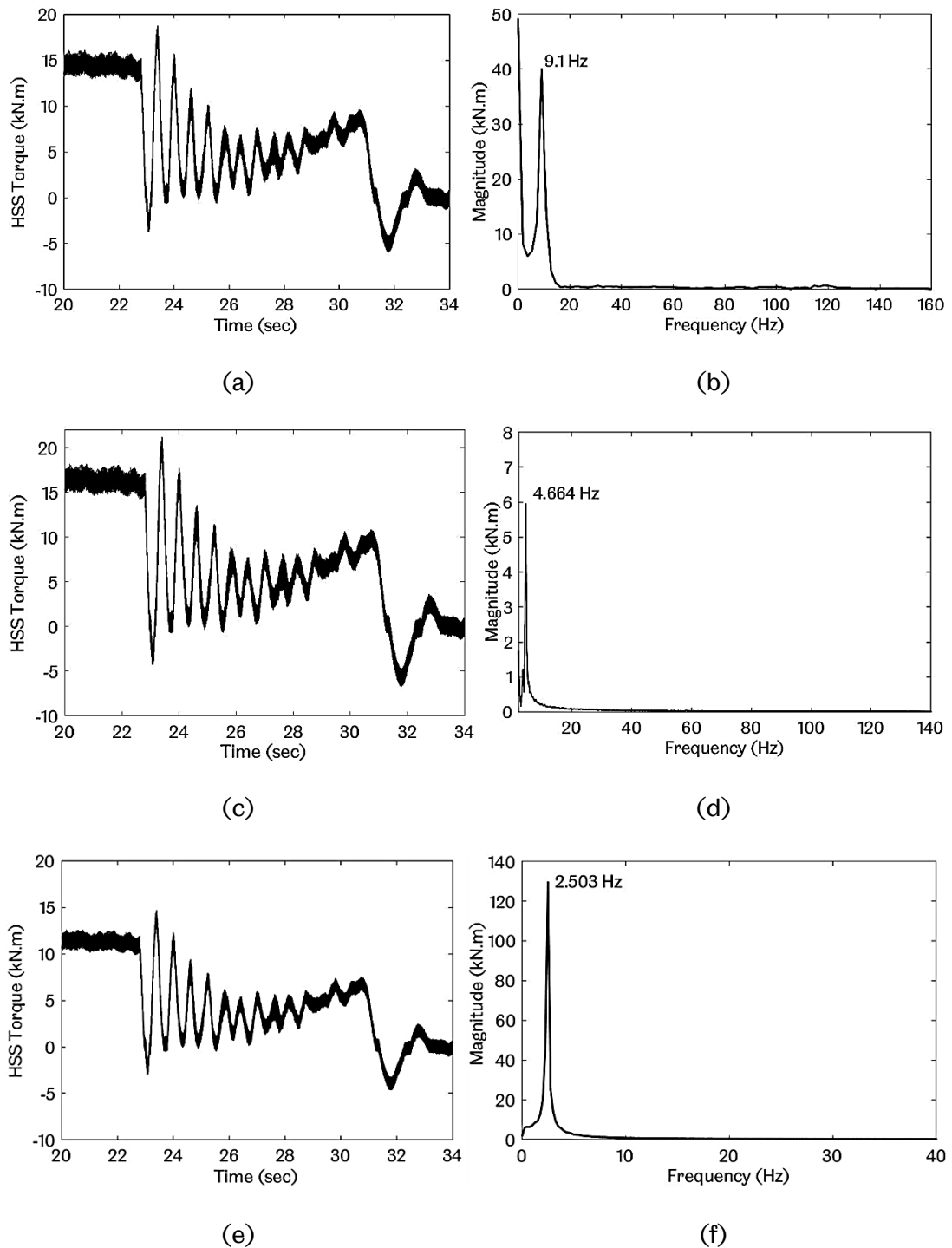


Figure 6.19: HSS torque in time and frequency domains during shutdown: (a, c and e) Torque spectrum of Drivetrain-A, B and C (b, d and f) Corresponding FFT analysis of Drivetrain -A, B and C.

6.2.4 Influence of HSS Stiffness on WT Drivetrain Natural Frequencies

The benefit of conducting a parametric study is related to the assumptions made throughout the design process in obtaining the design parameters of WT gearbox parameters and data required for dynamic modelling. These are not available when obtaining rotor torque measurement data for a real gearbox; therefore, it is important to understand how these can affect the dynamic response of the WT drivetrains. Girsang et al.[51] investigated the impact of varying the stiffness of the HSS for the 750 kW drivetrain, varying it from 10% to 1000% of its initial value. The parametric study in this study follows a similar approach; as the second non-zero natural frequency corresponds to the HSS; the parameters relating to this are adjusted. The stiffness of the HSS is chosen and varied from 10% to 1000% to investigate its influence on the torsional loads transmitted through the WT drivetrain and the natural frequencies of the system. Figure 6.20 shows the influence of different HSS stiffness values on eigenfrequencies of Drivetrain-A with fixed generator model. It is evident that the variation of the parameters does affect the steady state response of the WT drivetrain, with the HSS natural frequency shifting up or down as expected. Increasing the HSS stiffness value results in up-shift of the frequencies of the WT drivetrain and gearbox components but has no impact on the highest natural frequency, i.e. the highest gearbox mode and vice versa.

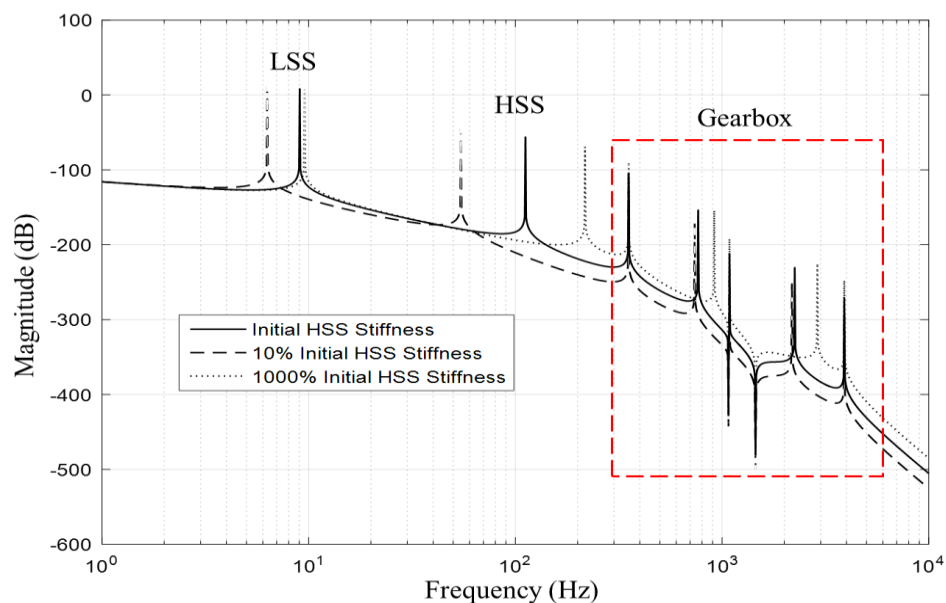


Figure 6.20: The influence of HSS stiffness on eigenfrequencies of Drivetrain-A

6.3 Summary

The system dynamic responses of NREL 750 kW WT drivetrain (Drivetrain-D) with different level of WTG complexity (i.e. 2, 5, 11-mass model) has been investigated under free and forced vibration. Then, system dynamic responses of three different drivetrain gearbox design configurations for 2MW (Drivetrain-C) and 3MW (Drivetrain-A and B) have been investigated under normal operation and shutdown conditions. The following conclusions may be drawn:

➤ **Result summary of 750kW WT drivetrain models:**

The model complexity influences the eigenfrequencies and the eigenmodes of the WTG, LSS, HSS and the generator. The 11-mass drivetrain model developed by using MATLAB/Simulink captures the torsional loading on all stages within the gearbox. FFT analysis highlights the importance of developing detailed WT drivetrain models. It has been found that increasing the gear mesh stiffness value results in a wider frequency range and raises the gearbox frequencies but has no impact on the 1st, 2nd and 3rd lowest frequencies of the WT drivetrain. Moreover, it has no influence on the two lowest and dominant frequencies of the drivetrain (i.e. 0.84 and 2.44 Hz) during normal operation and shutdown.

➤ **Result summary of 2MW and 3MW WT drivetrains models:**

Comparison between Drivetrains-A, B and C with different power (2MW and 3MW) rate and different WTG configurations (2-stage gearbox and 3-stage gearbox) shows that similar levels of torsional loads are acting on the shafts during normal operation. However, during shutdown, the drivetrains are under higher levels of torsional loads when compared to that under normal operation, increasing by 10% in LSS for Drivetrain-A and B and by 16% in HSS for Drivetrain-C. During shutdown condition, the drivetrain system may be excited close to a natural frequency of the system, possibly causing system resonant oscillations. The modelling results show that larger drivetrain configurations result in a reduction of system natural frequencies. Drivetrain-B shows the lowest levels of gearbox modes however it may have the highest probability of resonance occurrence, while Drivetrain-C shows a better dynamic response regarding resonance occurrences within the operation

speed range and smaller torque ranges during shutdown, when compared with that of Drivetrains A and B. During shutdown, the variation range of the meshing force between the planet and sun gears of all drivetrains is five to six times higher than that in normal operation.

The comparison between two different loading conditions shows that the shutdown condition is one of the most critical loading conditions that the WT gearbox components may experience which may contribute to premature failures. The connection or disconnection of the generator with the WT drivetrain affect the natural frequency of the WT drivetrain system and change the system from free-fixed to free-free system. A lower stiffness for HSS appears to transmit more severe loads to the WT gearbox. This phenomenon is a result of reduction in the second drivetrain eigenfrequency due to the lower stiffness and vice versa. This is very important, and the WT gearbox designer should consider this when designing the shafts within the WTG. A negative trend of natural frequencies is observed toward the larger WT drivetrains. Many possible resonances due to internal excitations are found in Campbell diagrams; they either should be avoided by design change or verified by more detailed analysis and back to back test.

7

RESULTS AND DISCUSSION OF RIGID AND DISCRETE FLEXIBLE MULTIBODY DYNAMIC MODELLING OF WIND TURBINE DRIVETRAINS

This Chapter investigates the dynamic response of the wind turbine gearbox (WTG) under normal operation and shutdown. The multibody system (MBS) dynamic models developed by using SIMPACK MBS software are discussed in Chapter 5. These models include the WTG's critical components, the gears and bearings with each component being modelled by 6 degrees of freedom (DOF). Field measurement torque spectrums measured under two operational conditions, normal operation and shutdown, are used as an input to the models to investigate dynamic responses of these critical components.

This Chapter is divided into three main sections. The 1st section focuses on the validation of the simulation results with test data during rated input torque and normal operation using the NREL 750kW WTG models. The 2nd section mainly investigates and compares the dynamic behaviour during two different operational condition, the normal operation and the shutdown of the 2MW WTG models.

During the normal operation and the shutdown of the 2MW WTG, the gear contact load, tilt angle of planet gears, bearing contact load, number of bearing rollers in contact with the race, maximum surface and subsurface stresses on gears and bearings contact surfaces are analysed and compared.

The final section compares cumulative fatigue damage of the WTG gears and bearings under two operational conditions, the normal operation and shutdown, within the service lifetime of the 2MW WTG.

7.1 NREL750 kW WT Drivetrain Model

7.1.1 Model Validation

The first stage of WTG MBS dynamic model validation is to compare the radial load calculated by the developed SIMPACK MBS model of the UW and DW planet gear bearings in planetary gear stage with the dynamometer measured data and MBS models developed by LaCava [34]. The model is loaded at rated torque and operated under steady state condition. Figure 7.1 and Figure 7.2 show the bearing radial load variation for UW and DW bearings of planet 'A' within one rotation for planet carrier under rated input torque calculated by this study and LaCava [34]. In this study, it has been found that the developed WTG MBS models provide detailed comparison, especially for the DW bearing radial load, with that produced by MBS models developed by LaCava using different levels of model complexity and with the dynamometer test measurement data [34]. The reference locations for planet gears A, B and C and their upwind bearings radial load variation within the planet carrier rotation is shown Figure 7.3. It has been found that the highest load level of the upwind bearings occurred when each planet gear is aligned horizontally to right of the sun gear when viewed from the upwind side. As Figure 7.3 demonstrate, the highest load level for planet gears occurred when the planets gears A, B and C moves clockwise from their reference location in by 90° , 210° , and 330° respectively.

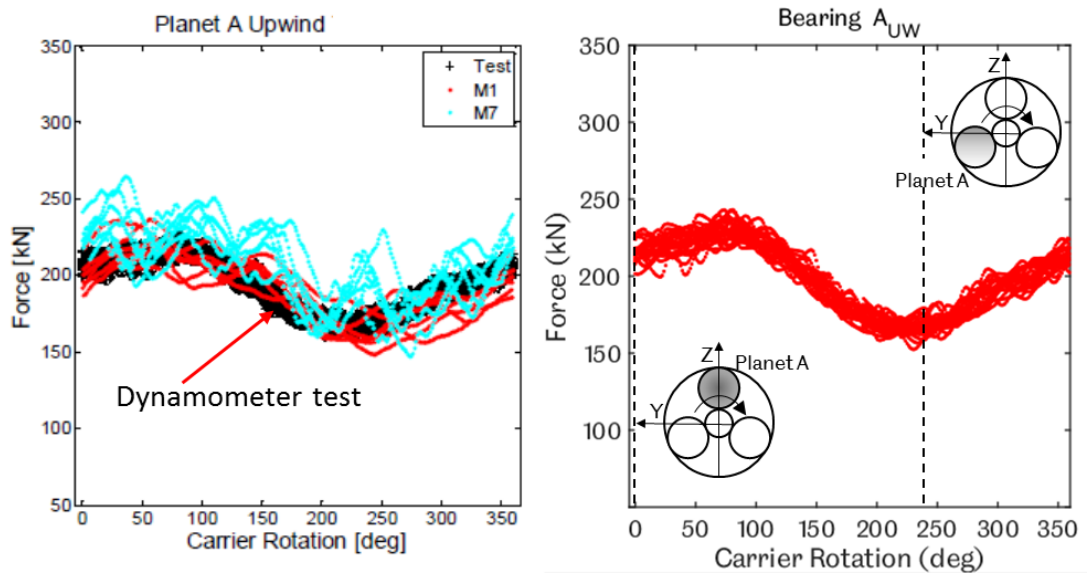


Figure 7.1 : Upwind bearing load of planet 'A' under rated input torque for 750 kW WTG during one planet carrier rotation. MBS model of this study (right) and LaCava [34] dynamometer test (in black) and their MBS models (left)

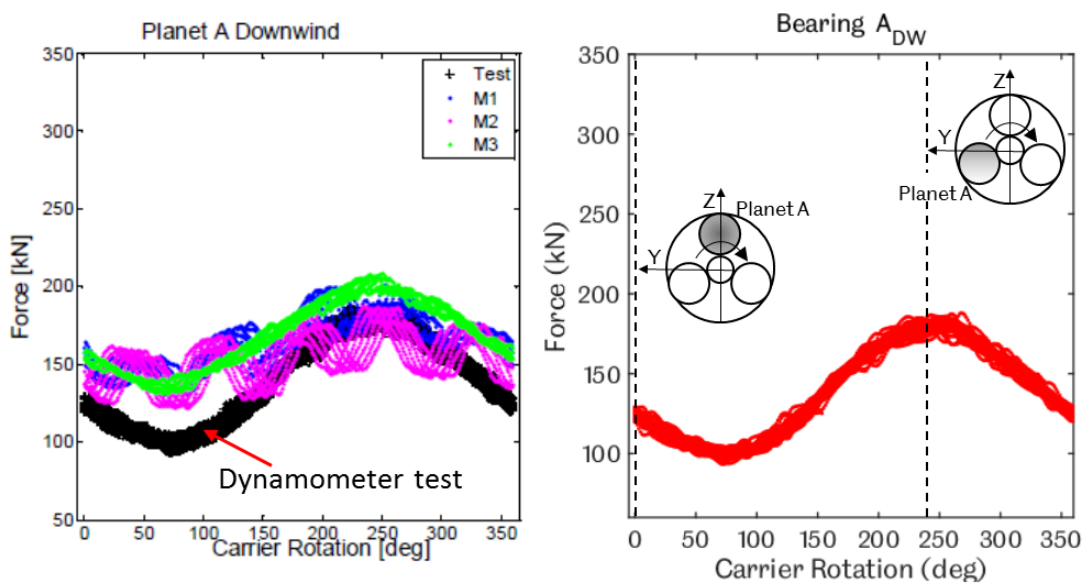


Figure 7.2: Downwind bearing load of planet 'A' under rated input torque for 750 kW WTG during one planet carrier rotation. MBS model of this study (right) and LaCava [34] dynamometer test (in black) with their MBS models (left)

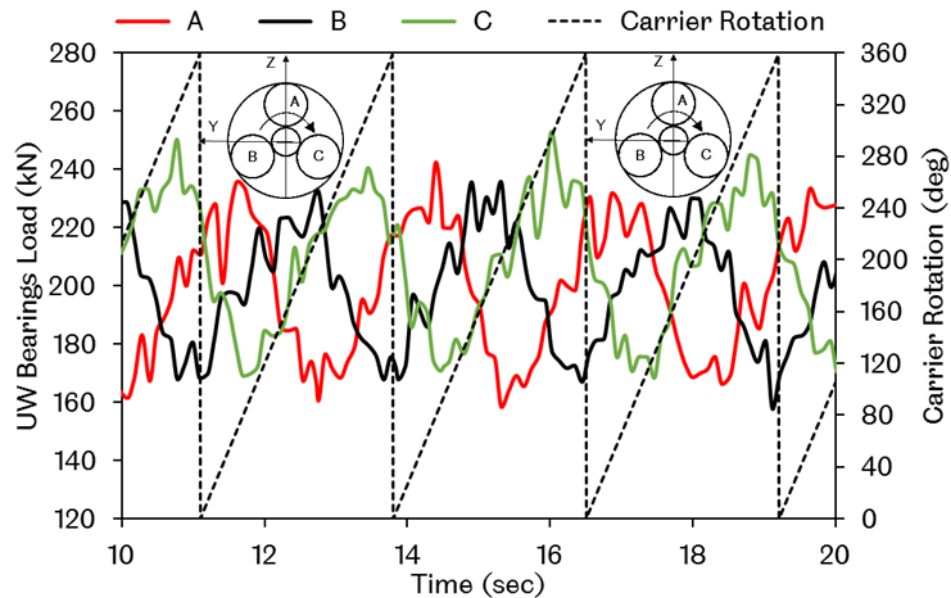


Figure 7.3: The out of phase of upwind bearings load of planets A, B and C under rated input torque for 750 kW WTG during rotation of the planet carrier.

As Figure 7.1 and Figure 7.2 demonstrate, comparison of the results of this study with results of different MBS models developed by LaCava et al. [34], denoted by M1, M2, M3 and M7, with different levels of complexity for the NREL 750kW WTG together with the dynamometer test measurement data, denoted by 'Test', for the same WTG under rated constant torque input [34]. It showed that the developed SIMPACK MBS model in this study has:

- ✓ Accurately predicted the out of phase load of planet gear bearings, i.e. the UW and the DW, caused by the effect of gravity which is considered in this study as shown in Figure 7.3.
- ✓ Accurately predicted the location of the maximum and minimum loads of the UW and the DW bearings of planet A, B and C, during the rotation of planet carrier, as shown in Figure 7.1, Figure 7.2 and Figure 7.3.

The second stage of validation for the developed SIMPACK MBS model is to compare the tooth contact stress distribution of meshing gears with that published by the NREL round robin project results [121]. The contact stress distribution between the ring and the planet gears has been calculated along the tooth face width, as shown in Figure 7.4.

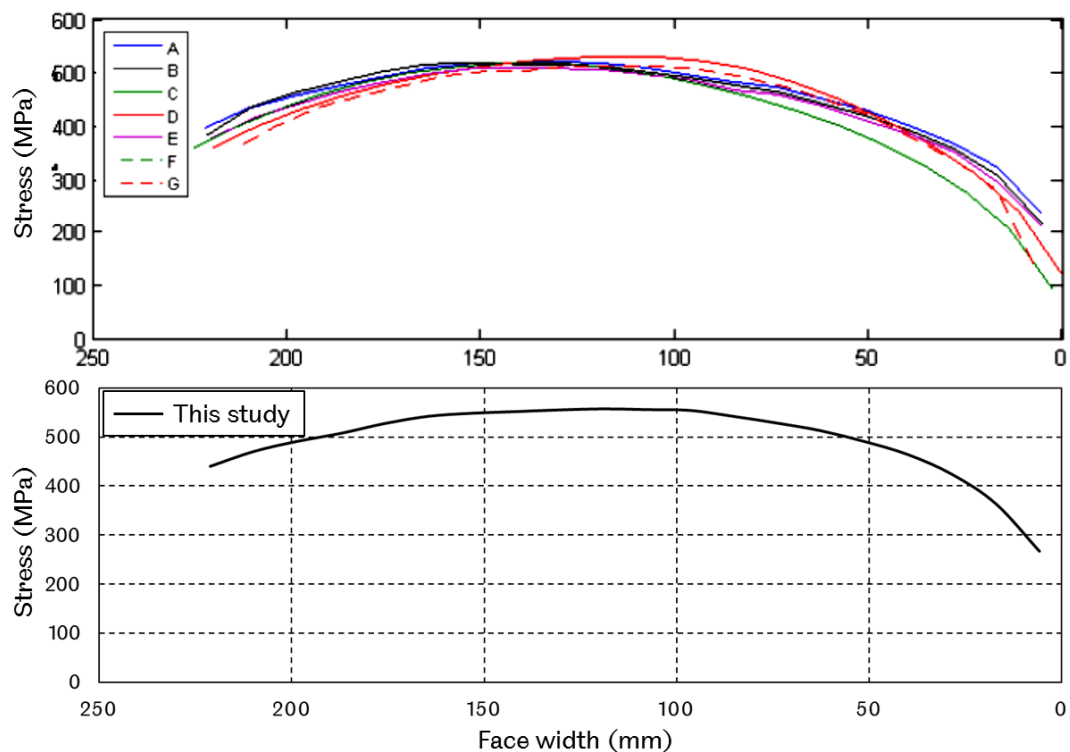


Figure 7.4: Comparison of contact stress distribution between the ring and planet gears along the face width under rated torque input. NREL 'Round Robin' project [121] (top) and this study (bottom)

As discussed in Chapter 5, the sliced model for gear contact, using a 35 slices along the tooth face width, was selected [34], and was found to be accurate. The chosen number of slices along the tooth face width influenced the accuracy of the results. It has been found that the number of slices producing valid results at a high computational time [34]. As explained in Chapter 5, a 35 slices model is recommended and therefore, has been chosen [34]. The results obtained by this study showed good agreement with the results obtained by NREL round robin project [121], as shown in Figure 7.4. The contact path of the sun gear should start at the tip of the tooth and end at the tip of the tooth of the planet gear. This validates the model's ability to produce accurate contact stress distribution, proving that the WTG ratios and the dimensions of the key component, the gears and the bearings, within the WTG have been set up correctly.

The third phase of validation the model's accuracy is shown in Figure 7.5. It includes comparing the modelling results of this study with the measured tilting angle of planet 'B' and its UW and DW bearing loads during rated torque operation obtained by Guo et al. [124]. As illustrated in Figure 7.5, the radial load of planet gear B UW bearing increases to the highest level with the decrease of the tilt angle to its lowest value. However, planet gear B DW bearing load decreases to the lowest level with the decrease of the tilt angle.

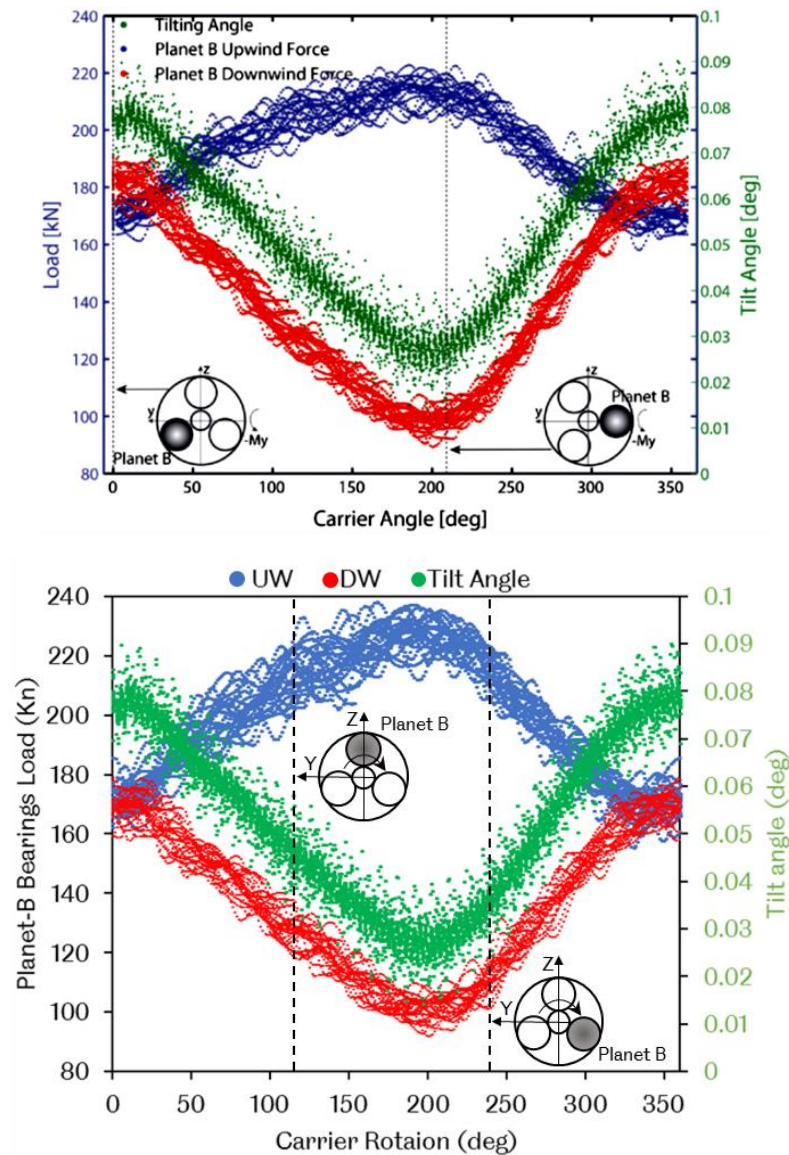


Figure 7.5: Comparison of calculated tilt angle of planet B and its bearings force for UW and DW bearings during rated input torque. This study (bottom) and measurement [124] (top)

The planet gear bearings load changed significantly when the planet gear moves upwind or downwind about its radial axis when it rotates with planet carrier. This validates the model's ability to calculate planet gears tilt angle and the unequal load sharing between the planetary bearings pairs. However, as shown in Figure 7.1, Figure 7.2 and Figure 7.5, it is evident that the load on UW bearing is much higher than the DW bearing which is agreed with the finding of measured test data produced by LaCava [34]. For planet 'B', the maximum UW bearing load occurs when the planetary gear tilt angle is at its lowest value and the planet gear moves within the carrier rotation to reach the position 210° . At this position, the planet gear 'B' aligned horizontally to right of the sun gear with the DW bearing has the lowest of load level. For planet 'B', the lowest difference between the load of UW and DW bearings occurs when the planet gear tilt is at its highest tilt angle.

The fourth stage of validating the model's accuracy includes comparing the measured total load sharing factor of planet gears calculated by [34] during normal operation, as shown in Figure 7.6. The results show that the developed multibody dynamic model in this study is valid, producing unbalanced load sharing between planet gear bearings pairs. It shows a good agreement with the measured one and thus, the model's ability to simulate unbalanced load sharing between the planetary bearing pairs.

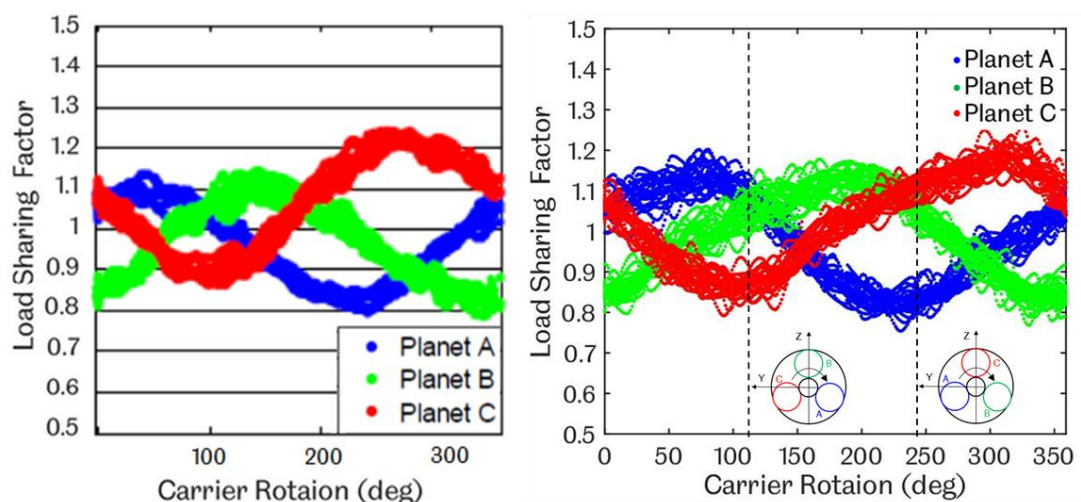


Figure 7.6: Load sharing factor of planet gears during normal operation of NREL 750kW WT. This study (right) and LaCava measurement [34] (left)

Finally, the last stage of validating the models' accuracy includes comparing the results of this study with the measured load sharing factor under varied tilt angle of the planets gears during normal operation of NREL 750kW WT obtained by LaCava [34], as shown in Figure 7.7. The load sharing factor of the planet gears increases with the increasing of the tilt angle. Moreover, the load sharing factor increases as the planet gear moves upwind about its radial axis.

The comparison showed good agreement with LaCava results [34] and emphasised the importance of the gear slicing approach consideration when modelling the gear contact to calculate the tilt angle of the planet gears during the rotation of the planet carrier because the number of slices within the gear contact model influences the mean and maximum contact load of meshing gears [34].

It should be noted that all the validation is only carried out during constant rated torque input and normal operation as there is no field measurement data available for shutdown to compare with the modelling results obtained in this study. The model validation results proved that the model could accurately simulate unequal planetary bearing loads, out of phase planet bearing loads, planet tilt angle, gear contact stress distribution along the face width. From the validation results, it can be concluded that the MBS model developed is accurately enough to model a multi-Megawatt wind turbine gearbox and that many assumptions made are acceptable.

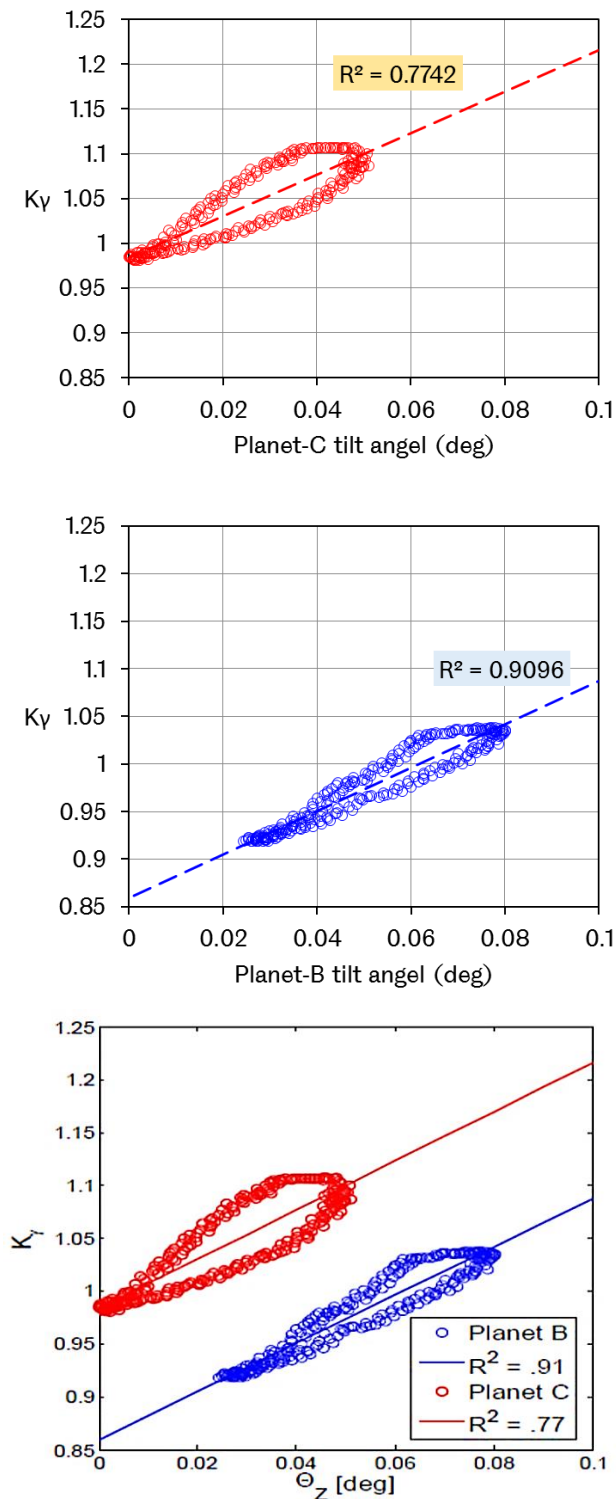


Figure 7.7: Planet B and C load sharing factor variation with planet tilt angle during normal operation of NREL 750kW WT. This study (top and middle) and test results ([34]) (bottom)

7.1.2 Cross-coupling Effect on Loads of Planetary Bearings Under Rated Torque and Normal Operation

Figure 7.8 shows the radial loads on upwind and downwind bearings within one planet carrier rotation when operating under rated torque and normal operation. The results show the loads acting on each bearing following a uniform sinusoidal curve during rated torque operation however the loads follow a nonuniform and noisy sinusoidal curve during normal operation. The frequency of the peaks of the bearing loads corresponds with the time taken for the planetary carrier to make one rotation. This cyclic loading variation may have implications on bearing lifetime, which will need to be investigated.

The planet gears A, B and C, aligned horizontally to the right of the sun gear when they move from their reference position in clockwise direction by 90° , 210° , and 330° respectively (see Figure 7.3). As explained before, this position represents the location of the highest loads for UW bearings. However, for the DW bearings this position shows the location of the lowest load.

The bearings model within the SIMPACK MBS model capture the load variations in planet gear bearings corresponding to the input torque to the WTG. It is evident that the mean load of the UW planet bearings is higher than that of DW bearings by 42% for planet A, 47% for planet B and 41% for planet C when the WTG is operated under the rated input torque. However, the mean load of the UW planet bearings is 60% higher during the normal operation. This shows good agreement with the test results presented by LaCava [34].

For the cylindrical roller bearings (CRB), i.e. planet gear bearings, and according to the bearing life L_{10} calculation based on Lundberg-Palmgren theory, the bearing life can be calculated by [125] :

$$L_{10} = \left(\frac{C}{P_{CRB}} \right)^{10/3} \quad 7.1$$

$$P_{CRB} = XF_r \quad 7.2$$

where C and P_{CRB} are the basic rating load and dynamic equivalent radial load, F_r is the bearing radial load, $X = 1$ for CRB which is the radial bearing factor and can be chosen according to the bearing type from [125]. According to equation 7.2, this means $P_{CRB} = F_r$ and when the UW bearing carries 60% higher load than the DW bearing that means its fatigue life is reduced by $1.6^{10/3} = 4.79$ times during normal operation only. This highlights the importance of focusing on the extreme and transient events, such as shutdown, that the wind WTG may experience during its service.

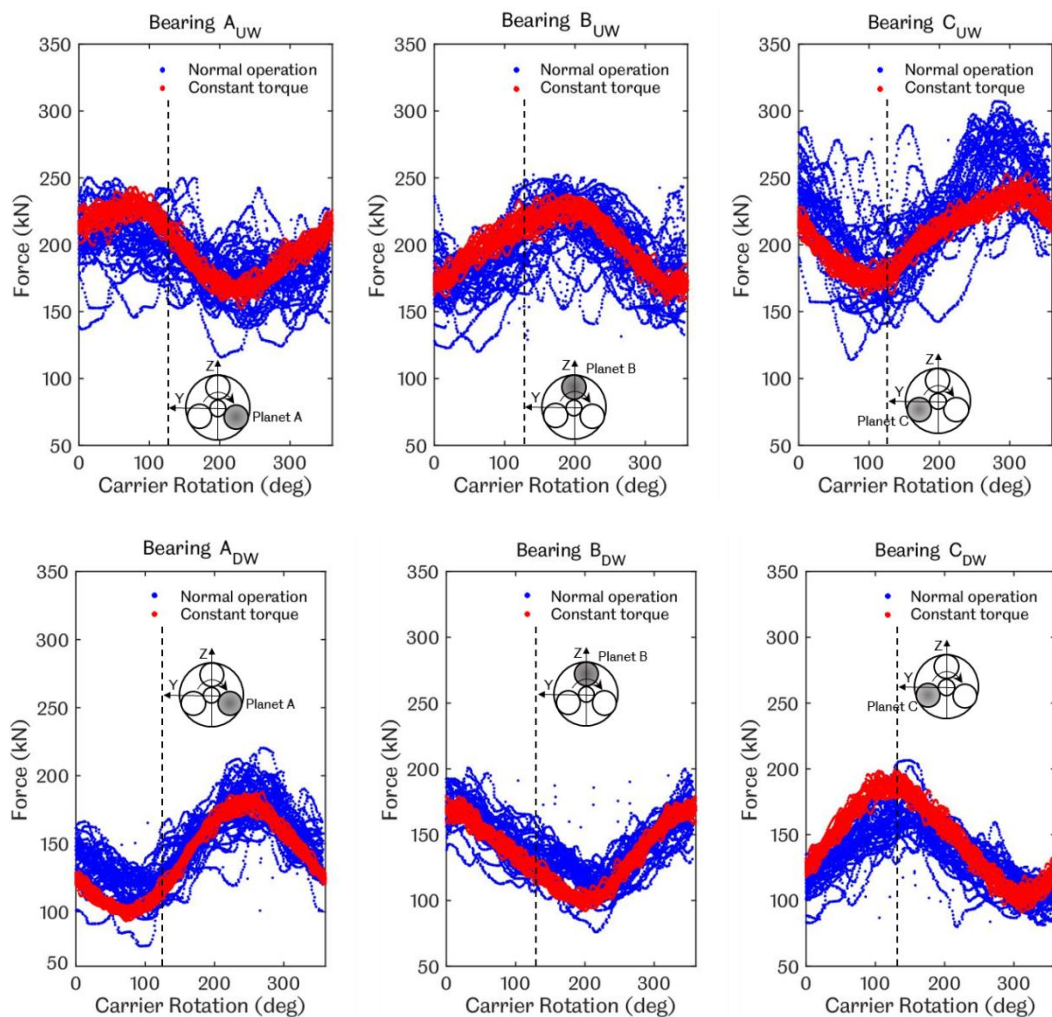


Figure 7.8: Planet bearings radial loads during rated torque and normal operation.

The load distributions of the UW and DW planet bearings along the planet carrier pin during rated input torque and normal operation are shown in Figure 7.9. The out of phase of loads of the planet gear UW and DW bearings is clear.

This is caused by the effect of gravity which is considered in this study. During the normal operation, the UW bearings carry lower load than the DW for a very short period of time within the planet carrier rotation. This is in agreement with the finding of Guo [124]. However, this is not the case when the WTG operates during the rated input torque. The explanation derives from the effect of the noisy input torque spectrum to the WTG during the normal operation together with the pitching moment, the non-torque load, which is considered in this study. This emphasises the important effect of pitching moment on load variations of the planet gear bearings. Moreover, the pitching moment influences the planet gear tilt along its radial axis which affects the radial load transfer to the planet gear bearings.

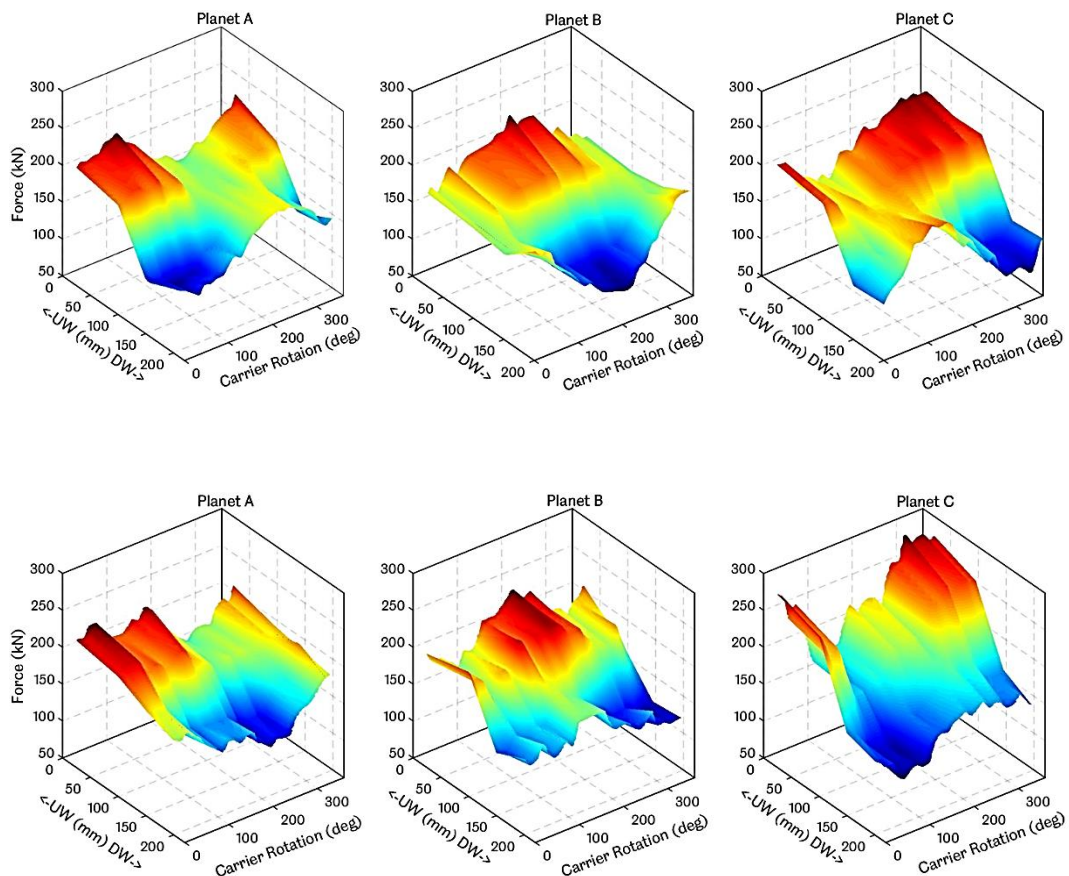


Figure 7.9: Upwind and downwind bearing load distribution within one carrier rotation during rated input torque (top) and normal operation (bottom)

Figure 7.10 illustrates the fast Fourier transformation (FFT) analysis for the upwind and downwind bearing loads during normal operation. The planet bearing load is excited with high amplitude in frequency equal to $1P$ (i.e. the 1st frequency of the WT rotor rotation) followed by lower amplitude in frequency equal to $2P$ (i.e. the 2nd frequency of the WT rotor rotation) and with lower amplitude close to the frequency of the sun-gear. This emphasises the importance of the representation of the main-shaft flexibility within the WTG MBS model's accuracy and to planet gear bearings load variation.

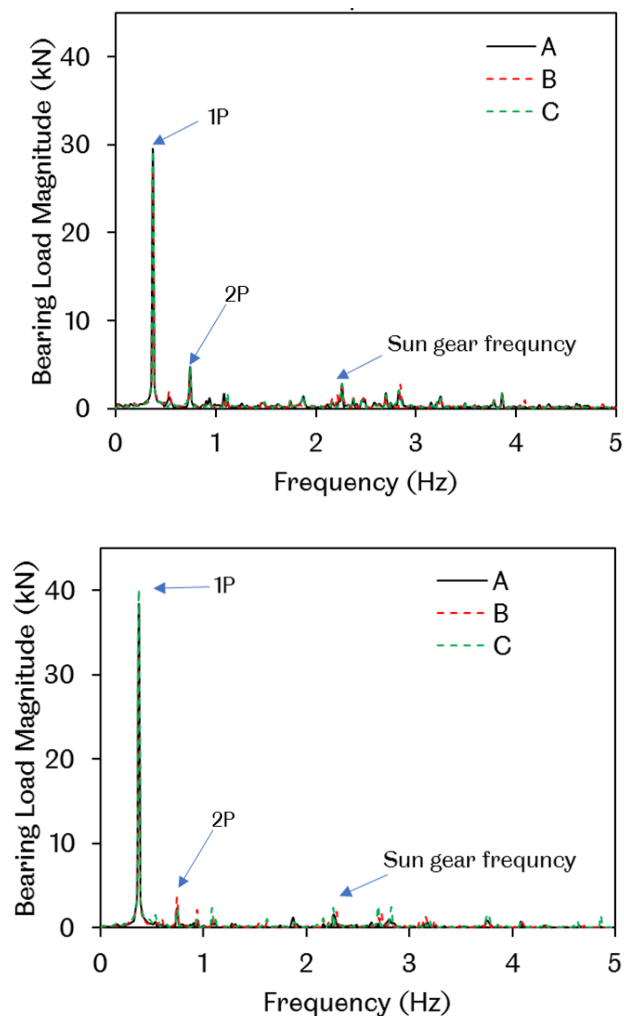


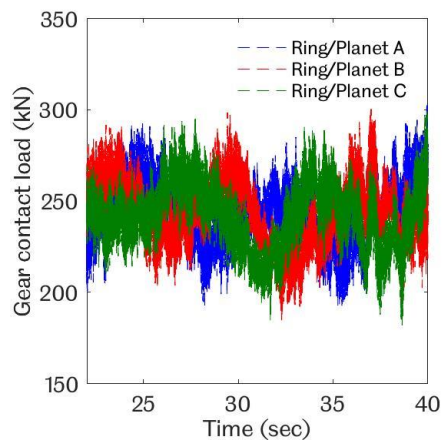
Figure 7.10: FFT analysis of planet bearings loads for UW (top) and DW (bottom) bearings during normal operation

7.2 2MW WT Drivetrain Model

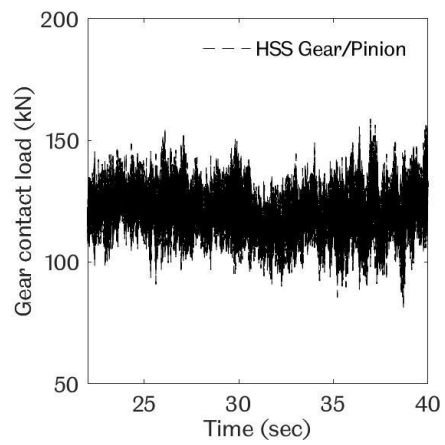
7.2.1 Load Distribution on Gears and Bearings During Normal Operation and Shutdown

Figure 7.11(a) and (b) show the simulation results of SIMPACK MBS WTG model for contact load variations of the ring and planet gears (labelled as A, B and C) and the HSS gears during normal operation. The out of phase in gear contact load between the ring gear and planet gear is caused by the effects of the gravity and the bearing clearance. The time histories of the gear contact loads were converted to frequency histograms as shown in Figure 7.11. During normal operation, the contact loads for all gears within the WTG stages show a normal distribution trend as illustrated in Figure 7.11 (c) to (f). The contact load range between the gears within the planetary gear stage is higher than that of other stages within the WTG. This is because the torque applied on the planetary gear stage is much higher than that applied on the intermediate and the high-speed stage. However, lower gear contact load dose not means lower stress range on gears and this will be discussed later.

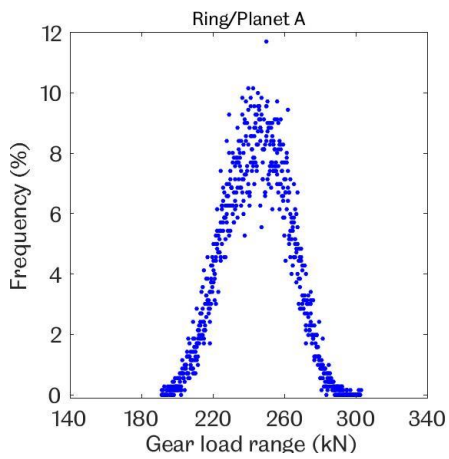
The gear contact load transfers to the WTG bearings. Figure 7.12(a) shows time histories of load variations of the downwind bearings of planet A, B and C, during normal operation. The time history of each bearing load is converted to a histogram as shown in Figure 7.12(b) to (d). The histogram summarises the percentage frequency of each bearing load range within the simulation time during normal operation. The maximum frequency of bearing load range occurs close to the mean value of bearing load while the lowest bearing frequency combines with the lowest or the highest bearing load range. The bearing loads on planet gear bearings show normal distribution similar to that on planet gears during normal operation. As expected, during normal operation, the load on upwind bearings of the planet gears is higher than that on downwind bearings as illustrated in Figure 7.13.



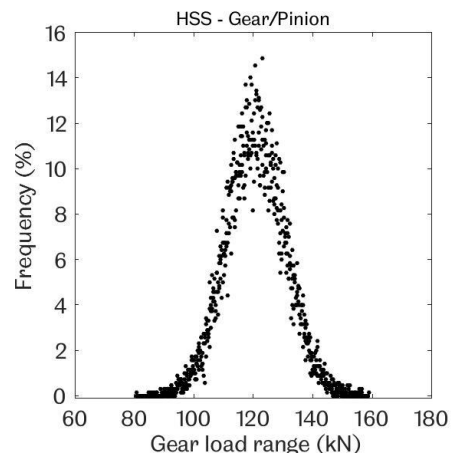
(a)



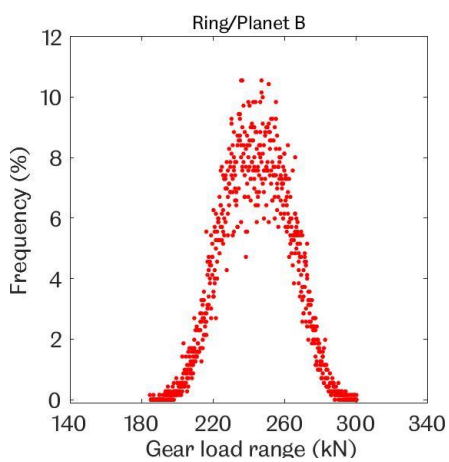
(b)



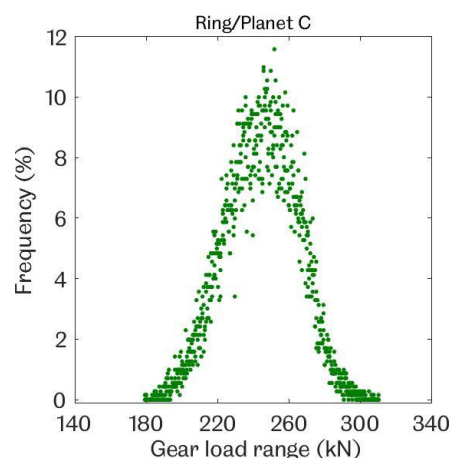
(c)



(d)



(e)



(f)

Figure 7.11: Variation of circumferential gear contact load and frequency histogram in different stages during normal operation

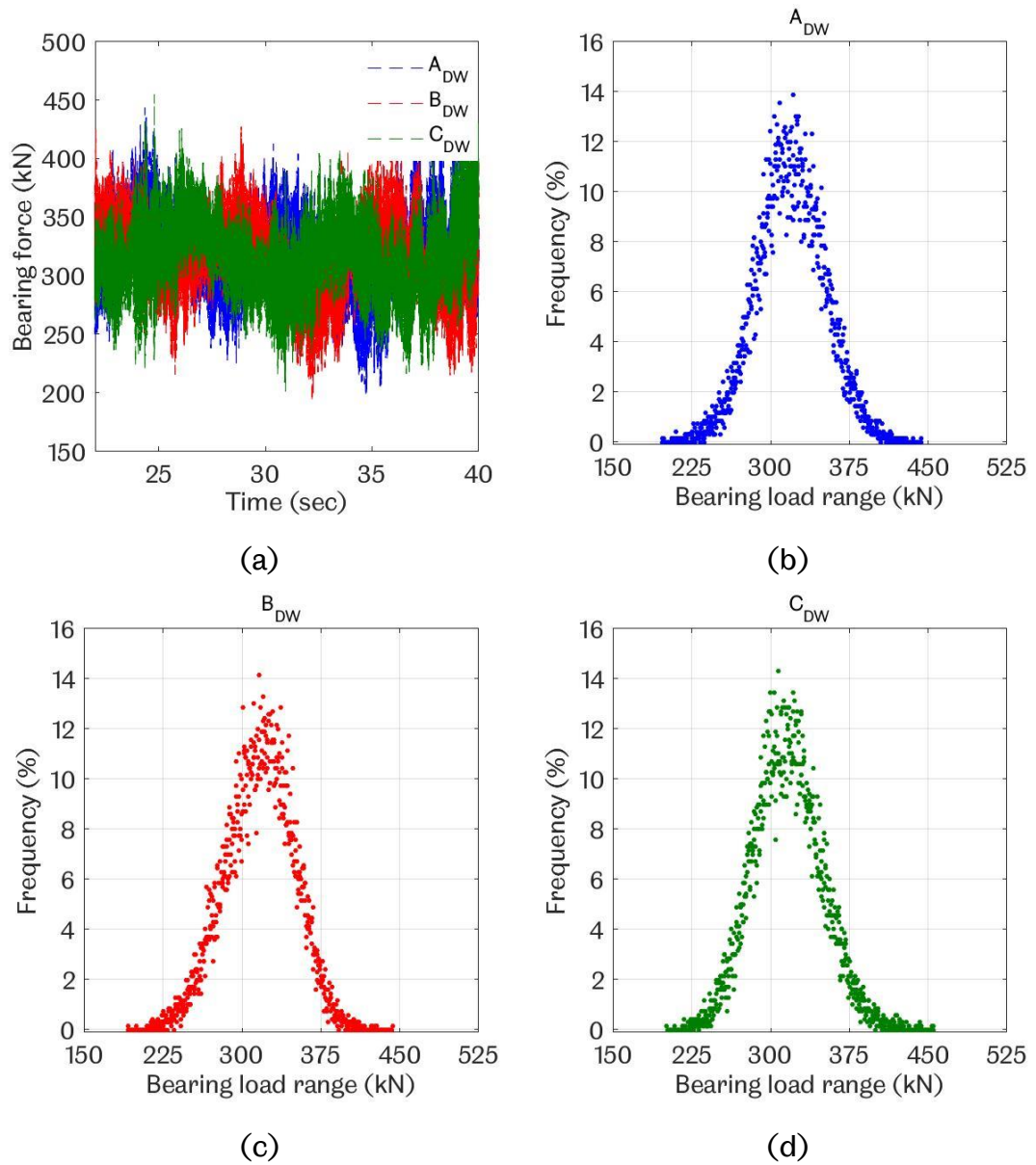


Figure 7.12: Variation of downwind bearing load and related frequency histogram during normal operation

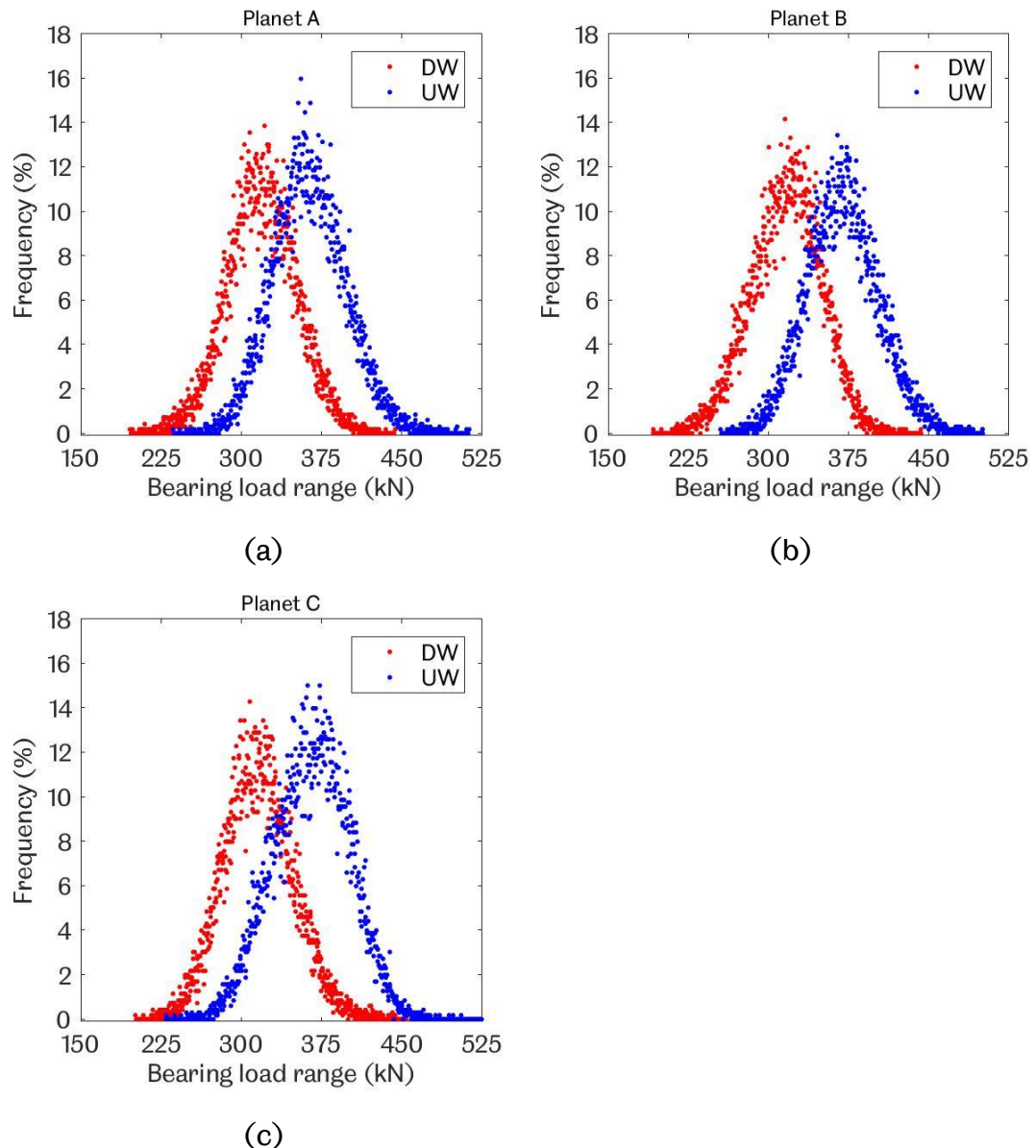


Figure 7.13: Histograms of bearing load ranges of planet gear bearings during normal operation

As shown in Figure 7.13, the distribution of the bearing load ranges for upwind and downwind planet gear bearings have different mean values and different standard deviations. Both the standard deviation and the mean value of the UW planet gear bearings load being higher than that on DW bearings. In other words, the unbalanced load sharing between the planetary bearings, the upwind and the downwind, is clear in the simulation results.

During shutdown the load levels in all gears and bearings become higher than that under normal operation, as shown in Figure 7.14 and Figure 7.16. As illustrated in Figure 7.14(b), the time history of load on gears and bearings during shutdown condition can be divided into four main regions. The 1st region labelled by the letter 'A', represents normal operation, while the 2nd region, labelled by the letter 'B', occurs when the WT drivetrain mechanical brake is engaged to reduce the WT drivetrain speed in preparing to stop. The 3rd region, labelled by the letter 'C', represents the stopping period. The 4th region, labelled by the letter 'D', represents the torque reversal occurrence and negative gear load occurrences on gears. This occurs after the mechanical brake is engaged.

The distributions of gear contact load range for different stages within the WTG are shown as histograms in Figure 7.14(c-f). Each histogram reveals the four regions as shown in Figure 7.14(b) in non-uniform distribution shapes divided into four main regions as shown in Figure 7.14(c). The 1st region, labelled as 'X1', shows normal distribution for the gear contact load range of 202 ~ 302 kN. This region represents the gear contact load range during the normal operation period (see Figure 7.11(c)). The 2nd region, labelled as 'X2', represents the highest gear contact load range occurs immediately after the mechanical brake is applied. The gear contact load range in this region is higher than that in region X1; however, it occurs with low frequency. The effect of the load in this region on gear surface damage will be discussed later in Section 7.2.4. The 3rd region, labelled as 'X3', represents the fluctuation in gear contact load range during braking and stopping periods. The final region, labelled as 'X4' includes the negative gear contact load range that occurs after the mechanical brake is engaged. However, this negative load on the gears is still lower than the load occurred immediately after the mechanical brake applied, as shown in region X2.

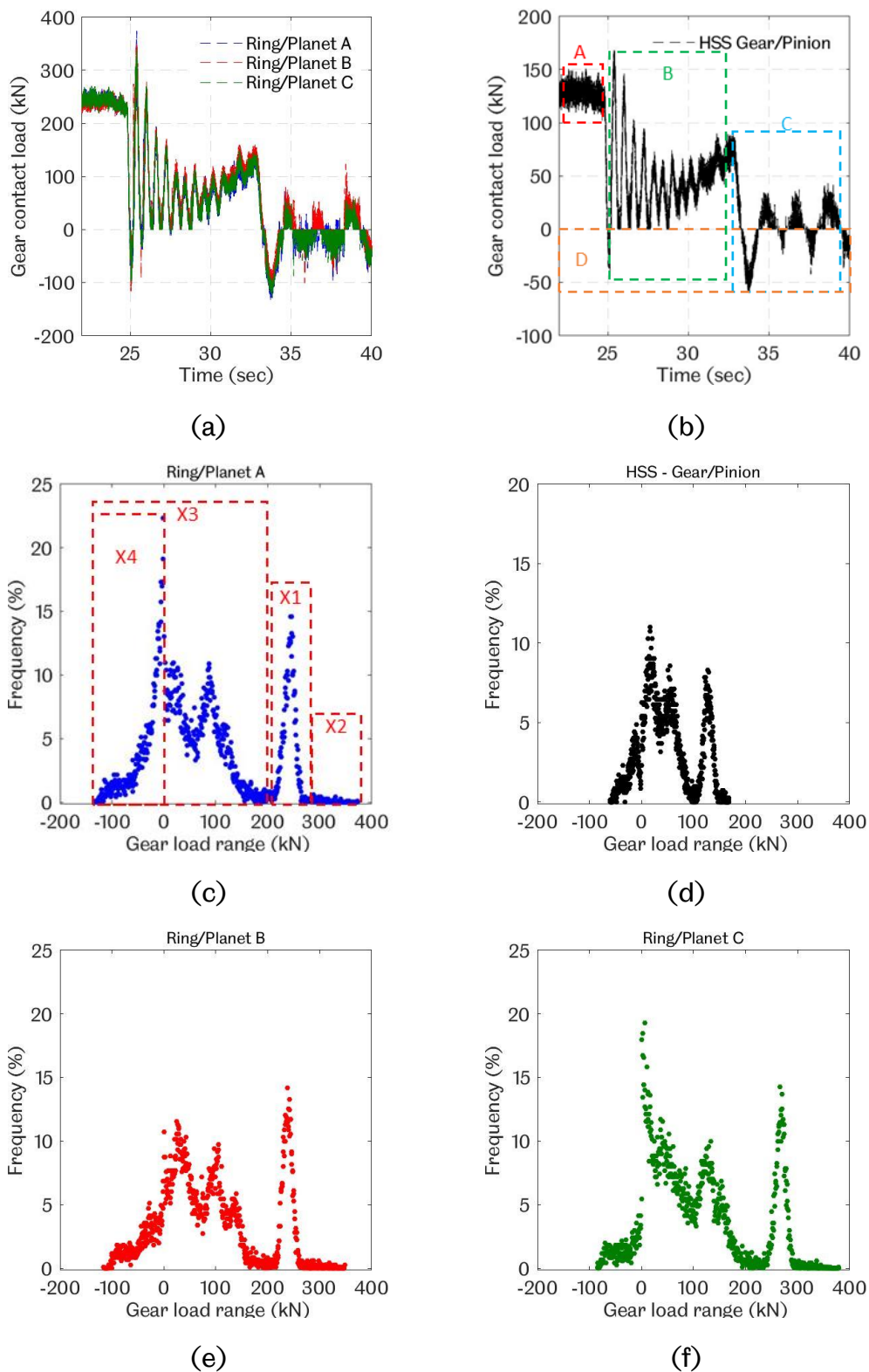


Figure 7.14: Variation of circumferential gear contact loads and related frequency histograms in different stages during shutdown

As illustrated in Figure 7.15, the comparison between the normal operation and shutdown shows that the maximum gear contact loads are higher during shutdown than that during normal operation. It is higher by 27% in contact load between ring gear and planet gear, by 12% in contact load between sun gear and planet gear, and by 31% and 37% between intermediate gears and HSS gears respectively. The effect of this increase in gear contact load on fatigue life of gears will be analysed and discussed later in Section 7.2.4.

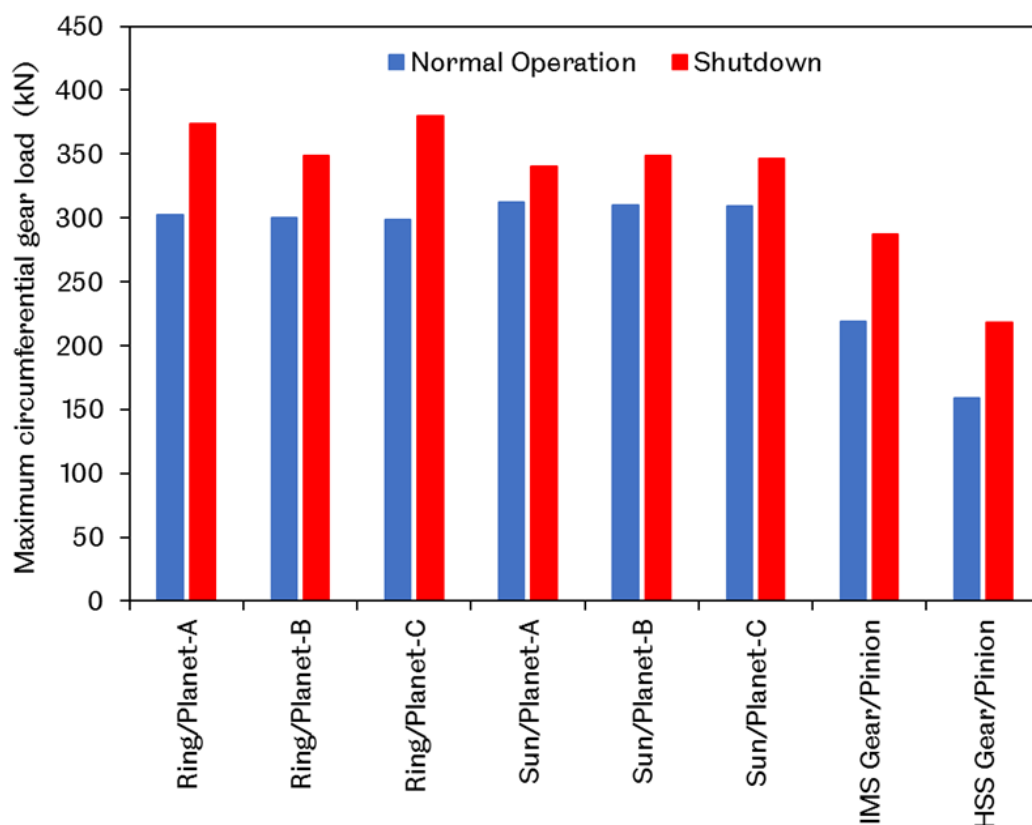


Figure 7.15: Comparison of maximum gear contact loads during normal operation and shutdown

The significant change in gear contact load during shutdown will transfer to the bearings within the WTG and affect the load distribution of the bearings. Figure 7.16 and Figure 7.17 illustrate the bearing loads of planetary gears during shutdown. As shown in Figure 7.16(a), the maximum bearing load occurs immediately after the engagement of the brake on the HSS side. The frequency histograms shown in Figure 7.16(b-d) illustrate the conversion of the time domain planet gears downwind bearings load shown in Figure 7.16(a).

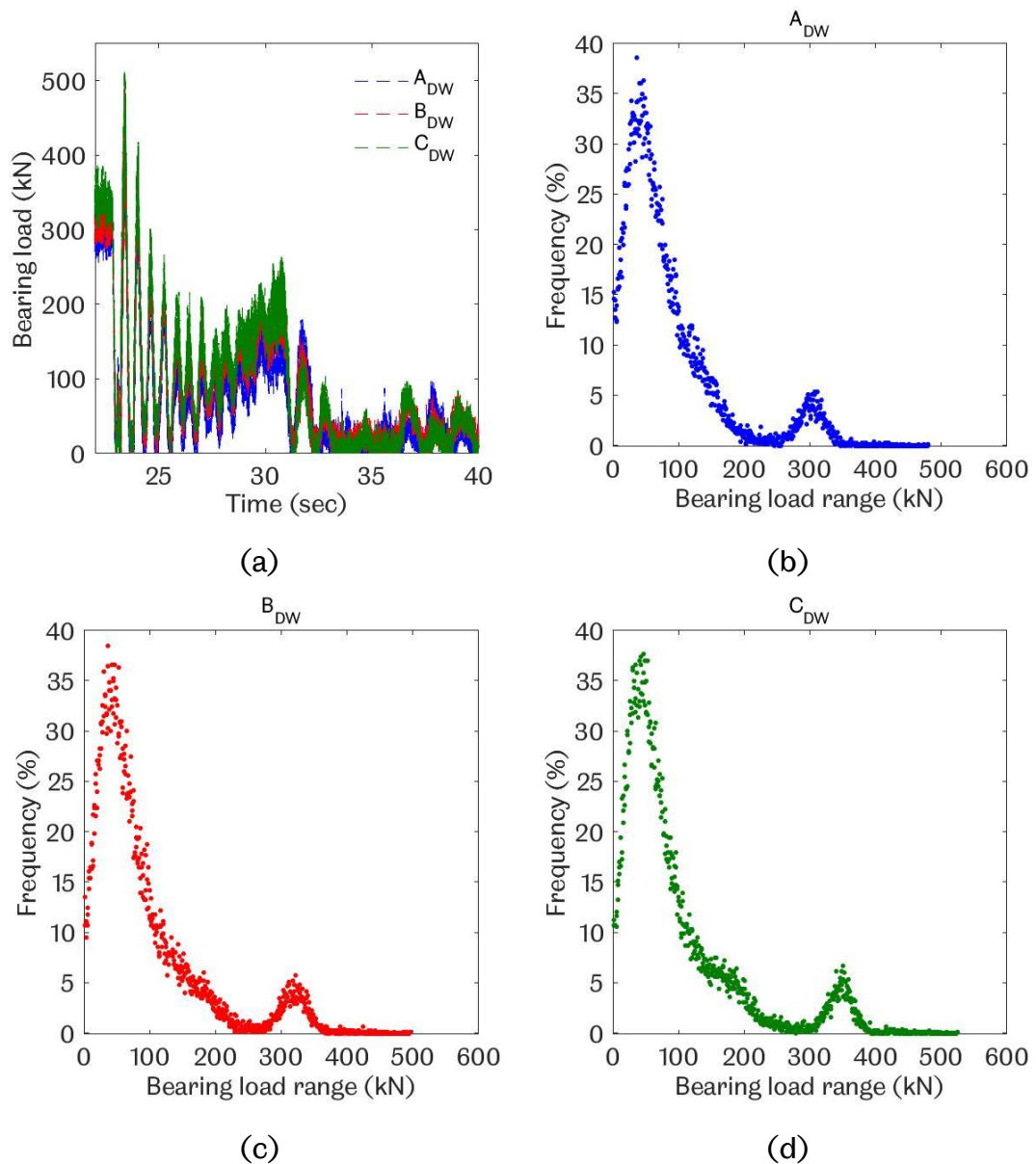


Figure 7.16: Variation of downwind bearing loads and related frequency histograms during shutdown

As shown in Figure 7.17, the non-uniform distribution of bearing load during shutdown is similar to that in the gears except there is no negative load on bearings. During shutdown all the upwind bearings of the planet gears carry higher loads than that on downwind bearings. During shutdown and after the mechanical brake is engaged the calculated maximum load in upwind bearings for planet gear A, B and C is higher than that on downwind bearings by 20%, 13% and 5% respectively. According to equation 7.1 and 7.2, this means the

fatigue life of these bearings is reduced by $1.2^{10/3} = 1.84$, $1.13^{10/3} = 1.5$ and $1.05^{10/3} = 1.17$ times during the shutdown. It is worth to mention that according to Germanischer Lloyd rules and guidelines [123] shutdown occurs 1000 times per year at cut-in speed, 50 times per year at cut-out and 50 times per year at rated wind speed. This means 1100 braking events per year during shutdown only. The load applied to the bearing during this short period is too high and should be considered in bearing surface fatigue calculations, which will be discussed in Section 7.2.4.

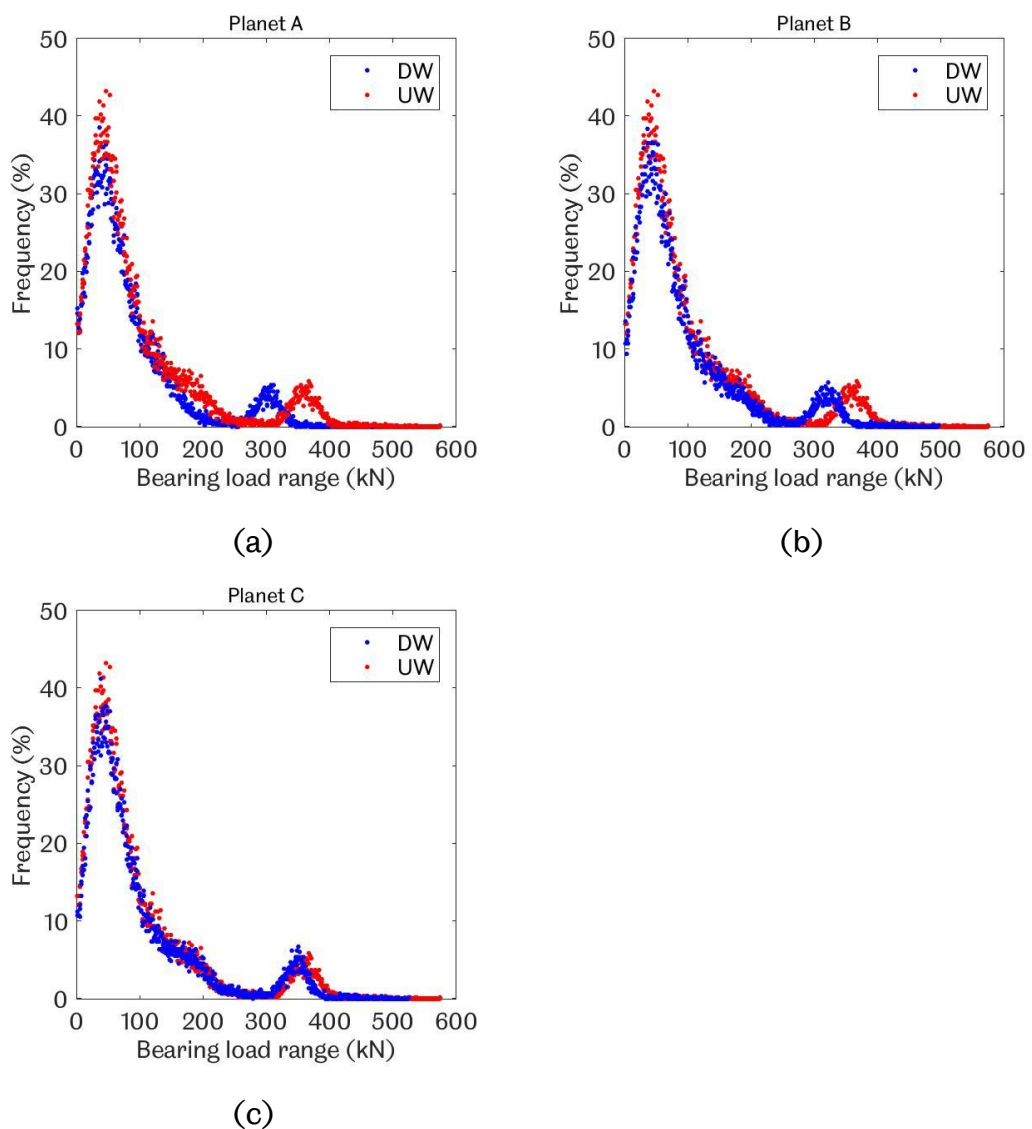


Figure 7.17: Comparison of load range histograms of UW and DW planet gear bearings during shutdown

As illustrated in Figure 7.18, the comparison of the maximum bearing loads of all bearings between the normal operation and shutdown shows higher loads in shutdown. It should be noted that the planet gear bearings carry higher load than that carried in other stages. However, the load on HSS bearings during shutdown is twice that during normal operation. The effect of this increase in bearing load on bearings fatigue life should be considered as will be discussed in Section 7.2.4.

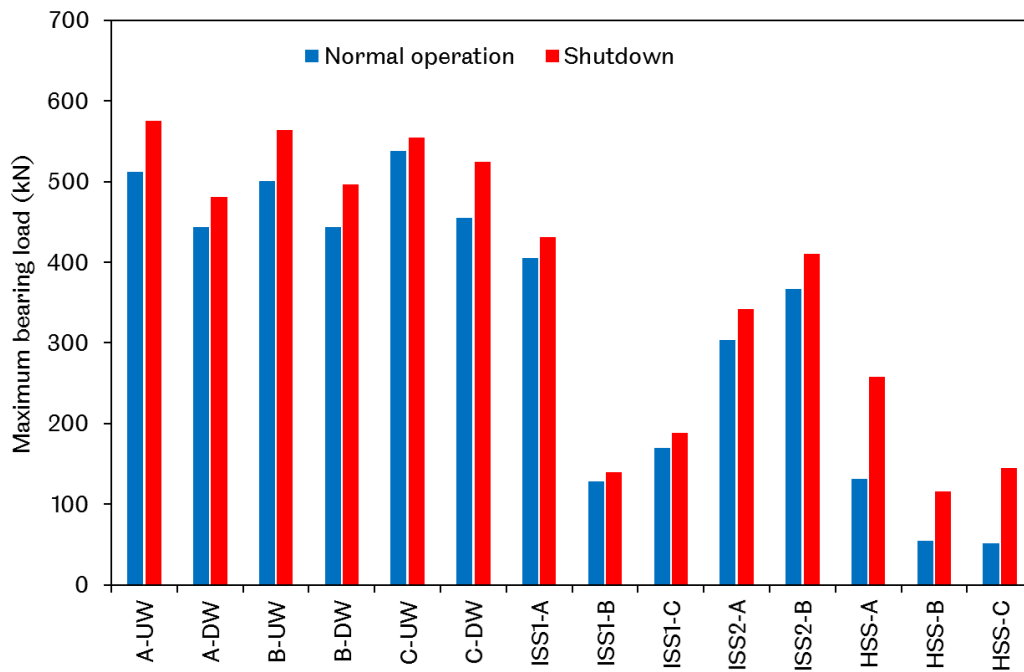


Figure 7.18: Comparison of maximum bearing loads during normal operation and shutdown

7.2.2 Surface Contact Stress on Gears and Bearings During Normal Operation and Shutdown

Figure 7.19 shows the frequency histograms of maximum contact stress range distribution in different gear stages during normal operation. The contact stresses of gears increase gradually from the lowest speed gear stage to those in the highest speed gear stage. In fact, the gear contact stress in the high-speed stage is 2.32 times of the contact stress between the ring gear and planet gear, 1.32 times of the contact stress between planet gear and sun gear and 1.22 times of the contact stress between the gear and pinion in intermediate stage.

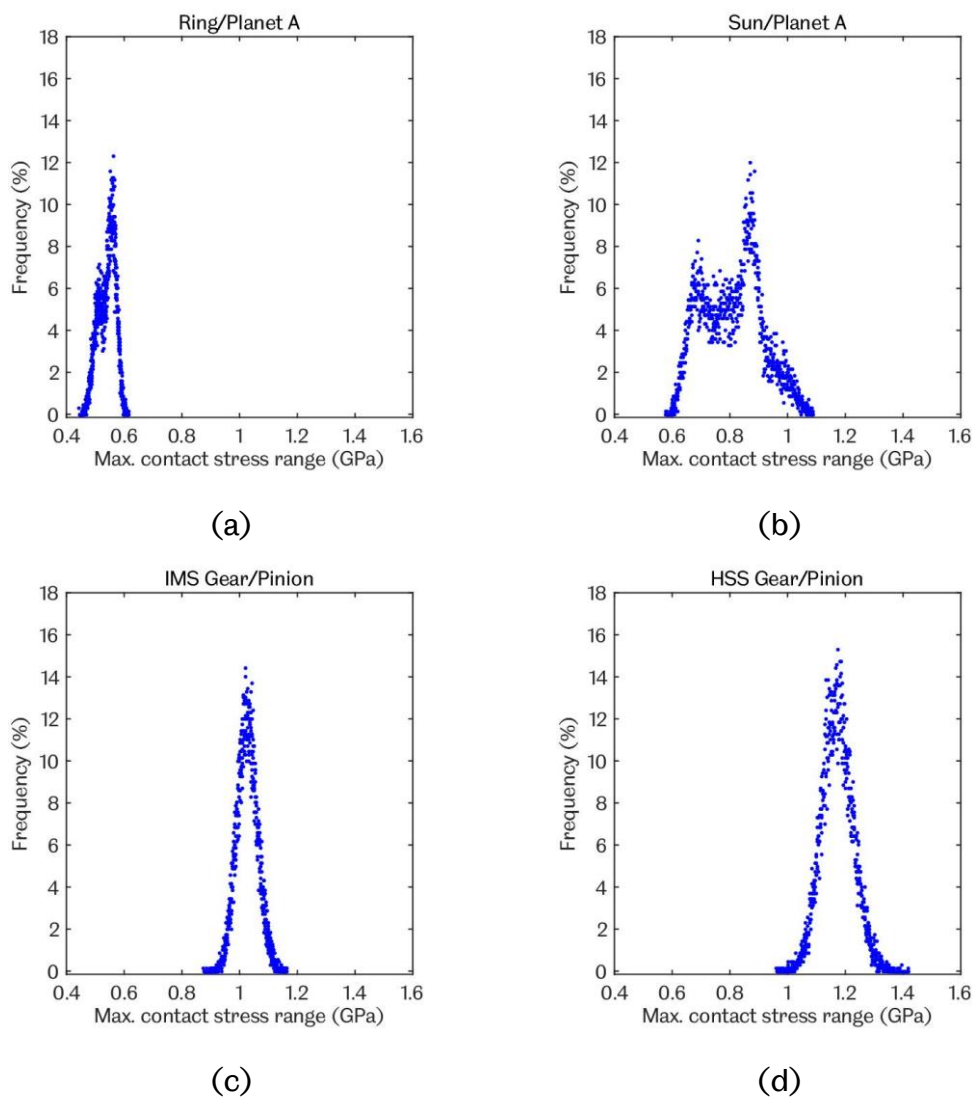


Figure 7.19: Maximum gear contact stress distributions during normal operation

During shutdown, the maximum gear contact stress range varies dramatically, and the stress range expands as shown in Figure 7.20. As illustrated in Figure 7.20(c), the gear contact stress distribution can be divided into three main regions. The 1st region, labelled by number 1, represents the gear contact stress range during normal operation. The stress distribution of this region is similar to that in Figure 7.19(c) which is for the same gear stage. The 2nd region, labelled by number 2, is for the gear contact stress range occurred immediately after brake engagement on the HSS. During this period, the gears are subjected to the highest contact stress. The 3rd region, labelled by number 3, is for the gear contact stress range occurred during braking and stopping. During this region, the gears are subjected to contact stress lower than that during normal operation and after the brake is engaged.

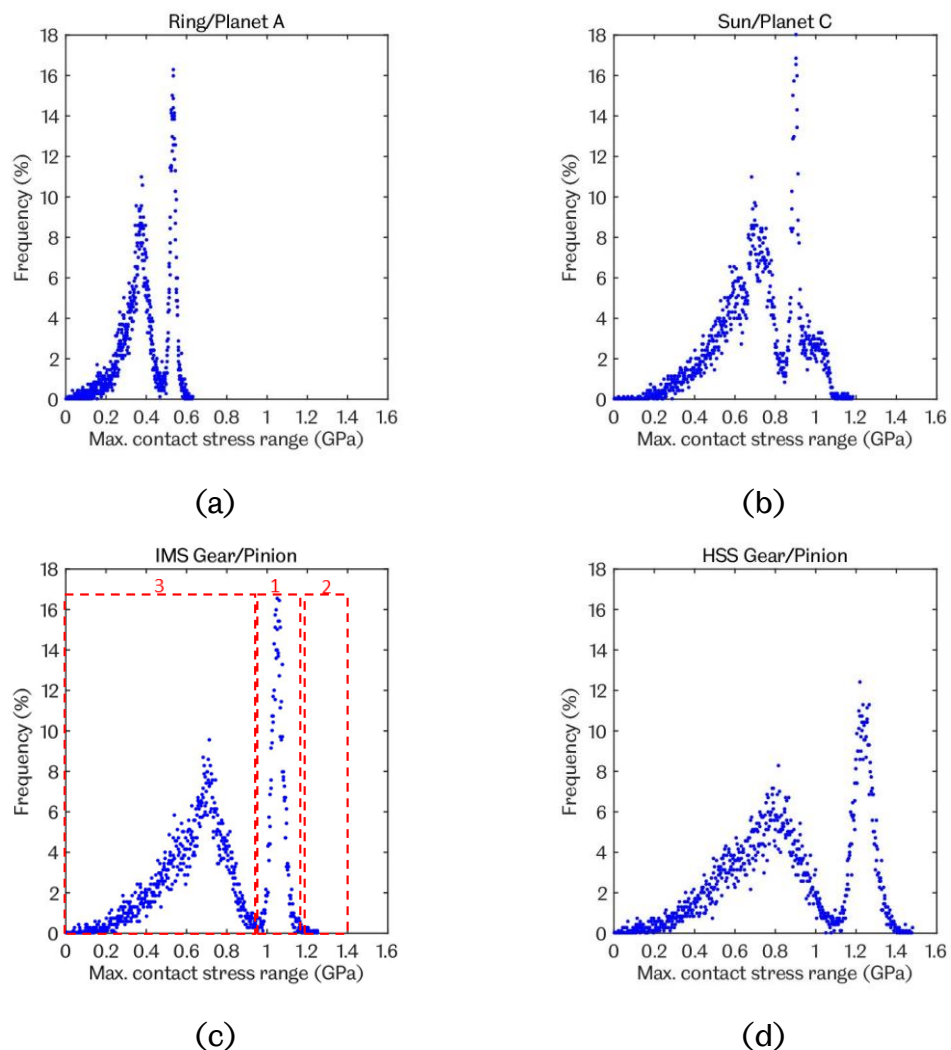


Figure 7.20: Maximum gear contact stress distributions during shutdown

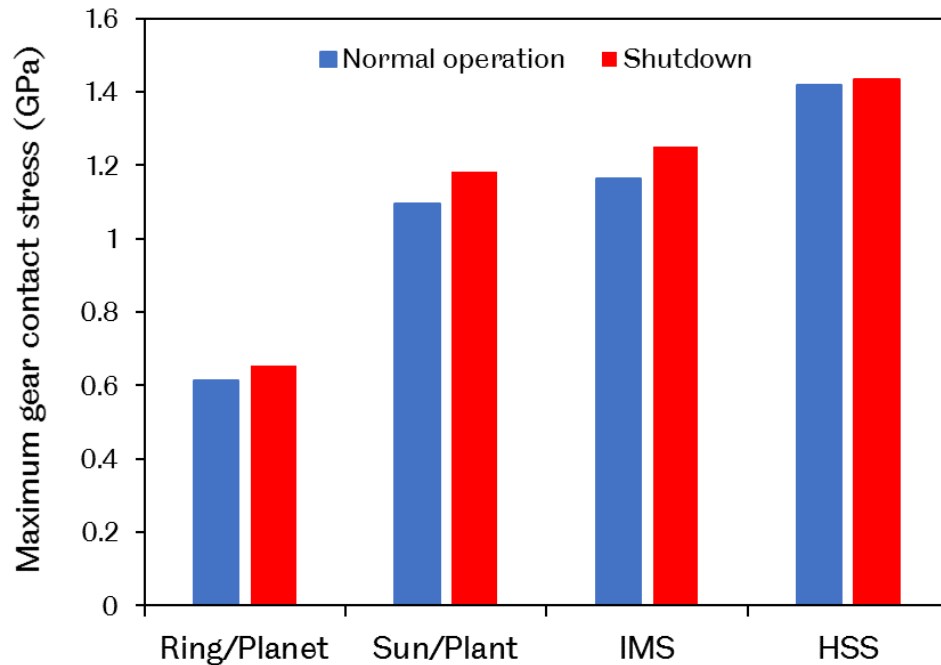


Figure 7.21: Comparison of maximum gear contact stress during normal operation and shutdown.

It is very interesting to compare the maximum gear contact stress levels during normal operation and shutdown. Figure 7.21 shows that the maximum contact stress level increases for all gears during the shutdown. It is worth to mention that the gear face width of the HSS stage is smaller than that in intermediate and planetary stage, which means there is less area of contact between the mating gear teeth. Moreover, the rotational speed of the HSS stage gears is much higher than that in the planetary stage. This could explain why there is higher gear contact stresses in the HSS stage than in the lower speed stage within the WTG.

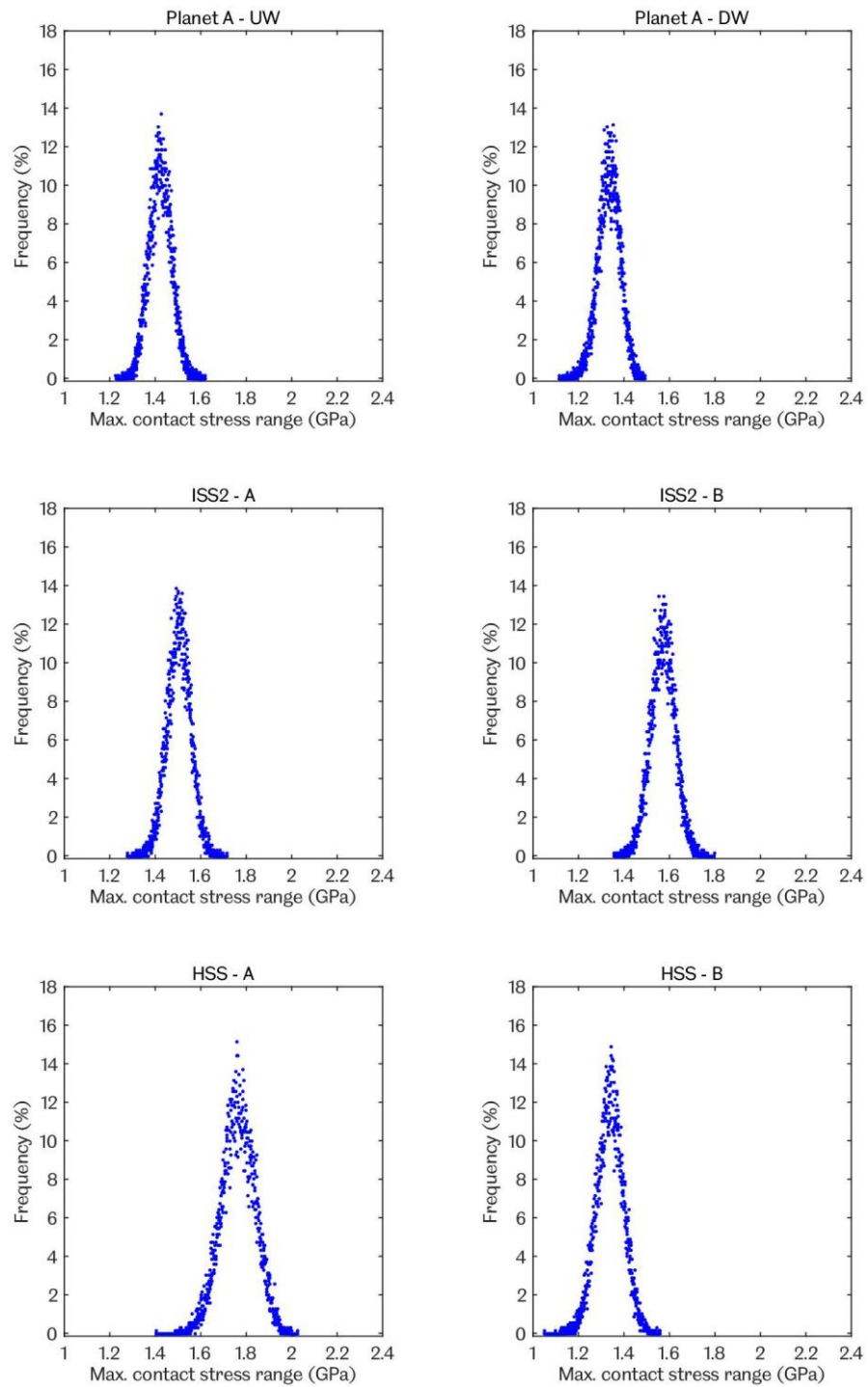


Figure 7.22: Maximum bearing contact stress distributions during normal operation

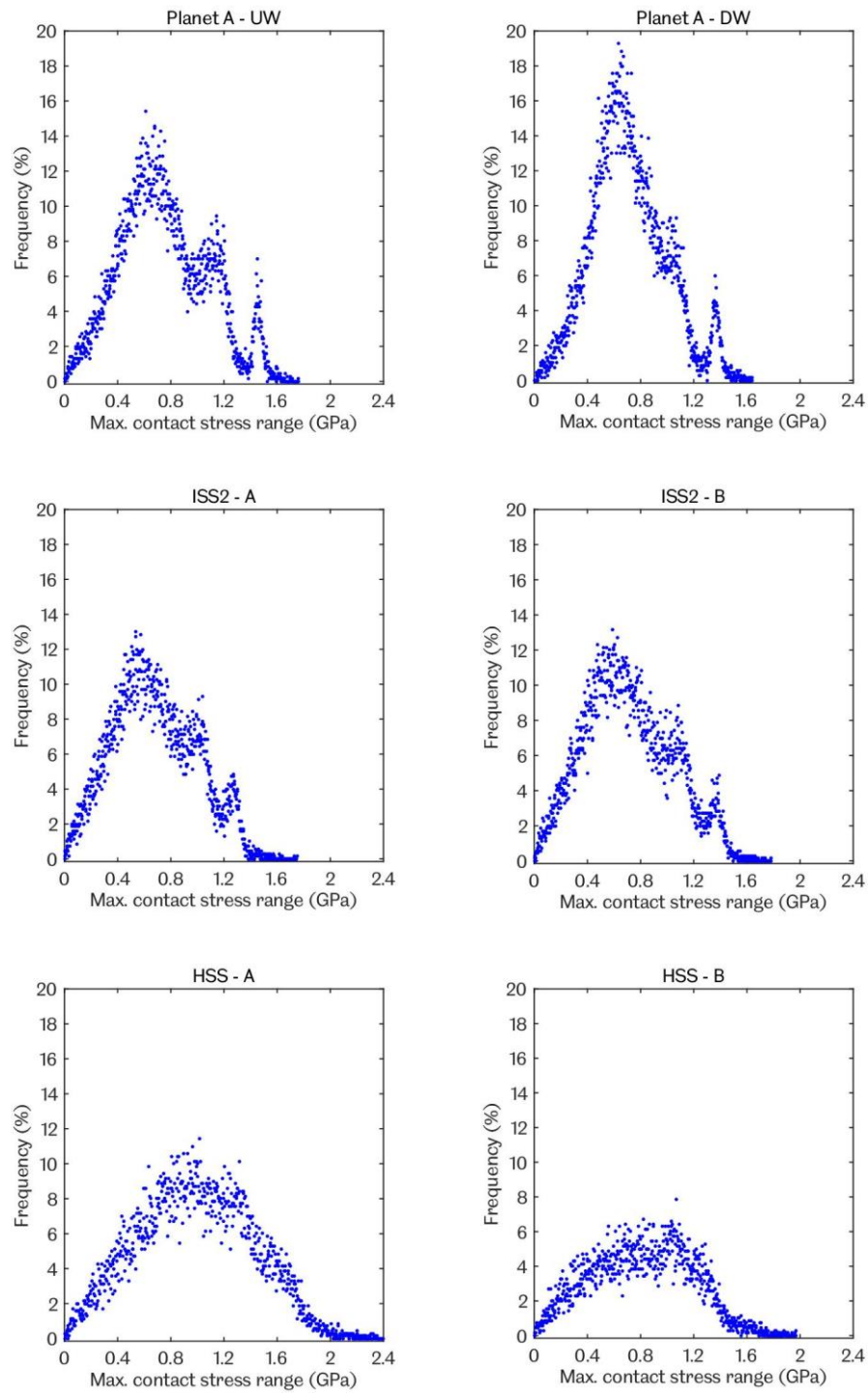


Figure 7.23: Maximum bearing contact stress distributions during shutdown operation

Figure 7.22 and Figure 7.23 show frequency histograms of the maximum contact stress range on bearings in different gear stages during normal operation and shutdown. As shown in Figure 7.22, during normal operation, the maximum contact stress range for all bearings has a normal distribution. During shutdown, as shown in Figure 7.23, the maximum bearing stress varies dramatically, with a stress range much higher than that during normal operation. During shutdown, the highest bearing stress level occurs immediately after the brake is applied but the fluctuations in stress level are lower during this period of shutdown than that during normal operation. The increases in bearing stress level could have harmful effects on the bearings fatigue life. It should be noted that the contact stress level in downwind planetary bearings is lower than that in upwind bearings during both normal operation and shutdown.

Figure 7.24 shows that even during the normal operation, the maximum contact stresses of all bearings within the wind turbine gearbox are close to or exceed the maximum allowable contact stress values, recommended in the international standard IEC 61400-4. The maximum contact stresses values recommended by IEC 61400-4 standard depend on the bearing location within the WTG. These values are, 1.5 GPa for planetary gear bearings (i.e. Planet A, B, C -UW/DW bearings), 1.65 GPa for intermediate shafts bearings (i.e. ISS1-A, B, C and ISS2-A, B bearings) and 1.3 GPa for the high-speed shaft bearings (i.e. HSS-A, B and C bearings). As shown in Figure 7.24, during shutdown, the maximum contact stresses in HSS bearings increase dramatically and exceed the recommended stress value by 85% for bearing HSS-A, 52% and 55% for bearing HSS-B and C respectively. The finding by this study of maximum contact stress on HSS bearings occurs after braking condition agrees with the test results reported by [57]. Moreover, during shutdown the maximum contact stress in upwind planet bearing A (i.e. Planet A-UW) exceeds the recommended stress value by 17%. This result is in agreement with the previous findings reported by [75] and [80].

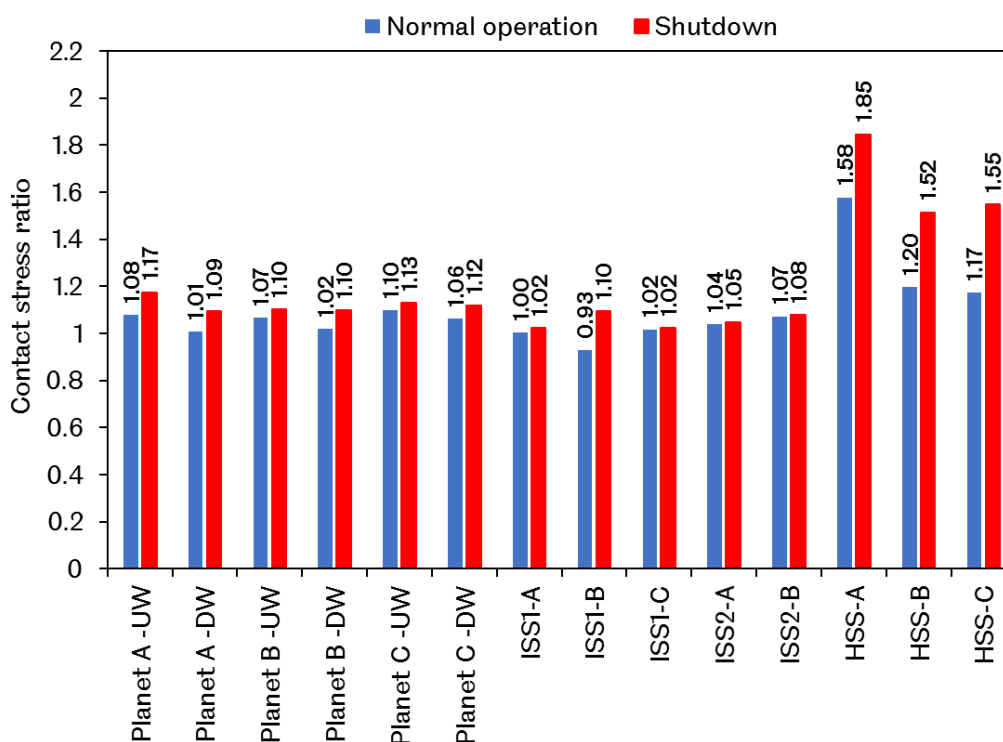


Figure 7.24: Comparison of ratios of maximum bearing contact stress and the recommended allowable contact stress during normal operation and shutdown.

The decrease in bearing contact loads reduces the number of rollers in contact with the bearing raceways. Equally when the bearing contact load increases the number of rollers in contact with the raceways increases. Figure 7.25 shows that the number of rollers in contact for upwind bearing A changes dramatically during shutdown. The number of rollers in contact changes from 6~7 rollers in contact consistently during normal operation to only one roller in contact within same time instances during shutdown. This results in occurrence of overloading condition and subjects the bearings to maximum contact stresses higher than the recommended value of 1.5 GPa for planetary gear bearings, which may contribute to higher fatigue damage of some bearings within the WTG. The simulation results show that during normal operation the bearings within the WTG are subjected to the maximum contact stress within the range of 1.51 GPa (i.e. upwind bearing B) to 2.05 GPa (i.e. HSS-A bearing). However, during shutdown the bearing contact stress increases to be in the range of 1.64 to 2.4 GPa. The effect of bearing contact stress variation on subsurface stresses will be investigated in the following section.

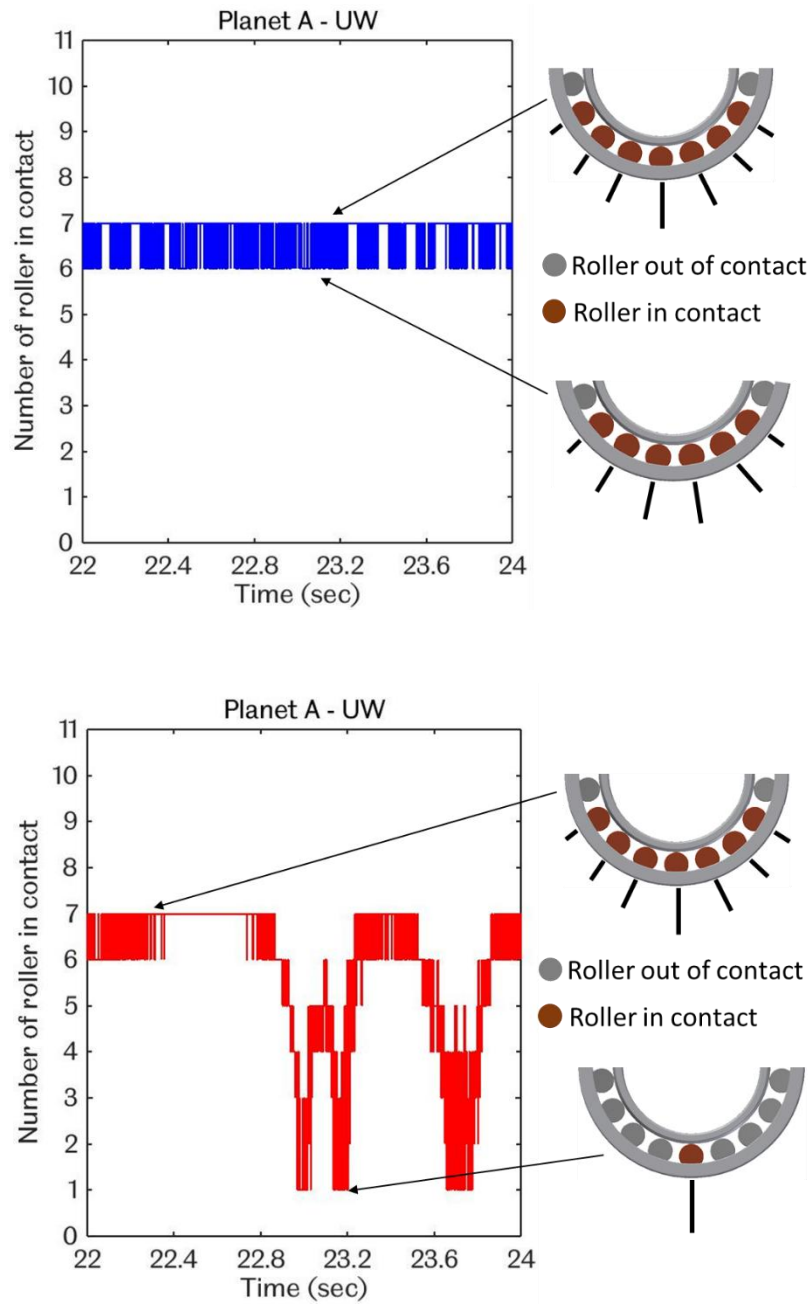


Figure 7.25: Number of rollers in contact for UW bearing A during normal operation (top) and shutdown (bottom)

7.2.3 Subsurface Contact Stresses of Gears and Bearings During Normal Operation and Shutdown

Figure 7.26 shows the subsurface maximum shear stress and maximum von Mises stress of gears during normal operation and shutdown (see section 5.3 for surface and subsurface stress calculations). Generally, the subsurface stresses on HSS gears are the highest among all gears. Conversely, the depth of subsurface stress in HSS gears is the lowest in comparison with the other gears. This could explain the high failure rate in HSS gears in the WTG. The shutdown condition results in increases of the subsurface stresses in all gears.

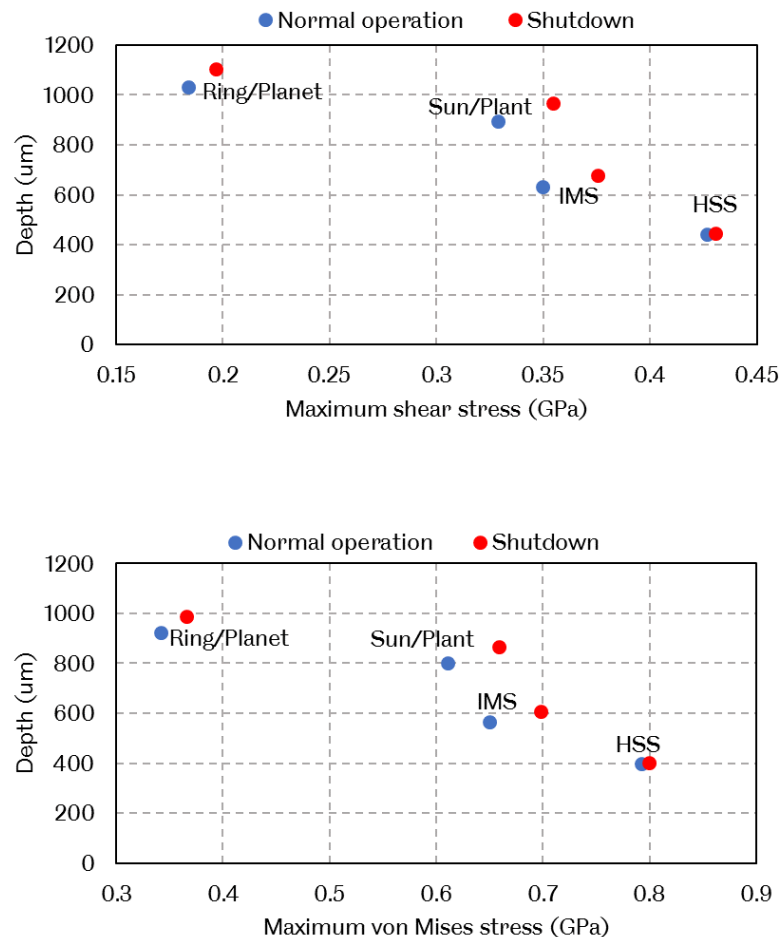


Figure 7.26: Maximum subsurface stresses and depths in gears during normal operation and shutdown, maximum shear stress (top) and maximum von Mises stress (bottom)

Figure 7.27 and Figure 7.28 show the comparison of the subsurface maximum shear stress and maximum von Mises stress in bearings between normal operation and shutdown. Generally, the subsurface stresses on HSS-A are the highest among all the bearings. Figure 7.27 and Figure 7.28 show that the maximum subsurface stresses for all bearings are located in the depth range of 350 μm to 650 μm . However, the effect of surface traction force between contact surfaces in bearings is ignored in this study which may move the location of the maximum subsurface stresses closer to the surface.

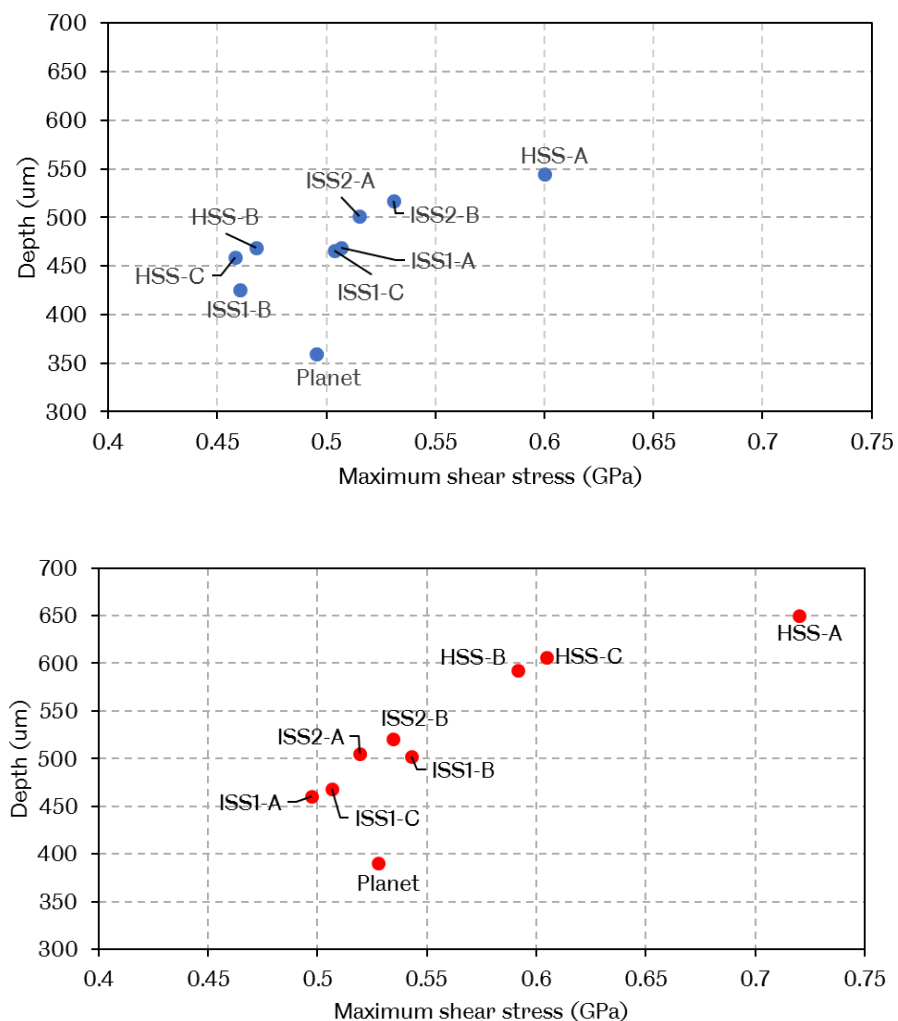


Figure 7.27: Maximum subsurface shear stress and depth in bearings during normal operation (top) and shutdown (bottom)

The subsurface stresses calculation emphasises the importance of studying the effect of subsurface stress depth variation corresponding to various surface contact stress levels. However, during both normal operation and shutdown, the maximum subsurface stresses, including both shear and von Mises stresses, are still below the yield strength of the bearing material.

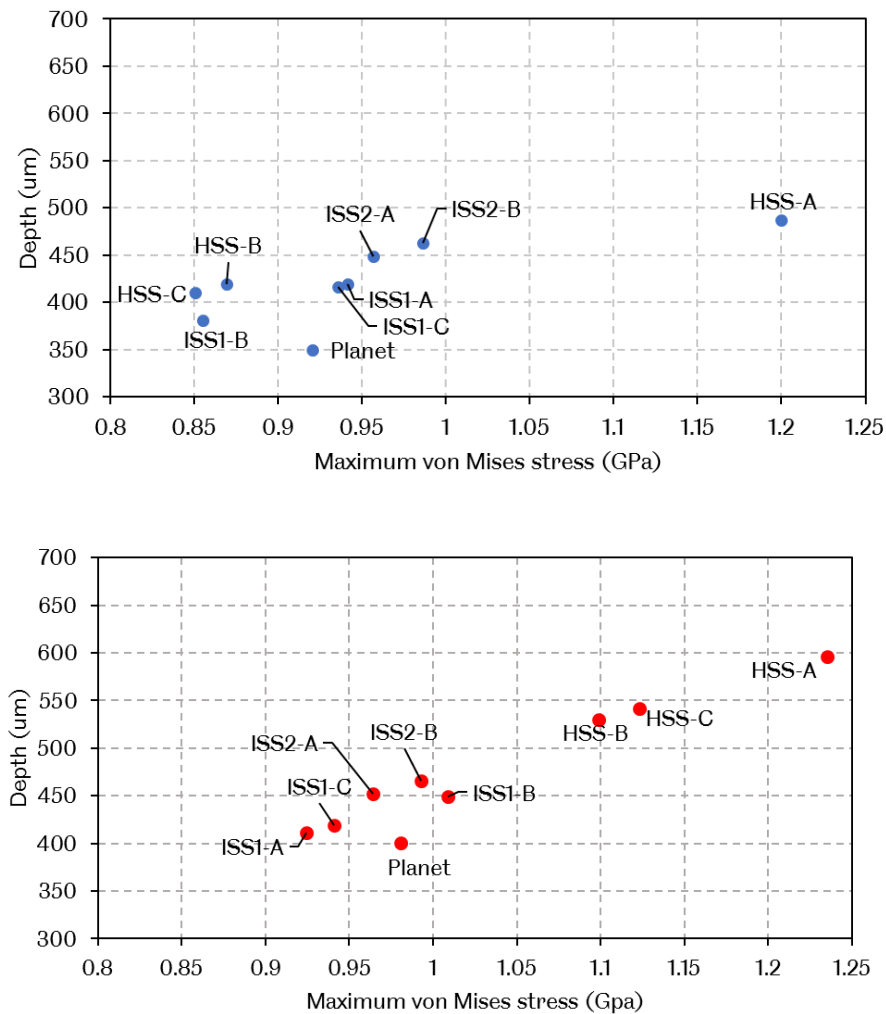


Figure 7.28: Maximum subsurface von Mises stress and depth in bearings during normal operation (top) and shutdown (bottom)

7.2.4 Gears and Bearings Fatigue Damage During Normal Operation and Shutdown

For fatigue life calculations, the simulation time of the SIMPACK MBS model of the 2MW WT drivetrain during normal operation and shutdown must be upscaled to the real number of operational hours given by the Weibull distribution depending on the design load cases recommended by the international standard [16]. The Weibull distribution for the normal operation of the 2MW WT occurrence at different wind speed is presented according to IEC 61400-4 as shown in Figure 7.29. When using the rainflow counting algorithm discussed in Chapter 3 to analyse the time histories of contact stresses of the gears and the bearings, the number of contact stress cycles must be multiplied by the time factor to obtain an estimation of the accumulated fatigue damage over a lifetime of 20 years. The time factor is calculated as the operational hours of 3600 seconds in one hour, divided by the simulation time in seconds during normal operation. It is assumed that operation condition within the simulation time (20 seconds) during normal operation is representative of the whole lifetime. The total life time is represented in hours of operation at different wind speeds for 20 years is equivalent to 20 years * 365 days * 24 hr = 175200 hr. This means that the wind turbine operates for around 92% of its 20 years design life, 161950 hr, under normal operation as shown in Figure 7.29 and Table 7.1. During normal operation, the torque measurement spectrums for all operational wind speeds are not available, the only torque spectrum available for normal operation and used in this study is under the rated wind speed (i.e. 16 m/s). The other torque measurement spectrum is for shutdown and the number of shutdown occurrences recommended by Germanischer Lloyd rules and guidelines [123] during the WT lifetime will be used for fatigue calculations.

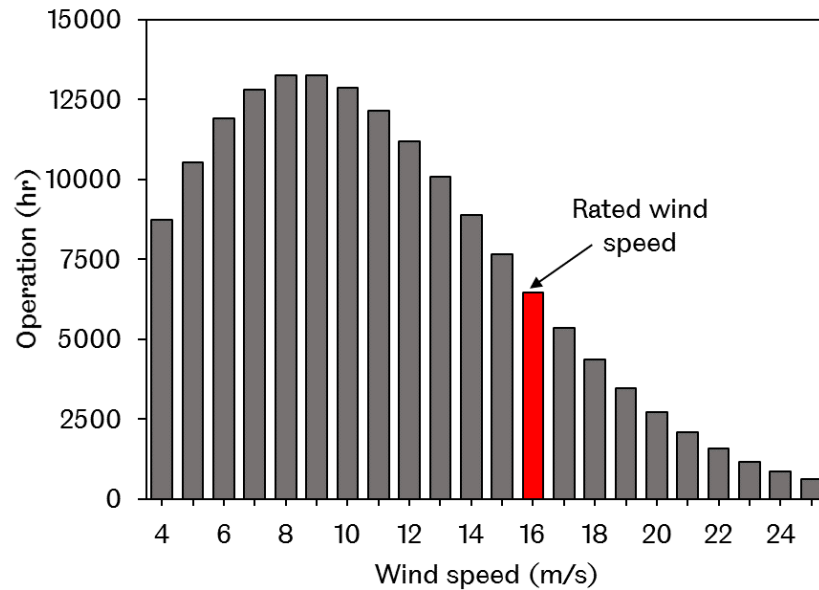


Figure 7.29: Operation hours for wind turbine corresponding to wind speed according to IEC 61400-4

The calculated time factor is reduced when the gear meshes with another gear. Another important factor to note is that the sun gear is in meshing with teeth of the three planet gears in each rotation. Therefore, the fatigue from the calculated stresses of teeth in contact of the sun gear must be added together. Regarding the sun gear, instead of having three 20 second simulations it corresponds to a fatigue calculation over a longer time of simulation of 60 seconds. The same method used for the sun gear can also be used for a full ring gear cycle, which sees three planet gears meshing with the ring gear. One rotation of the planet gear, however, corresponds to only a 40 second of the simulation time because one gear tooth will always mesh with another tooth from the ring gear and from the sun gear. Tooth adjusted time factors are summarised in Table 7.2.

Table 7.1: Hours of operation and time factor at different wind speeds

| Wind Speed (m/s) | In operation (hr) | Time-Factor |
|------------------------|-------------------|-------------|
| 4 (Cut-in speed) | 8733 | 1571855 |
| 5 | 10545 | 1898039 |
| 6 | 11916 | 2144818 |
| 7 | 12817 | 2307084 |
| 8 | 13251 | 2385178 |
| 9 | 13247 | 2384376 |
| 10 | 12856 | 2313997 |
| 11 | 12146 | 2186246 |
| 12 | 11194 | 2014953 |
| 13 | 10080 | 1814352 |
| 14 | 8878 | 1598001 |
| 15 | 7655 | 1377938 |
| 16 (Rated speed) | 6467 | 1164124 |
| 17 | 5356 | 964148 |
| 18 | 4351 | 783209 |
| 19 | 3468 | 624278 |
| 20 | 2713 | 488421 |
| 21 | 2084 | 375193 |
| 22 | 1573 | 283052 |
| 23 | 1165 | 209761 |
| 24 | 848 | 152726 |
| 25 (Cut-out speed) | 607 | 109270 |
| Total operation | 161950 | |

Table 7.2: Adjusted factor time scaling for different gears

| Wind speed (m/s) | Operation (hr) | Time Factor | Adjusted Time Factor | | | | | | |
|---------------------|-------------------|-------------|----------------------|-------|-------|-------|--------|------|--------|
| | | | Planetary stage | | | IMS | | HSS | |
| | | | Planet | Ring | Sun | Gear | Pinion | Gear | Pinion |
| 12 | 11194 | 2014953 | 34741 | 13896 | 17370 | 17370 | 4343 | 4343 | 1135 |
| 14 | 8878 | 1598001 | 27552 | 11021 | 13776 | 13776 | 3444 | 3444 | 900 |
| 16 | 6467 | 1164124 | 20071 | 8028 | 10036 | 10036 | 2509 | 2509 | 655 |
| 18 | 4351 | 783209 | 13504 | 5401 | 6752 | 6752 | 1688 | 1688 | 441 |
| 20 | 2713 | 488421 | 8421 | 3368 | 4211 | 4211 | 1053 | 1053 | 275 |
| 22 | 1573 | 283052 | 4880 | 1952 | 2440 | 2440 | 610 | 610 | 159 |
| 24 | 848 | 152726 | 2633 | 1053 | 1317 | 1317 | 329 | 329 | 86 |

As shown in Figure 7.30, the maximum contact stress of HSS gears is higher than that on other gears within the WTG and it exceeds the allowable material contact stress of 1450 N/mm^2 recommended by ISO 6336-5 standard; thus, it may contribute to higher fatigue damage during the WTG operation.

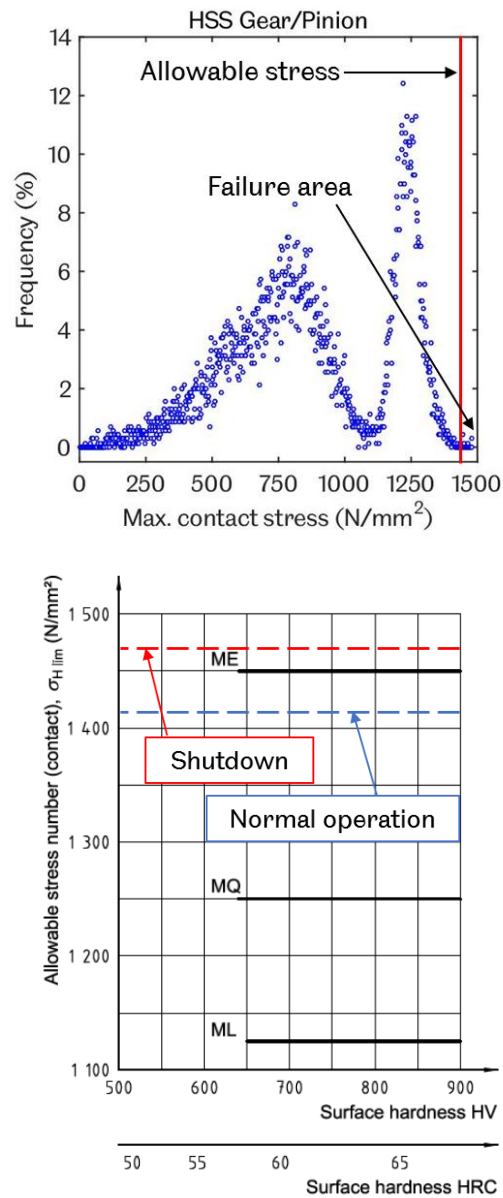


Figure 7.30: Histogram of maximum contact stress of HSS stage gears (top) and comparisons with the allowable contact stress recommended by ISO 6336-5 (bottom)

Figure 7.31 and Figure 7.32 show the fatigue damage calculations for gears and bearings for the design life of 20 years during normal operation and shutdown respectively. It is very clear that the shutdown produces the most harmful damage on WTG gears and bearings, in comparison with that resulted from normal operation. During shutdown, the HSS gears are subjected to high level of contact stresses with low cycles (see Figure 7.30). The stress level during the shutdown exceeded the maximum allowable stress thus exposed to the highest fatigue damage, in comparison with the gears of other stages. During shutdown, the bearings of the HSS gears and the planet gears have higher probability of failure than the other bearings, as shown in Figure 7.32. These results highlight the importance of gears and bearings loads during shutdown and suggest inadequacy in the selection of the key components of the WTG design and that a more robust transient gears and bearings configuration should be employed in future designs. This outcome can give the advantage of detecting the source of fault in shorter time. These results are in line with previous field research [11]. By using this outcome, the maintenance inspector looks for defects from those with higher probability of failure, rather than examining all gears and bearings.

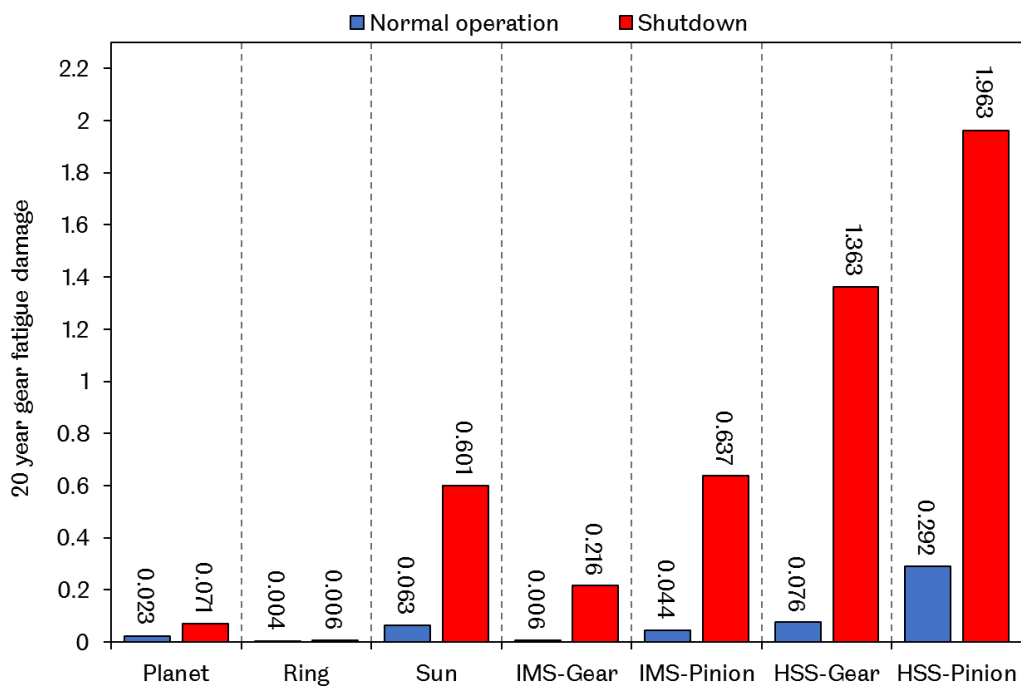


Figure 7.31: Comparison of gear fatigue damage during normal operation and shutdown

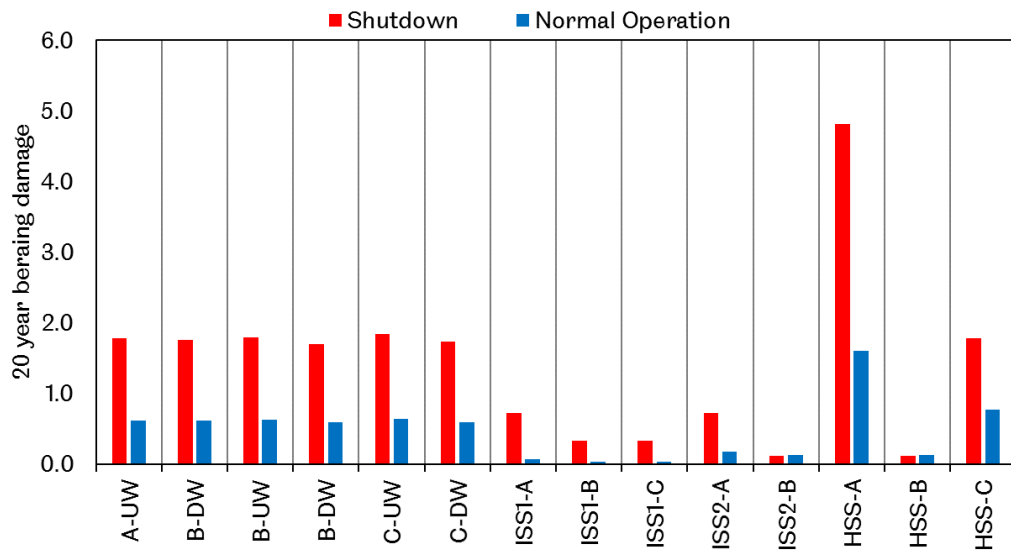


Figure 7.32: Comparison of bearing fatigue damage during normal operation and shutdown

7.3 Summary

The validation of the SIMPACK MBS model using NREL 750 kW WTG has shown that the developed model is capable of accurately modelling the dynamics behaviour of the WTG under different operational conditions. The results of this Chapter have shown the considerable fatigue damage of gears and bearings caused by transient operational events, such as the shutdown. Regarding the 2MW WTG, during normal operation, the bearings on the intermediate gearbox stage are working under contact stress very close to or equal to the maximum level of the recommended contact stress. However, the planet gear bearings and the high-speed stage bearings are subjected to high contact stresses in a range of 1.6 – 2GPa, which is higher than the recommended maximum bearing contact stress. During shutdown, the minimum bearing contact stress is further increased to be in the range of 1.64 – 2.4 GPa. The resulting high contact stress levels on bearings contributes to increases of the subsurface stress levels and change their locations at depth from the contact surface around 1 mm for gears and around 0.65 mm for bearings. The results also show that high-speed shaft gears are subjected to the highest contact stress during both normal operation and shutdown, in comparison with the other gears within the wind turbine gearbox. It indicates the high-speed shaft gears have high risk of early fatigue failure.

8

CONCLUSIONS AND FUTURE WORK

The important findings and achievements of this study and the main conclusions from the obtained results have been summarised in this chapter. The first section of this Chapter highlights the key findings and conclusions in each Chapter of this study. The second section presents the suggestions for improving the methodologies and possible techniques used in this study for the recommended future work.

8.1 Conclusions

The main objective of this study was to understand and analyse the dynamic behaviour and response of key components in a wind turbine gearbox (WTG), such as the gears and bearings, under transient loading conditions. This could enhance understanding of the reasons behind these components failure prematurely before the designed lifetime. Moreover, it could improve the design of these components and reduce the overall maintenance cost. Without improving the design of the WTG key components, costs related to the downtime, repair, replacement and maintenance is likely to increase.

As described in Chapter 3, field measurement data of a megawatt class wind turbine (WT) provides the torque spectrums of the low speed shaft (LSS) and

the high-speed shaft (HSS) for four different operational conditions comprising, normal operation, normal stop, start-up and shutdown. The data of these operational conditions were analysed and compared by using the rainflow counting (RFC) method and damage equivalent load (DEL) method. The results were used to define which operation conditions have the least and most harmful effects on the key components of the WTG. The field measurement torque spectrums related to these operational conditions were normalised and used as a direct input to the wind turbine drivetrain model to analyse their effect on the key components, bearings and gears, and how they behave under these dynamic conditions. The dynamic models of 750kW, 2MW and 3MW wind turbines drivetrains, considered different levels of model complexity as detailed in Chapters 4 and 5. The pure torsional models discussed in Chapter 4 for WT drivetrains of the 750kW (Drivetrain-D), 2MW (Drivetrain-C), and 3MW (Drivetrain-A and B), showed clear limitations in capturing the important phenomena of the WTG bearings and gears under normal operation and shutdown as results shown in Chapter 6. Therefore, more advance models of wind turbine drivetrains presented in Chapter 5 were detailed the development of the rigid and discrete flexible body dynamic modelling. The results presented in Chapter 7 showed good agreements with the measurement and lab test results reported in previous studies [34, 124], which captured the most important behaviour in dynamic response of the gears and bearings during different operational conditions.

The effects of different operational conditions on surface and subsurface stresses of gears and bearings and their fatigue damage were also investigated and analysed. The main conclusions of this study are listed in the following sections.

8.1.1 Conclusions from The Field Measured Data Analysis of 2MW Wind Turbine

Field measured torque spectrums corresponding to four operational conditions of an operating wind turbine (WT) were examined, analysed and compared in detail (Chapter 3). The examined operational conditions comprised of normal operation, start-up, normal stop and shutdown. The rainflow counting (RFC) method was used to convert the time domain data of a complicated loading history into number of loading levels and cycles. The

damage equivalent load (DEL) method was used to calculate the accumulative damage caused by each operational condition. During shutdown, immediately after the mechanical brake was engaged, the mean torque on input shaft (i.e. the LSS) and the WTG output shaft (i.e. the HSS) exceeded the rated torque by up to 30%. Consequently, the load range on the LSS and HSS increased to eight times and five times higher respectively than that during the normal operation. The greater range of torque variations was associated with low number of load cycles. However, these low load cycles of the high load ranges caused higher damage than that during normal operating. Therefore, the field measured torque spectrums for normal operation and shutdown were used as a direct input to the wind turbine drivetrains models developed. The effect of these critical load cycles on the bearings and gears fatigue damage was investigated.

8.1.2 Conclusions from Pure Torsional Multibody Dynamic Modelling of Different Wind Turbine Drivetrain Configurations

The developed WT drivetrain models had different level of complexity in forms of 2-Mass, 5-Mass and 11-Mass models, with different configurations of WT gearbox design and different WT power rating. The required parameters for the developed models were calculated by using CAD models. The dynamic response of the developed WT drivetrains under free vibration and forced vibration was studied and validated with the published studies in Chapter 6. Field measured torque spectrums of the normal operation and shutdown were used as a direct input to the WT drivetrains models developed in Chapter 4. The gear contact loads were calculated and analysed during normal operation and shutdown. The effect of gear mesh frequency on the WT drivetrains excitation were studied and analysed by using fast Fourier transformation (FFT) and Campbell resonance analyses. The key conclusions are:

1. The simple WT drivetrain model represented by two, five and eleven masses (i.e. 2-Mass, 5-Mass and 11-Mass models) showed the influence of neglecting the generator resistance torque on the natural frequencies of the WT drivetrain system. This happened when the WT drivetrain was switched from constant generator speed (i.e. free-fixed end frequency

- mode) during normal operation to variable generator speed (i.e. free-free end frequency mode) during shutdown.
2. During normal operation, the WT drivetrain behaved as a free-fixed end dynamic system. Thus, there was no zero mode and the dominant frequency was the lowest natural frequency, i.e. the 1st mode of the WT drivetrain. During shutdown, the WT drivetrain behaved as a free-free end dynamic system. Thus, there was a zero mode and the dominant frequency was the lowest natural frequency of the WT drivetrain after the zero mode (i.e. the 2nd mode).
 3. The lowest natural frequency of the WT drivetrain was always in correspondence to the heaviest mass within the WT drivetrain (i.e. the rotor, the blades and the hub). Increasing the rotor inertia decreased the lowest natural frequency of the WT drivetrain and vice versa. Consideration of WTG components had no influence on the lowest natural frequency of the WT drivetrain. However, the gear mesh stiffness had shown direct effect to the WTG frequencies.
 4. The stiffness of the WT drivetrain shafts had direct effect on the natural frequency of the WT drivetrain system while the generator inertia and the WTG gearbox ratio had inverse effect on it.
 5. The WTG configuration, size, and the gear mesh frequency influenced the gearbox torque level different gear stages during shutdown. Moreover, the internal excitation of the WTG caused by gears during shutdown was very close to the natural frequency of the WT drivetrain, which could cause possible system resonances within the WT operational speed range.
 6. The range of the gear meshing forces during shutdown was 5~6 times wider than that during normal operation.

8.1.3 Conclusions from Rigid and Discrete Flexible Multibody Dynamic Modelling of Wind Turbine Drivetrain

More advance MBS dynamic models of WT drivetrains were developed by using SIMPACK MBS software with six degrees of freedom (6-DOF) per component. There were three DOFs in rotational direction and three DOFs in translation direction as detailed in Chapter 5. The main shaft and the gearbox shafts within the WT drivetrain were considered as flexible bodies. The WTG gears and the spline shaft were considered as rigid bodies with discrete

flexibility in the contact region between the meshing teeth by using the slicing approach. The bearings model considered the cross-coupling effect between the rollers and the races. The contact between the roller and the race was represented by using a lamina model. The model considered the clearance in bearings, backlash in gears. The real geometry of bearing and gears was used in determining the maximum contact stress on bearing and gears based on the Hertz contact theory. Field measured torque spectrums of the normal operation and shutdown were used as a direct input to the WT drivetrains models developed in Chapter 5. The developed MBS model results were validated in Chapter 7 with the measured data published by previous studies [34, 124]. The key conclusions are:

1. During normal operation, the highest load level of the upwind (UW) bearings of the planet gears occurred when the planet gear is aligned horizontally to right of the sun gear when viewed from the upwind side. At the same position, the downwind bearings carried the lowest loads. However, the downwind (DW) bearings carried less load than the UW bearing for a short period during the planetary carrier motion.
2. The load sharing factor of planet gears increased when the planet gear tilt toward upwind about the planet gear radial axis.
3. The loads of the WTG bearings and gears showed normal distribution during normal operation. However, this distribution changed dramatically during the WT shutdown. The loads on gears and bearings were always higher during shutdown.
4. The maximum contact stress on gears increased progressively from the low speed gears to the high-speed stage gears during the normal operation of wind turbine gearbox. The maximum stress levels were still below the recommended allowable stress of gears material. However, during shutdown the maximum contact stress on the high-speed gears exceeded the allowable maximum stress level.
5. During normal operation and for the 2MW WTG, the maximum contact stress on upwind bearings of planet gears A, B and C was 8%, 7% and 10% higher than the maximum stress value of 1.5 GPa, recommended by IEC 61400-4 standard. During shutdown, the maximum contact stress of these bearings was 17%, 10% and 13% higher than the recommended value. These were in total agreements with finding of two recent studies of the 750kW

WT drivetrain [80, 126]. However, during shutdown the HSS bearings A, B and C were subjected to higher contact stresses than that on the planet bearings which exceeded the maximum recommended stress level by 85%, 52% and 55% respectively.

6. Fluctuations in the bearing contact loads influenced the number of rollers in contact with the bearing raceways. During shutdown, the number of rollers in contact changed dramatically until only one roller was in contact with the bearing race in some instants.
7. During normal operation and shutdown, the gear subsurface stresses (von Mises stress and maximum shear stress) located in subsurface depth around 1 mm. The lowest subsurface stresses depth was found in high speed gears at around 400 μm . For the WTG bearings, the subsurface stresses (von Mises stress and maximum shear stress) located in subsurface depth of around 600–650 μm . The lowest subsurface stresses depth was found in planet gear bearings, at around 350–380 μm . This could explain the finding of damaged inclusions in planet gear bearing raceways within subsurface depth of around $\sim 350 \mu\text{m}$ [80] [127]. It was very clear that the shutdown increased the surface contact stress in gears and bearings and this extended the subsurface stress field into deeper locations. This could explain the reason behind the finding of damaged inclusions [127] or micro cracks [80] in planet gear bearing raceways at subsurface depth of around $\sim 600 \mu\text{m}$.
8. Long term fatigue calculation showed that during shutdown, all the planet gear bearings (i.e. 6 bearings) and two of the high-speed shaft bearings (A and C) had high probability to fail prematurely less than the designed lifetime of 20 years. Regarding the gears, the high speeds shaft gears, both the gear and pinion had the highest damage induced during shutdown, in comparison with the other gears.

8.1.4 Research Novelty and Contributions

The findings from Chapters 6 and 7 have contributed to new knowledge and understanding regarding to the WTG and WT drivetrain modelling and premature failure of key components:

1. The cross-coupling effect and a more advance lamina model for bearing roller contact with raceways, must be considered to ensure that the WTG

MBS model can capture the important dynamic behaviour of the WTG's key components during normal and transit events. The good agreement between the simulation results of this study and the measured results of previous studies [34, 124] demonstrated the important effect of the bearings modelling on the dynamic response of the WTG MBS model.

2. During normal operation and shutdown, the gear contact stress in the high-speed stage gears was considerable higher than that in other stages within the WTG. It exceeds the allowable material contact stress, thus contributed to higher fatigue damage.
3. The number of bearing rollers in contact with bearing race changed consistently during normal operation and varied dramatically during shutdown condition. This resulted in occurrence of overloading condition and subjected the bearings to maximum contact stresses higher than the recommended level, thus contributed to higher fatigue damage of planet gear bearings and the high-speed shaft bearings.
4. The findings of this research may provide essential information and understanding on monitoring and inspection of those components within the WTG which have higher failure probabilities, such as the planetary bearings, the bearings of the HSS and the HSS gears. Thus, this could reduce the operation and maintenance costs due to the failures of these key components.

8.2 Suggestions for Future Work

This study focussed on developing advance system dynamic models for WTGs of different configurations which operated under normal and shutdown conditions and can capture the important dynamic phenomena of WTG key components within the wind turbine drivetrain. The following are the recommended future research directions to further develop the work done in this study.

1. The pure torsional model developed in this study ignored the bearings within the wind turbine drivetrain and the gear mesh stiffness was assumed as constant. This model could be improved to include the bearings and variable gear mesh stiffness to predict the loads of the bearings or other gearbox components to draw new conclusions and to

provide new insights which are relevant to the design of wind turbine gearboxes.

2. For the 3MW WT drivetrains, the input torque spectrums to the multibody system models were scaled up from the field measured data of 2MW. Using real measured torque spectrums for these machines (if available) as a direct input could be useful in studying the dynamic behaviour of WTG components under real operational conditions.
3. This study focused on studying the dynamic behaviour of WTG components under two operational conditions, normal operation and shutdown. Future studies could include prediction of loads and contact stresses of the WTG gears and bearings under other transient loading conditions experienced by the WT within its lifetime, such as the start-up and grid loss or fault.
4. In this study, the base plate of the WT drivetrain was assumed to be rigid. It would be interesting to study the effect of a flexible base plate on the dynamic response of the WTG under transient events such as shutdown.
5. The simulation period used was very short in this study, around 20 seconds for normal operation and 30 seconds for shutdown. Further studies could consider the effect of longer simulation time on the dynamic behaviour of the WTG components would be interesting.

REFERENCES

- [1] J. Ribrant and L. Bertling, "Survey of failures in wind power systems with focus on Swedish wind power plants during 1997-2005," in *Power Engineering Society General Meeting, IEEE*, 2007, pp. 1-8.
- [2] J. Helsen, G. Heirman, D. Vandepitte, and W. Desmet, "The influence of flexibility within multibody modeling of multi-megawatt wind turbine gearboxes," in *Proceedings of the International Conference on Noise and Vibration Engineering*, 2008, pp. 2045-2072.
- [3] K. Smolders, H. Long, Y. Feng, and P. Tavner, "Reliability analysis and prediction of wind turbine gearboxes," in *European Wind Energy Conference and Exhibition*, 2010, pp. 2660-2682.
- [4] "The economics of wind energy" vol. 13, European Wind Energy Association (EWEA), 2009.
- [5] "Global Wind 2015 Report: Annual Market Update," *Global Wind Energy Council (GWEC), Brussels, Belgium*, 2016.
- [6] "Wind energy in Europe: Scenarios for 2030," September, 2017.
- [7] "Pure power-wind energy targets for 2020 and 2030," European Wind Energy Association (EWEA), 2011.
- [8] K. Scott, D. Infield, N. Barltrop, J. Coultate, and A. Shahaj, "Effects of extreme and transient loads on wind turbine drive trains," in *50th AIAA Aerospace Sciences Meeting including the New Horizons Forum and Aerospace Exposition*, 2012, p. 1293.
- [9] W. Musial, S. Butterfield, and B. McNiff, "Improving wind turbine gearbox reliability: preprint," National Renewable Energy Lab.(NREL), Golden, CO (United States)2007.
- [10] F. Oyague, "Gearbox modeling and load simulation of a baseline 750-kW wind turbine using state-of-the-art simulation codes," National Renewable Energy Laboratory (NREL), Golden, CO.2009.
- [11] H. Link, W. LaCava, J. van Dam, B. McNiff, S. Sheng, R. Wallen, *et al.*, "Gearbox reliability collaborative project report: findings from phase 1 and phase 2 testing," National Renewable Energy Lab.(NREL), Golden, CO (United States)2011.

-
- [12] M. Grujicic, S. Ramaswami, J. Snipes, R. Galgalikar, V. Chenna, and R. Yavari, "Computer-aided engineering analysis of tooth-bending fatigue-based failure in horizontal-axis wind-turbine gearboxes," *International Journal of Structural Integrity*, vol. 5, pp. 60-82, 2014.
- [13] Tavner P. , Spinato F. , van Bussel G. , and K. E., "Reliability of Different Wind Turbine Concepts with Relevance to Offshore Application," in *Wind Energy*, 2008.
- [14] J. Peeters, "Simulation of dynamic drive train loads in a wind turbine," *Katholieke Universiteit Leuven, Leuven (Heverlee), Belgium*, 2006.
- [15] International Organisation for Standardization IEC 61400-4:2012 "IEC 61400-4: Wind turbines-Part 4: Design requirements for wind turbine gearboxes," 2012.
- [16] International Organisation for Standardization IEC 61400-1:2005, "IEC 61400-1: Wind turbines part 1: Design requirements," 2005.
- [17] G. Lloyd and G. Hamburg, "Guideline for the certification of wind turbines," *July 1st*, 2010.
- [18] H. Link, J. Keller, Y. Guo, and B. McNiff, "Gearbox reliability collaborative phase 3 gearbox 2 test plan," National Renewable Energy Laboratory (NREL), Golden, CO.2013.
- [19] W. Dong, Y. Xing, and T. Moan, "Time domain modeling and analysis of dynamic gear contact force in a wind turbine gearbox with respect to fatigue assessment," *Energies*, vol. 5, pp. 4350-4371, 2012.
- [20] H. J. Sutherland, "On the fatigue analysis of wind turbines," Sandia National Labs., Albuquerque, NM (US); Livermore, CA (US)1999.
- [21] E. Hau, "Wind turbine economics," in *Wind Turbines*, Springer, 2013, pp. 845-870.
- [22] D. Rivkin and L. Silk, *Wind turbine operations, maintenance, diagnosis, and repair*. Jones & Bartlett Publishers, 2012.
- [23] Z. Zhang, A. Verma, and A. Kusiak, "Fault analysis and condition monitoring of the wind turbine gearbox," *IEEE transactions on energy conversion*, vol. 27, pp. 526-535, 2012.

-
- [24] W. Yang, P. Tavner, and M. Wilkinson, "Condition monitoring and fault diagnosis of a wind turbine with a synchronous generator using wavelet transforms," 4th IET International Conference on Power Electronics, Machines and Drives, 2008, p.6-10.
- [25] N. Perisic, B. J. Pedersen, and P. H. Kirkegaard, "Gearbox fatigue load estimation for condition monitoring of wind turbines," in *The International Conference on Noise and Vibration Engineering*, 2012, pp. 4381-4392.
- [26] J. Van Dam, T. Riddle, and E. Overly, "Torque measurements on GRC test turbine 1," *National Renewable Energy Laboratory, Golden, CO*, 2007.
- [27] J. Coultate, Z. Zhang, C. Halse, A. R. Crowther, and R. House, "The impact of gearbox housing and planet carrier flexibility on wind turbine gearbox durability," in *Proc of European Wind Energy Conf*, 2009, pp. 1-8.
- [28] Z. Zhang, N. Al-Zaidi, C. Halse, A. R. Crowther, and R. House, "The effect of transient loading on the stresses of wind turbine drivetrain components," in *Proceedings of the European Wind Energy Conference and Exhibition (EWEC), Marseille, France*, 2009, pp. 16-19.
- [29] A. Heege, P. Viladomiu, J. Betran, Y. Radovic, M. Latorre, J. Cantons, *et al.*, "Impact of wind turbine drive train concepts on dynamic gearbox loads," *Proceedings DEWEK 2006*, pp. 22-23, 2006.
- [30] J. Keller, H. F. Link, Y. Guo, W. LaCava, and B. P. McNiff, *Gearbox reliability collaborative phase 1 and 2: testing and modeling results*: National Renewable Energy Laboratory, 2011.
- [31] S. Li, A. Kahraman, and M. Klein, "A fatigue model for spur gear contacts operating under mixed elastohydrodynamic lubrication conditions," *Journal of Mechanical Design*, vol. 134, 2012.
- [32] J. L. Peeters, D. Vandepitte, and P. Sas, "Analysis of internal drive train dynamics in a wind turbine," *Wind Energy*, vol. 9, pp. 141-161, 2006.
- [33] A. Flodin and S. Andersson, "A simplified model for wear prediction in helical gears," *Wear*, vol. 249, pp. 285-292, 2001.
- [34] W. LaCava, Y. Xing, C. Marks, Y. Guo, and T. Moan, "Three-dimensional bearing load share behaviour in the planetary stage of a wind turbine gearbox," *IET Renewable Power Generation*, vol. 7, pp. 359-369, 2013.

-
- [35] W. LaCava, Y. Xing, Y. Guo, and T. Moan, "Determining Wind Turbine Gearbox Model Complexity Using Measurement Validation and Cost Comparison: Preprint," National Renewable Energy Laboratory (NREL), Golden, CO.2012.
- [36] W. Dong, Y. Xing, T. Moan, and Z. Gao, "Time domain-based gear contact fatigue analysis of a wind turbine drivetrain under dynamic conditions," *International Journal of Fatigue*, vol. 48, pp. 133-146, 2013.
- [37] T. M. Wasfy and M. L. Stark, "Multibody Dynamics Model for Predicting the Vibration Response and Transient Tooth Loads for Planetary Gear Systems," in *ASME 2011 International Design Engineering Technical Conferences and Computers and Information in Engineering Conference*, 2011, pp. 449-457.
- [38] O. Lundvall, N. Strömberg, and A. Klarbring, "A flexible multi-body approach for frictional contact in spur gears," *Journal of sound and vibration*, vol. 278, pp. 479-499, 2004.
- [39] A. Heege, J. Betran, L. Bastard, and E. Lens, "Computation of dynamic loads of wind turbine power trains," *Mecánica Computacional*, vol. 26, pp. 2985-3004, 2007.
- [40] H. J. Sutherland and D. P. Burwinkle, "The spectral content of the torque loads on a turbine gear tooth," *Wind energy*, vol. 16, pp. 91-97, 1995.
- [41] Y. Guo, J. Keller, T. Moan, and Y. Xing, "Model Fidelity Study of Dynamic Transient Loads in a Wind Turbine Gearbox: Preprint," National Renewable Energy Laboratory (NREL), Golden, CO.2013.
- [42] A. R. Nejad, Z. Gao, and T. Moan, "Long-term analysis of gear loads in fixed offshore wind turbines considering ultimate operational loadings," *Energy Procedia*, vol. 35, pp. 187-197, 2013.
- [43] A. R. Nejad, Z. Gao, and T. Moan, "On long-term fatigue damage and reliability analysis of gears under wind loads in offshore wind turbine drivetrains," *International Journal of Fatigue*, vol. 61, pp. 116-128, 2014.
- [44] Y. Guo and R. G. Parker, "Analytical determination of back-side contact gear mesh stiffness," *Mechanism and Machine Theory*, vol. 78, pp. 263-271, 2014.

-
- [45] J. Lin and R. Parker, "Planetary gear parametric instability caused by mesh stiffness variation," *Journal of Sound and vibration*, vol. 249, pp. 129-145, 2002.
- [46] J. Lin and R. G. Parker, "Mesh stiffness variation instabilities in two-stage gear systems," *Journal of vibration and acoustics*, vol. 124, pp. 68-76, 2002.
- [47] R. Parker and J. Lin, "Mesh phasing relationships in planetary and epicyclic gears," *Journal of Mechanical Design*, vol. 126, pp. 365-370, 2004.
- [48] W. Shi, C.-W. Kim, C.-W. Chung, and H.-C. Park, "Dynamic modeling and analysis of a wind turbine drivetrain using the torsional dynamic model," *International journal of precision engineering and manufacturing*, vol. 14, pp. 153-159, 2013.
- [49] M. Todorov, G. Vukov, and J. Genov, "Parametric Torsional Vibrations of a Drive Train of a Wind Turbine with Faults in Meshing Stiffness," *Proc. of CFSE-2010*, 2010.
- [50] G. Mandic, A. Nasiri, E. Muljadi, and F. Oyague, "Active torque control for gearbox load reduction in a variable-speed wind turbine," *IEEE Transactions on Industry Applications*, vol. 48, pp. 2424-2432, 2012.
- [51] I. P. Girsang, J. S. Dhupia, E. Muljadi, M. Singh, and L. Y. Pao, "Gearbox and drivetrain models to study dynamic effects of modern wind turbines," *IEEE Transactions on Industry Applications*, vol. 50, pp. 3777-3786, 2014.
- [52] J. Gallego-Calderon and A. Natarajan, "Assessment of wind turbine drive-train fatigue loads under torsional excitation," *Engineering Structures*, vol. 103, pp. 189-202, 2015.
- [53] A. R. Nejad, P. F. Odgaard, Z. Gao, and T. Moan, "A prognostic method for fault detection in wind turbine drivetrains," *Engineering Failure Analysis*, vol. 42, pp. 324-336, 2014.
- [54] A. R. Nejad, Z. Jiang, Z. Gao, and T. Moan, "Drivetrain load effects in a 5-MW bottom-fixed wind turbine under blade-pitch fault condition and emergency shutdown," in *Journal of Physics: Conference Series*, 2016, p. 112011.

-
- [55] C. Zhu, S. Chen, C. Song, H. Liu, H. Bai, and F. Ma, "Dynamic analysis of a megawatt wind turbine drive train," *Journal of Mechanical Science and Technology*, vol. 29, pp. 1913-1919, 2015.
- [56] Y. Guo, R. Bergua, J. Dam, J. Jove, and J. Campbell, "Improving wind turbine drivetrain designs to minimize the impacts of non-torque loads," *Wind Energy*, vol. 18, pp. 2199-2222, 2015.
- [57] Y. Guo and J. Keller, "Investigation of high-speed shaft bearing loads in wind turbine gearboxes through dynamometer testing," *Wind Energy*, vol. 21, pp. 139-150, 2018.
- [58] D. Qin, J. Wang, and T. C. Lim, "Flexible multibody dynamic modeling of a horizontal wind turbine drivetrain system," *Journal of Mechanical Design*, vol. 131, p. 114501, 2009.
- [59] J. Helsen, F. Vanhollebeke, B. Marrant, D. Vandepitte, and W. Desmet, "Multibody modelling of varying complexity for modal behaviour analysis of wind turbine gearboxes," *Renewable Energy*, vol. 36, pp. 3098-3113, 2011.
- [60] J. Helsen, D. Vandepitte, and W. Desmet, "Flexible modelling of wind turbine gearboxes with special focus on shaft flexibilities," in *Proceedings of 10th international conference on recent advances in structural dynamics (RASD)*, 2010.
- [61] A. Kahraman, "Effect of axial vibrations on the dynamics of a helical gear pair," *Journal of Vibration and Acoustics*, vol. 115, pp. 33-39, 1993.
- [62] F. Oyague, "Progressive Dynamical Drive Train Modeling as Part of NREL Gearbox Reliability Collaborative: Preprint," National Renewable Energy Laboratory (NREL), Golden, CO.2008.
- [63] J. Helsen, B. Marrant, F. Vanhollebeke, F. De Coninck, D. Berckmans, D. Vandepitte, *et al.*, "Assessment of excitation mechanisms and structural flexibility influence in excitation propagation in multi-megawatt wind turbine gearboxes: experiments and flexible multibody model optimization," *Mechanical Systems and Signal Processing*, vol. 40, pp. 114-135, 2013.
- [64] T. M. Ericson and R. G. Parker, "Planetary gear modal vibration experiments and correlation against lumped-parameter and finite element models," *Journal of sound and vibration*, vol. 332, pp. 2350-2375, 2013.

-
- [65] A. Kahraman, A. Kharazi, and M. Umrani, "A deformable body dynamic analysis of planetary gears with thin rims," *Journal of sound and vibration*, vol. 262, pp. 752-768, 2003.
- [66] K. Mao, "Gear tooth contact analysis and its application in the reduction of fatigue wear," *Wear*, vol. 262, pp. 1281-1288, 2007.
- [67] S. Baud and P. Velex, "Static and dynamic tooth loading in spur and helical geared systems-experiments and model validation," *Journal of Mechanical Design*, vol. 124, pp. 334-346, 2002.
- [68] A. Heege, J. Betran, and Y. Radovicic, "Fatigue load computation of wind turbine gearboxes by coupled finite element, multi-body system and aerodynamic analysis," *Wind Energy*, vol. 10, pp. 395-413, 2007.
- [69] Y. Xing and T. Moan, "Multi-body modelling and analysis of a planet carrier in a wind turbine gearbox," *Wind Energy*, vol. 16, pp. 1067-1089, 2013.
- [70] L. Vedmar and A. Andersson, "A method to determine dynamic loads on spur gear teeth and on bearings," *Journal of Sound and Vibration*, vol. 267, pp. 1065-1084, 2003.
- [71] F. Rasmussen, K. Thomsen, and T. J. Larsen, "The gearbox problem revisited," *Risø Fact-Sheet AED-RB-17 (en)*, *Risø National Laboratory, Roskilde, Denmark*, 2004.
- [72] M.-H. Evans, "White structure flaking failure in bearings under rolling contact fatigue," University of Southampton, 2013.
- [73] S. Sheng, "Wind turbine gearbox condition monitoring round Robin study-vibration analysis," National Renewable Energy Lab.(NREL), Golden, CO (United States)2012.
- [74] International Organisation for Standardization ISO-10825:1995, "ISO 10825:1995: Gears - Wear and damage to gear teeth - Terminology," 1995.
- [75] T. Bruce, H. Long, and R. S. Dwyer-Joyce, "Dynamic modelling of wind turbine gearbox bearing loading during transient events," *IET Renewable Power Generation*, vol. 9, pp. 821-830, 2015.
- [76] P. Fernandes and C. McDuling, "Surface contact fatigue failures in gears," *Engineering Failure Analysis*, vol. 4, pp. 99-107, 1997.

-
- [77] P. Fernandes, "Tooth bending fatigue failures in gears," *Engineering Failure Analysis*, vol. 3, pp. 219-225, 1996.
- [78] R. Errichello and J. Muller, "Gearbox Reliability Collaborative Gearbox 1 Failure Analysis Report: December 2010-January 2011," National Renewable Energy Laboratory (NREL), Golden, CO.2012.
- [79] International Organisation for Standardization BS ISO15243: 2017 "*Rolling bearings damage and failures terms, characteristics and causes*", 2017.
- [80] H. Al-Tameemi, H. Long, and R. Dwyer-Joyce, "Investigation of wind turbine gearbox bearing subsurface damage considering transient loading," in *WindEurope Summit*, 2016.
- [81] M. Matsuishi and T. Endo, "Fatigue of metals subjected to varying stress," *Japan Society of Mechanical Engineers, Fukuoka, Japan*, vol. 68, pp. 37-40, 1968.
- [82] S. D. Downing and D. Socie, "Simple rainflow counting algorithms," *International journal of fatigue*, vol. 4, pp. 31-40, 1982.
- [83] ASTM, "E1049," in *Standard Practices for Cycle Counting in Fatigue Analysis, Phila-delphia, PA* vol. 19, ed, 1985.
- [84] International Organisation for Standardization BS IEC61400-1:2013,"Wind turbines: Design requirements," 2013.
- [85] J. Bannantine, "Fundamentals of metal fatigue analysis," *Prentice Hall, 1990*, p. 273, 1990.
- [86] International Organisation for Standardization *ISO/IEC 81400-4:2005*, "Wind Turbines – Part 4: Standard for Design and Specification of Gearboxes," 2005.
- [87] A. G. Rodriguez, A. G. Rodríguez, and M. B. Payán, "Estimating wind turbines mechanical constants," in *Proc. Int. Conf. Renewable Energies and Power Quality (ICREPQ'07)*, 2007, pp. 27-30.
- [88] W. Shi, H.-C. Park, S. Na, J. Song, S. Ma, and C.-W. Kim, "Dynamic analysis of three-dimensional drivetrain system of wind turbine," *International journal of precision engineering and manufacturing*, vol. 15, pp. 1351-1357, 2014.

-
- [89] W. F. Hahn, "Study of instantaneous load to which gear teeth are subjected," University of Illinois at Urbana-Champaign, 1969.
- [90] H. H. Lin and C.-H. Liou, "A parametric study of spur gear dynamics," MEMPHIS UNIV TN1998.
- [91] International Organisation for Standardization BS ISO 6336-5:2016 "Calculation of load capacity of spur and helical gears - Part 5: Strength and quality of materials," 2016.
- [92] R. Kasuba and J. W. Evans, "An extended model for determining dynamic loads in spur gearing," *Journal of mechanical design*, vol. 103, pp. 398-409, 1981.
- [93] J. M. Jonkman, MLB Jr, "FAST User's Guide, 2005.
- [94] E. Bossanyi, "GH Bladed user manual," *Garrad Hassan Bladed*, 2009.
- [95] The MathWorks, "Simscape User's Guide, " MA, USA 2012.
- [96] A. Romero, Y. Lage, S. Souza, B. Wang, and T.-H. Gan, "Vestas V90-3MW Wind Turbine Gearbox Health Assessment Using a Vibration-Based Condition Monitoring System," *Shock and Vibration*, vol. 2016, 2016.
- [97] G. S. Doman, "Structural Dynamic Considerations in Wind Turbine Design," in *Wind Turbine Technology: Fundamental Concepts in Wind Turbine Engineering, Second Edition*, ed: ASME Press, 2009.
- [98] G. Sieros, P. Chaviaropoulos, J. D. Sørensen, B. Bulder, and P. Jamieson, "Upscaling wind turbines: theoretical and practical aspects and their impact on the cost of energy," *Wind energy*, vol. 15, pp. 3-17, 2012.
- [99] J. F. Manwell, J. G. McGowan, and A. L. Rogers, *Wind energy explained: theory, design and application*. John Wiley & Sons, 2010.
- [100] K. Scott, D. Infield, N. Barltrop, J. Coultate, and A. Shahaj, "Effects of extreme and transient loads on wind turbine drive trains," in *50th AIAA Aerospace Sciences Meeting including the New Horizons Forum and Aerospace Exposition*, 2011, p. 1293.
- [101] L. Mauer, "Force element 225 gear wheel," *Internal Repo~, Intec GmbH, Wessling, Germany*, 2005.

-
- [102] International Organisation for Standardization DIN, "Calculation of Load Capacity of Cylindrical Gears; Introduction and General Influence Factors," in *1-12* vol. 12, ed. Berlin: Beuth-Verlag, 1987.
- [103] International Organisation for Standardization ISO 6336–3:2006 "Calculation of load capacity of spur and helical gears-part 3: calculation of tooth bending strength," 2006.
- [104] S. Timoshenko and J. Gere, "Mechanics of Materials. van Nordstrand Reinhold Company," *New York*, 1972.
- [105] A. R. Nejad, Y. Xing, Y. Guo, J. Keller, Z. Gao, and T. Moan, "Effects of floating sun gear in a wind turbine's planetary gearbox with geometrical imperfections," *Wind Energy*, vol. 18, pp. 2105-2120, 2015.
- [106] Y. Guo and R. G. Parker, "Stiffness matrix calculation of rolling element bearings using a finite element/contact mechanics model," *Mechanism and machine theory*, vol. 51, pp. 32-45, 2012.
- [107] W. LaCava, Y. Xing, Y. Guo, and T. Moan, "Determining wind turbine gearbox model complexity using measurement validation and cost comparison," *European Wind Energy Association Annual Event, Copenhagen, Denmark, April*, pp. 16-19, 2012.
- [108] International Organisation for Standardization ISO/TS16281:2008, "Rolling bearings-methods for calculating the modified reference rating life for universally loaded bearings," 2008.
- [109] "Simpack Documentation," Simpack, 2016.
- [110] T. A. Harris and M. N. Kotzalas, *Advanced concepts of bearing technology: rolling bearing analysis*. CRC Press, 2006.
- [111] G. Niemann and H. Winter, *Maschinenelemente: Band 2: Getriebe allgemein, Zahnradgetriebe-Grundlagen, Stirnradgetriebe*. Springer-Verlag, 2013.
- [112] H. Hertz, "Hertz's miscellaneous papers," ed: MacMillan, London, 1881.
- [113] R. G. Budynas and J. K. Nisbett, *Shigley's mechanical engineering design* vol. 9: McGraw-Hill New York, 2008.
- [114] R. L. Norton, "Machine design: an integrated approach, 1996," *Prentice-Hall Inc: NJ, USA*, 2000.

-
- [115] G. Fajdiga, "COMPUTATIONAL FATIGUE ANALYSIS OF CONTACTING MECHANICAL ELEMENTS," *Tehnicki vjesnik/Technical Gazette*, vol. 22, 2015.
- [116] A. Palmgren, "Die Lebensdauer von Kugellagern (Durability of ball bearings)," *ZDVD*, vol. 68, p. 339, 1924.
- [117] M. A. Miner, "Cumulative damage in fatigue," *J. appl. Mech.*, vol. 12, pp. A159-A164, 1945.
- [118] G. Lundberg and A. Palmgren, "Dynamic capacity of rolling bearings," *Journal of Applied Mechanics-Transactions of the ASME*, vol. 16, pp. 165-172, 1949.
- [119] M. F. Jørgensen, N. L. Pedersen, and J. N. Sørensen, "Gear fatigue damage for a 500 kW wind turbine exposed to increasing turbulence using a flexible multibody model," *Modeling, Identification and Control*, vol. 35, p. 109, 2014.
- [120] Y. Guo, J. Keller, and W. LaCava, "Combined Effects of Gravity, Bending Moment, Bearing Clearance, and Input Torque on Wind Turbine Planetary Gear Load Sharing: Preprint," National Renewable Energy Laboratory (NREL), Golden, CO.2012.
- [121] F. Oyague, C. Butterfield, and S. Sheng, "Gearbox reliability collaborative analysis round robin," *National Renewable Energy Laboratory, Golden, CO, Report No. NREL/CP-500-45325*, 2009.
- [122] International Organisation for Standardization BS EN61400-4:2013, "Wind turbines Part 4: Design requirements for wind turbine gearboxes," 2013.
- [123] G. Lloyd, "Guideline for the certification of wind turbines," *Germanischer Lloyd Industrial Services*, 2003.
- [124] Y. Guo, J. Keller, and W. LaCava, "Planetary gear load sharing of wind turbine drivetrains subjected to non-torque loads," *Wind Energy*, vol. 18, pp. 757-768, 2015.
- [125] International Organisation for Standardization ISO 281:2007, "Rolling Bearing—Dynamic Load Ratings and Rating Life," 2007.

- [126] Z. Jiang, Y. Xing, Y. Guo, T. Moan, and Z. Gao, "Long-term contact fatigue analysis of a planetary bearing in a land-based wind turbine drivetrain," *Wind Energy*, vol. 18, pp. 591-611, 2015.
- [127] T. Bruce, E. Rounding, H. Long, and R. Dwyer-Joyce, "Characterisation of white etching crack damage in wind turbine gearbox bearings," *Wear*, vol. 338, pp. 164-177, 2015.